The Aerostatic Seal: Analysis and Development of a New Dynamic Seal Concept for Steam Turbine Application

ANDREW MESSENGER

The Aerostatic Seal: Analysis and Development of a New Dynamic Seal Concept for Steam Turbine Application

Andrew Messenger

A thesis presented for the degree of

Doctor of Philosophy

Department of Engineering

Durham University

United Kingdom

2018

"An expert is a person who has made all the mistakes that can be made in a very narrow field."

Niels Bohr

The Aerostatic Seal: Analysis and Development of a New Dynamic Seal Concept for Steam Turbine Application

Andrew Messenger

Submitted for the degree of Doctor of Philosophy

Abstract

This thesis describes the development of a new seal concept for steam turbines called the Aerostatic Seal. The Aerostatic Seal is a dynamic seal, and so can respond to rotor radial movement to maintain a low clearance between the seal and the rotor. As the seal is dynamic, smaller clearances can be achieved without rotor contact compared to conventional static seals such as the labyrinth seal, hence increasing the efficiency of the turbine through reduced leakage. Furthermore, as the seal is dynamic it can tolerate larger radial transients typically found during start up and shut down of the steam turbine, and so also contributes to increasing the flexibility of the turbine plant.

In this thesis an analytical design and analysis methodology was developed for the Aerostatic Seal. The methodology was used to generate a number of seal designs which were experimentally tested in a non-rotating test facility using room temperature air. The results confirmed that the seal would operate dynamically, and the experimental campaign provided valuable data on the operation of the seal. The non-rotating rig was also used to test a second generation seal design.

The seal was then tested in a rotating test facility, which modelled high speed rotor radial transients with an adjustable eccentric rotor. The Aerostatic Seal demonstrated the ability to respond to high speed transients.

A final test campaign was conducted in the high temperature steam rig at TU Braunschweig, Germany, enabling experimental demonstration of the Aerostatic Seal using realistic materials and represented realistic steam turbine conditions.

Finally, based on the experimental and analytical work carried out within this thesis, a proposed Aerostatic Seal design for steam turbine implementation is presented.

Declaration

The work in this thesis is based on research carried out in the Department of Engineering at Durham University. No part of this thesis has been submitted elsewhere for any other degree or qualification. It is all my own work unless referenced to the contrary in the text.

Acknowledgement

I would like to thank my supervisors, Grant Ingram, Richard Williams and Simon Hogg, for their expert supervision over the four years. I would also like to acknowledge the work of Richard Williams designing the 'Durham University Rotating Seals Rig' which was used to test the Aerostatic Seal.

I would also like to thank the Centre for Doctoral Training in Energy at Durham University. I am grateful for the extra 6 months of funding and the free lunch on Fridays! The seminars and workshops have broadened my knowledge on all aspects of energy.

Jon Seaton, Stacie Tibos, Bernard Charnley and Adrian Lord of GE Power in Rugby deserve mention for their input to and support of the project. Jon Seaton in particular for inventing the Aerostatic Seal.

I would also like to acknowledge the support of the mechanical and electrical workshops for their technical support and skill manufacturing various parts over the course of the project. The assistance of Gary Parker in the thermo lab was also much appreciated.

Thanks are also due to the Durham University Solar Car project. Whilst being a member of the team actively prevented work on this thesis, and delayed it's writing by several months, the chance to go on a 'once in a lifetime trip' twice was amazing. Finally I would like to mention all members of Team Turbo, past and present, the Ustinov GCR executive committee 2014-2015, the Durham Massive, and Mam, Dad, Amy and Sean.

This work was supported by the Engineering and Physical Sciences Research Council [grant number EP/K02115X/1] and GE Power, Rugby.

Contents

List of Figures

List of Tables

Nomenclature

Symbol	Definition		Unit	Dimension
A_c	Clearance area		m^2	L^2
A_{cf}	Contact face area		m^2	L^2
A_f	Area of single feed hole	$A_f = \frac{\pi d^2}{4}$	m^2	L^2
A_r	Projected radial area		m^2	L^2
A_s	Surface area of segment side		m^2	L^2
A_Δ	Area experiencing pressure difference		m^2	L^2
a	Acceleration of seal segment		$\mathrm{m\,s}^{-2}$	LT^{-2}
a_c	Streamline area (Fig. 2.3)		m^2	L^2
a_{cont}	Area of contact face		m^2	L^2
C_D	Discharge coefficient		1	-
Cf_r	Radial force coefficient	$Cf_r = \frac{F_r}{\Delta P A_r}$	1	-
Cf_s	Radial side force coefficient	$Cf_s = \frac{F_s}{\frac{1}{2}\Delta P A_s}$	1	-
Cf_μ	Frictional force coefficient	$Cf_\mu = \frac{F_r}{\Delta P A_r}$	1	-
C_{ke}	Kinetic energy carry over coefficient		1	-
Cp	Pressure coefficient	$Cp_i = \frac{P_i - P_{out}}{\Delta P}$	1	-
c	Clearance		m	L
c_m	Mean clearance		m	L
c_r	Centroid radial coordinate		m	L
c_x	Centroid axial coordinate		m	L
c_{ret}	Seal retracted clearance		m	L
c_p	Specific isobaric heat capacity		$\mathrm{J\,kg}^{-1}\,\mathrm{K}^{-1}$	$L^2T^{-2}\Theta^{-1}$
D	Rotor diameter		m	L

Continued on next page

Continued from previous page

Symbol	Definition	Unit	Dimension
D_H	Hydraulic diameter	m	L
d	Feed hole diameter	m	L
e	Eccentricity	m	L
F_{ax}	Total axial spring force	N	MLT^{-2}
$F_{ax0,1,2,3}$	Individual axial spring force	N	MLT^{-2}
F_{gr}	Radially resolved segment weight	N	MLT^{-2}
F_{pr}	Radial pressure force	N	MLT^{-2}
F_{px}	Axial pressure force	N	MLT^{-2}
F_r	Net radial force excluding friction and inertia	N	MLT^{-2}
F_s	Side pressure force resolved radially	N	MLT^{-2}
F_{sp}	Total radial spring force per segment	N	MLT^{-2}
F_{sp0}	Spring pre load	N	MLT^{-2}
F_{spk}	Spring force due to spring compression	N	MLT^{-2}
F_x	Net axial force	N	MLT^{-2}
F_μ	Frictional force	N	MLT^{-2}
f	Darcy friction factor	1	-
g	Acceleration due to gravity	$\mathrm{m\,s^{-2}}$	LT^{-2}
h	Specific enthalpy	$\mathrm{J\,kg^{-1}}$	L^2T^{-2}
I	Integral		
i	Restriction number	1	-
k_{ax}	Axial spring stiffness	$\mathrm{N\,m^{-1}}$	MT^{-2}
k_{sp}	Spring stiffness	$\mathrm{N\,m^{-1}}$	MT^{-2}
L_{fr}	Length of spring when segment retracted	m	L
L_{sp0}	Free length of spring	m	L
l	Turbulent length scale	m	L
M	Mach number	1	-
M_{px}	Pressure moment about axial direction	N m	ML^2T^{-2}
$M_{p\theta}$	Pressure moment about tangential axis	N m	ML^2T^{-2}

Continued on next page

Continued from previous page

Symbol	Definition		Unit	Dimension
M_r	Net applied moment about radial axis		N m	ML^2T^{-2}
M_x	Net applied moment about axial axis		N m	ML^2T^{-2}
M_θ	Net applied moment about tangential axis		N m	ML^2T^{-2}
M_μ	Frictional moment about x axis		N m	ML^2T^{-2}
m	Mass of seal segment		kg	M
$\dot{m}$	Mass flow rate		kg s^{-1}	MT^{-1}
$\hat{\dot{m}}$	Standardised mass flow rate		kg s^{-1}	MT^{-1}
N	Number of restrictions/fins		1	-
P	Pressure		Pa	$ML^{-1}T^{-2}$
PR	Pressure ratio	$PR = \frac{P_{in}}{P_{out}}$	1	-
Q	Volumetric flow rate		m^3 s^{-1}	M^3T^{-1}
q	Under-relaxation factor		1	-
R	Specific gas constant		J kg^{-1} K^{-1}	$L^2T^{-2}\Theta^{-1}$
R_x	Axial reaction force		N	MLT^{-2}
Re_{D_H}	Reynolds number based on hydraulic diameter	$Re_{D_H} = \frac{\rho v D_H}{\eta}$	1	-
Re_x	Axial Reynolds number	$Re_x = \frac{2\dot{m}}{\eta\pi D} = \frac{2\rho v c_m}{\eta}$	1	-
R_σ	Contact stress ratio		1	-
r	Radial dimension / radial coordinate		m	L
$\hat{r}$	Radial dimension about centroid		m	L
s	Labyrinth fin pitch		m	L
s	Specific entropy		J kg^{-1}	L^2T^{-2}
T	Temperature		K	Θ
Ta	Taylor number	$Ta = \frac{2uc_m\rho}{\eta}\sqrt{\frac{2c_m}{D}}$	1	-
t	Thickness of contact face		m	L
t	Time		s	T
u	Rotor surface velocity		m s^{-1}	LT^{-1}
V	Volume		m^3	L^3
V	Voltage		V	$M^{\frac{1}{2}}L^{\frac{1}{2}}T^{-1}$

Continued on next page

Continued from previous page

Symbol	Definition		Unit	Dimension
v	Fluid velocity		m s^{-1}	LT^{-1}
v_r	Radial rotor displacement		m	L
$\dot{v}_r$	Radial rotor velocity		m s^{-1}	LT^{-1}
x	Axial dimension or axial coordinate		m	L
z	Vertical coordinated		m	L
α	Seal segment angle		◦	-
β	Circumferential pocket angle		◦	-
Γ	Kinetic energy carry over fraction		1	-
γ	Ratio of specific heats		1	-
ΔP	Pressure difference	$\Delta P = P_{in} - P_{out}$	Pa	$ML^{-1}T^{-2}$
δ	Gravitational angle		◦	-
ϵ	Expansibility factor		1	-
ζ	Friction moment coefficient		m	L
η	Dynamic viscosity		Pa s	$ML^{-1}T^{-1}$
θ	Tangential coordinate		◦	-
Λ	Turbulent intensity		%	-
μ	Coefficient of friction		1	-
μ_{stat}	Coefficient of static friction		1	-
ξ	Moment criterion		1	-
ρ	Fluid density		kg m^{-3}	ML^{-3}
σ	Contact stress		Pa	$ML^{-1}T^{-2}$
Φ	Objective function		1	-
ϕ	Angle about θ axis		◦	-
ψ	Angle about x axis		◦	-
ω	Rotor angular velocity		rad s^{-1}	T^{-1}

Table of Subscripts

	Definition
$ax0, 1, 2, 3$	Axial spring 0,1,2,3
Down	Downstream
DRS	Down Rotation Side
f	Feed hole
in	Inlet to seal
Max.	Maximum
Min.	Minimum
n	Iteration
out	Outlet from seal
s	Standard conditions
t	Top surface (e.g. Cp_t)
Up	Upstream
URS	Up Rotation Side
0	Stagnation quantity
1,2,3	First, second and third seal pockets

Chapter 1

Introduction

The steam turbine is one of mankind's most important inventions. The steam turbine revolutionised electricity production and hence helped create the modern society. Invention of the modern steam turbine is largely attributed to Charles Parsons in 1884 [1], [2], although important contributions were made by Carl Gustav de Laval, Auguste Rateau and Charles Curtis [3].

Today the steam turbine is responsible for generating electricity from coal, nuclear fission and biomass, and forms part of a combined cycle gas turbine (CCGT) plant. Table 1.1 shows the different fuels used globally to generate electricity, and the percentage contribution of each fuel to meet world electrical demand. The steam turbine is responsible for the majority of electricity production worldwide.

In the future the steam turbine is likely to remain generating significant proportions

Fuel Type	Percentage	Turbine type
Coal	39.3	Steam
Oil	4.1	Steam
Gas	22.9	GT (66 %) & ST (33 %) approx.
Nuclear	10.6	Steam
Hydro	16.0	Hydraulic
Solar, wind, geothermal, tide	4.9	Various
Biofuels & waste	2.2	Steam
		Approx 63.8 % from Steam Turbine

Table 1.1: 2015 world gross electricity production by fuel type. Data from the International Energy Agency [4].

of world electricity in technologies such as 'small modular reactors' (SMR) [1], concentrated solar power (CSP) plants [6], biomass and nuclear fusion [7] (assuming that technology reaches maturity).

Overall, improvements to the steam turbine will have significant impact on current and future electricity production.

1.1 Future energy challenges

As shown in Table 1.1, the generation of electricity worldwide is as of 2015 still dominated by fossil fuels, and with coal as the largest single fuel source [4]. The fuels used to generate electricity are constantly changing as new technologies emerge, fuel prices change, or due to political will. Now there is also the requirement to reduce greenhouse gas emissions, principally carbon dioxide (CO_2), to prevent excessive global warming [8].

To reduce the CO_2 emitted generating electricity by burning fossil fuels, and to meet demand once fossil fuels have ran out, there is increasing deployment of renewable and low carbon electricity resources.

Figure 1.1 displays the total yearly electricity supplied from the major types of electrical generation in the UK, using data taken from the UK Department for Business, Energy and Industrial Strategy quarterly 'Energy Trends' reports [9]–[14]. Since 2010 the electricity produced by wind and solar PV has risen to over 14% of total electricity production. The amount of electricity generated by low carbon technologies is likely to increase as the cost of these technologies decreases.

The increased deployment of new intermittent sources of electricity onto the grid, and the desire to reduce CO_2 emissions, creates new challenges for conventional power generation plant.

Challenge 1: Increased flexibility. Wind and solar are intermittent energy resources, and so this means that the amount of electricity produced depends on the weather. Whilst it is largely predictable over a 24 to 48 hour time scale, it is not possible to produce electricity when there is no wind and no sun light. Therefore to meet consumer electrical demand, conventional generation technologies need to respond quickly. For the steam (and gas) gas turbine, this means starting more frequently and reaching full

[1] Small nuclear fission reactors, typically with an electrical output less than 700 MW [5]

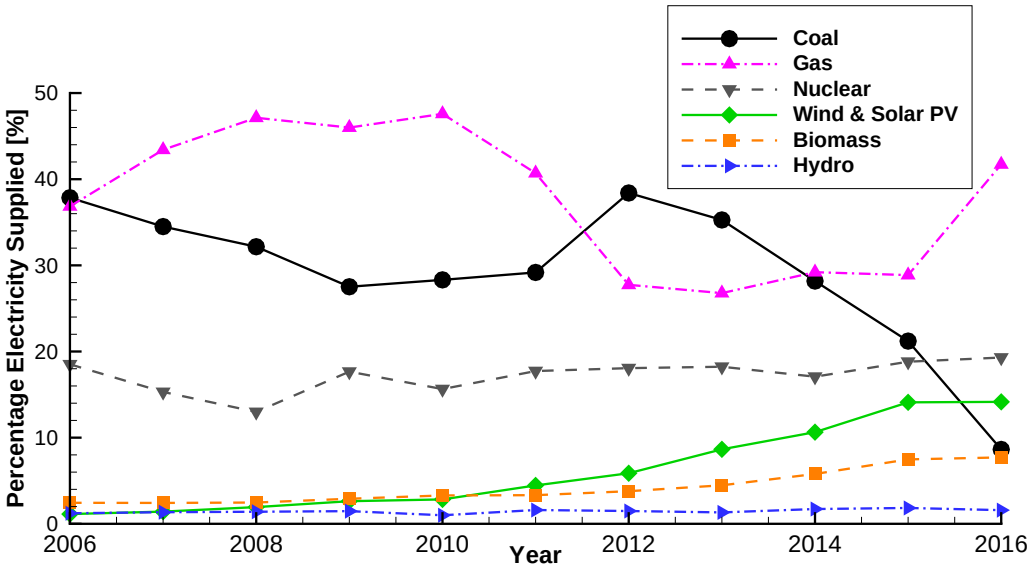

Figure 1.1: Percentage UK electricity supplied by fuel type. Data from [9]–[14]

load as fast as possible.

More frequent and faster starts has its own challenge for the steam turbine: i) differential thermal expansion of turbine rotor and casing during start up [15], and ii) thermal stress and low cycle fatigue (LCF) of turbine components [16]–[18]. Differential thermal expansion requires detailed assessment of axial and radial turbine clearance to ensure that adequate clearance is maintained during turbine start [19], [20], increasing leakage and decreasing efficiency, and raising the temperature of the turbine slow enough that the thermal gradients have time to even out, reducing the differential expansion. Differential thermal expansions of the rotor cause maximum stress as the rotor is heating up, and so increased number of fast starts decreases the life of the turbine.

Challenge 2: Increased efficiency. Increasing the efficiency of the turbine ultimately reduces the amount of fuel required to generate the same quantity of electrical energy. Therefore increasing the efficiency reduces the amount of CO_2 emitted and also reduces the operating cost of the turbine.

This thesis contributes to these two challenges by developing a new dynamic seal called the **Aerostatic Seal**. A seal is used between rotating and non-rotating components to limit the amount of steam leaking between turbine stages and from the turbine itself. Steam that does not pass through the blade passages produces no work and hence reduces the efficiency of the turbine. Also the leakage flow can disrupt the flow

through the blade passages further decreasing efficiency. The seal also has to tolerate relative movement between the rotating and non-rotating components, and so is affected by the differential thermal expansions. For a fixed seal, such as the labyrinth seal commonly employed in turbomachinery (see Section 2.2.1), this means that the clearance must be sufficient to prevent the rotor coming into contact with the seal, causing damage. To tolerate large differential thermal expansions and rotor excursions a fixed seal such as the labyrinth seal requires a greater clearance, therefore increasing the leakage flow through the seal, decreasing the overall efficiency of the turbine. Installing new seals in a steam turbine to reduce leakage is a cost effective way of increasing the power output and efficiency of the steam turbine [21].

A dynamic seal, such as the Aerostatic Seal, is a seal that is able to respond to the rotor movements. Therefore the seal can maintain a small clearance to reduce the leakage flow and increasing the turbine efficiency, but also tolerate radial rotor movements.

1.2 The Aerostatic Seal: a new dynamic seal

The Aerostatic Seal is a new dynamic seal invented by Jon Seaton [22]. The seal is similar in construction to the 'retractable seal' (see Section 2.2.2) which has seen wide deployment in steam turbines already. Figure 1.2 shows a potential application of the Aerostatic Seal in a low reaction steam turbine diaphragm.

The seal is made up from a number of circumferential seal segments; each seal segment consists of a labyrinth seal with an enlarged central pocket supplied with fluid from immediately upstream of the seal [22]. This central pressurised pocket allows the seal segment to move away from the rotor when at low clearances, preventing the seal contacting the rotor surface. At high clearances reduced pressure in the central pocket moves the seal towards the rotor surface. As in a retractable seal, the seal segments are held apart by springs which push the seal segment radially out from the rotor when there is no pressure drop across the seal, shown in Fig. 1.2. The seal segments are pushed against the contact face of the seal holder by the difference between upstream and downstream pressure, and to be able to move each segment has to overcome the frictional force between the holder and seal segment. Each seal segment is also divided circumferentially to create circumferential pockets, each one with its own feed

hole. These pockets are intended to ensure that each seal segment maintains an even clearance along the circumferential length of the segment. See Section 3.2 for a full description of the operation of the Aerostatic Seal.

The standard design of the Aerostatic Seal shown in Fig. 1.2, is referred to as the Generation Ⅰ design, and is the focus of most of the investigation in this thesis. The seal is as drawn in Fig. 1.2 with no rotor castellations as in the retractable seal typically deployed in a steam turbine diaphragm. The Generation Ⅱ design includes axial thrust compensation springs to reduce the frictional force acting on the seal segments.

The Aerostatic Seal was initially the subject of four MEng final year projects at Durham University, [23]–[26]. The work of Auld [23] and Rafferty [24] conducted initial investigation on the Aerostatic Seal by developing an analytical model and conducting computation fluid dynamics (CFD) studies, and showed that the Aerostatic Seal was worth experimental investigation. Durnan [25] developed an initial design for a non-rotating test facility that was used in this thesis, and MacDonald [26] designed the seal for initial testing. For full details see Section 2.5.

1.3 Project Objectives and Outline

This thesis documents the development of the Aerostatic Seal from October 2013 to October 2017, which was part of the Future Conventional Power Research Consortium, and received funding from the Engineering and Physical Sciences Research Council [grant number EP/K02115X/1] and GE Power, Rugby. The work on the Aerostatic Seal was largely experimental on two experimental facilities at Durham University. A third test facility using steam was utilised at TU Braunschweig. The analytical methodology of Auld and Rafferty [23], [24] was extended to produce Aerostatic Seal designs for use in the experimental campaigns.

The key aims of this project were as follows:

- Development of the analytical Aerostatic Seal design methodology.
- Experimental proof of concept of the Aerostatic Seal. This was initially in a non-rotating test facility operating in air, initial design work carried out by Durnan [25]. Following successful proof of concept in the non-rotating rig, the seal was tested in

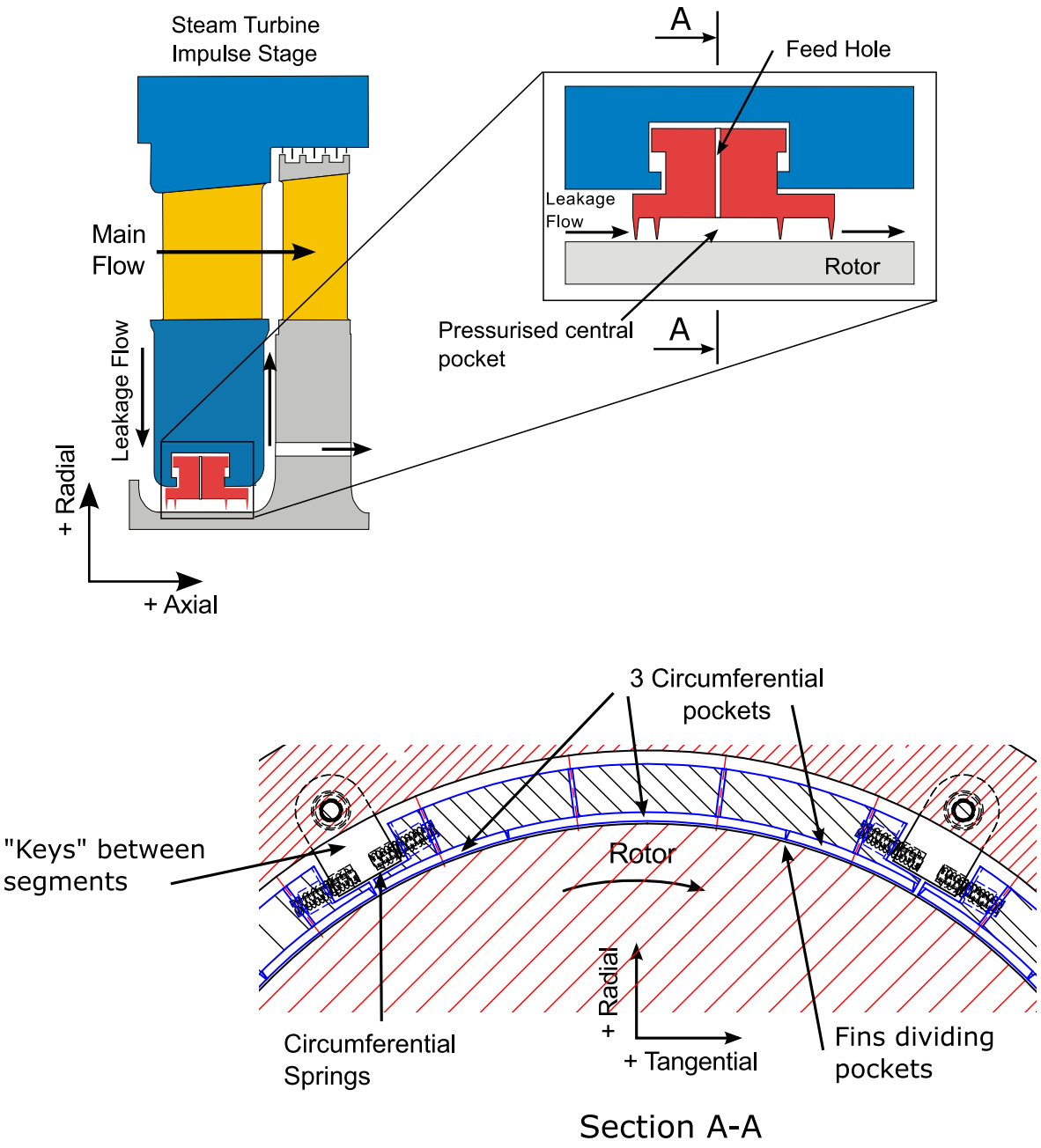

Figure 1.2: Diagram of the Aerostatic Seal.

a rotating test facility designed by Richard Williams.

- Experimental validation (or otherwise) of the design tool.
- Identify the key design features and parameters for a successful Aerostatic Seal design.

The remainder of the thesis begins with Chapter 2, a review of competing sealing concepts, with particular relevance to steam turbine application. Also discussed is the theory of the labyrinth seal as this was also relevant to the Aerostatic Seal, particularly for the design and analysis tool and understanding experimental results.

The design and analysis methodology is described in detail in Chapter 3. The chapter ends with a summary of the designs manufactured for testing in the experimental test campaigns.

The 'Non-Rotating test rig' and the 'Durham Rotating Seals Rig' are both described in Chapter 4. Tests were also conducted in the steam test rig at TU Braunschweig - this is briefly described in Chapter 9.

The experimental results from the 'Non-Rotating test rig' and the 'Durham Rotating Seals Rig' are described in Chapters 5 and 6 respectively. Chapter 5 begins with an overview of the whole test campaign across all of the test facilities.

Along the way a diversion was made to investigate the Gen II design, a possible Aerostatic Seal variant which used 'axial thrust compensation springs' to reduce the frictional force acting on the seal segment and hence make it more responsive. This is the subject of Chapter 7. The whole of Chapter 8 was dedicated to understanding why the seal segments would typically operate with one side of the seal segment at a lower clearance than the other.

Finally the thesis closes with experiments conducted in steam, and a description of a proposed Aerostatic Seal concept in Chapter 9, and conclusion in Chapter 10.

Overall the work described within this thesis has demonstrated the dynamic capabilities of the Aerostatic Seal, and leaves the seal in state ready for a first test in a steam turbine.

Chapter 2

Literature Review

2.1 Introduction

Today there are many different and competing sealing technologies available to the designer of turbomachines. However until recently it was only the labyrinth seal that has seen wide scale deployment into steam turbines. Developments of the labyrinth seal have been implemented into steam turbines, such as the retractable gland and spring back gland (Section 2.2.2), and more recently the brush seal (Section 2.3.1). As the designer of the steam turbine has tried to achieve higher efficiency and lower cost, novel seals are under consideration, including the Aerostatic Seal. In order to place the Aerostatic Seal into context, and the role that the Aerostatic Seal would play in the sealing technologies available to the designer, a review of existing and potential technologies is reviewed in this chapter.

Within this thesis, different sealing technologies applicable to steam turbines have been divided as follows:

- **Non-contacting seals.** These are fixed seals with a clearance between the seal and the rotor. Discussed here are the labyrinth seal, the retractable seal and the fluidic seal.
- **Compliant seals.** These seals are made from a series of flexible 'seal elements' that contact the rotor, but are compliant to allow rotor movement. Examples discussed here are the brush seal, finger seal and leaf seal.
- **Dynamic seals.** These are seals that dynamically respond to the rotor position,

and typically operate at very low clearances. Seal types in this category are the Dry Gas Seal (DGS), floating ring annular seal, the HALO seal, and the Aerostatic Seal, the subject of this thesis.

2.2 Non-contacting seals

Non-contacting seals maintain a small, constant clearance between the rotating and non-rotating components. The designer of such a seal is faced with the challenge of minimising the leakage through the seal, which is achieved by minimising the clearance, but also allowing enough clearance to allow for rotordynamic movement or thermal growth of the rotor. Therefore non-contacting seals typically have a relatively large leakage compared to compliant or dynamic seals, but have the advantage of being relatively cheap to manufacture.

2.2.1 Labyrinth seal

The labyrinth seal was the invention of Charles Parsons, and was introduced at the same time as the steam turbine [27], [28]. The popularity of the labyrinth seal in steam and gas turbines is due to their ease of manufacture and inexpensiveness, even though reduced leakage can be obtained using other types of seal (such as brush seals for example) [29].

Labyrinth seals are a series of restrictions, found in various different configurations shown in Fig. 2.1. The fluid accelerates to travel under each restriction and then expands uncontrollably in the next cavity. Some of the kinetic energy gained from the loss of static pressure is lost through viscous effects in the uncontrollable expansion by formation of turbulent vortices, hence reducing the total pressure of the fluid.

There are many variants of labyrinth seals. Typically 'see through' or 'straight' labyrinth seals (Fig. 2.1a) have the worst leakage performance but the lowest manufacture cost, while stepped (Fig. 2.1b), Castellated (Fig. 2.1c) or staggered (Fig. 2.1d) labyrinth seals have the best leakage performance due to the obstruction of the high velocity jet from under the tooth. This high velocity jet continuing under the next restriction results in kinetic energy carry over, which reduces the effectiveness of the seal. Inclined fin seals (Fig. 2.1e) have improved leakage characteristics over non-inclined fins at the expense

of decreased leakage performance if the flow is reversed due to changing pressure conditions.

Other configurations of labyrinth seal have abradable coatings (Fig. 2.1f) or honeycomb materials opposite the labyrinth fins. This allows the seal to cut the minimum necessary clearance, minimising the leakage. This will be the clearance when the rotor goes through an excursion or has expanded due machine heating, so a compliant seal could operate at a lower clearance during more stable conditions. The honeycomb material also introduces flow features that disrupt the flow through the labyrinth seal, reducing leakage. All of the seals shown in Fig. 2.1 are equally valid with sealing fins on the rotor instead of the stator.

Thermodynamic and fluid mechanics of the labyrinth seal

The flow through a labyrinth restriction can be thought of as two thermodynamic processes. The first process is the acceleration of the fluid to pass through the restriction, which is reversible (assuming no viscous losses), followed by uncontrolled expansion of the fluid into the next cavity. The acceleration of the fluid converts pressure energy into kinetic energy. Some of the kinetic energy is converted into heat through viscous mixing in the cavity, some is recovered back into pressure, and some is 'carried over' into the next restriction [30], [31]. These processes are plotted on an enthalpy - entropy plot for a three fin 'see through' labyrinth seal in Fig. 2.2.

The narrowest part of the streamtube as it passes through the restriction is actually smaller than the area of the restriction. This is called the 'vena contracta', and is demonstrated in Fig. 2.3. The vena contracta is affected by the pressure ratio at each restriction [32].

The kinetic energy 'carried over' into the next cavity reduces the pressure drop that could otherwise be achieved if all the kinetic energy was destroyed in the cavity. This is because the fluid begins to accelerate before all the kinetic energy has been dissipated, and so more energy is available at the end of the labyrinth seal as pressure, rather than been converted into heat. The kinetic energy carry over is mainly governed by clearance to pitch ratio [31] and axial Reynolds number [33].

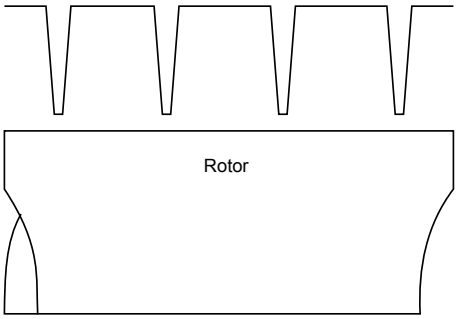

(a) 'See through' or straight labyrinth seal

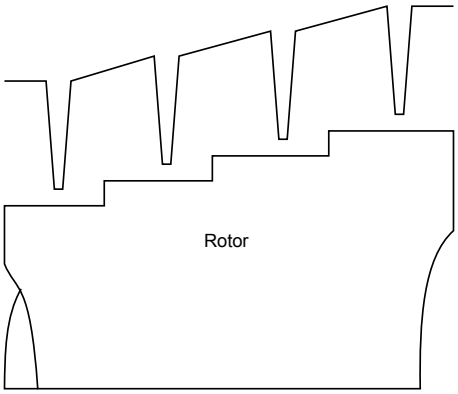

(b) Stepped labyrinth seal

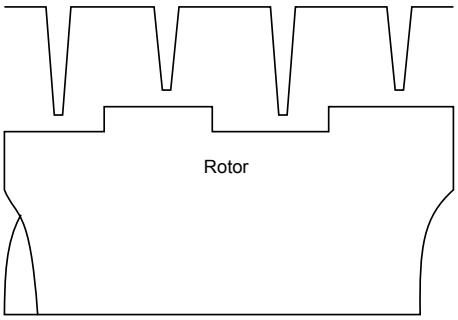

(c) Castellated labyrinth seal

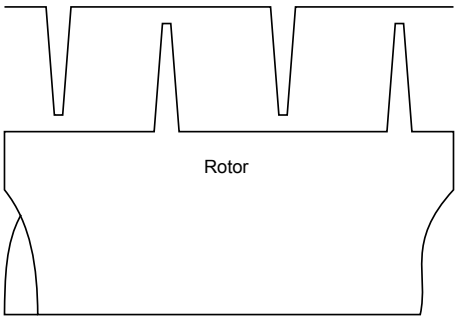

(d) Staggered labyrinth seal

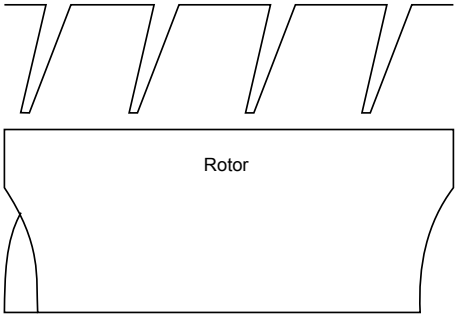

(e) Inclined labyrinth seal

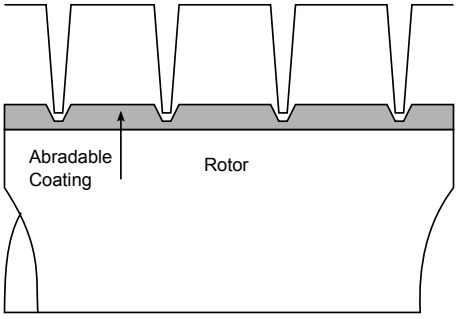

(f) Abradable labyrinth seal

Figure 2.1: Labyrinth seal configurations

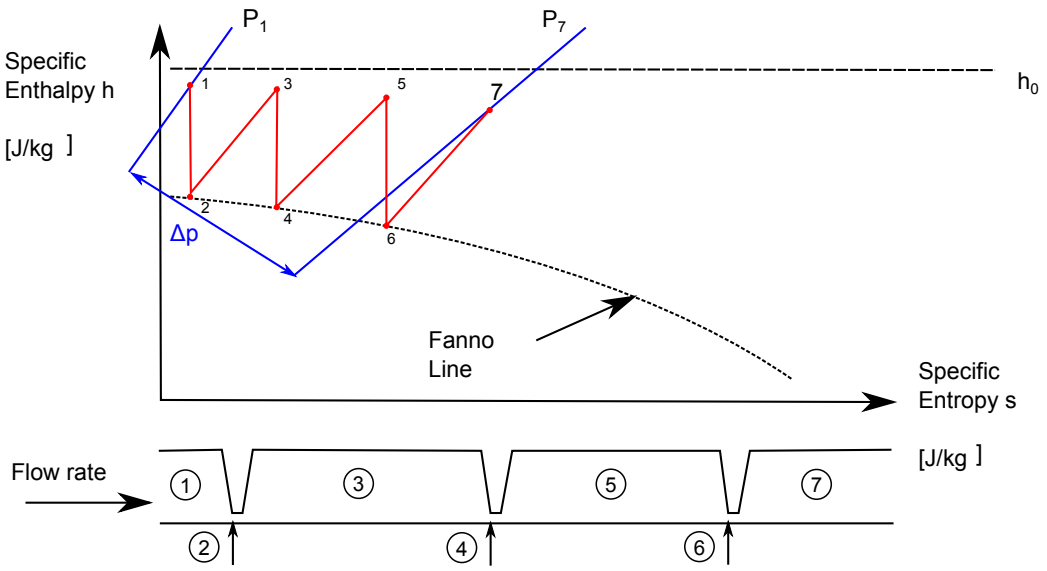

Figure 2.2: Enthalpy - entropy diagram for a three fin labyrinth seal.

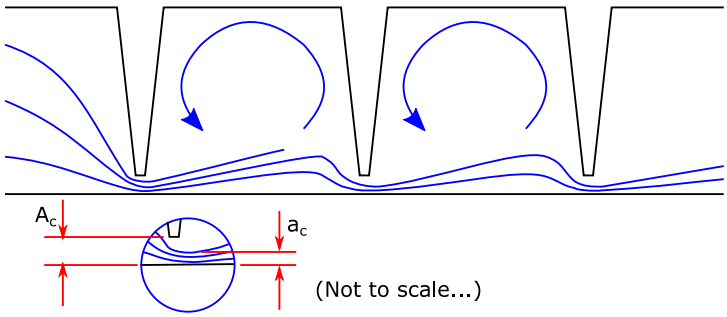

Figure 2.3: The 'vena contracta' through a labyrinth restriction

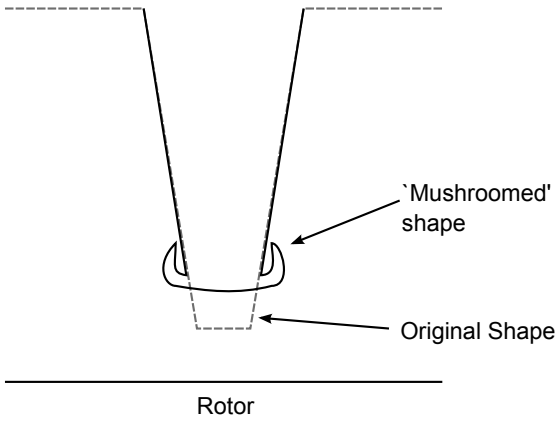

Figure 2.4: Cross section of 'mushroomed' labyrinth fin.

Damage

The easiest way to reduce the leakage through a labyrinth seal is to either increase the number of restrictions, or to decrease the restriction clearance. Often there is a limit to axial space and so it is not possible to keep on adding restrictions indefinitely, and decreasing the clearance will increase the possibility of the labyrinth seal becoming damaged due to rotor excursions.

Labyrinth fins can 'mushroom' when rotor contact is made, which makes the end of the fin more nozzle like, increasing the leakage through the seal shown in Fig. 2.4. This has been examined using CFD by Dogu et al [34]. Zimmermann et al [35] investigated the flow through worn labyrinth seals with rounded fin tips. They found for fully rounded fin tip the discharge coefficient of the fins could be increased by up to $35\,\%$ for a stepped labyrinth seal.

It is possible to increase the performance of the labyrinth seal without adding more fins or decreasing the restriction clearance by changing the geometry of the fin and the cavity, and this has been investigated by other researchers. Chougule et al [36] demonstrate with CFD how adding an extra small fin on the tip on a honeycomb labyrinth seal improved the leakage behaviour. Vakili et al [37] investigated a 'C' shaped labyrinth fin which was shown, using CFD, to decrease the leakage through the seal. The fins were de-

signed to deflect if rotor contact was made, and it was intended that the clearance could be reduced to further decrease leakage as the seal fins were damage resistant. Similarly Herrmann et al [38] investigated using flexible labyrinth fins with a reduced clearance to reduce the leakage flow rate, the flexibility of the fins reducing damage and wear. Kuwamura et al [39] showed that it was possible to optimise the shape of the labyrinth cavity to decrease the leakage flow through the seal. In the studies above, geometry of the labyrinth seal fins and cavities reduce leakage by influencing the vena contracta as the fluid passes underneath the labyrinth restriction.

2.2.2 The Retractable Gland

The retractable labyrinth seal is a development of the labyrinth seal [40] and has been widely deployed in steam turbines. The seal is divided into circumferential segments with springs that push the segments apart when the turbine is unloaded, creating a larger clearance between the teeth and the rotor. This enlarged clearance is useful to prevent damage to the labyrinth fins due to increased rotor radial movement during start up. As the turbine load is increased, the pressure across each stage is also increased, and the pressure force on the seal segment outer surface overcomes the spring force and frictional force, reducing the seal clearance. The segments rest locked together at the designed clearance and with the seal segments resting on the T slot shoulders [41], shown in Fig. 2.5. If the rotor was to move radially towards the segments, there is no mechanism for the segments to increase clearance without rotor contact.

The retractable gland and the Aerostatic Seal are similar in design and construction, the key difference is the ability of the Aerostatic Seal to move away from the rotor without contact. The retractable gland has been successfully implemented into steam turbines.

2.2.3 Fluidic Seals

Fluidic seals utilise air curtains to improve the performance of labyrinth seals. A fluidic seal is made up from an axisymmetric jet forming a curtain of high pressure fluid usually angled towards the oncoming leakage flow. A pressure drop is produced by the oncoming leakage flow turning the jet flow downstream. Curtis et al [42] tested such a seal in

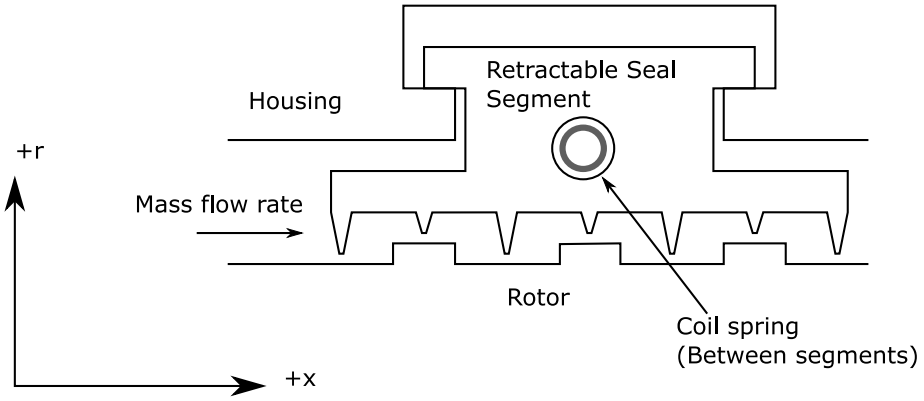

Figure 2.5: A retractable seal segment at minimum clearance.

a single stage turbine operating in air and demonstrated leakage reduction and overall efficiency gain accounting for the jet mass flow rate. Hogg and Ruiz [43] used Computational Fluid Dynamics (CFD) simulations to predict the potential leakage reduction in a steam turbine, and found an improvement of 25% (including the air curtain flow) over a labyrinth seal operating at the same conditions. The fluidic seal is usually operated in conjunction with other sealing devices [44], [45]. The benefits are greater if the fluid supplied to the fluidic curtain was 'free', such as fluid used for blade cooling in a gas turbine [46].

2.3 Compliant Seals

Compliant seals are made up from a number of flexible seal elements that form a barrier to the oncoming leakage flow. In this thesis the brush seal, leaf seal and finger seal have been considered. The brush seal has been employed in steam and gas turbines for a number of years, and offers significant leakage performance gains over the labyrinth seal. The leaf seal and finger seal have not yet been employed in the steam turbine. Film riding (i.e. non-contacting) versions of the leaf seal and finger seal are available but they are still considered as compliant seals in this thesis.

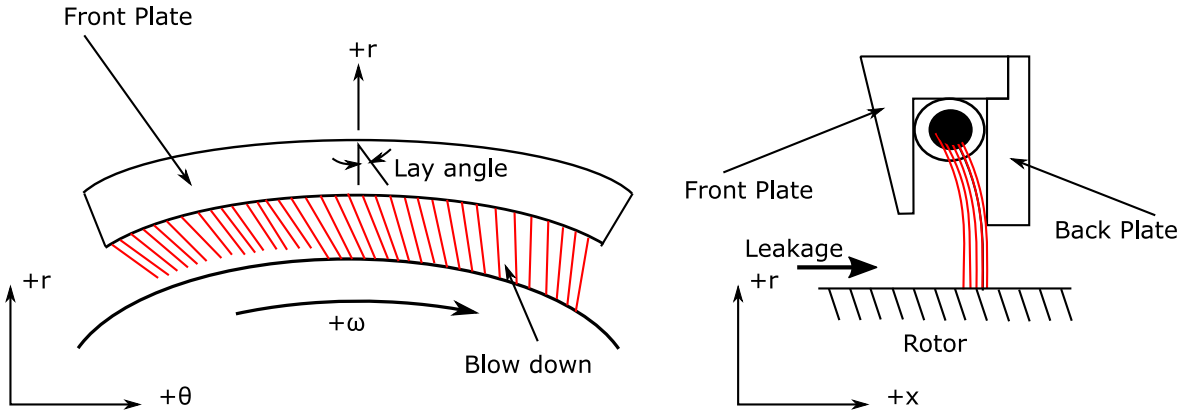

Figure 2.6: Configuration of a typical brush seal.

2.3.1 Brush seal

Brush seals were the first alternative to labyrinth seals and have produced extensive leakage performance benefits. Brush seals have enabled upwards of 80% leakage reduction compared to labyrinth seals [47], as well as more stable leakage characteristics, better accommodation of shaft movements and they require less axial space than labyrinth seals [29]. Brush seals are made from fine diameter bristles (typically $0.1\,\mathrm{mm}$) layered together to make a dense pack. The bristles are held between two rings and can have a slight interference fit to the rotor. The bristles are radially angled with the shaft rotational direction to accommodate rotor radius changes without the bristles buckling (lay angle), and can be axially inclined [48]. Figure 2.6 shows the configuration of a typical brush seal. As the brush seal is compliant, it is able to tolerate radial movement of the rotor.

Brush seals are typically a contacting seal. Therefore there will be heat generation due to frictional heating in the rotor, and also bristle wear which will lead to deterioration in the sealing performance over time [49]. One of the key challenges for the design of brush seals is to ensure good leakage performance over the time between turbine overhaul, and to ensure that the heating of the rotor is not excessive. Excessive heating of the rotor surface can lead to thermal instability. This is where the thermal heating due to rotor contact increases the rotor diameter due to thermal expansion, which causes further brush seal heat production, in turn increasing rotor thermal expansion until the rotor contacts the backing plate [29]. 'Thermal bow' has also been described by Little et al [41] where the rotor of a steam turbine can become bowed due to an unbalanced ro-

tor. With an unbalanced rotor there is a single point on the surface of the rotor that will have the greatest interference with the seal, and so will be the hottest region. This creates an asymmetric temperature profile around the circumference of the rotor, leading to a bowed rotor. Thermal heating of the rotor due to brush seals have been investigated by a number of researchers [50]–[52].

Brush seals are sensitive to the pressure drop across the seal. For example Crudgington and Bowsher [53] demonstrated that increasing the pressure drop across the seal leads to bristle 'blow down', also known as 'pressure closing'. This is where the bristles move radially inwards towards the rotor surface, and can decrease the life of the seal due to extra rotor contact pressure and hence greater seal wear. Increasing the axial inclination angle of the brush seal increases the radial stiffness of the seal and decrease the blow down effect on the seal, and so reduces wear of the seal [54]

Friction also influences the performance of the brush seal [29]. The pressure drop across the seal exerts a pressure force onto the bristles, which get pushed against the back plate and also into each other giving rise to frictional forces. Therefore if the seal is deformed due to a rotor radial excursion or thermal growth, then the seal bristles would stay at a greater clearance until the seal is de-pressurised or the blow down forces sufficient to push the bristles back down towards the rotor. This is known as hysteresis.

2.3.2 Leaf seals

Leaf seals are made from a stack of thin plates, welded along the top surface [55]. The seal is radially compliant and axially stiff. A diagram of a leaf seal is shown in Fig. 2.7. Variations in front and back plate gap are used to control the lift forces on the leaves and hence reduced wear. The leakage performance of the leaf seal is reported as 33% of an equivalent four stage $0.5\,\mathrm{mm}$ gap labyrinth seal, measured experimentally [56]. The leaf seal was implemented into a Mitsubishi M501G gas turbine by Nakane et al [56].

The leaf seal offers advantages over the brush seal. Due to the greater axial stiffness of the leaves, there is less friction between the leaves and the rear plate, hence the radial stiffness of the seal is reduced. This gives the seal a greater ability to accommodate rotor movements, which was experimentally demonstrated by Jahn et al [57]. Due to hydrodynamic lift forces acting on the leaf elements, the leaves are able to overcome the mechanical stiffness of the leaves and the blow down effect due to the pressure

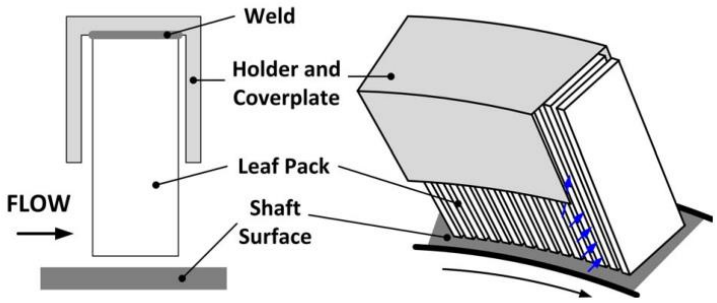

Figure 2.7: Configuration of a typical leaf seal, from Jahn et al [58].

difference, which reduces wear and rotor heating when the rotor is turning [56], [58]. However despite these apparent advantages, the leaf seal has not been implemented in a steam turbine that the author is aware.

2.3.3 Finger seals

The finger seal is a sealing concept that has similar leakage performance as brush seals, but with the cost estimated to be 40 to 50% of the brush seal [59]. The finger seal is composed of a number annular rings with a series of radial slots cut into it to create slender finger elements, shown in Fig. 2.8. These have an elongated contact pad at the tip. The fingers are held between fore and aft cover plates with a spacer in between. Each of the annular plates are shifted circumferentially so the finger elements of one ring cover the gaps between elements of the other rings. The whole assembly is then riveted together at the outer radius [60].

As with the brush seal and the leaf seal, the finger seal is compliant, rotor movement accommodated through deflection of the fingers radially. As for the brush seal and to a lesser extend the leaf seal, there is hysteresis in the ability of the seal fingers to respond to the rotor [61].

The basic finger seal concept has contact between the finger contact pad and the ro-

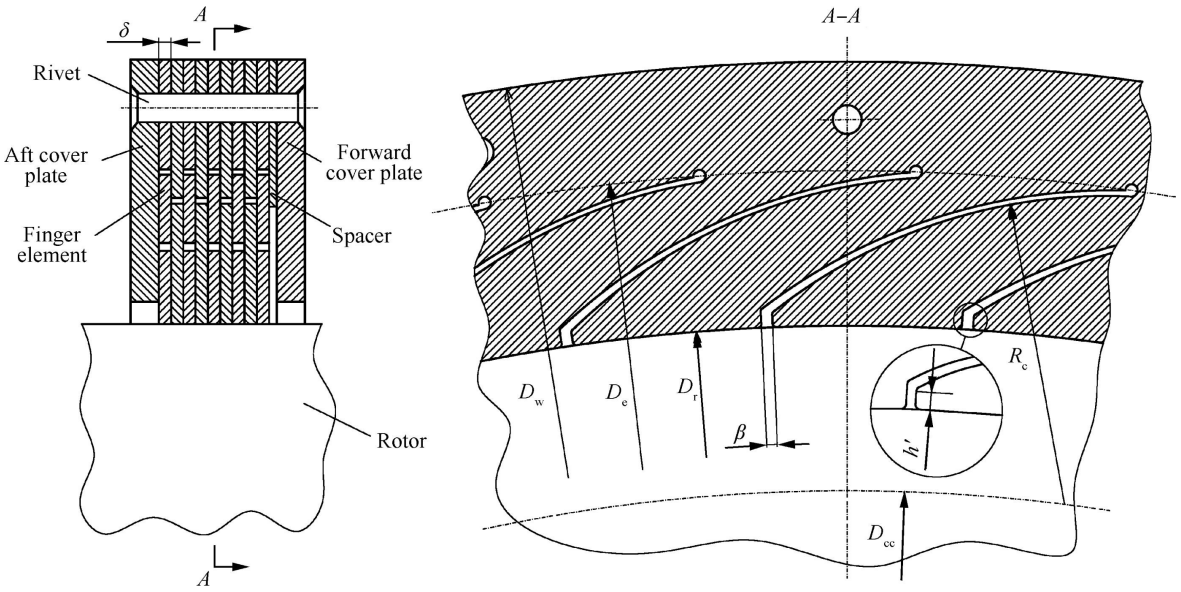

Figure 2.8: Configuration of a typical finger seal, from [63].

tor. This has been developed further by shaping the contact pads to generate hydrodynamic lift forces which prevent contact during normal running, called the non-contacting finger seal. This is intended to increase the life time of the seal at the expense of a slight increase of leakage flow through increased clearance. Testing of the non-contacting finger seal has shown that friction between the finger elements will influence the behaviour of the seal, causing hysteresis. When increasing the pressure differential, the finger elements will move towards the rotor and 'bind' (i.e. contact the rotor surface) [62].

2.4 Dynamic seals

There are many dynamic seal concepts at varying levels of technology readiness, and a selection of promising designs are summarised here. It can be summarised that dynamic seal concepts utilise hydrostatic and/or hydrodynamic forces to achieve a seal operating at small clearances by providing a radial force away from the rotor surface. Discussed within this chapter are 'dry gas seals ' (DGS), the carbon segmented seal, the 'HALO' seal and the floating ring annular seal. Some types such as the 'dry gas seal' and floating ring annular seal have been in operation for many years in small gas compressors in the oil and gas industry. The HALO seal has more recently been commercialised.

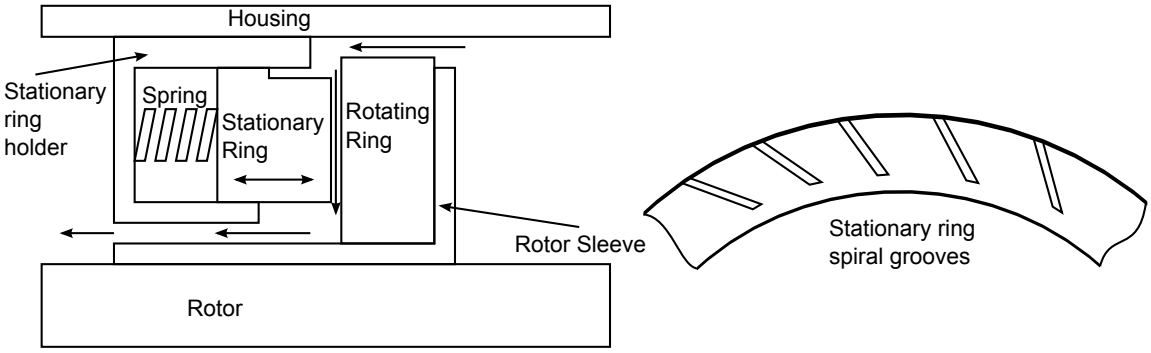

Figure 2.9: Typical configuration of a dry gas seal.

However none of the above have found their way into steam turbines as of 2017.

The Aerostatic Seal is a dynamic seal, and is specifically developed with the steam turbine as the intended application, although other turbomachinery applications are feasible.

2.4.1 Dry gas seal (DGS)

One type of dynamic seal that has seen extensive deployment in small high pressure compressors in the oil and gas industry are 'Dry Gas Seals'. A typical layout of a dry gas seal is shown in Fig. 2.9. The seal is a face seal rather than an annular seal, and consists of a rotating ring and a stationary ring, which is loaded towards the rotating ring by springs. Dry gas seals use hydrodynamic forces to control the gap between the stationary and rotating rings, the hydrodynamic pressure force generated by grooves on the face of the stationary ring (see Fig. 2.9), which produces variations in fluid film thickness [64].

A recent driver to dynamic sealing concepts is the proposal of supercritical carbon dioxide (sCO_2) Brayton cycles for advanced coal power plants, which offer higher thermal efficiency over typical steam cycles [65], [66]. Leakage from the turbine in sCO_2 cycles becomes more significant as there is the penalty of re-compressing the CO_2 that leaks out from the turbine back up to cycle pressure [67], [68].

Dry gas seals have been proposed as a potential end shaft seal for large scale (500 MW) sCO_2 turboexpanders [66]. Dry gas seals are already commercially available in small diameters, see [69] for example. Bidkar et al [66] performed analysis on a hydrodynamic face seal (basically a dry gas seal) for larger shaft diameters. One of the key issues they

found was deformation of the seal face due to the large diameter and high pressure drop across the seal. The deformation is detrimental to the development of hydrodynamic lift forces. The seal analysed was 600 mm in diameter, and so was comparable to a steam turbine diaphragm seal. Deflection of the diaphragm of impulse steam turbines in operation has been documented and can amount to 0.1 inch (2.54 mm) [70]. Typical fluid film thickness is 0.005 mm to 0.013 mm [66].

Dry gas seal requires a clean gas supply. Typically the seal buffer gas supply would be filtered to prevent small particles or condensate getting into the seal [69], which would need to be considered for steam turbine application. As there are impurities in the steam of a typically steam turbine, this may make the dry gas seal unsuited to steam turbine operation.

Dynamic seals have also been developed for more exotic components such as buffer seals in liquid oxygen turbo pumps for rocket engines [71]. In these applications low leakage is essential. In an oxygen turbo pump, expanding hydrogen rich steam, which drives the turbine connected to the oxygen pump, is separated by an external helium gas supply acting as an inert buffer. Reducing the leakage of the buffer gas requires less buffer gas to be carried on-board the rocket, freeing up rocket payload. Shapiro and Lee [71] investigated many different configurations of sectored seals, floating ring seals, and face seal (similar to dry gas seal). The segmented seal analysed used aerostatic feed holes to provide radial and axial force balance using the high pressure buffer gas flow as the supply, shown in Fig. 2.10.

2.4.2 Carbon segmented seal

The carbon segmented seal is a segmented seal that utilises hydrodynamic forces to control the clearance of the seal segments. A circumferential or garter spring forces the segment towards the rotor surface, and so during coast down the seal segment will contact the rotor. Circumferentially spaced pockets are used which produce hydrodynamic lift. Arghir and Mariot [72] analyse the carbon segmented seal, and present an analytical model with three degrees of freedom. Similar segmented seals are available commercially [73], [74].

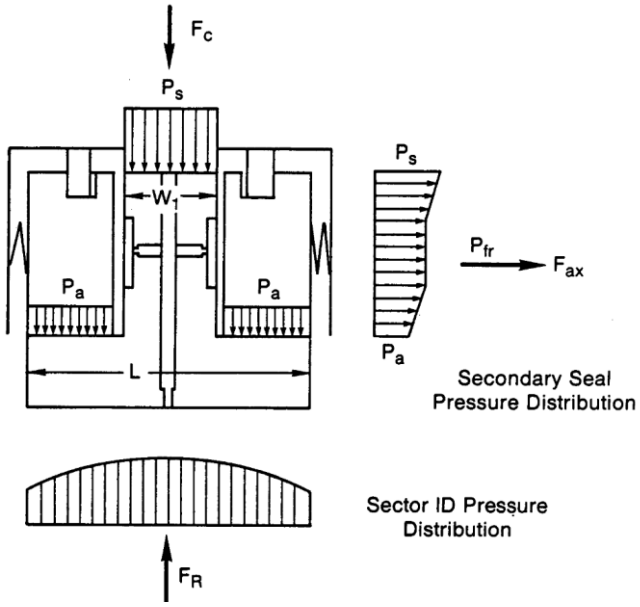

Figure 2.10: Oxygen turbo pump seal utilising aerostatic forces, from [71].

2.4.3 'HALO' seal

The ATGI 'HALO' seal is a dynamic seal that consists of cantilevered pads that are able to move radially. The pads are held by a radially soft but axially stiff spring, with a downstream secondary seal to prevent leakage through the spring section [75], and is shown in Fig. 2.11. Hydrodynamic and hydrostatic forces are used to control seal clearance [76]. The secondary seal can be a brush seal or a plate seal [76]. The HALO seal has been tested in a high temperature seal test rig and a significant leakage reduction was achieved [77]. The HALO seal has been successfully implemented in a number of compressors [78], [79], and is commercially available [80].

By having an axially stiff spring which connects the sealing 'shoe' to the stator, friction between the secondary seal, which consists of a simple flat plate, is reduced, although a low friction nickel-boron coating is still used.

2.4.4 Floating ring annular seal

Floating ring annular seals are dynamic seals that consists of a single annular ring made from carbon. A cross section is shown in Fig. 2.12. For seal movement to occur, the seal ring has to overcome friction between itself and the stator, as in the Aerostatic Seal. The seal ring is made of carbon, and therefore the frictional forces acting on the seal ring

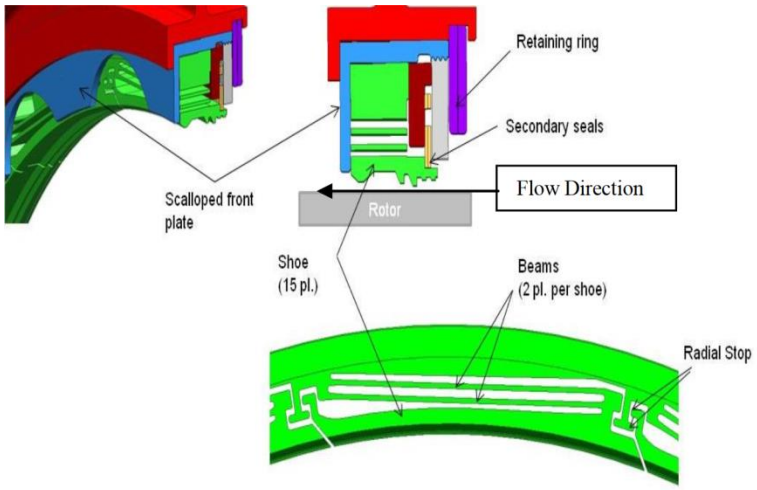

Figure 2.11: Halo seal general arrangement, from [79].

are low. Including the effects of mixed lubrication, the equivalent coefficient of friction is expected to be below $\mu = 0.1$ [81]. The ability of the seal to track high speed and low amplitude rotor vibrations has been demonstrated in a rotating test facility [82].

2.4.5 A note on hydrostatic and hydrodynamic forces

The generation of hydrostatic and hydrodynamic forces are of great importance in the field of lubrication theory and for the design of hydrodynamic or hydrostatic/aerostatic bearings. Hydrostatic and aerostatic devices (bearing or seals) are supplied with an external supply of fluid to increase pressure on the surfaces of the bearing, or by the pressure drop across a restriction (seals).

Hydrostatic (or aerostatic) forces are pressure forces due to the static pressure on the surfaces of the seal or bearing. An example would be pressure forces acting on the retractable seal segment to cause the segment to move towards the rotor, or the Aerostatic Seal which uses the feed hole to manipulate the pressure distribution to generate different radial forces depending on the clearance of the seal segment.

In the aerostatic bearing, high pressure fluid is supplied externally. The bearing operates at a low clearance, and the load on the bearing is taken by the pressure force on the bearing surface. If the bearing face was perturbed, then the flow through the feed hole

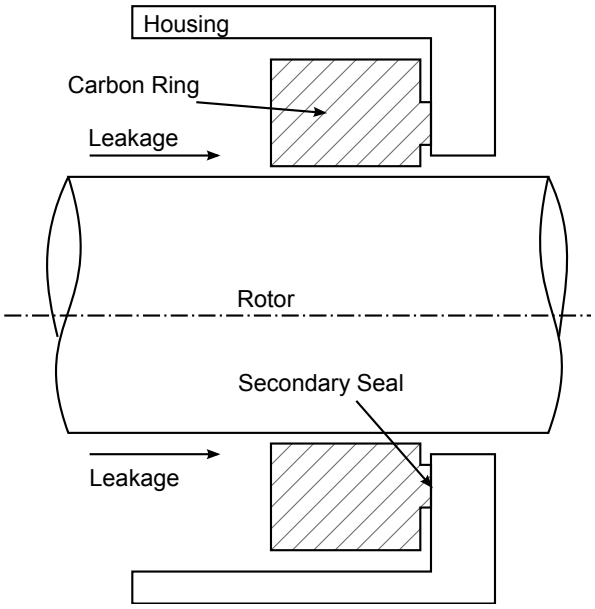

Figure 2.12: Floating ring annular seal

would be increased, increasing the pressure drop through the feed hole and reducing the pressure supplied to the bearing surface. This keeps the bearing operating at a low clearance, and reduces the amount of externally provided fluid.

Hydrodynamic forces are generated by the flow of the leakage fluid through a clearance of varying height, and are governed by the Reynolds equation [64]. Typically such forces are generated by the use of the 'Rayleigh Step' as in the carbon segmented seal analysed by Arghir and Mariot [72] or spiral grooves such as those in the dry gas seal. Arghir and Mariot [72] also report the ability to produce hydrodynamic lift force from the 'waviness errors' on the surface of the seal and the rotor surface. The 'waviness errors' are the deviations from the mean surface position due to surface roughness. However the forces generated are small, and film thickness is less than $1\,\mu m$.

2.5 The Aerostatic Seal

Previous work and development on the Aerostatic Seal concept has been carried out at Durham University with a series of four final year MEng projects - these are summarised in this section.

Auld [23] conducted the first study on the Aerostatic Seal concept, and produced the first analytical model. The pocket pressure was calculated to give force equilibrium of

the seal segment and the feed hole diameter calculated to achieve the required pressure. The analytical model was verified using 2D CFD results which showed good pressure and mass flow rate agreement at low clearances. A force balance was performed on a seal design based on an existing retractable gland design. A range of feasible geometries that would rest at a non-zero clearance and move away from the rotor at low clearances were found. Auld estimated that the Aerostatic Seal could operate at a clearance of $0.2\,\mathrm{mm}$ and hence have a leakage mass flow rate of 27% that of a typical labyrinth seal. This was similar to the level of leakage associated with a brush seal (20% of labyrinth seal flow) [47].

Rafferty [24] used a similar analytical model as developed by Auld [23]. He made an assumption about the mass flow rate through the feedholes where $2\dot{m}_f = \dot{m}_{out}$ at clearances of 0.1mm or less. This was used to calculate the feed hole diameter in the same way as by Auld. Rafferty uses this model to develop a Aerostatic Seal calculation tool which performs a search of all possible designs of seal segment shape within a number of geometrical limits, set by the user. A design was designated as feasible if it meets force equilibrium, moment equilibrium and has a positive total force when the segment is at zero clearance. This was used to obtain a number of possible seal designs; however there was no seal design in which there were no net pressure forces acting on the seal at the desired clearance.

Rafferty also conducted 3D CFD analysis on the seal and showed agreement in the pressures calculated by the analytical model. This was to investigate the effect of the feed hole flow on the fluid in central the pocket of the seal segment.

Rafferty found it was necessary to increase the width of the segment to achieve a seal with no net force acting upon it when at the design clearance; the initial width of the segment was based on a current retractable gland design to retrofit to existing steam turbines. Rafferty also investigated the conditions required for the segment to move towards the rotor after a rotor excursion, as well as away from the rotor during the excursion. It was concluded that the segment would move away from the rotor at zero clearance and move back towards the rotor at $0.35\,\mathrm{mm}$ clearance.

Damage to the seal was investigated by considering what would happen if a feed hole becomes blocked. Rafferty concludes that in a seal segment of 3 feed holes any one of them becoming blocked would reduce the radial force to the extent that the segment

would move towards the rotor.

Durnan [25] conducted work to alter the design tool by Rafferty [24] to model a segment rather than a unit length seal. Durnan developed the non-rotating rig concept, as detailed in Chapter 4. Originally it was envisaged to have a hydraulically actuated rotor which would simulate a rotor excursion; however it was deemed too expensive for an initial test rig.

MacDonald [26] analysed the dynamics of the gland in more detail, as well as the start-up conditions. The conclusion was that in order to make the seal segment responsive enough that it would move away from the rotor and move back again, the coefficient of static friction would have to be reduced or the frictional force reduced via a reduction in the normal force. It was noted at start-up that the seal segment could stick at the clearance where the radial force acting on the segment reduces below the dynamic frictional force of the segment. A number of methods of reducing the frictional force were investigated, including a pressurised cavity in the contact face and low friction coatings on the seal segment and seal holder. A number of new seal designs were then produced using these methods and taking into account the dynamic considerations. One of these seal designs was designated 'MacDonald 1' and was manufactured for testing on the non-rotating test rig.

2.6 Conclusion

Table 2.1 compares the leakage reduction of competing seal technologies. The leakage reduction was compared to a 'comparable' labyrinth seal. As the different researchers in the references providing the data in Table 2.1 have not all used the same configuration of labyrinth seal, then the values quoted do not represent a definitive leakage improvement values, but serve as a useful comparison nevertheless.

Dinc et al [47] compares a brush seal to what they described as a typical labyrinth seal (no other data was given presumably as it was commercially sensitive) in a rotating seal test facility capable of operating with air or steam as the working fluid. Typically the leakage through the brush seal was 20% that of the labyrinth seal, although different configurations of brush seal gave greater leakage benefit. The brush seals tested combined a brush seal with labyrinth restrictions rather than a single brush.

Technology	Flow through seal as percentage of comparable labyrinth seal flow	Reference
Brush Seal	20%	Test rig results - fig 2 from Dinc et al [47]
HALO Seal	30%	San Andrés and Anderson [77] (test rig)
Aerostatic Seal	27%	Auld [23] (calculation)

Table 2.1: Comparison of potential leakage reductions of competing seal technologies

San Andrés and Anderson [77] compare the leakage performance of the HALO seal and a 3 fin labyrinth seal in a rotating seals rig which uses high temperature air. The labyrinth seal clearance was $0.255\,\text{mm}$. The leakage reduction of the HALO seal was 50% compared to that of the labyrinth, or when the pressure ratio (P_{in}/P_{out}) was greater than 3, then the leakage reduction was increased to 70%.

Auld [23] calculated the flow rate through an Aerostatic Seal operating at a clearance of $0.2\,\text{mm}$ which was considered a feasible operating clearance for the seal. It was found that the leakage reduction through the Aerostatic Seal compared to the same seal but with no feed holes at a clearance of $0.7\,\text{mm}$ gave a 73% leakage reduction.

Overall the brush seal and HALO seal both offer significant leakage reduction over the labyrinth seal, and initial investigation on the Aerostatic Seal suggest similar levels of leakage reduction are also possible. Obviously the level of leakage reduction possible with the Aerostatic Seal is dependent on the operating clearance of the seal.

A number of competing seal designs have been reviewed in this chapter. The seals reviewed were categorised as 'non-contacting seals' such as the labyrinth seal or retractable, 'compliant seals' such as the brush seal, and 'dynamic seals' such as dry gas seals or the HALO seal.

In order to reduce the leakage and hence increase the efficiency of steam turbines, whilst also increasing the operational flexibility of the turbine, then implementing compliant or dynamic seals becomes necessary. This is because without any method for the seal to respond to rotor movement, 'non-contacting' seals such as the labyrinth seal become damaged through rubs, increasing the leakage through the seal. Brush seals, whilst allowing for rotor movement and achieving significant leakage reductions are a contacting seal. This leads to heat generation at the rotor and seal interface, and also

the seal wears over time, leading to a gradual reduction in leakage performance.

The Aerostatic Seal offers advantages over other dynamic seal concepts as it is a development of currently used sealing technology in steam turbine diaphragm seals. The addition of 'feed holes' from the top surface of the seal segments to a central pocket allow the seal to respond to rotor movement. Due to the similarity of the design to existing diaphragm and end gland segments, the seal design could be retrofitted into existing diaphragm and end gland constructions.

The disadvantages of the dry gas seal, HALO seal and floating ring annular seal for application to steam turbines are the complex manufacturing due to the requirement for close tolerances. Typical hydrodynamic fluid film thickness in such seals are of the range 0.005-$0.013\,\mathrm{mm}$ [66]. These seals would also require change to current diaphragm construction, and are sensitive to deflections or distortions present in steam turbines due to the high temperature and pressures.

Previous development work on the Aerostatic Seal has used a mixture of analytical modelling and computational fluid dynamics (CFD) simulations [23]–[26]. The results of these investigations identified that friction presented the greatest unknown, and which would also have significant impact on the performance of the Aerostatic Seal. Other dynamic seals are more tolerant to the effects of friction by the choice of material (carbon in the floating ring annular seal), or in the case of the HALO seal the axially stiff support structure and low friction coatings. The gap that this work fits into is to experimentally test this promising seal technology to confirm that friction can be overcome to achieve bidirectional dynamic behaviour of the seal.

Chapter 3

Design and Analysis Methods

3.1 Introduction

This chapter describes the standard design and analysis methodology of the Aerostatic Seal, as well as the theory behind the operation of the seal. The design and analysis methodology builds upon the earlier work conducted by Auld [23], Rafferty [24], Durnan [25] and MacDonald [26].

The standard analysis methodology is an analytical tool used to determine the fluid flow through a particular seal design. From the fluid flow and pressures, the forces acting on the Aerostatic Seal segment are found and the success or otherwise of the design obtained.

The design methodology uses the standard analysis methodology to test a wide range of possible Aerostatic Seal designs within a solution space defined by the user. The design code then outputs the best seal designs within the solution space that the designer can pick from.

Throughout the project a number of Aerostatic Seal designs have been generated for use in various test rigs described within this thesis. These have been generated using different versions of the methodology as it developed, although they are compared using the same analysis methodology at the end of this chapter.

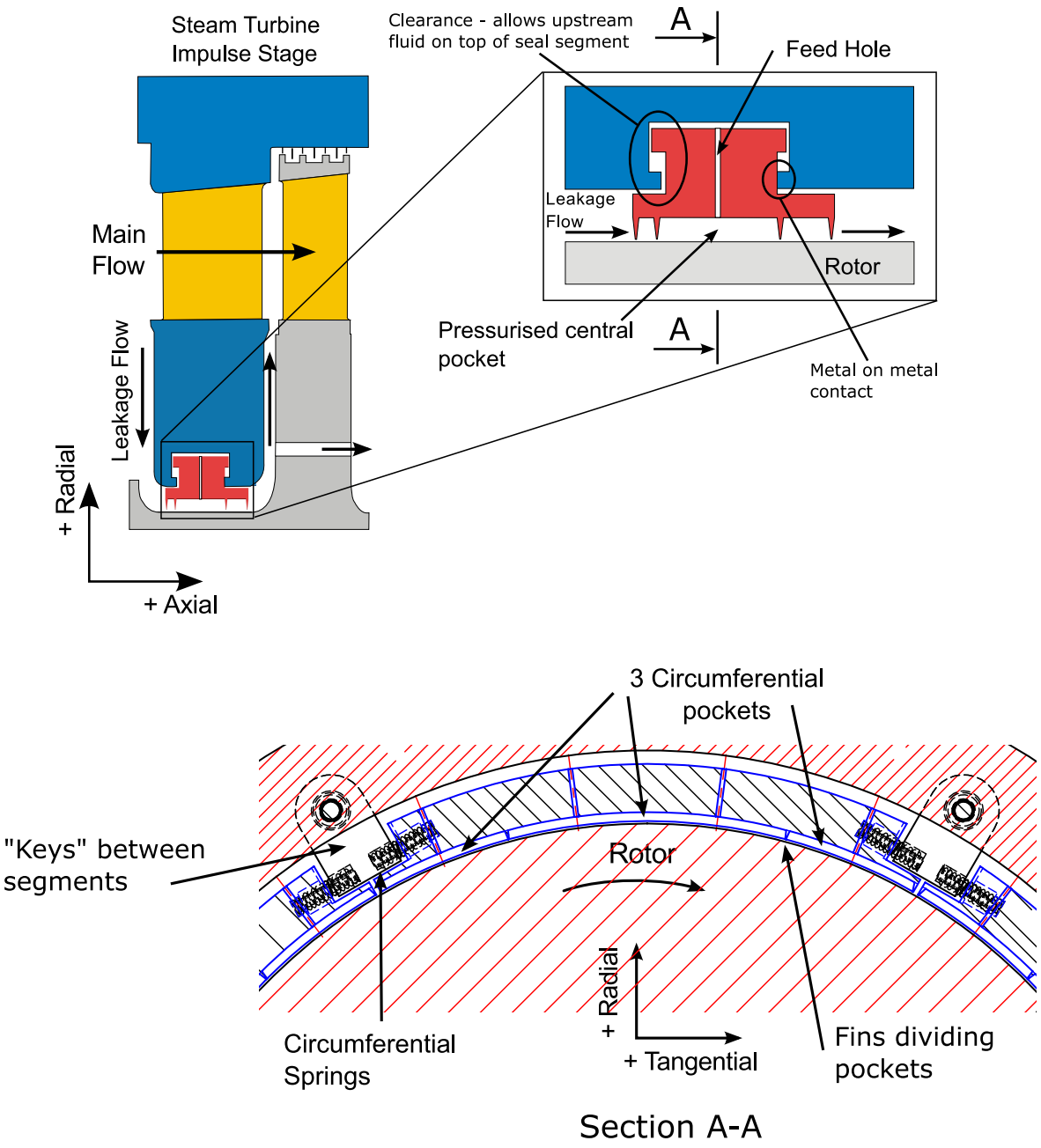

Figure 3.1: The Aerostatic Seal concept, installed in a steam turbine diaphragm.

3.2 Theory of Operation

The Aerostatic Seal is a segmented seal, similar to the retractable seal described in Section 2.2.2, and is shown in Fig. 3.1. Each seal segment is free to move inside the diaphragm tee slot, which sets the maximum and minimum clearance. Circumferential springs between the seal segments 'retract' the segments when there are no pressure forces acting on the segment. Labyrinth fins throttle the leakage flow between the seal segment and the rotor surface, providing the seal.

The key feature of the Aerostatic Seal is the 'feed hole' which allows upstream steam on top of the segment to flow into the central seal pocket. Upstream pressure is present on the top of the seal segment as there is a clearance between the upstream face of the Tee slot and the seal segment, shown in Fig. 3.1. This increases the pressure in the central pocket, and provides the seal with a mechanism to passively control the segment clearance in a similar manner as the aerostatic bearing. The segment is divided into circumferential pockets, each pocket having at least one feed hole as shown in Fig. 3.1. These pockets are intended to ensure an even clearance along the circumference of the seal segment.

For the Aerostatic Seal segment to move in response to the rotor surface, then the pressure force must overcome the frictional force between the seal segment and the diaphragm. If the frictional force is too high, then the seal segment may be unresponsive. Too little friction and the seal segment will be constantly moving which could lead to wear of the seal segment, and risks rotor rubs due to under damped seal segment behaviour.

3.2.1 Pressure Distribution

Consider a cross section of a 'see through' or 'straight' labyrinth seal with four restrictions, shown in Fig. 3.2, and operating at a typical labyrinth seal clearance of $0.7\,\mathrm{mm}$. As steam flows through each restriction in turn, there is a pressure drop due to mixing losses after each fin. (See Section 2.2.1 for a full description of labyrinth seal function.) The largest pressure drop is at the last restriction due to decreasing density as pressure decreases. As the density decreases, the velocity is greater under the restrictions, and hence there is greater energy dissipation at the restriction and therefore a larger

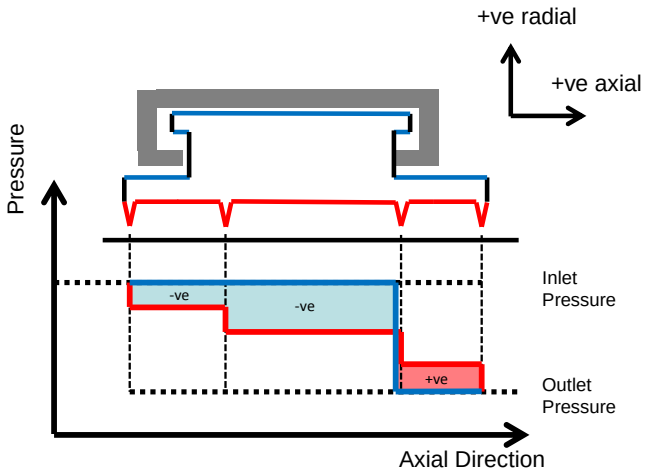

Figure 3.2: Pressure distribution in a 'see through' 4 fin labyrinth seal.

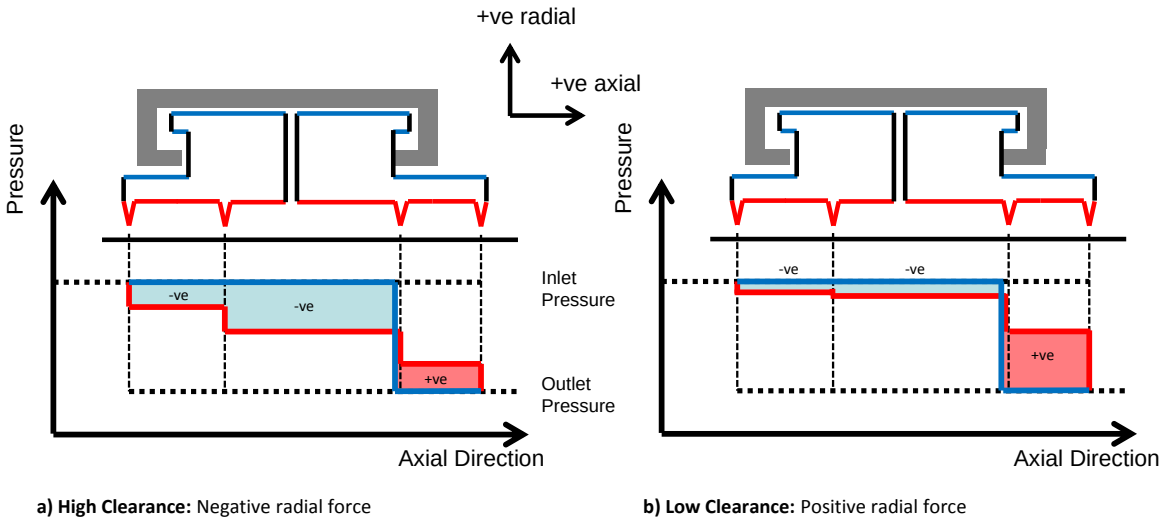

a) High Clearance: Negative radial force

b) Low Clearance: Positive radial force

Figure 3.3: Pressure distribution at high and low clearance.

pressure drop. Steam is free to pressurise the top surface of the seal segment, and is prevented from flowing around the back of the segment by the metal on metal contact between the diaphragm, shown in Fig. 3.1. In reality there will be a small amount of leakage through this 'secondary seal'. As the pressure on top of the seal segment is inlet pressure, there will be a net pressure force pushing the segment towards the rotor. This is represented by the blue shaded area on the graph on Fig. 3.2. On the rear section of the seal segment there is a net force away from the rotor as the pressure on top of the segment is outlet pressure. This is indicated by the red shaded area on Fig. 3.2. The blue area is greater than the red area, therefore the net pressure force is acting towards the rotor surface.

Now consider what happens if the seal was turned into an Aerostatic Seal by drilling a series of small 'feed holes' from the top surface into the central labyrinth seal cavity. If the seal was operating at the same clearance as before, then the pressure drop across each restriction is also similar, and is illustrated in Fig. 3.3a. This is because the flow rate through the feed holes is much smaller than the main leakage flow rate. As before there is a net pressure force acting towards the rotor surface.

If the seal segment was now operating at a reduced clearance, shown in Fig. 3.3b, then the main leakage flow rate is reduced. However as the feed hole area will stay the same, a greater proportion of the flow will be going through the feed holes. Therefore the velocity of the steam going under the first two restrictions will be reduced, and the pressure drop reduced accordingly. The last two restrictions will now be providing the majority of the seal pressure drop. If the seal segment geometry is chosen correctly, then there will be a net pressure force generated that is away from the rotor surface. Figure 3.4 demonstrates how the pocket pressures vary continuously with clearance, calculated analytically. See Section 3.3 for the method. This continuously varying pressure gives rise to a continuously varying pressure force acting in the radial direction. A pressure coefficient, Cp has been defined, see Eq. (3.1), to non-dimensionalise the pressure in each pocket of the seal segment. The pressure coefficient would be 1 if the pocket was at inlet pressure, and 0 if the pocket at outlet pressure. In Eq. (3.1), $i = 1, 2, 3$, $Cp1$, $Cp2$, and $Cp3$ refer to the pressure coefficient in the first, second and third pockets respectively and P_1, P_2 and P_3 refer to the pressure in the first, second and third pockets respectively.

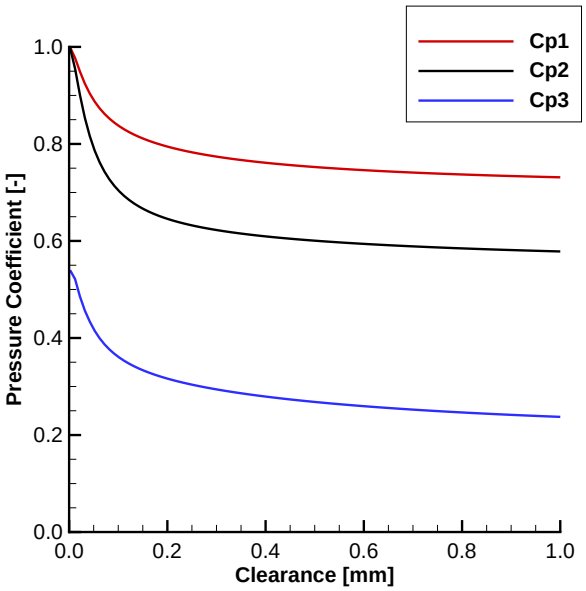

Figure 3.4: Variation of Aerostatic Seal pressure distribution with seal clearance. Inlet pressure 6 bar(a), outlet pressure 4 bar(a), MESS01 seal design. Calculated using the standard analysis methodology (see Section 3.3)

$$Cp_i = \frac{P_i - P_{out}}{P_{in} - P_{out}} \tag{3.1}$$

Auld [23] and Rafferty [24] consider the operation of the Aerostatic Seal more like an aerostatic bearing. In some respects the Aerostatic Seal does indeed operate in a manner similar to an aerostatic bearing, particularly the way the central feed holes limit the feed hole flow into the central pocket when the seal segment is at a high clearance, leading to a reduction of seal segment clearance. Other aspects of the Aerostatic Seal operation are dissimilar to an aerostatic bearing. The pressure loss on the underside of a bearing is due to viscous shearing, rather than a series of throttling processes as in a labyrinth seal.

3.2.2 Forces and Moments

The previous section has explained how varying clearance will give rise to a varying pressure force. However the pressure force is not the only force acting on the seal segment.

The circumferential springs exert a radial force component onto the seal segment. The force applied can be thought of in two parts. The force due to change in clearance and the stiffness of the springs, and the 'pre load' which is the constant force applied due

to initial compression of the springs when the seal segment is in the retracted position. Pre load is important to ensure that the seal segment is retracted when there is no load (i.e. pressure drop) on the turbine stage.

Other forces acting on the seal segment are weight, a d'Alembert equivalent acceleration force if the segment is accelerating, the diaphragm reaction force counteracting the axial pressure force due to the pressure drop. There is also friction between the seal segment and the diaphragm opposing the applied radial forces. A free body diagram is shown later in Fig. 3.10.

The frictional force acting on the seal segment determines if the segment will move. If the applied forces are large enough to exceed the frictional force, then the seal segment will move. If the applied forces are smaller than the maximum frictional force, then the segment will remain in static equilibrium. Friction is proportional the axial pressure load on the seal segment, the proportionality constant called the coefficient of friction μ [83]. As the axial pressure force can be controlled to an extent by the geometry of the seal segment, then the frictional force can be influenced. The coefficient of friction however is a function of material and material finish. Friction can be modelled with a static coefficient of friction, and a lower dynamic coefficient of friction.

Figure 3.5 shows radial forces acting on the seal segment at varying clearance. The radial applied force, F_r, is the vector sum of the pressure force, the spring force and weight in the radial direction. Also plotted is the positive and negative static friction force. The minimum clearance limit is called the 'minimum static clearance' and the maximum clearance the 'maximum static clearance'. If the Aerostatic Seal is between these clearances, then the segment will remain stationary. If the rotor moves and the clearance is reduced so it is below the minimum static clearance, the segment will move away from the rotor. If the rotor moves sufficiently away from the segment so the clearance is greater than the maximum static clearance, then the segment will move towards the rotor. The segment will stop moving once the applied radial force is below the dynamic friction force and seal segment inertia is overcome.

As the pressure forces acting around the seal segment are not evenly distributed about the centroid of the segment, then a net pressure moment is generated. If the segment was able tilt forwards inside the diaphragm, then the segment could jam. If the segment was to tilt forwards the pressure distribution would be effected and could

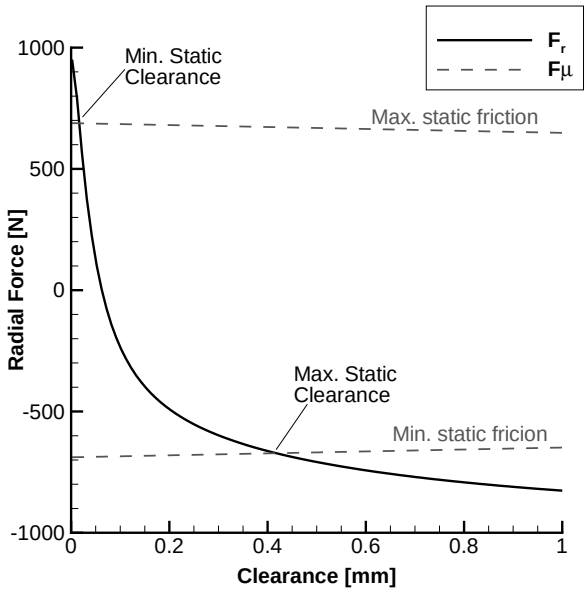

Figure 3.5: Variation in radial force with clearance. Inlet pressure 6 bar(a), outlet pressure 4 bar(a), coefficient of static friction $\mu_{stat} = 0.6$, MESS01 seal design. Calculated using the standard analysis methodology (see Section 3.3).

prevent the segment moving away from the rotor as designed. A certain level of applied moment can be tolerated however as the seal segment contact face is curved. This allows the axial reaction force to be applied above or below the centroid location to balance the applied moments. This is further discussed in the following section.

As explained earlier, the intended function of the circumferentially spaced pockets was to ensure that the seal segment operated at an even clearance. As each pocket has at least one feed hole (the central pocket has two as it occupies a greater circumferential portion of the seal segment), then the pockets are individually pressurised. If one side of the seal segment is at a lower clearance then the pressure in that individual pocket will be higher (by the same mechanism as discussed previously), and consequently there will be a righting force generated. (It was discovered in the experimental test campaign that the mechanism for providing this functionality was more complicated - see Chapter 8.)

The circumferential pockets also contribute to disrupting swirling flow inside the labyrinth seal cavities. Due to the high level of turning on impulse design steam turbine stators, the is a large tangential component to the steam entering the Aerostatic Seal. Disrupting this flow improves the rotordynamic stability of the seal, as discussed in Section 2.2.1. However by disrupting the flow, a tangential force is generated on the

seal segment. This force is taken on the circumferential springs.

3.2.3 Pressure Effects

The radial pressure force generated by the Aerostatic Seal segment is to a first order approximation proportional to the pressure difference across the seal. In reality the pressure ratio, PR, also effects the discharge coefficient of the labyrinth fins, which in turn effects the pressure distribution underneath the seal segment [84]. The axial pressure force is proportional to the pressure difference; hence the frictional force is also, assuming a constant coefficient of friction. The spring forces are not affected by the pressure difference, and therefore at low pressure drops, spring forces are dominant which retracts the seal segment.

At a particular set of inlet and outlet pressure conditions, the radial force can be plotted with clearance (as in Fig. 3.5), and the maximum and minimum static clearances determined. If one were now to plot the maximum and minimum static clearances with pressure difference, as in Fig. 3.6, then the performance of the seal can be found over a range of pressure differences. If the seal was operating at a clearance between the minimum and maximum static clearance lines, then the seal will be stationary. At low pressure difference both the minimum and maximum static clearances are large, and hence the seal will be retracted.

Figure 3.6 can be used to imagine how the seal will operate as the pressure is steadily increased and then decreased. If the pressure is initial low, then the seal segment starts in a retracted position. The pressure is increased, and when the maximum static clearance is equal to the retracted clearance, the seal segment will move to its operating clearance, termed 'close in', and is indicated in Fig. 3.6. The seal should then remain static until the pressure is reduced again at which point the segment will retract, shown on Fig. 3.6, or if thermal growth or another rotor radial transient reduced the clearance enough that the clearance is below the minimum static clearance.

The pressure drop across a steam turbine stage is roughly proportional to the load on the turbine. During start up the pressure will be increased enough to spin the turbine up to speed and the generator synchronised to the grid. The load is then steadily increased to the desired load. It is desirable for the Aerostatic Seal to be retracted during the initial run up to speed as this is when the largest rotor radial transient events occur. Once the

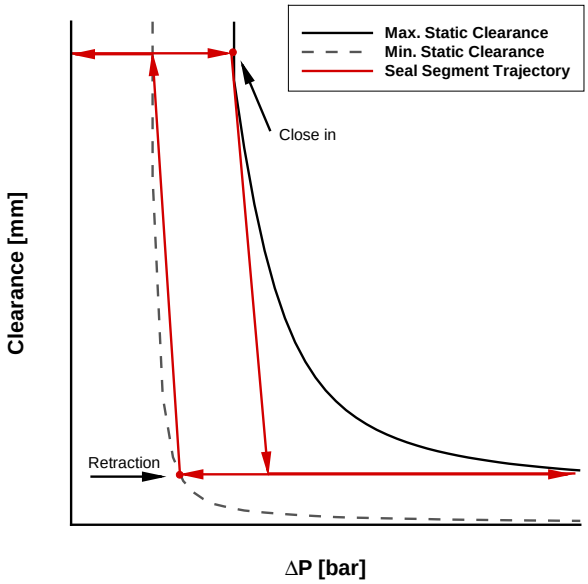

Figure 3.6: Example variation in maximum and minimum static clearance as a function of pressure difference, with trajectory of seal segment.

rotor is up to speed, then the seal should be at the operating clearance to maximise the efficiency of the turbine at part load.

3.2.4 Frictional Effects

The maximum and minimum static clearance is sensitive to the coefficient of static friction. The variation of maximum and minimum static clearance with coefficient of friction is shown in Fig. 3.7, and was calculated using the analytical model described in this chapter, and based on the seal design 'MESS01' at $\Delta P = 0.5\,\text{bar}$. At low coefficients of friction the maximum and minimum static clearance was similar. Increasing the coefficient of friction increases the maximum static clearance and decreases the minimum static clearance, making the seal less responsive. Beyond a coefficient of static friction of $\mu = 0.3$, the gradient of the maximum static clearance decreases, and so a relatively small increase in coefficient of friction has a relatively large increase in maximum static clearance. Therefore it is possible that small changes in friction over time, or small differences in the assumed coefficient of friction at the design stage compared to in operation could have a significant effect on the operating clearance of the Aerostatic Seal. Testing at representative steam turbine conditions is important to ensure that the Aerostatic

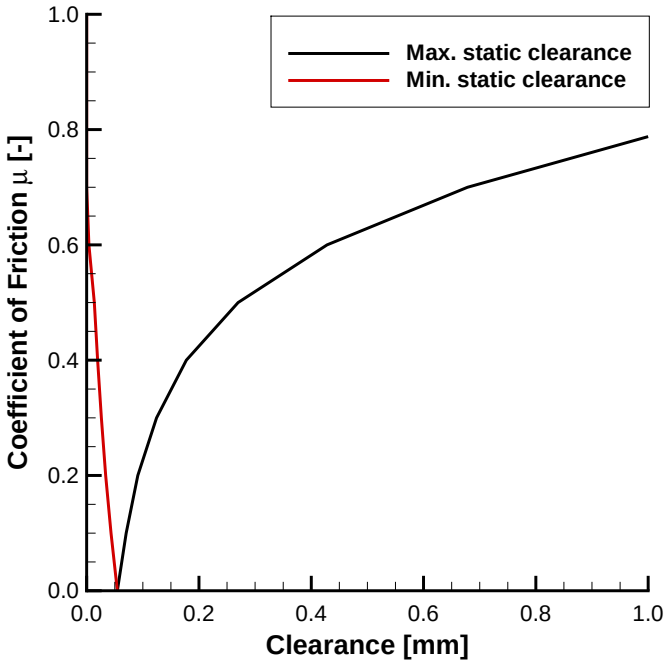

Figure 3.7: Variation of max. and min. static clearance with coefficient of static friction. Inlet pressure $1.5\,\text{bar(a)}$, outlet pressure $1.0\,\text{bar(a)}$, $\Delta P = 0.5\,\text{bar}$, coefficient of static friction $\mu_{stat} = 0.6$, MESS01 seal design. Calculated using the standard analysis methodology (see Section 3.3).

Seal will operate successfully in a steam turbine and not just in the laboratory.

Gen II seal design attempts to reduce the impact of friction by lowering the axial force on the seal segment, thereby reducing the sensitivity of seal performance to variations in friction. This is described in detail in Chapter 7.

3.3 Standard Analysis Methodology

The following section describes how an Aerostatic Seal design may be analysed. The analysis calculates the radial force acting on a seal segment at a range of clearances, and hence determines at what clearance the seal segment is expected to move away and towards the rotor. Figure 3.8 shows a cross section of the Aerostatic Seal segment, and the nomenclature used in the pressure distribution calculation method. For a full description of the seal dimensions see Appendix H.

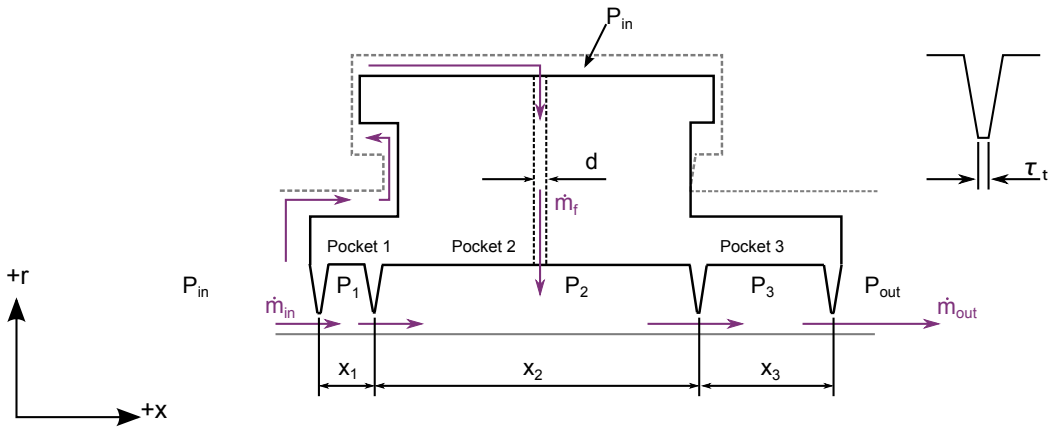

Figure 3.8: Segment cross section and the notation used in the static analysis.

The steps in the analysis method are as follows:

1. Determine the pressure distribution around the seal segment over the full range of seal segment operating clearances.
2. Integrate the pressure field over the seal segment to obtain the net pressure forces.
3. Based on the geometry of the seal segment, calculate the location of the seal segment centroid.
4. Calculate the total radial force, including the spring force and gravitational force.
5. Calculate the clearances at which the total radial force and static friction force are equal.

3.3.1 Pressure calculation method

The flow rate through the seal and pressure distribution is calculated in an iterative process. In order to determine the pressure in each of the seal segment pockets, a leakage equation for a labyrinth seal is used which relates the flow through the seal to the inlet and outlet pressure, fluid temperature and the leakage area of the seal. A summary of different leakage models for labyrinth seals is given in Appendix A. There are three widely used leakage equations available - the 'St. Venant Wantzel' equation, 'Martin's' equation [27], and what is commonly referred to as 'Neumann's' equation [85].

Martin's equation calculates the flow through the seal in a single equation, whereas the St. Venant Wantzel equation and Neumann's equation are used to develop a system of simultaneous equations, each equation applying to a single labyrinth restriction. In the analytical model developed for the Aerostatic Seal, Neumann's equation has been used as it is the easiest equation to invert.

To begin the analysis of the Aerostatic Seal at a particular clearance an initial inlet mass flow is guessed and the pressures in the downstream pockets P_1 and P_2 calculated from Eqs. (3.2) and (3.3). Subscript 'n' refers to the iteration number.

$$P_{1(n)} = \sqrt{P_{in}^2 - \left[\frac{\dot{m}_{in(n)}}{C_D C_{ke} \frac{A_c}{\sqrt{RT_{in}}}}\right]^2} \tag{3.2}$$

$$P_{2(n)} = \sqrt{P_{1(n)}^2 - \left[\frac{\dot{m}_{in(n)}}{C_D C_{ke} \frac{A_c}{\sqrt{RT_{in}}}}\right]^2} \tag{3.3}$$

A constant coefficient of discharge of $C_D = 0.716$ is assumed for all restrictions, as per Eser and Kazakia [86]. There are other methods which account for the variation of discharge coefficient with pressure ratio, see Appendix A. The kinetic energy carry over coefficient, C_{ke}, is unity for the first restriction. In subsequent restrictions, the kinetic energy carry over is calculated using the method of Eser and Kazakia [86], given in Eqs. (3.4) and (3.5). In Eq. (3.5), s is the restriction pitch (i.e. the axial distance between restrictions), N is the number of restrictions, 4 in this case, and c the clearance.

$$C_{ke} = \sqrt{\frac{1}{1 - \frac{\Gamma(N-1)}{N}}} \tag{3.4}$$

$$\Gamma = 1 - \frac{1}{(1 + 16.6\frac{c}{s})^2} \tag{3.5}$$

Within the central cavity there is mixing with the feed hole flow and the main leakage flow. The feed hole flow is modelled using the St. Venant Wantzel' equation (see next section). The mass flow out of the seal segment is given by Eq. (3.6).

$$\dot{m}_{out(n)} = \dot{m}_{in(n)} + \dot{m}_{f(n)} \tag{3.6}$$

The pressure in the third cavity can then be calculated using Eq. (3.7)

$$P_{3(n)} = \sqrt{P_{2(n)}^2 - \left[\frac{\dot{m}_{out(n)}}{C_D C_{ke} \frac{A_c}{\sqrt{RT_{in}}}}\right]^2} \tag{3.7}$$

The mass flow out can then be calculated based the pressure drop between cavity 3 and the outlet pressure, which is known, using Eq. (3.8).

$$\dot{m}_{out(n+1)} = C_D C_{ke} \frac{A_c}{\sqrt{RT_{in}}} \sqrt{P_{3(n)}^2 - P_{out}^2} \tag{3.8}$$

The initial inlet mass flow rate is then updated using Eq. (3.9).

$$\dot{m}_{in(new)} = \dot{m}_{out(n+1)} - \dot{m}_{f(n)} \tag{3.9}$$

To ensure that the iteration procedure is stable, numerical damping is introduced as in Eq. (3.10) where q is an under-relaxation factor, normally set to $q = 0.1$. This was reduced when calculating a clearance less than 0.1 mm.

$$\dot{m}_{in(n+1)} = \dot{m}_{in(n)} + q(\dot{m}_{in(new)} - \dot{m}_{in(n)}) \tag{3.10}$$

The procedure is used for calculations of both air and steam assuming steam is a perfect gas through the seal. Steam fluid properties such as ratio of specific heats γ, specific gas constant R and dynamic viscosity ν are calculated based on the inlet pressure and temperature. *XSteam*, a Matlab code freely available [87] has been used to calculate steam thermodynamic properties based on the 'International Association for Properties of Water and Steam Industrial Formulation 1997' (IAPWS IF-97).

Feed hole flow model

Auld [23] and Rafferty [24] used the St. Venant-Wantzel equation with a discharge coefficient of $C_D = 0.6$ to calculate the mass flow rate through the feed holes, Eq. (3.11). This is the same method described by Powell in his book on aerostatic bearings [88] to calculate the flow through the feed holes.

A second method, based on pipe friction and the Blassius smooth wall equation for friction factor and described in Appendix B, was used to check that the length of the feed

hole was not a significant factor in the flow through the feed holes. The two methods gave good agreement over the expected range of pressure ratios across the feed hole and length of feed holes. As the pipe friction model was iterative and took longer to solve, the St. Venant-Wantzel equation was used in the standard analysis methodology.

$$\dot{m}_f = C_D \frac{4A_f P_{in}}{\sqrt{RT_{in}}} \sqrt{\frac{2\gamma}{\gamma - 1}\left[\left(\frac{P_{in}}{P_2}\right)^{-\frac{2}{\gamma}} - \left(\frac{P_{in}}{P_2}\right)^{-\frac{\gamma+1}{\gamma}}\right]} \tag{3.11}$$

If the feed hole is choked, i.e. when Eq. (3.12) is satisfied, Eq. (3.13) is used instead:

$$\frac{P_{in}}{P_2} > \left(\frac{2}{\gamma+1}\right)^{\frac{\gamma}{1-\gamma}} \tag{3.12}$$

$$\dot{m}_f = C_D \frac{4A_f P_{in}}{\sqrt{RT_{in}}} \sqrt{\gamma \left(\frac{2}{\gamma+1}\right)^{\frac{\gamma+1}{\gamma-1}}} \tag{3.13}$$

Secondary Leakage

In addition to the mass flow between the seal restrictions and the rotor surface, there is a secondary leakage path between the seal segments and through the segment contact face. The analytical design tool models the secondary leakage flow using the St. Venant-Wantzel formula, as for the feed holes, and shown in Eq. (3.11), Eq. (3.12) and Eq. (3.13) when choked. The coefficient of discharge is taken as $C_D = 1.8$ based on measurements taken on the non-rotating test rig at fixed segment clearance - see Section 5.5.6. The area is the area between the seal segments, which neglects flow going through the contact face secondary seal, hence the discharge coefficient is greater than 1. As the secondary seal is formed over the circumference of the seal segment contact face, then even a small axial clearance between the seal segment and the seal holder contact face would have a significant effect on the total secondary leakage flow rate.

3.3.2 Force and Moment Analysis

The first step in calculating the forces acting on the seal segment is to integrate the pressure over every face of the seal segment to find the pressure forces acting in the axial and radial direction. Shear forces have been neglected. As absolute pressure was

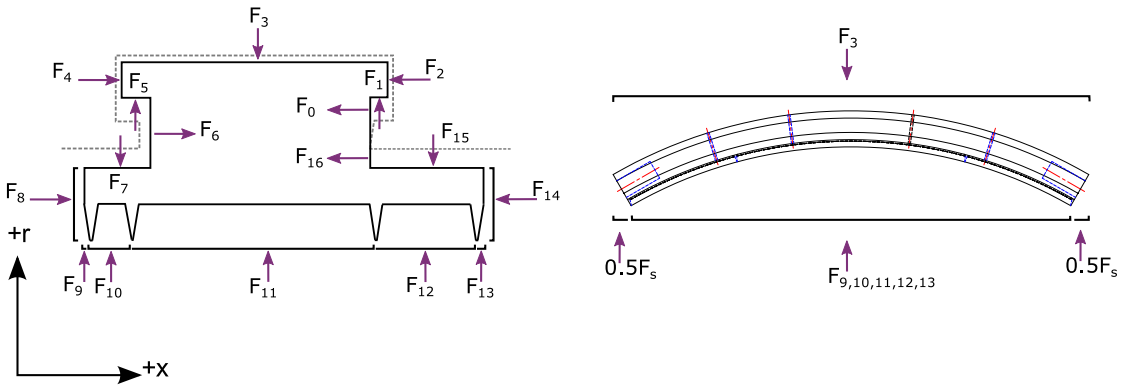

Figure 3.9: Pressure forces acting on the Aerostatic Seal segment.

used to calculate the pressure distribution, it was convenient to calculate the 'absolute' force acting on the seal segment surfaces. When summing all forces, the net force is the same. Figure 3.9 shows the area that different pressures are assumed to act on the seal segment. F_0 to F_9 assume inlet pressure on these areas of the segment. F_{10}, F_{11} and F_{12} assume P_1, P_2 and P_3 respectively. F_{13} to F_{16} assume outlet pressure.

The side pressure force acting in the radial direction, F_s, is calculated by Eq. (3.14). The method was developed by firstly assuming a linear pressure loss from the inlet of the seal segment to the outlet. Therefore the side force is the mean of the inlet and outlet pressure acting over the radially projected side area (A_s). In reality there is also flow from the top surface of the segment, and so the pressure distribution is not linear. Therefore a side pressure distribution coefficient Cf_s is introduced to account for this. This was experimentally found to be $Cf_s = 1.40$, and is reported later in Section 5.5.4. α is the segment angle, 60° for an Aerostatic Seal made from six segments.

$$F_s = 2Cf_s \frac{(P_{in} + P_{out})}{2} A_s \sin\frac{\alpha}{2} \tag{3.14}$$

The contact face, which acts as a secondary seal to prevent flow leaking over the top of the segment, also contributes a pressure force acting on the segment. Arghir et al [81] and Mariot et al [82] when analysing the floating ring seal (see Section 2.4.4) used the Greenwood and Williamson [89], [90] model for mixed lubrication to model the reduction in friction due to mixed lubrication, secondary seal leakage and to calculate the contact face force. The same approach has not been used in the Aerostatic Seal

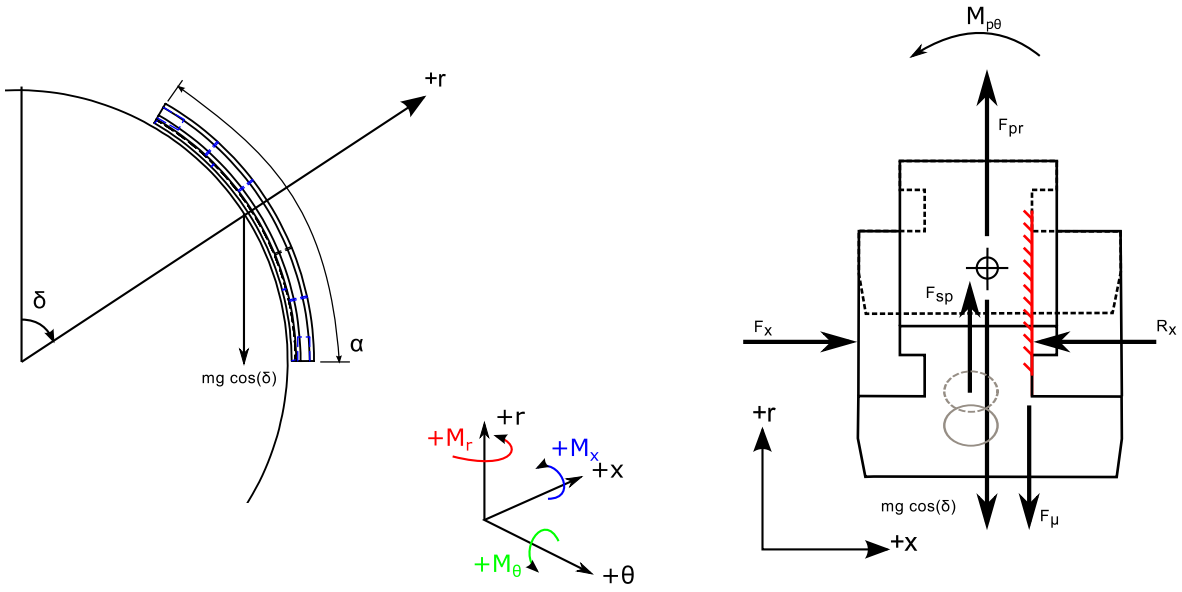

Figure 3.10: Free body diagram of the Aerostatic Seal and applied forces.

standard analysis methodology as the model includes more material variables that are unknown (such as the distribution and size of surface asperities). Instead, the contact face force has been modelled as the outlet pressure acting over the whole surface, which gives the greatest reaction force, and hence greatest frictional force, and is therefore the most conservative method to use during the design phase of the Aerostatic Seal.

Figure 3.10 shows the location of the forces acting on a Aerostatic Seal segment on a free body diagram, with forces resolved in the axial and radial direction. The pressure force has been drawn acting at the centroid of the segment with an applied pressure moment $M_{p\theta}$.

The spring force, resolved in the radial direction, is calculated as per Eqs. (3.15) to (3.17). The force is made up of two parts; the 'pre load' F_{sp0} which is the spring force when the seal segment is retracted, and the 'compression force' F_{spk} which is due to the compression of the springs as the segment moves to a lower clearance. The total spring force from both springs and resolved in the radial direction, F_{sp}, is the sum of both of these components. Figure 3.11 shows part of a seal segment and 'key' with the circumferential spring and the geometry of the spring holes. L_{sp0} is the free length of the circumferential spring, and L_{fr} is the length of the recess in the seal segment and adjacent key for the circumferential spring. c_{ret} is the retracted clearance of the seal segment measured vertically at the centre of the seal segment, as shown in Fig. 3.11. k_{sp}

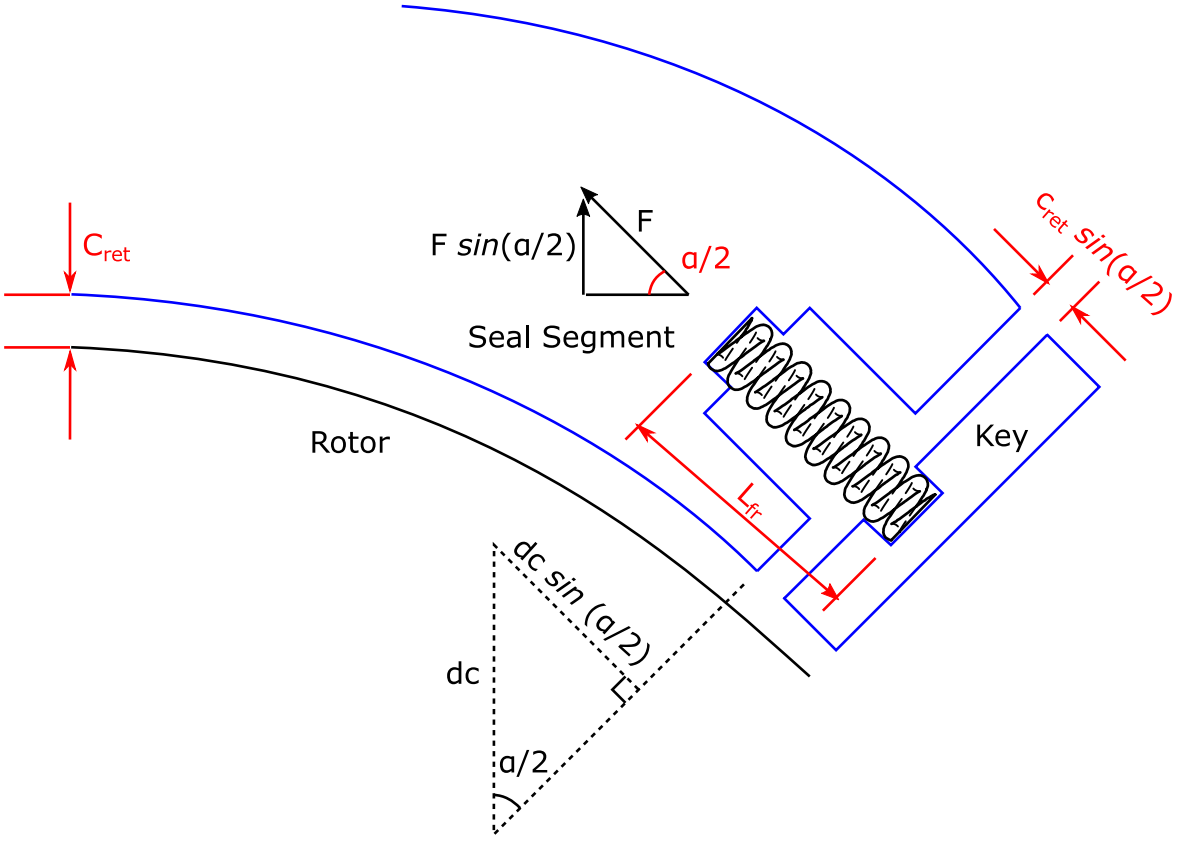

Figure 3.11: Spring shown in retracted seal segment showing spring nomenclature.

is the spring stiffness.

$$F_{sp0} = 2\sin\frac{\alpha}{2}(L_{sp0} - L_{fr})k_{sp} \tag{3.15}$$

$$F_{spk} = 2k_{sp}(c_{ret} - c)\sin^2\frac{\alpha}{2} \tag{3.16}$$

$$F_{sp} = F_{sp0} + F_{spk} \tag{3.17}$$

The gravitational vector acts in different directions for seal segment located at different circumferential positions, as shown in Fig. 3.10. Therefore the gravitational force is resolved in the radial direction dependant on the circumferential angle δ of the seal segment being analysed, as shown in Eq. (3.18).

$$F_{gr} = mg\cos\delta \tag{3.18}$$

If the seal segment was accelerating in the radial direction, then there would also be

the d'Alembert acceleration force, ma, acting on the segment for it to remain in dynamic equilibrium. This force is only of consequence if analysing seal segment moments about a point other than the segment centroid, or the seal segment was accelerating, and is calculated from dynamic equilibrium.

As described earlier in this chapter, friction has been modelled using simple static and dynamic coefficients of friction. When analysing the Aerostatic Seal segment statically, then only a static coefficient of friction is required, and is usually taken as $\mu_{stat} = 0.6$ as standard. The frictional force is determined from the reaction force F_R as given in Eq. (3.19).

$$F_\mu = \begin{cases} -\mu_{stat} F_x \operatorname{sgn}(F_r) & \text{if } |F_r| \geq \mu_{stat} F_x \\ -F_r & \text{if } |F_r| < \mu_{stat} F_x \end{cases} \tag{3.19}$$

where F_r is the net applied force acting on the seal segment, i.e. all forces except the frictional force and the d'Alembert equivalent acceleration force ma.

An important consideration in the design of an Aerostatic Seal is the moment stability of the segment i.e. ensuring that the segment does not tilt inside the seal holder. The procedure for determining the moment stability of the seal segment is as follows:

1. Determine the location of the seal segment centroid (centre of mass).
2. Determine the centre of pressure for each face the pressure is acting on, and therefore determine the moment arm for each pressure force.
3. Calculate the moment generated by each force acting on the seal segment and sum to find the net moment.
4. Calculate the moment generated by the reaction force acting on the extreme locations on the contact face. These moments are the maximum moments that can be tolerated before the seal segment will start to tilt.
5. Determine if the net moment is within the limits.

To determine the location of the centroid of the seal segment, the segment is divided into 17 simple blocks and the centroid of each component found in the axial and radial dimensions. Each of these blocks represented the main body of the seal segment,

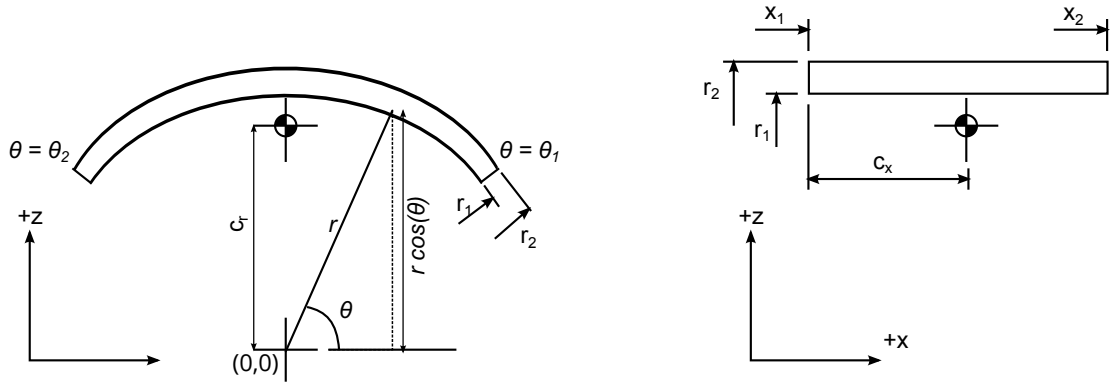

Figure 3.12: Centroid calculation method

the axial and circumferential fins, and the feed holes and spring holes. The centroid of the whole segment was then found by performing a volume weighted sum (Eqs. (3.20) and (3.21)) of each component shape. Figure 3.12 shows the local coordinate system used for a single block. Note that the blocks representing the holes for the circumferential springs and feed holes are treated as having negative volume. Calculation for each individual component block is as per equations Eqs. (3.22) and (3.23). The volume of a particular block is $V(n)$, where (n) is an index to the particular block. $\bar{c_r}$ and $\bar{c_x}$ is the radial and axial coordinates of the seal segment centroid, respectively. c_r and c_x is the radial and axial coordinates of the centroid of each individual block, respectively.

$$\bar{c_r} = \frac{\sum c_r(n)V(n)}{\sum V(n)} \tag{3.20}$$

$$\bar{c_x} = \frac{\sum c_x(n)V(n)}{\sum V(n)} \tag{3.21}$$

$$c_r = \frac{\iint\limits_A z\,dx\,dz}{\iint\limits_A dx\,dz} = \frac{2}{3}\frac{(r_2^3 - r_1^3)}{(r_2^2 - r_1^2)}\frac{(\cos\theta_1 - \cos\theta_2)}{(\theta_2 - \theta_1)} \tag{3.22}$$

$$c_x = \frac{\iint\limits_A x\,dx\,dz}{\iint\limits_A dx\,dz} = \frac{x}{2} \tag{3.23}$$

Once the centroid location has been found, the moment acting on the seal segment can then be calculated about the centroid. The pressure forces on each face of the seal segment can be analysed as acting at the centroid of each face, and summed together to

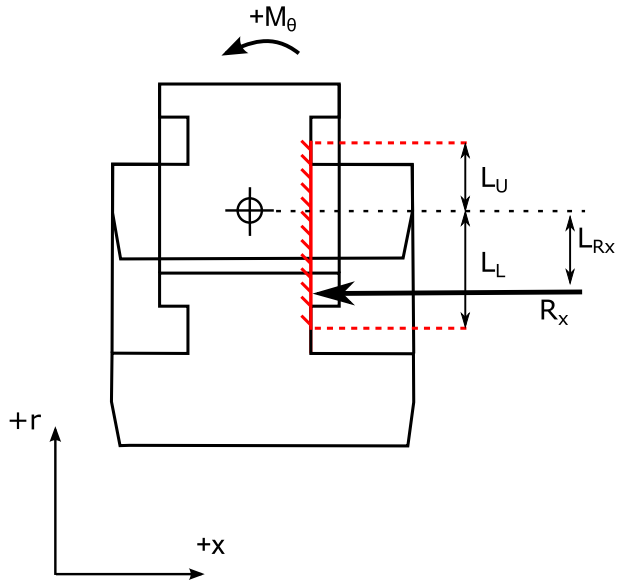

Figure 3.13: Moment stability of seal segment

find the pressure moment acting on the seal. Other forces also generate a moment acting on the seal, such as the reaction force, seal segment weight, the frictional force and the circumferential spring force. If the seal is moving then there is also an inertial force acting on the seal segment. These forces and locations are summarised in Fig. 3.10. Note that the net radial pressure force has been decomposed into a force and moment acting at the centroid of the seal segment. Other forces are drawn at the location at which they act on the seal segment.

The exact location of the reaction force applied by the diaphragm on the seal segment is found from the requirement of moment equilibrium, i.e. the location of the reaction force must be such that it balances all the other moments acting on the seal segment. The reaction force must act somewhere on the contact face of the seal segment, hence the maximum and minimum reaction moment can be found.

L_U and L_L are the distances from the centroid of the segment (or any other place about which moments are taken) to the maximum and minimum radial location of the contact face respectively. This is shown in Fig. 3.13. M_U and M_L are defined in Eqs. (3.24) and (3.25) and are the greatest range of reaction moments available to balance the applied moments.

$$M_U = F_x L_U \tag{3.24}$$

$$M_L = F_x L_L \tag{3.25}$$

$$\xi = \frac{M_U + M_\theta}{M_U + M_L} \tag{3.26}$$

If the reaction moment is not big enough to balance the other moments acting on the seal segment, then moment stability is lost which could lead to the segment tilting forward and loosing positive radial force, or becoming jammed inside the diaphragm. The design aim is to have a reaction contact force somewhere in between so as to maintain moment equilibrium, with a suitable margin. The seal moment criterion (ξ) is defined as +1.0 when the pressure moment exactly opposes the contact anticlockwise moment and 0.0 when it exactly opposes the contact clockwise moment, as shown in Eq. (3.26). Therefore if $0.0 < \xi < 1.0$ the seal segment is stable and the moment criterion met. Figure 3.14 shows typical graphs of moment stability criterion. The shaded region is the clearance at which the seal segment has no net force acting on it. The discontinuity in slope is where the net radial force is able to overcome the static friction force, and hence move away or towards the rotor surface.

Moments can be taken about any point on the seal segment. This has been confirmed by taking moments about the lowest point on the contact face, which gives the same moment criterion.

3.3.3 Limitations

The model described above is a simple one dimensional leakage model. The advantage of such a simple model is that it is fast to solve making it ideally suited to analysing a wide range of designs quickly. The rest of this section discusses the limitations of the standard analytical methodology set out above:

- All the flow is assumed to be axial. In reality the incoming flow will have a level of swirl due to the stator blades and due to the high rotor surface velocity. This will effect the leakage flow through the seal, and if the level of circumferential flow changes through the seal due to the circumferential pockets on the seal, then the pressure distribution would be affected. Waschka et al [91] found no effect of

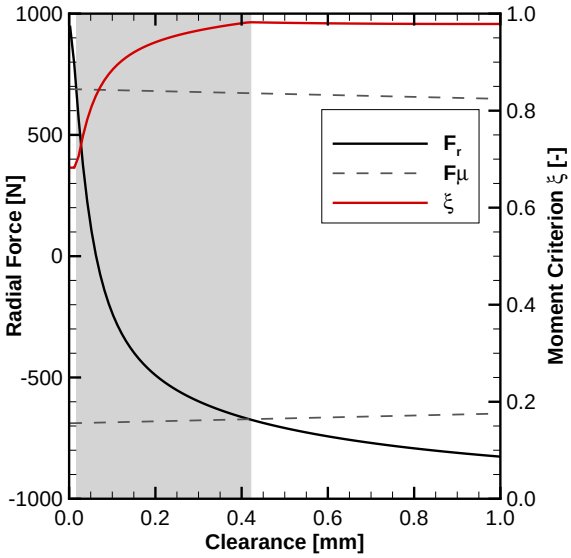

Figure 3.14: Applied radial force and moment acting on a typical Aerostatic Seal design.

rotational speed on seal discharge coefficient for $Ta/Re_x < 0.2$, although this was without circumferential pockets. Ta is the Taylor number (see Eq. (3.27)) and Re_x is the axial Reynolds number (see Eq. (3.28)).

$$Ta = \frac{2uc_m\rho}{\eta}\sqrt{\frac{2c_m}{D}} \tag{3.27}$$

$$Re_x = \frac{2\dot{m}}{\eta\pi D} = \frac{2\rho v c_m}{\eta} \tag{3.28}$$

There will also be circumferential flow components due to differing pressures in the circumferential pockets and in the side leakage path.

- The leakage model used is that described by Eser and Kazakia [86] (see Appendix A), which assumes isothermal flow through the seal, and a constant discharge coefficient in Eq. (3.2). Other researchers have found that the discharge coefficient changes depending on the pressure ratio [32] and also between different restrictions in the seal [92].

- The leakage model assumes that the flow never becomes choked across a single restriction.

- The model is static, and does not analyse the dynamic behaviour of the seal segment directly. The method of judging the dynamic performance is to look at the stiffness curve (force v clearance), and to judge when there is a net radial force that will move the seal segment away or towards the rotor. The leakage model assumes steady flow. The change in volume of the seal pockets will vary the pressure when the seal segment moves.

- The force model assumes uniform pressure on the seal faces. There is likely to be variation in pressure in the seal cavities and on the side face of the seal segment.

- A static friction model is used. There are more detailed friction models available, although more detail introduces more model variables, for which there is a lack of available data. Changing the assumed value for the static coefficient of friction has one of the biggest effects on the expected performance of the Aerostatic Seal.

3.4 Design Methodology

An Aerostatic Seal design tool was first implemented by Rafferty [24] which performed a full search of the solution space, with bounds set by the designer. The solution space is made up of the multi-dimensional region consisting of various Aerostatic Seal parameters such as the segment width, feed hole diameter, fin pitch etc. For a full list of dimensions, see Appendix H.

For the Aerostatic Seal a design is sought that is as responsive to rotor movement as possible but that maintains moment stability. To maximise the responsiveness of the seal segment, the change in force needs to be maximised, and this is achieved by making the seal segment with the greatest axial length possible. The radial force varies linearly with the radially projected area. The axial length of the segment cannot be increased indefinitely however as increasing the length also increases the pressure moment acting on the segment. In fact the moment increases with the square of the axial length, considering that the moment is the pressure force multiplied by the moment arm, both of which depend on the axial length of the segment. Whilst this is useful for the designer to understand, other variables such as the positioning of the restrictions below the seal segment also effect the pressure distribution, and hence affect the pressure moment

and the radial pressure forces.

As part of the work conduced in this project, the seal design methodology has been updated with the standard analytical model described in the previous section, and the tool given the ability to pick the best seal design at a given set of design pressures.

3.4.1 Design tool algorithm

The following subsection describes the design tool used for obtaining an Aerostatic Seal design. A flow diagram is given in Fig. 3.15. The user defines the pressure conditions that the seal is to operate at, and picks the minimum and maximum operating clearances. The design tool then loops through the solution space and finds 'feasible' seal designs that would operate at the minimum and maximum clearance. Feasible is defined as meeting moment stability with a suitable margin at both operating clearances.

Step 1: Define solution space

The first step in designing the Aerostatic Seal is to define the solution space, i.e. the range of values that each design parameter can take. As there are a large number of variables that affect the performance of the Aerostatic Seal, suitable limits are required to ensure the design code will complete in a suitable time. Some design parameters can be chosen by mechanical design considerations or design rules, such as the height of the seal for a given rotor radius. Other parameters may be limited through design experience or analytical considerations. Circumferential springs are chosen by including a number of standard spring designs with fixed free lengths and springs rates in the solution space. Circumferential spring pre-load is varied by changing the spring holder depth within the geometric constraints of the seal segment.

Step 2: Loop through solution space

Loop through the solution space and analyse the seal at the desired pressure conditions and at two fixed clearances: the user defined minimum and maximum clearance. Reject designs that are not in moment equilibrium.

An objective function, Φ, has been defined, given in Eqs. (3.29) to (3.31), which is used to measure how close the radial force is to overcoming the static friction force at

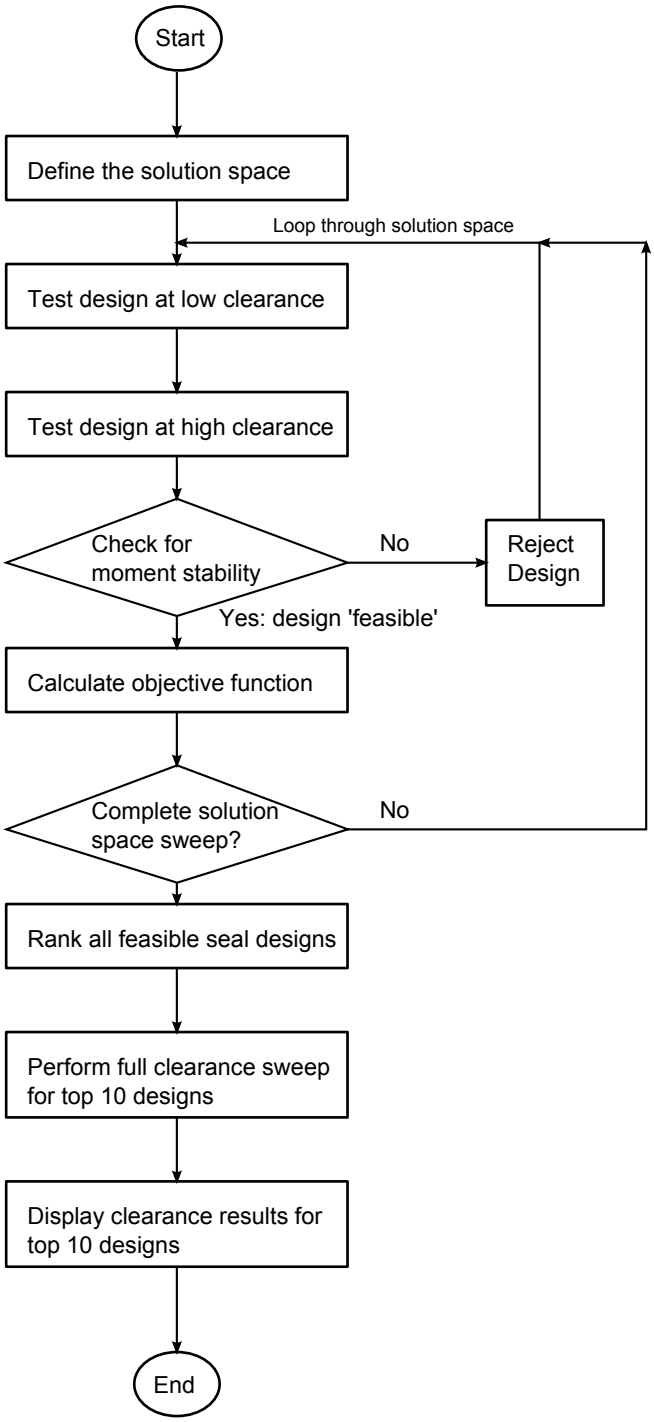

Figure 3.15: Flow diagram of the Aerostatic Seal design methodology.

the user defined minimum and maximum clearances. At the minimum clearance, the radial force should be positive and equal to the magnitude of the static friction force. At the maximum clearance the radial force should be negative and also equal in magnitude to the static friction force. The best seal design will minimise the net force at both of these clearances, i.e. $\frac{F_r}{F_\mu}$ will be the closest to 1. Figure 3.16 shows an example of a seal design, analysed at the minimum and maximum defined clearance, and the variation of the minimum and maximum objective functions Φ_{min} and Φ_{max} respectively. If the user chosen minimum clearance equals the minimum static clearance then $\Phi_{min} = 1.0$. Similarly if the user chosen maximum clearance equals the maximum static clearance then $\Phi_{min} = 1.0$. The perfect seal design for the user's choice of minimum and maximum clearances will have a combined objective function of $\Phi = 2.0$. The maximum and minimum functions refer to the maximum and minimum values of $\frac{F_r}{F_\mu}$ for all seal designs tested within the chosen solution space.

$$\Phi_{min} = \begin{cases} \left[\frac{1.0}{1.0-max(\frac{F_r}{F_\mu})}\right] . \left[\frac{F_r}{F_\mu} - 1.0\right] + 1.0 & \text{if } \frac{F_r}{F_\mu} \geq 1.0 \\ \left[\frac{1.0}{1.0-min(\frac{F_r}{F_\mu})}\right] . \left[\frac{F_r}{F_\mu} - 1.0\right] + 1.0 & \text{if } \frac{F_r}{F_\mu} \leq 1.0 \end{cases} \tag{3.29}$$

$$\Phi_{max} = \begin{cases} \left[\frac{1.0}{1.0-max(\frac{F_r}{-F_\mu})}\right] . \left[\frac{F_r}{-F_\mu} - 1.0\right] + 1.0 & \text{if } \frac{F_r}{-F_\mu} \geq 1.0 \\ \left[\frac{1.0}{1.0-min(\frac{F_r}{-F_\mu})}\right] . \left[\frac{F_r}{-F_\mu} - 1.0\right] + 1.0 & \text{if } \frac{F_r}{-F_\mu} \leq 1.0 \end{cases} \tag{3.30}$$

$$\Phi = \Phi_{min} + \Phi_{max} \tag{3.31}$$

As the shape of the force-clearance curve is steepest at low clearance and becomes less steep at increased clearance, see Fig. 3.16 for example, then the objective function is more sensitive at the minimum clearance than at the maximum clearance. Another way of looking at it is that a small offset in force F_r will affect the maximum clearance much more than the minimum clearance. A linear variation of objective function with $\frac{F_r}{F_\mu}$ has been chosen, but a different function could be used or different weightings of minimum and maximum objective functions to reflect the different sensitivity at the user defined minimum and maximum clearances.

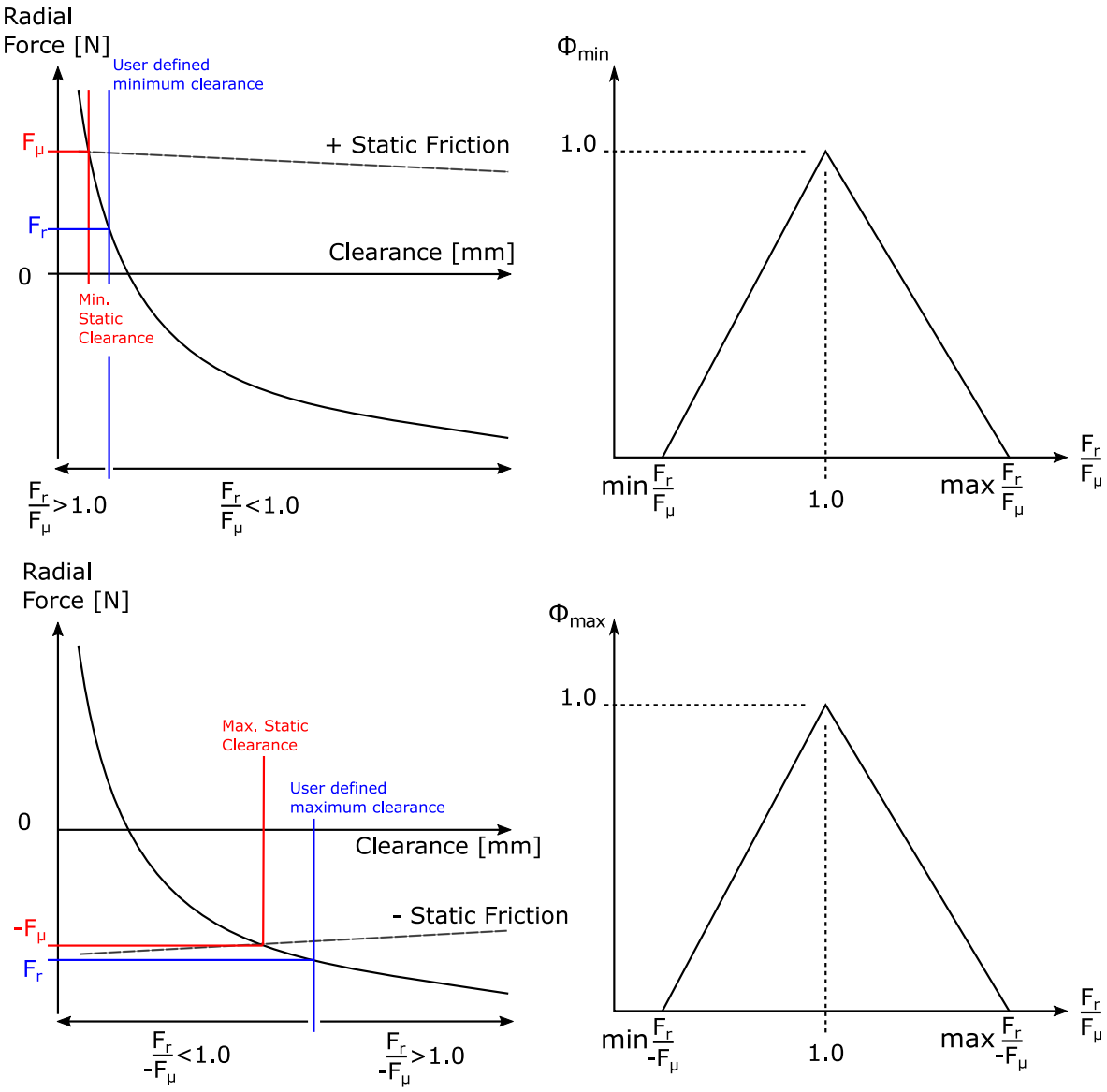

Figure 3.16: Example Aerostatic Seal force clearance curve and variation of maximum (Φ_{max}) and minimum (Φ_{min}) objective function.

Step 3: Pick top 10 designs

Using the objective function, the top designs from the solution space are chosen. For each of these designs, the seal is analysed over the full range of operating clearance and the force-clearance characteristic found. These 10 seal designs are then output to the user, to choose a design based on engineering judgement.

Step 4: Refinement

Based on the output from the design code, the user may choose to refine the solution space that the design tool searches or perform further analysis on the design, such as a sweep of different pressure conditions or friction sensitivity analysis.

3.4.2 Limitations

In addition to the assumptions and limitations associated with the standard analysis methodology described in Section 3.3.3, the design code, in its currently form does not consider the start-up behaviour of the seal. i.e. at what pressure the seal closes in.

3.5 Implemented Aerostatic Seal Designs

A number of Aerostatic Seal designs have been generated and are described in this section. Not all of the designs have been generated using the same version of the design method as the methodology has developed over the course of the project; however they are all analysed using version V20.0 so the expected performance can be compared. Figure 3.17 shows a scale drawing of all seal designs for comparison. Table H.1 in Appendix H lists the different seal designs and the design parameters.

To compare the different seal designs, the variation in maximum and minimum static clearance with pressure ratio has been plotted for each seal design in Fig. 3.18. When the seal segment clearance is greater than the maximum static clearance, the segment will move towards the rotor. When the seal segment clearance is lower than the minimum static clearance, the segment will move away from the rotor. Contours of moment criterion ξ are also plotted in Fig. 3.18. Moment stability is lost when the contour is red or blue. There is variation in the predicted design performance when analysed with

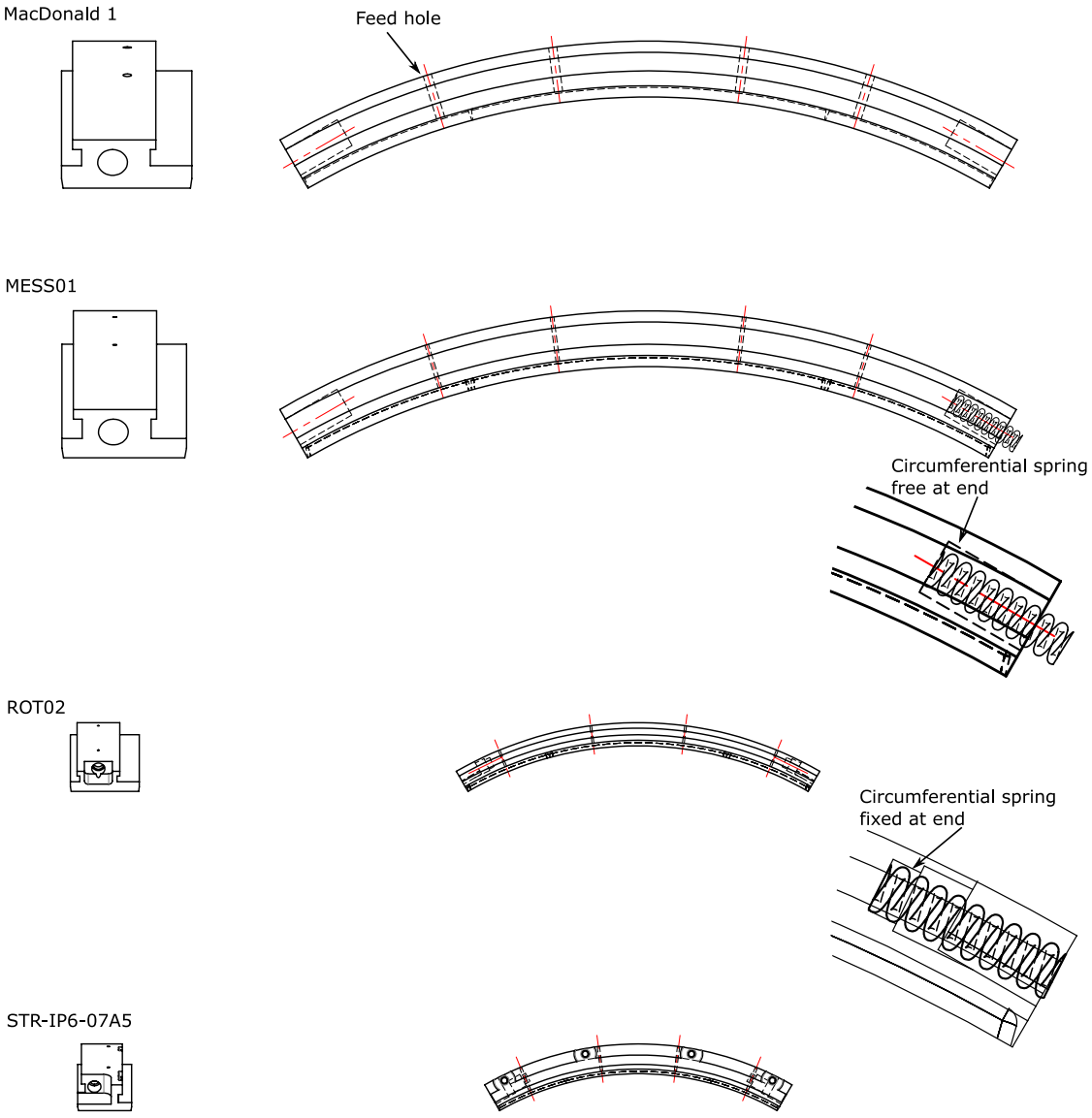

Figure 3.17: Comparison of Aerostatic Seal geometry for different seal designs.

the standard design methodology partly due to using different versions of the design methodology to design the seals, but also due to different seal designs operating at different inlet pressure conditions. The coefficient of friction was assumed to be $\mu_{stat} = 0.6$.

3.5.1 'MacDonald1'

The first seal design manufactured was designated 'MacDonald1', the design produced by MacDonald [26]. The design was produced for the non-rotating test rig described in Chapter 4, and was used for the initial testing of the Aerostatic Seal concept. The seal was designed to be made from aluminium as the weight of the segment was initially thought to be an issue when operating at lower pressures. Results from the experimental tests with this seal design are included in Sections 5.2 and 5.3. 'MacDonald 1' was designed with a nominal clearance of $0.4\,\mathrm{mm}$, so that the seal radius was 0.4 mm larger than the rotor radius. The spring hole design was a simple hole without fixing the ends of the springs, and is shown in Fig. 3.17. This gave $3\,\mathrm{mm}$ clearance around the spring.

The 'MacDonald1' seal design when analysed with version V20.0 of the Aerostatic Seal analysis code, shown in Fig. 3.18a, was predicted to operate at a high clearance, approximately $1.8\,\mathrm{mm}$ - much higher than desirable. This was mainly because of the large feed hole diameter and the high 'pre load' on the circumferential springs.

3.5.2 'MESS01'

'MESS01' seal design was the next seal design conducted, and was also to be used in the non-rotating test rig. The seal design aimed to improve over the 'MacDonald1' design by using smaller feed holes to increase the responsiveness of the seal. The segment was manufactured from S355J2, a structural mild steel, enabling the labyrinth fins to be sharper, and to reduce wear and damage occurring on the contact face of the seal segment. The expected performance is plotted in Fig. 3.18b.

This seal design introduces a smaller contact face on the seal holder, which reduces the frictional force by decreasing the axial force acting on the seal segment as the area 'F0' (see Fig. 3.9) is increased. The smaller contact face also would prevent the sealing point on the contact face, which acts as a secondary seal, from moving to a higher clearance due to diaphragm deflection. The spring hole design was a simple hole, as

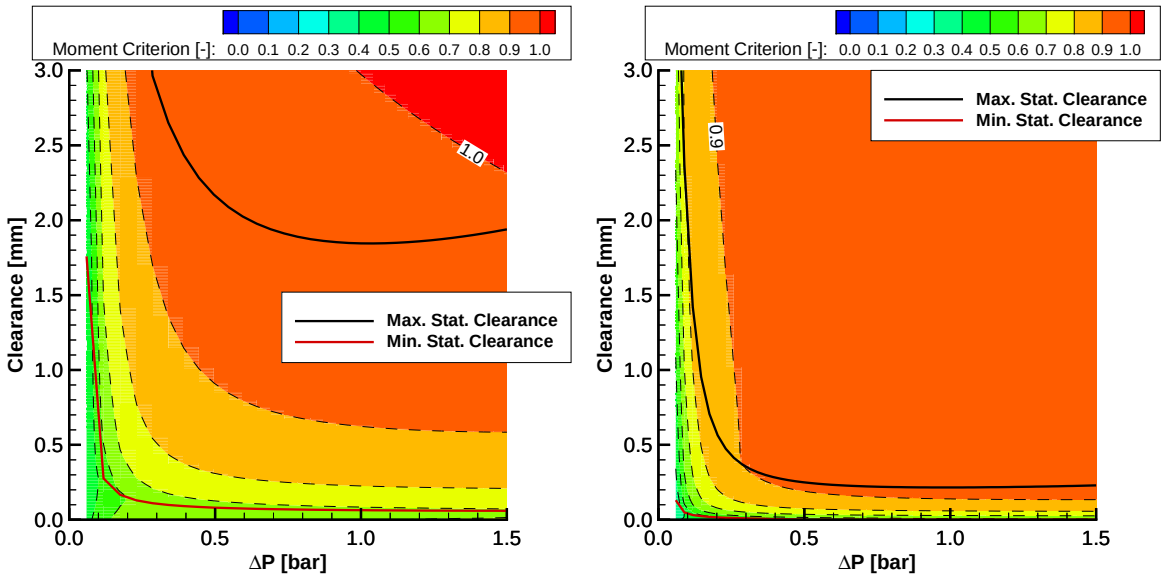

(a) 'MacDonald 1' Seal design. Inlet pressure 6.0 bar(a).

(b) 'MESS01' seal design. Outlet pressure 1.0 bar(a).

(c) 'ROT-02' seal design. Outlet pressure 1.0 bar(a).

(d) 'STR-IP6-07A5' seal design. Outlet pressure 6.0 bar(a).

Figure 3.18: Comparison of Aerostatic Seal designs. Coefficient of friction $\mu_{stat} = 0.6$.

in ‘MacDonald1’, although specially designed inserts can be used to fix the ends of the springs in the segment.

3.5.3 ‘ROT02’

‘ROT02’ seal design was for the Durham Rotating Seals Rig described in Chapter 4. The rotating rig has a smaller rotor diameter than the non-rotating rig, and models a full set of seal segments rather than a single seal segment as in the non-rotating test rig. The seal segments are each held between anti rotation keys which isolate the seal segments from each other. The keys are shown in Fig. 3.19 for the ‘STR-IP6-07A5’ seal design, which are similar to the design in ROT02. This is unlike the retractable seal which only has anti-rotating keys at the half joint in the turbine casing. The cut away which accommodates the keys was not included in the analysis of the seal performance. The spring hole design for ‘ROT-02’ was changed so that both ends of the spring are now fixed in the seal segment and the key, as shown in Fig. 3.17.

The ‘ROT-02’ seal design was made as responsive as possible for operation in the rotating rig, and as a result would lose moment stability at high clearance once the seal segment has closed in, as shown in Fig. 3.18c.

3.5.4 ‘MESS04’

‘MESS04’ is the same seal as MESS01, but with axial friction compensator springs included. The base design of the seal is the same as ‘MESS01’ except that lands have been included which allow axial springs to be fitted. Omitting the axial springs allows the seal to return to ‘MESS01’ configuration.

3.5.5 ‘STR-IP6-07A5’

‘STR-IP6-07A5’ is a seal design for the Braunschweig steam test rig. This seal design is to operating in steam at high temperature. Particular effort has been made to minimise the sensitivity to variations in friction coefficient, and as a result the expected operating clearance is low, as shown in Fig. 3.18d. Like seal design ‘MESS04’, the seal can be operated with axial friction compensator springs. The spring hole design was as ‘ROT-02’.

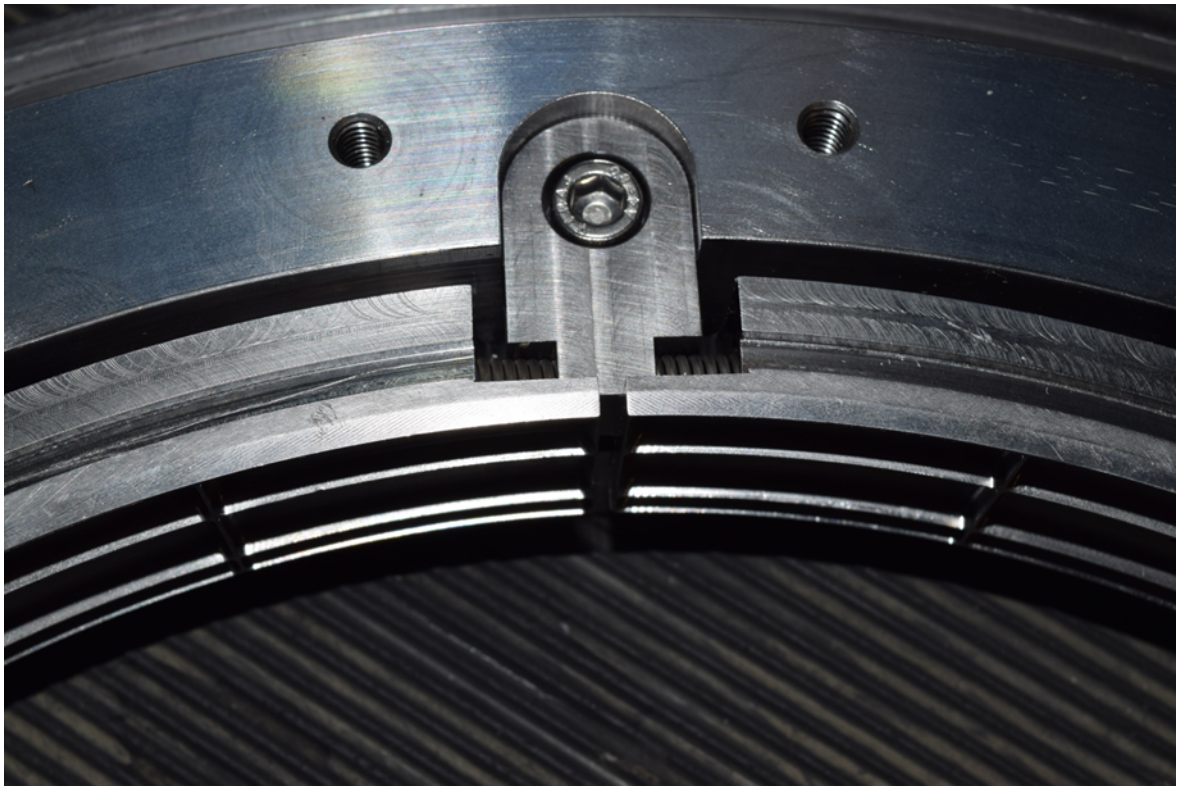

Figure 3.19: Keys between seal segment as on the ‘STR-IP6-07A5’ seal design.

3.6 Conclusion

This chapter has described the design and analysis methodology for the Aerostatic Seal, as well the theory behind the operation of the seal. The standard analysis methodology is a simple 1D steady flow model which can calculate the pressure distribution on the seal segment and hence the forces acting on the segment at different operating clearances. The analysis methodology is built into the design code which performs a solution space search to find suitable Aerostatic Seal designs. The design code has been used to generate a number of different designs which have been tested in the non-rotating and rotating test rigs described in Chapter 4.

Chapter 4

Rig Designs

4.1 Introduction

Three test rigs have been used in the development of the Aerostatic Seal : a non-rotating rig using air, a rotating rig using air, and a rotating rig using steam. The two rigs using air are installed on the Durham University Blowdown Facility, and the steam test rig located at TU Braunschweig, Germany. This chapter details the rigs and the instrumentation at Durham University. Table 4.1 compares the three test rigs used and the first stage of the intermediate cylinder of a typical coal fired generator set (IP1).

Initial testing was carried out in a non-rotating rig which was used in the development of the Aerostatic Seal concept, and modelled a single full scale seal segment. As the rig was non-rotating it was reasonably inexpensive to manufacture before development work in more advanced rotating rigs, however the rig could not model rotor excursions. The rig used capacitance sensors to track the position of the seal segment during operation of the test rig.

The rotating rig was the next stage of development which modelled a full seal at half

	Non-rotating Rig	Rotating Rig	Steam Rig	IP1 ST conditions
Fluid	Air	Air	Steam	Steam
Temperature / $^{\circ}$C	20	20	400-500	540
Rotor diameter D / mm	732	366	299.8	732
Inlet Pressure / bar(a)	6.0	1.5	7.5	37.2
Max. Surface Speed u / m s^{-1}	0	29 (1500 rpm)	138 (8784 rpm)	138 (3600 rpm)

Table 4.1: Comparison of test rigs.

scale. The rig used an eccentric rotor to model high speed radial rotor excursions and inductive sensors to track the position of three of the six seal segments. Pressures are measured at inlet and outlet from the rig, and static pressure measured by pressure taps drilled in a single seal segment.

A final set of tests was conducted in a steam test rig controlled by TU Braunschweig in Germany. This test rig used steam rather than air, and represented a closer representation to steam turbine conditions. The rig was able to offset the casing to simulate low speed rotor movements, although it cannot model high speed rotor movements. The rig is half scale, although operates up to 10000 rpm to match steam turbine rotor surface speed. As the TU Braunschweig rig is an existing test facility and details are previously published, a detailed description is not given here. Brief details are given in Chapter 9.

The rest of this chapter describes each of the test rigs in detail and the Durham University Blowdown Facility, which includes some common components to both the non-rotating and rotating rig.

4.2 Durham University Blowdown Facility

The Durham University Blowdown Facility is a transient open flow test facility capable of delivering high pressure and high flow rate air for short durations. The facility consists of a $10\,\mathrm{m}^3$ air receiver, with a maximum operating pressure of $30\,\mathrm{bar}$, and a control valve that regulates the supplied pressure. Pipework connects the control valve to a number of different rigs, housed in an adjacent underground test cell. The facility is equipped with an instrumentation and control suite external to the test cell to log data and control the facility.

The Blowdown facility is equipped with common instrumentation infrastructure for all individual rigs. Measurements typically include:

- Mass flow rate of supply air
- Tank temperature and pressure
- Rig static pressure and temperature

Individual rigs can include further instrumentation specific to that rig, such as load cells, opto couple speed sensors or displacement sensors.

Figure 4.1 shows the typical control and instrumentation layout on the blowdown facility, which can be loosely divided into instrumentation, data acquisition and control and processing. Instrumentation is built up from a number of rack mounted modules that are interchangeable across other facilities within the thermo-fluids laboratory and output an analogue voltage signal. Data acquisition consists of multiple analogue to digital (A/D) converters: National Instruments USB6218 are used on the blowdown facility. Control and processing is via the 'Durham Software for Wind tunnels' suite of programs which logs and processes data, and LabView (version 2013 SP1) which is used to control the facility.

4.2.1 Instrumentation

Two ScaniValve DSA 3217 pressure scanners are used for logging pressures, each with 16 pressure transducers. Each scanner consists of 8 high pressure (max 17.2 bar) and 8 low (6.9 bar) pressure transducers. The pressure scanners output pressure in engineering units (e.g. pascals) over the network and operate up to 800 Hz per channel. The pressure scanners are supplemented with single First Sensor BTE and CTE series pressure transducers. These output a linear voltage typically in the range 0 to 10 V which is proportional to the measured pressure.

Mass flow rate through the facility is measured with an orifice plate upstream to the control valve. The orifice plate is manufactured to BS EN ISO 5167-1/2, and uses interchangeable plates of different bore to allow different flow rates to be measured accurately. Mass flow rate is calculated from the differential pressure across the orifice restriction P_{diff}, the upstream pressure P_u, and the stagnation temperature T_0 measured in the air receiver. See Appendix E for details on the calculation method.

Temperature was measured using T or K type thermocouples, connected to an amplifier (Omega Engineering TXDIN1620) which outputs a programmable voltage output.

4.2.2 Acquisition

Voltage signals are digitised using a National Instruments USB-6218 analogue to digital converter operated using the 'Durham Software for Wind Tunnels' suite of programs for data acquisition and analysis. The USB-6218 multiplexes between 16 differential chan-

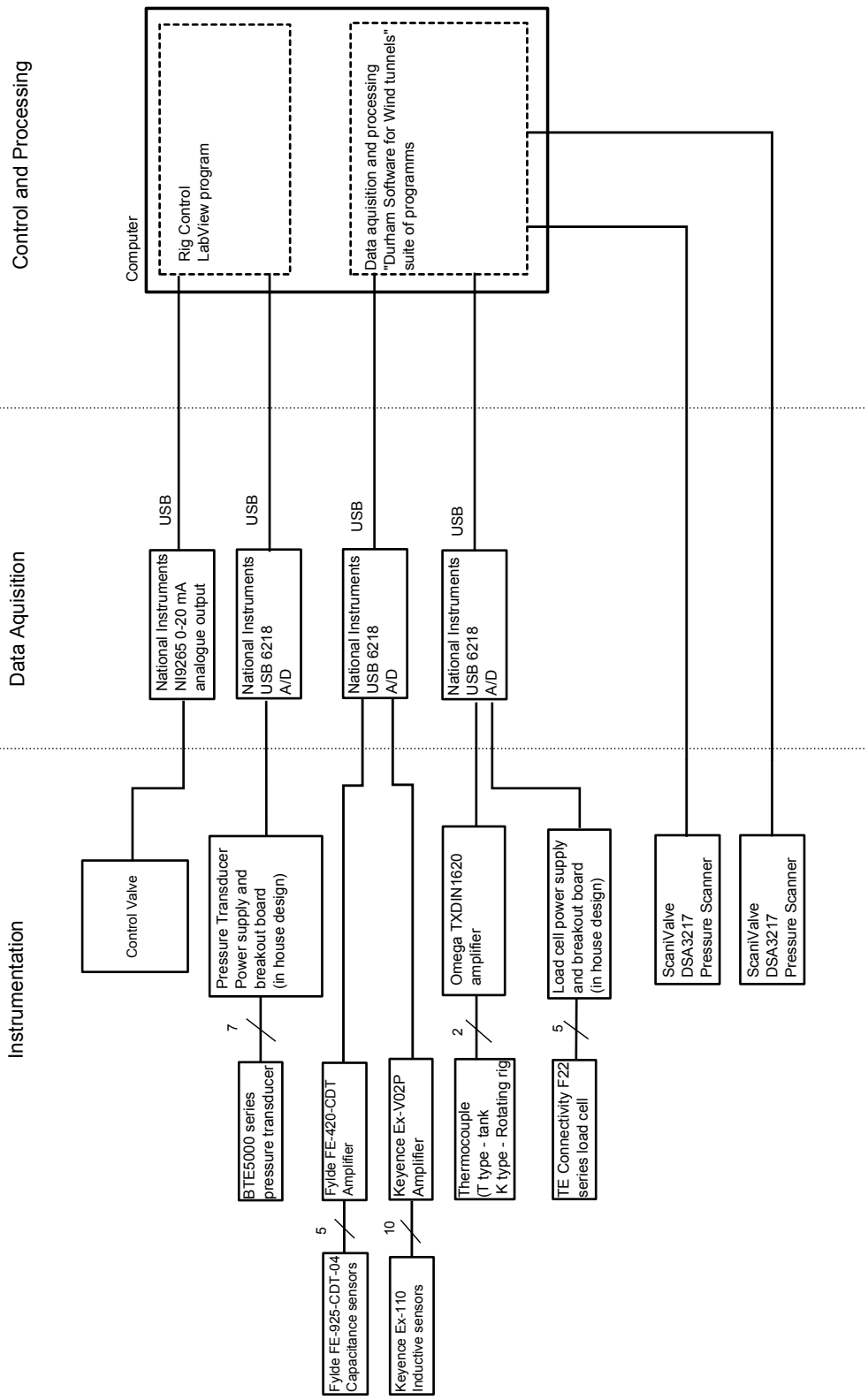

Figure 4.1: Instrumentation layout diagram for the blowdown facility.

nels at a frequency up to 250 kS/s and can measure signals between ± 10 V. The resolution of the digitised signal is 320 µV, well below the accuracy of the pressure transducers.

4.2.3 Control and Processing

The 'Durham Software for Wind tunnels' suite of programs is used to record the voltage signals from the analogue to digital converters and also the data from the pressure scanners. A new program was created by the author to simultaneously log the data from multiple pressure scanners and multiple A/D converters. The suite also includes programs to convert voltage signals into engineering units for individual transducers, calculate mass flow rate from an orifice plate, and to average and non-dimensionalise data.

A series of LabView programs are available for controlling the blowdown facility. The program interfaces with the control valve via a National Instruments NI9265 which generates an analogue current signal, and can vary the valve position. A separate A/D converter is used to display data in real time and to measure a set point for controlling the valve position. The program includes a PID controller which can maintain a steady pressure during operation of the facility.

4.3 Non-Rotating Rig

A non-rotating rig, referred to as the 'non-rotating rig', was built to carry out initial testing on the Aerostatic Seal concept. The initial design was carried out by Durnan [25] and built and developed as part of this project. Figure 4.2 shows the rig installed in the test cell. The rig rotor diameter and seal holder dimensions were based on a steam turbine intermediate pressure diaphragm. The modifications from Durnan's original design are outlined at the end of this section.

The rig models a single full scale Aerostatic Seal segment. The rotor was non-rotating and cannot be actuated during a test, although the position could be changed during rig set up. The seal segment was free to move as it would in a turbine, and capacitive sensors were used to measure segment position. Figure 4.3 shows a cross section of the rig with a seal segment installed, and highlights key features. The rig consists of the seal holder, made in two parts, which models the diaphragm of the turbine, and

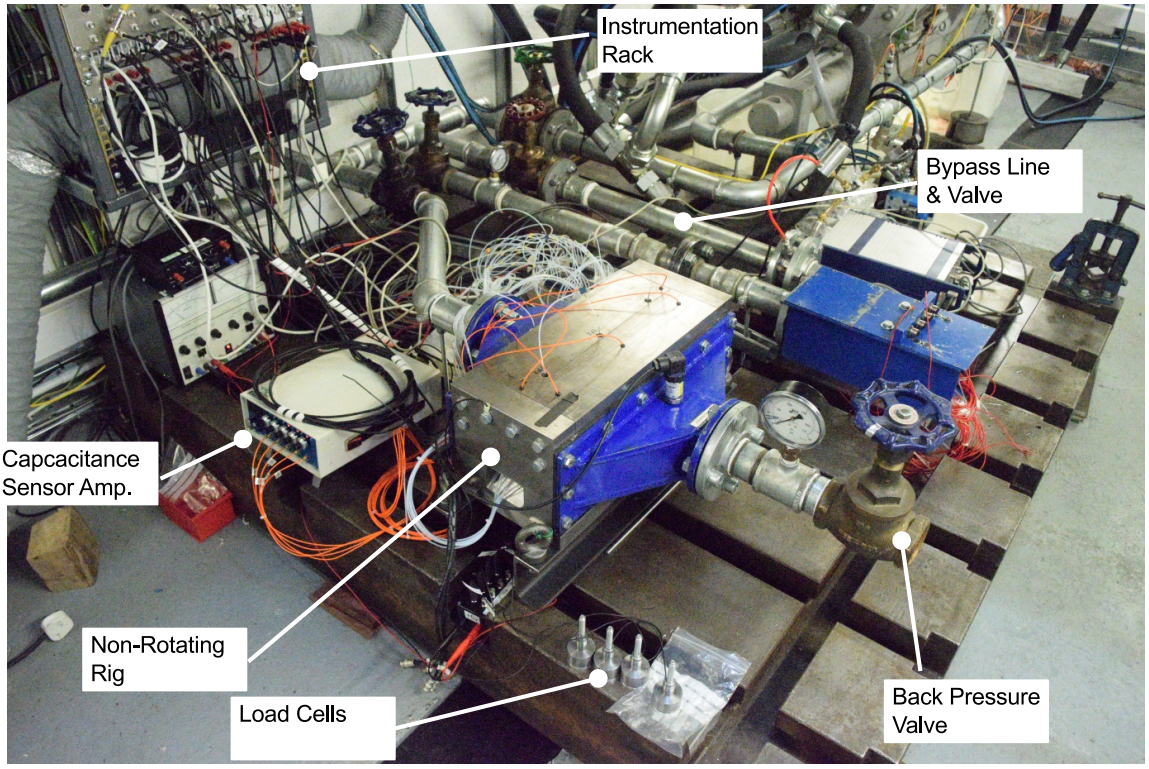

Figure 4.2: Picture of non-rotating rig within the test cell.

a rotor section with static pressure taps. The seal holder contains spacers which limit the retracted clearance of the seal segment, and are used in conjunction with the rotor position to set the initial clearance of the seal segment.

Air was supplied to the rig from the Durham University Blowdown Facility described previously, and a schematic diagram of the air supply is shown in Fig. 4.4. Maximum inlet pressure permitted to the rig was $16\,\mathrm{bar(g)}$ and was controlled by the blowdown facility main control valve. Back pressure could be controlled using a manual valve. The rig was operated with a bypass line to prevent excessive spikes in pressure when the seal segment clearance changes (i.e. when the seal segment moves from the retracted position to the operating clearance).

Mass flow rate through the seal was measured using the blowdown facility main orifice plate installed upstream of the control valve, and an orifice plate installed in the bypass line.

A total of 5 Fylde FE-925-CDT-04 capacitive sensors were used to measure the seal segment position. The sensors were arranged in two measurement planes and distributed circumferentially in order to be able to fully describe the motion of the seal

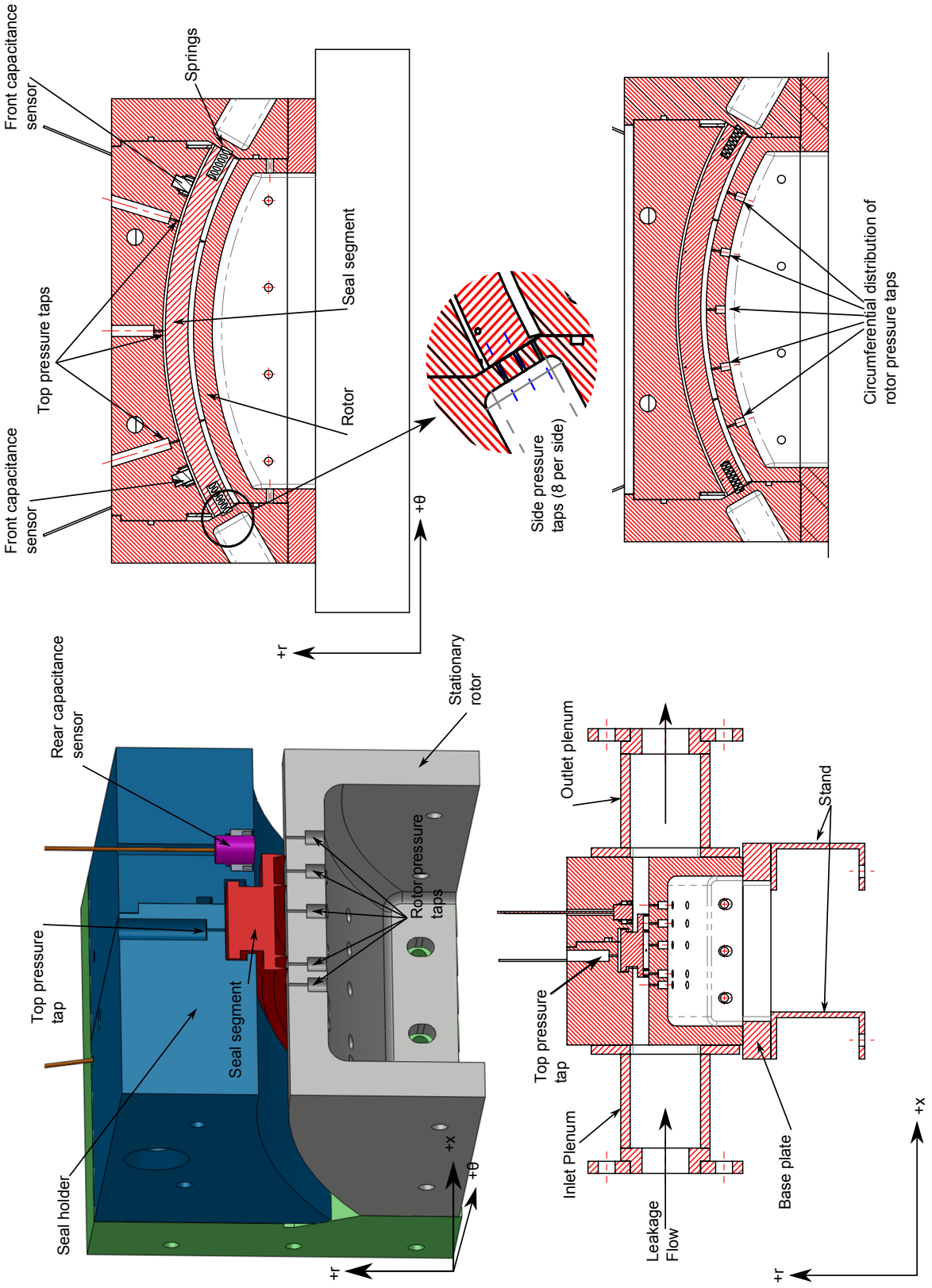

Figure 4.3: Non-rotating rig internal detail.

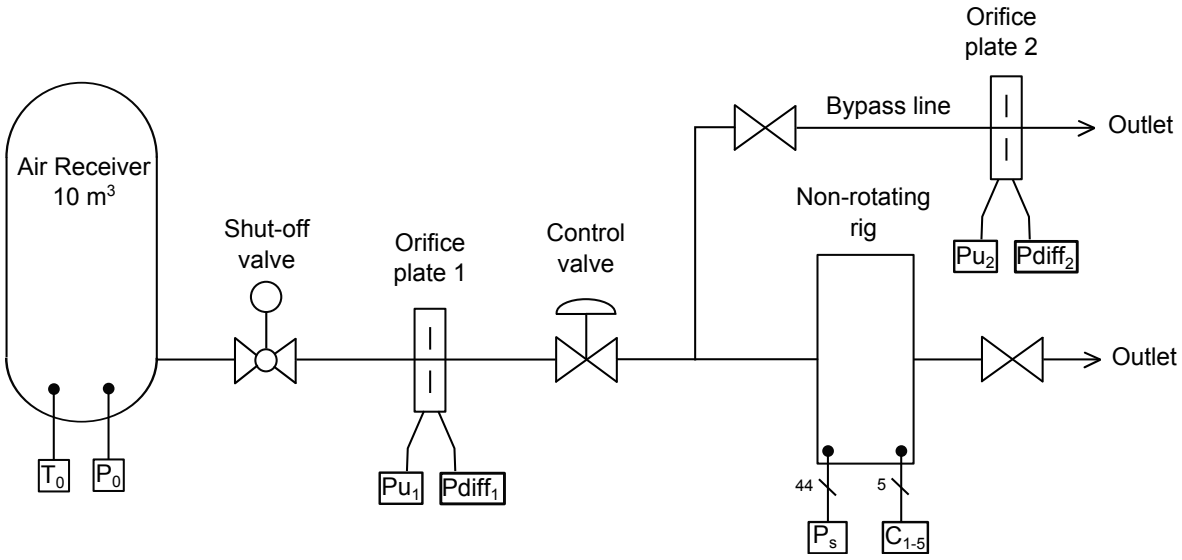

Figure 4.4: Schematic diagram of non-rotating rig pipework and instrumentation.

segment. The position of the sensors can be seen in Fig. 4.3. Circumferential distribution of the sensors captures uneven seal segment clearances, while sensors on two measurement planes captures rotation of the segment about the tangential axis.

Capacitance sensors work by measuring the change in capacitance due to changes in clearance. Capacitive sensors are only linear over a limited range of clearance due to fringe effects. A larger diameter of sensor is required to measure larger clearances. For the sensors installed in the non-rotating rig, this limit was 4 mm. A Fylde FE-420-CDT amplifier unit was used to convert capacitance to a voltage signal output. Linearity of the voltage signal was checked during calibration, which was performed installed in the non-rotating rig.

A total of 44 pressure taps were installed in the rig, the position of these is shown in Fig. 4.3. 25 pressure taps were included on the surface of the rotor to determine the pressure distribution under the seal segment. The taps were distributed circumferentially on the rotor, 5 positioned upstream the seal, 5 in each of the P1, P2 and P3 cavities, and 5 at seal outlet. A total of 16 pressure taps were installed to measure the pressure distribution on the side of the seal segment, 8 on each side. A further 3 taps measure the pressure on the top surface of the segment. The pressures are measured with two Scanivalve DSA 3217 pressure scanners. Inlet pressure was measured in the inlet plenum chamber for automatic control of rig inlet pressure, and used a single First Sensor BTE5000 series transducer. The position of the pressure taps are given in Ta-

	Axial Position / mm	Circumferential position / °						
		-20	-17	-10	0	10	17	20
Top	44.3		X		X		X	
P_{in}	-7.8	X		X	X	X		X
P_1	2.72	X		X	X	X		X
P_2	33.32	X		X	X	X		X
P_3	56.42	X		X	X	X		X
P_{out}	75.82	X		X	X	X		X

Table 4.2: Pressure tap locations

Tap Number	Axial location / mm	Radial location / mm
LS/RS 1	7.72	5.68
LS/RS 2	23.72	5.68
LS/RS 3	39.72	5.68
LS/RS 4	55.72	5.68
LS/RS 5	15.72	20.68
LS/RS 6	39.72	15.68
LS/RS 7	15.72	25.68
LS/RS 8	39.72	25.68

Table 4.3: Side pressure tap locations

bles 4.2 and 4.3. The origin for the pressure taps axial coordinates is the upstream face of the seal segment. The radial origin is the centre of the seal segment arc, i.e. point (0,0) in Fig. 3.12.

The Gen II Aerostatic Seal designs use axial springs to compensate for axial force, thereby reducing the frictional force and making the seal segment more responsive. Axial spring holders were designed which allow the level of axial force to be adjusted by screwing the spring holder in or out from the seal holder. A total of four holders are distributed around the circumference of the downstream seal holder as required by the seal design. The axial spring holders were designed not to interfere with the outlet plenum so testing could be still conducted with back pressure. Figure 4.5 shows a cross section of the rig with the axial springs installed. For Gen II testing at atmospheric back pressure, another set of axial spring holders were manufactured which each contained a single TE connectivity F22 series load cell to enable the measurement of the axial force. The load cell includes an on board amplifier which outputs a voltage signal. As with the plain axial spring holder, the load cells can be screwed in and out from the downstream seal holder to vary the level of applied axial force. Figure 4.5 shows a cross section of

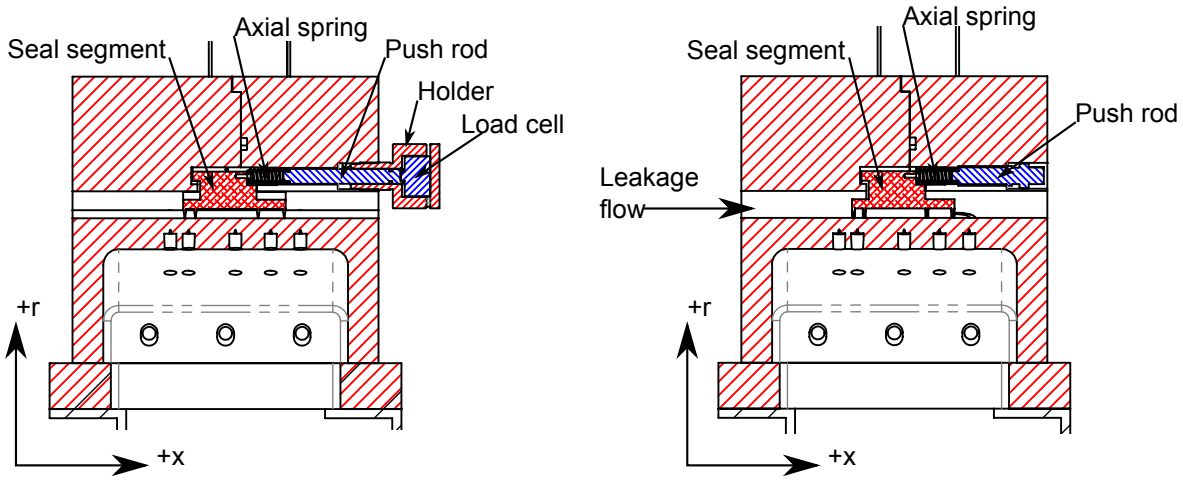

Figure 4.5: Cross section showing axial spring and load cell arrangement.

Measurement	Equipment	Range	Accuracy
Static Pressure	DSA3217 pressure scanner	0.000 to 17.240	$\pm$0.0086 bar
Seal Clearance (C1 and C2) (Upstream)	FE-925-CDT-04 capacitive sensors	0 to 4	$\pm$0.004 mm
Seal Clearance (C3 to C5) (Downstream)	FE-925-CDT-04 capacitive sensors	0 to 4	$\pm$0.01 mm
Axial force AX0-AX3	F223 Load Cell	0 to 222	$\pm$2.2 N
Tank Pressure P_0	CTE8035 Press. transmitter	0 to 35	$\pm$0.035 bar
Tank Temperature T_0	TXDIN1620 temp. transmitter and T type thermocouple	-100 to 400	$\pm$0.5 °C
Mass flow rate	Orifice Plate	0.05 to 0.25	$\pm$0.002 kg s^{-1}

Table 4.4: Non-rotating rig instrumentation and capability.

the load cell installed in the rig.

Table 4.4 summarises the installed instrumentation on the non-rotating rig, and lists the range and accuracy. The Accuracy quoted is based on full scale accuracy from manufacturer data sheets, except seal clearance which is based on the experimental range, and mass flow rate which is based on the calculated uncertainty as per BS EN ISO 5167-1/2.

In the initial stages of this project, Durnan's design was reviewed before manufacture was commenced. Also a new seal design was undertaken by MacDonald, and so design modifications were required to test the seal 'MacDonald 1'. As part of the design, Durnan specified the capacitance sensor instrumentation. The following details the changes

made from Durnan's original concept:

- Introduction of second plane of capacitance sensors for measuring 'tangential rotation' of the seal segment, described in the next chapter.
- A new base design was manufactured to enable better set up consistency of the rotor.
- Introduction of pressure taps above the seal segment and on the sides of the non-rotating rig to enable the pressure distribution on the side of the seal segment to be measured.
- Modification for testing the axial thrust compensation springs.
- Redesigned the fixing method for the capacitance sensors.

4.4 Rotating Rig: 'Durham Rotating Seals Rig'

A rotating seal test facility was constructed that was able to demonstrate the ability of the Aerostatic Seal to tolerate large transient radial rotor excursions at a wide range of rotor speeds. The design and manufacture of the test facility was undertaken and directed by Dr. Richard Williams, although a full description of the rig is given here. A picture of the rig is shown in Fig. 4.6. The rig was half scale to limit the mass flow rate through the rig and the axial force acting on the rotor. A cross section is shown in Fig. 4.7. The facility consists of a two part rotor cantilevered on a stub shaft, driven by a variable speed electric motor. The outer portion of the rotor can be mounted in either a low eccentric position (0.09 mm) or a high eccentric position (0.55 mm) to simulate transient rotor movements. The shaft between the rotor and the motor runs through the centre of the stub shaft, and by having a stationary stub shaft the cyclic stresses are eliminated on the motor shaft. This arrangement also allows easy assembly and disassembly of the Aerostatic Seal from the front of the rig by removing the front casing. The rig has a maximum rotational speed of 1500 rpm. Key rig parameters are summarised in Table 4.5.

Air to the facility was supplied from the Durham University Blowdown Facility, as shown in Fig. 4.8. The rig was operated with a bypass line, as was the non-rotating rig.

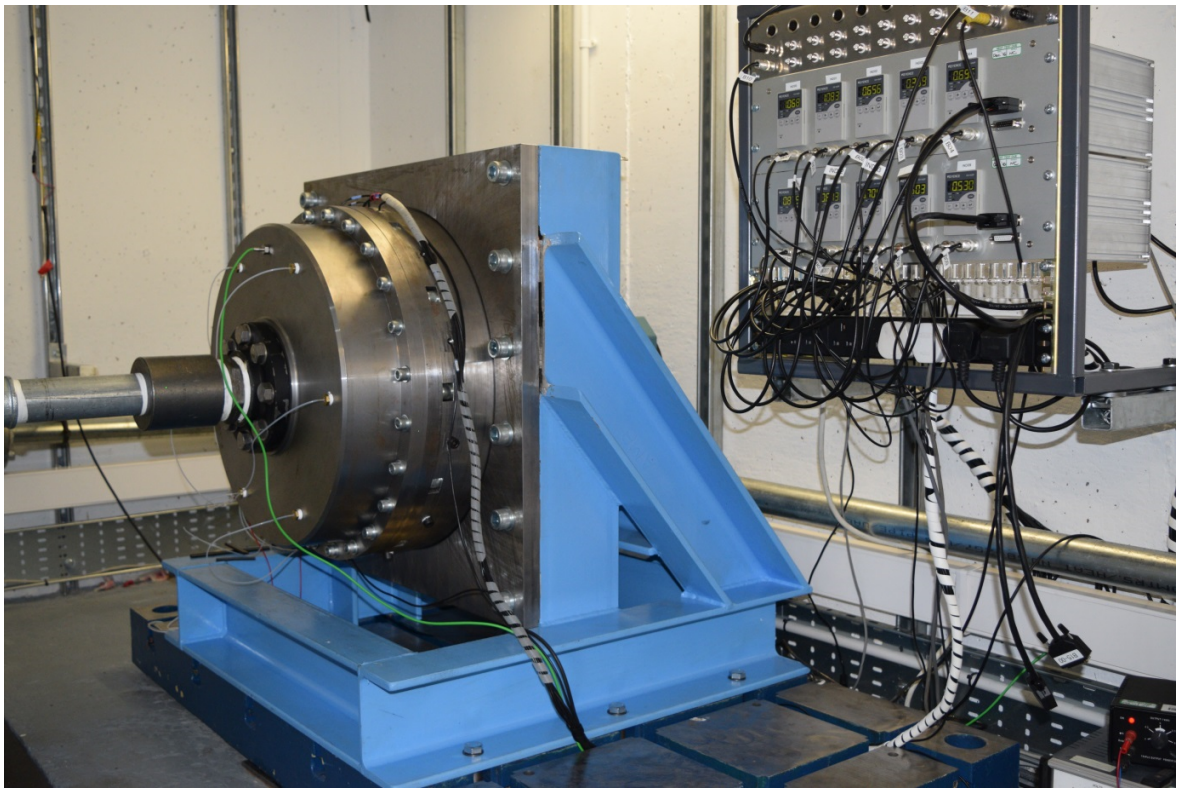

Figure 4.6: Picture of the 'Durham Rotating Seals Rig'

Parameter		Value
Rotor Diameter	D	366 mm
Max. Inlet Pressure	P_{in}	6 bar(a)
Rotational Speed	ω	26-1500 rpm
High Eccentricity Setting	e	0.55 mm
Low Eccentricity Setting	e	0.09 mm
Surface Velocity at 1500 rpm	u	28.7 m/s
Max. Mass Flow Rate	$\dot{m}$	0.75 kg/s

Table 4.5: Key parameters of 'Durham Rotating Seals Rig'.

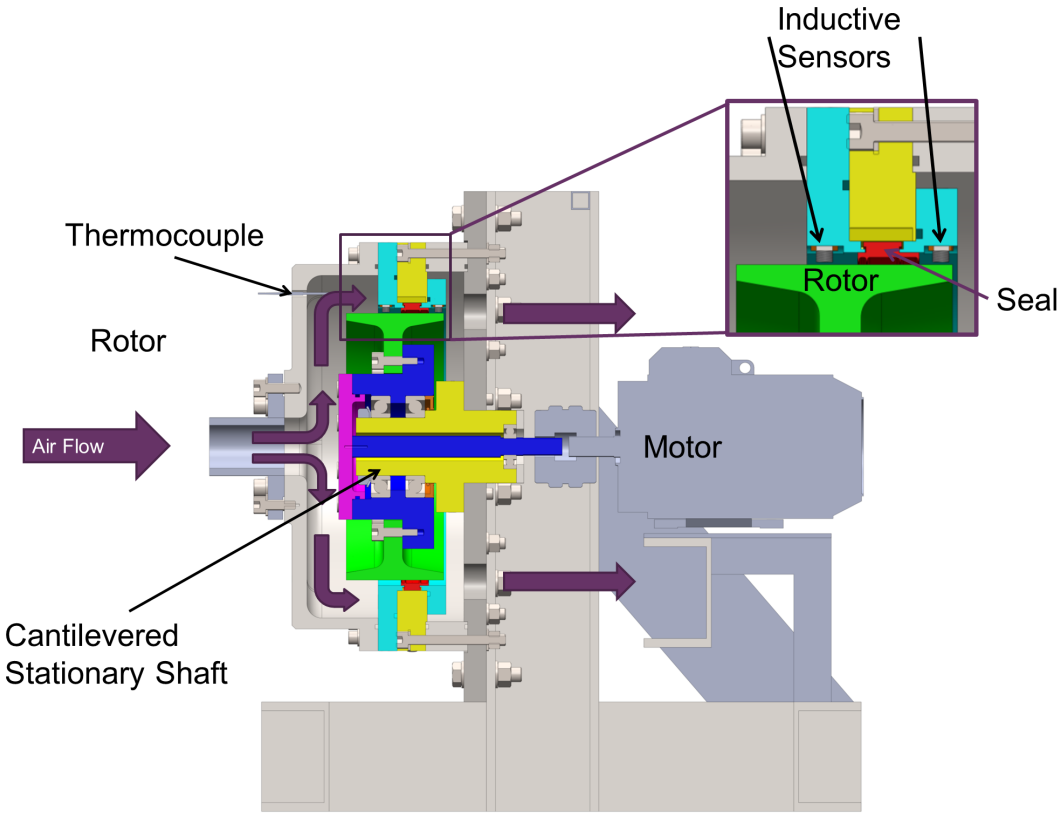

Figure 4.7: Cross section of 'Durham Rotating Seals Rig'

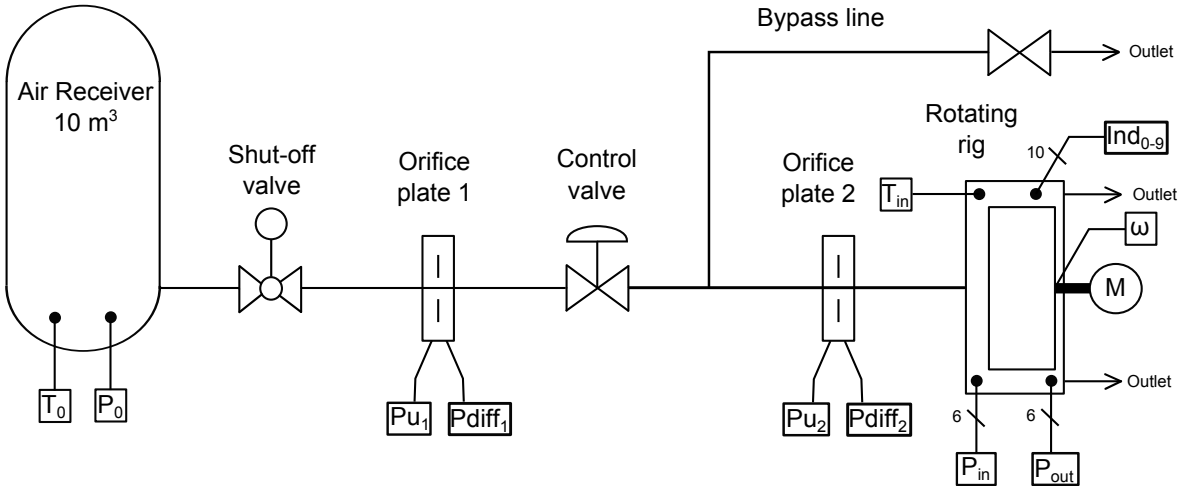

Figure 4.8: Schematic diagram of 'Durham Rotating Seals Rig' pipework and instrumentation.

The rig operated with atmospheric pressure at outlet, and up to a maximum of $1.5\,\mathrm{bar(a)}$ at inlet. The outlet pipes from the rig, shown in Fig. 4.7, were positioned directly behind each seal segment, and facilitated using a camera to monitor seal segments during tests. The inlet and outlet pressure was measured at six locations on the front casing and the mounting plate respectively, and was measured using the DSA3217 pressure scanner (see Section 4.2). The inlet temperature was measured with a K type thermocouple probe mounted on front casing.

The rotating facility used ten Keyence Ex-110 inductive displacement sensors to measure the seal segment positions: six sensors were mounted around the periphery of the seal, and were used to measure the clearance between the rotor and the seal segments. In the configuration used in the testing described in this paper, all 6 sensors were used on the top 3 seal segments, 2 per segment. Two sensors measured the rotation of the top-dead-centre segment about the tangential axis. A further two sensors were used to measure the rotor position, measuring upstream and downstream of the top dead centre seal segment.

An analogy of a clock face is used when describing positions of seal segments and sensors, shown in Fig. 4.9, the rotor rotating in a clockwise manner. For example the top-dead-centre seal segment is designated the *12 O'clock segment*. Each seal segment on the top half of the rotor (10, 12 and 2 O'clock seal segment) was monitored by two inductive sensors, as shown in Fig. 4.9, and so the radial position of the seal segment

Measurement		Range	Accuracy
Seal Clearance	c	0.00 to 2.00	0.01 mm
Inlet Pressure	P_{in}	0.00 to 17.24	$\pm$0.0086 bar
Outlet Pressure	P_{out}	0.00 to 6.89	$\pm$0.0035 bar
Tank Temperature	T_0	-100 to 400	$\pm$0.5 °C
Inlet Temperature	T_{in}	-200 to 1370	$\pm$0.5 °C
Seal Leakage	$\dot{m}$	0.05 to 0.25	0.001 kg/s
Rotor Speed	ω	60 to 1500	0.1 rpm

Table 4.6: Durham Rotating Seals Rig' instrumentation and capability.

was fully defined. Each sensor is referred to as either the 'Up Rotation Side' (URS) or 'Down Rotation Side' (DRS) sensor, with a point on the rotor surface moving from URS to DRS.

The seal leakage mass flow rate was measured using the orifice plate mounted immediately before the test rig, shown in Fig. 4.8. The rotor speed was determined using an optical sensor which would detect a reflective strip on the motor coupling. A comparator circuit amplified the signal from sensor to give a 5 V square wave, the frequency corresponding to the rotor frequency.

Table 4.6 summarises the installed instrumentation on the rotating rig, and lists the range and accuracy of each measurement. The accuracy quoted is based on full scale accuracy from manufacturer data sheets, except seal clearance which is based on the experimental range and mass flow rate which is based on the calculated uncertainty as per BS EN ISO 5167-1/2.

4.5 Conclusion

This chapter has described the two different rigs used to generate the results described in Chapters 5 to 8. The non-rotating and rotating rigs have been built specifically for testing the Aerostatic Seal concept, and the primary aim was to demonstrate the viability of the concept and validate the analytical design tool. The following four chapters present and discuss the results from these tests.

Testing with steam represents the next level of development by testing at elevated temperature and using representative materials to achieve in operation levels of friction. The test facility for this is described in Chapter 9.

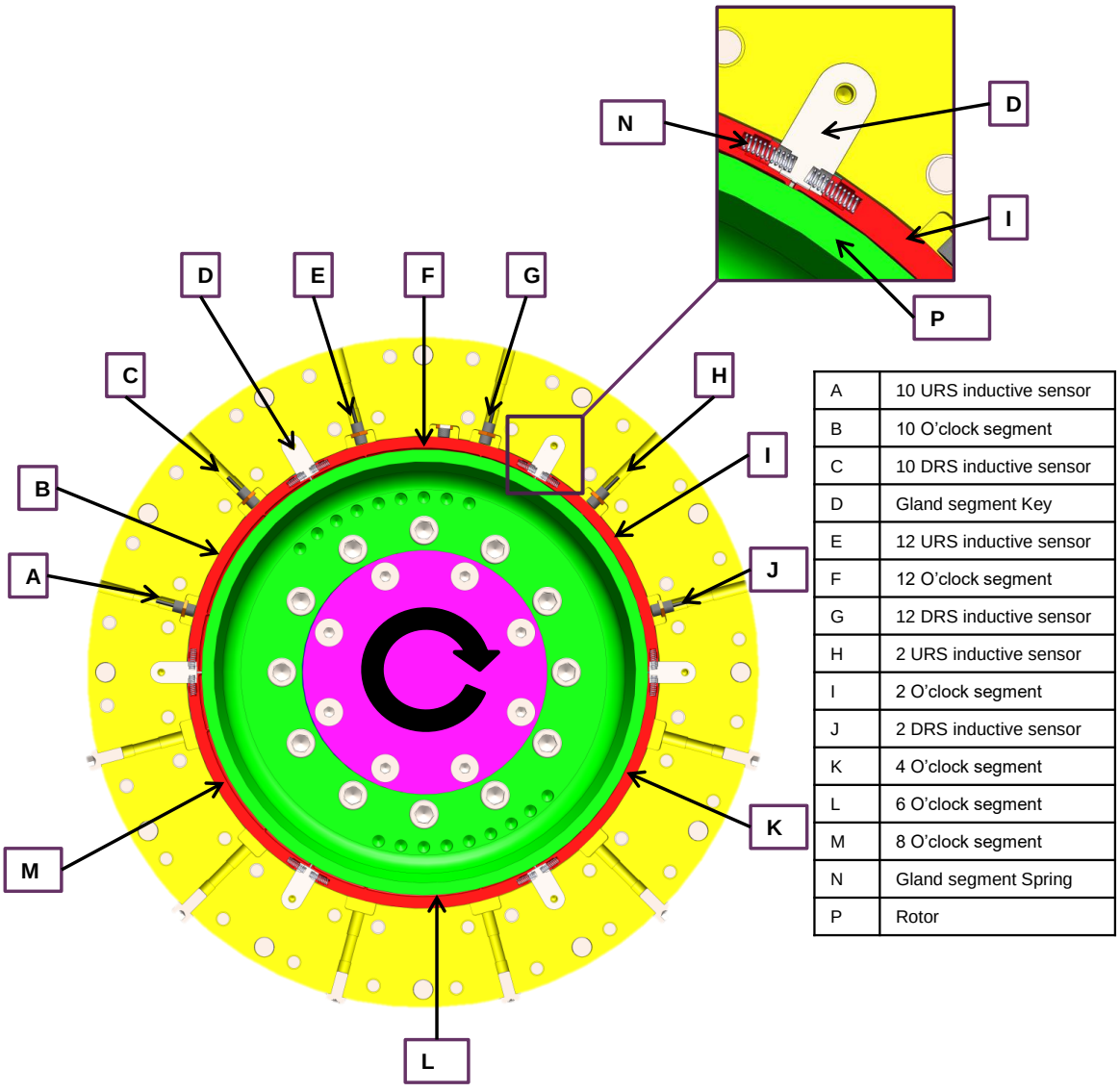

A	10 URS inductive sensor
B	10 O'clock segment
C	10 DRS inductive sensor
D	Gland segment Key
E	12 URS inductive sensor
F	12 O'clock segment
G	12 DRS inductive sensor
H	2 URS inductive sensor
I	2 O'clock segment
J	2 DRS inductive sensor
K	4 O'clock segment
L	6 O'clock segment
M	8 O'clock segment
N	Gland segment Spring
P	Rotor

Figure 4.9: Front cross section of 'Durham Rotating Seals Rig', viewed from upstream.

Chapter 5

Experimental Results: Non-Rotating Rig

5.1 Introduction

The following five chapters, (Chapters 5 to 9) present the experimental results gathered whilst testing the Aerostatic Seal concept. This chapter presents experimental results for the two GEN Ⅰ designs, 'MacDonald 1' and 'MESS01' tested in the non-rotating test rig. Chapter 6 deals with the demonstration of the Aerostatic Seal in the non-rotating test facility, and Chapter 7 the testing of the GEN Ⅱ seal design with axial thrust compensation springs. Chapter 8 provides detailed analysis and additional experimental results of 3D effects observed in Chapters 5 to 7. Chapter 9 provides results from a set of steam tests conducted at TU Braunschweig, and brings all the experimental work together in a proposed generic Aerostatic Seal design.

Figure 5.1 shows an overview of the whole experimental campaign on the Aerostatic Seal, and how it links together and which results are presented in which chapter.

It should be noted that not every result is presented in this thesis. A large number of individual tests have been carried out and to present every result would over burden the reader. The key results are presented in detail, and which capture the characteristics of the Aerostatic Seal and of its development.

5.1.1 Testing in the non-rotating test rig

The test campaigns conducted in the non-rotating test rig were primarily concerned with demonstrating the Aerostatic Seal working before the project proceeded to commission the rotating test facility. Once the seal concept had been proven the rig was used to perform seal pressure distribution tests with fixed seal segment clearance which were not possible in the rotating rig. Finally testing of the Gen Ⅱ Aerostatic Seal design, detailed in Chapter 7 was carried out in the non-rotating rig as initial testing would have been more risky to perform in the rotating rig.

The testing presented in this chapter is divided into 4 main sections: Proof of concept, tangential rotation testing, frictional effects and fixed clearance testing. The Aerostatic Seal provides two critical new functions over the retractable seal: namely that it is able to move away from the rotor surface if required, as well as moving towards the rotor during start up. The proof of concept testing, described in Section 5.2, aims to demonstrate these key functions. The testing conducted within this section gave enough confidence in the Aerostatic Seal for the rotating test facility to be commissioned.

Possible seal segment tangential rotation, where the upstream side of the seal segment is at a lower clearance than the downstream side, (see Section 3.2, or Fig. 5.2) was investigated with the 'MacDonald 1' in the non-rotating test rig, and is described in Section 5.3. Seal segment tangential rotation was also investigated as part of the test campaign in the rotating test facility using the 'ROT01' seal design and is reported in Chapter 6. Early on it was recognised that the seal segment tilting forward could lead to the seal segment jamming inside the seal holder, and would also produce a loss of seal radial force away from the rotor.

An attempt was made to observe the effect of variations in seal performance due to friction by applying grease to the contact face, described in Section 5.4. It was found that variations in the set-up of the rig between tests also had a significant effect on the performance of the seal, and this is discussed in the section.

The seal segment has also been tested in a series of fixed clearances to assess the variation in radial pressure force with clearance, and these tests are described in Section 5.5. The fixed clearance testing was complimented with 3D CFD calculations, and a comparison made to the analytical model. These tests show important flow features that have a significant effect on the Aerostatic Seal performance, and which are not well

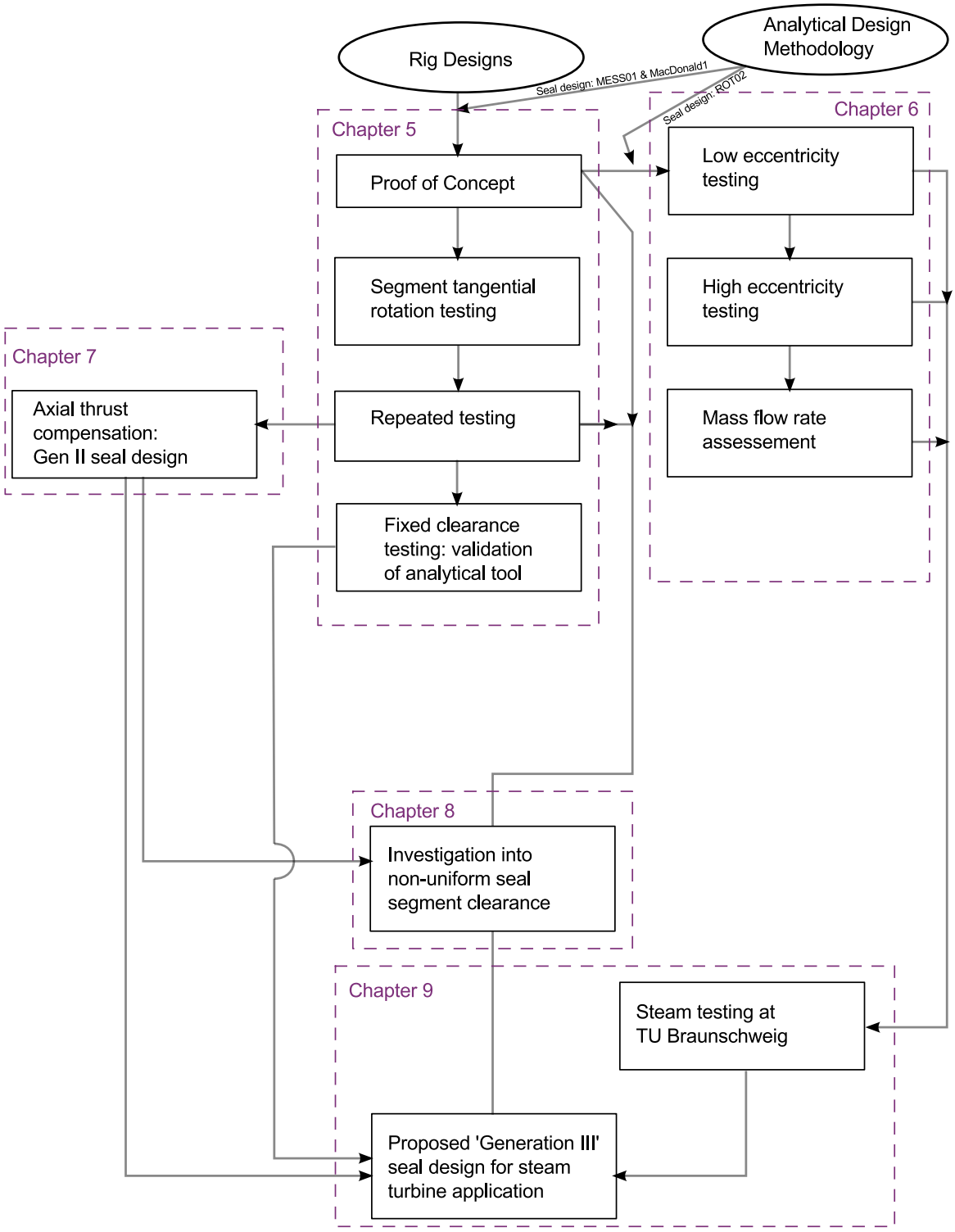

Figure 5.1: Overall ‘map’ of experimental campaign

captured by the analytical design methodology in Chapter 3.

The seal segment would often operate with a non-uniform circumferential clearance, and there were differences between tests due to test rig set up.

As experimental testing progressed various improvement were made to the non-rotating test facility. These included side pressure tappings which were introduced for the fixed clearance testing, a stiffer base to improve rotor positioning repeatability, again for the fixed clearance testing, and finally the second plane of capacitance sensors for measuring seal segment 'tangential rotation' (see Fig. 5.2). Therefore not all rig functionality was available during the tests described in this chapter.

5.1.2 Definitions

Before presenting the results within this chapter and subsequent chapters, it is worth explaining some of the terminology used. The seal segment starts off in the **retracted** position when the steam turbine is not loaded. This is a high clearance position to allow for large radial transients during start up. The pressure difference across the turbine stages is small. As the turbine is brought up to full load, the pressure drop increases across the stage and hence the seal, and the seal segment moves down to the **operating clearance**. This is a low clearance position while the turbine is operating, minimising leakage. As the load is reduced the pressure drop reduces and the seal segments move back to the retracted position.

The seal segment degrees of freedom are shown in Fig. 5.2. The seal segments are not restricted to move only in the radial direction. As a consequence the seal segment may rotate about the axial direction axis, and hence have a lower clearance on one side of the segment compared to the other. When operating in this configuration, the seal segment is said to be operating with a **non-uniform** clearance. The angle ψ is the angle of rotation about the axial axis and is a measure of the non-uniformity of the seal segment clearance. As discussed earlier, the seal segment can also rotate about the tangential axis, leading to a lower seal clearance at the upstream side of the segment compared to the downstream side of the segment. The angle ϕ is the measure of such rotation.

In the non-rotating rig and 'Durham Rotating Seals Rig', **Up Rotation Side (URS)** and **Down Rotation Side (DRS)** are used to refer to different sides of the seal segment and

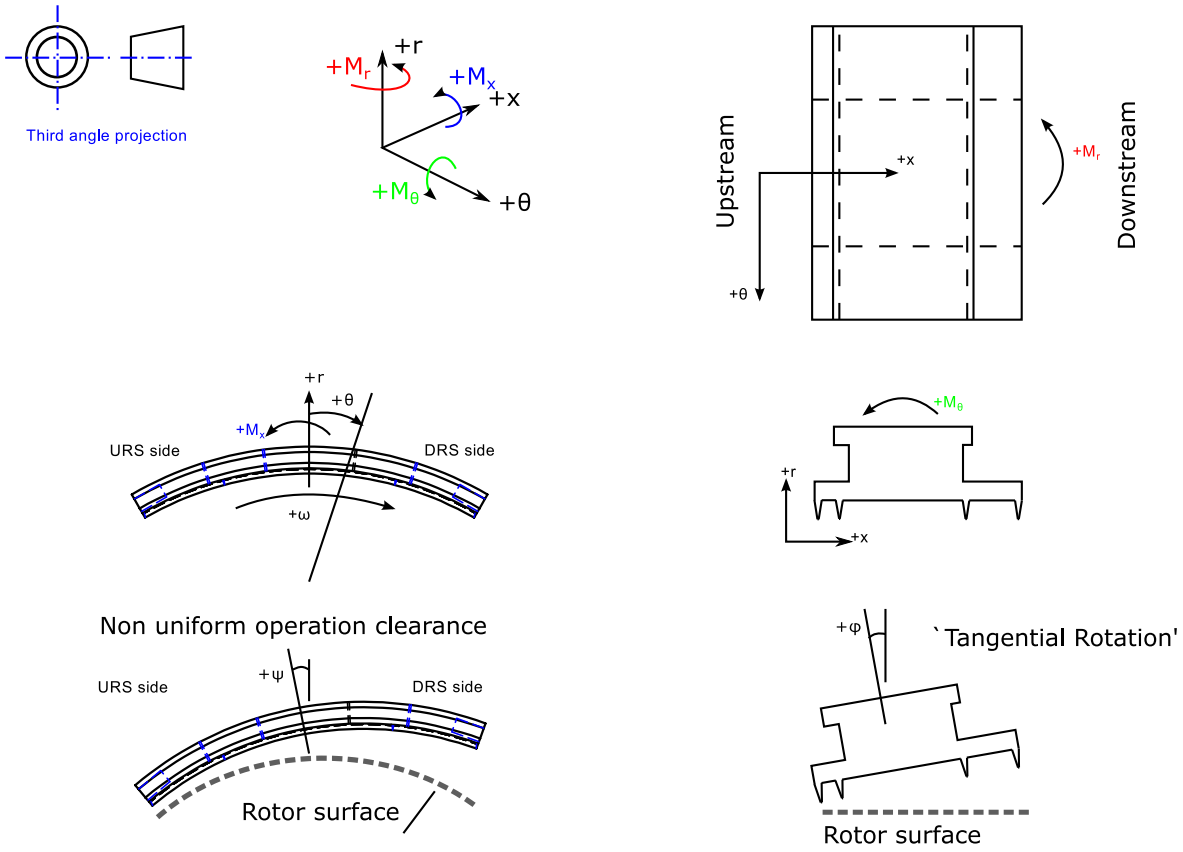

Figure 5.2: Nomenclature and definitions

the position sensors - see Section 4.4. A point on the rotor surface is moving from URS to DRS, in an analogue to a particle in the leakage flow through the seal travelling from upstream to downstream. In the rotating rig, the rotor was always moving in the same direction: when viewed from upstream looking downstream, the rotor is travelling in a clockwise direction. In the non-rotating rig, the rotor was fixed, but the same convention was used for consistency.

5.2 Proof of Concept: Non-rotating Test Facility

The Aerostatic Seal is a dynamic seal concept, and so key to proof of concept is demonstrating dynamic behaviour of the seal segment. In the non-rotating test rig, which had a non-actuated rotor, an investigation into the dynamic operation of the Aerostatic Seal was limited to observing the seal segment transitions from the retracted position to the operating position. Therefore this section aims to demonstrate the following behaviour:

1. The seal segment will move from the retracted position to a lower operating position when the pressure difference across the seal segment is increased. The operating clearance is set by a radial force equilibrium and not by the T slot shoulders, as in the retractable seal.

2. The seal segment moves away from the rotor when at a low clearance. This was achieved by removing the circumferential springs, and so the seal segment would initially be resting on the rotor when no pressure was applied. After increasing the pressure difference across the segment, the segment was observed to lift off from the rotor surface.

5.2.1 Movement towards the rotor

In order to demonstrate the ability of the seal segment to move from the retracted position to a lower operating position, a number of different tests were performed with both ‘MacDonald 1’ and ‘MESS01’ Aerostatic Seal designs.

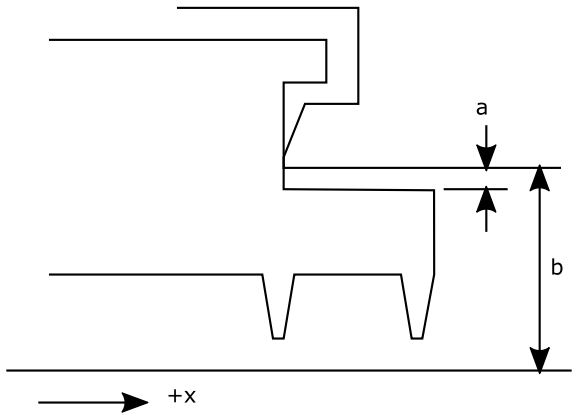

Figure 5.3: Seal segment and rotor set up position cross section.

'MacDonald 1' seal design

The 'MacDonald 1' Aerostatic Seal design was tested as part of the phase 1 test campaign, with atmospheric back pressure. The URS and DRS circumferential springs were 'Sp1 14.83' and 'Sp2 14.83' respectively. See Appendix D for details on the circumferential springs. The rotor central position, dimension b, was 17.03 mm from the seal holder, and the segment 0.96 mm from the seal holder, dimension a, see Fig. 5.3. The mean retracted clearance of the segment was 3.1 mm. The test duration was 100 s and the pressure and voltages (capacitance sensors, mass flow rate) logged at 20 Hz and 800 Hz respectively. The bypass valve was closed in this particular set of tests. The outlet flange was attached to the rig, but the back pressure valve fully opened. The control valve was manually operated.

The seal segment clearance and pressure ratio for a typical test with the 'MacDonald' seal design is shown in Fig. 5.4. The seal segment was initially in the retracted position when there was no pressure applied to the test rig as the circumferential springs lift the segment off the rotor. When the pressure difference across the seal segment had increased sufficiently that the pressure force can overcome the radial spring force, the seal segment transitioned to the operating clearance. This occurs at approximately 47 s in Fig. 5.4a and 66 s in Fig. 5.4b. Because the bypass valve was closed, the transition to the

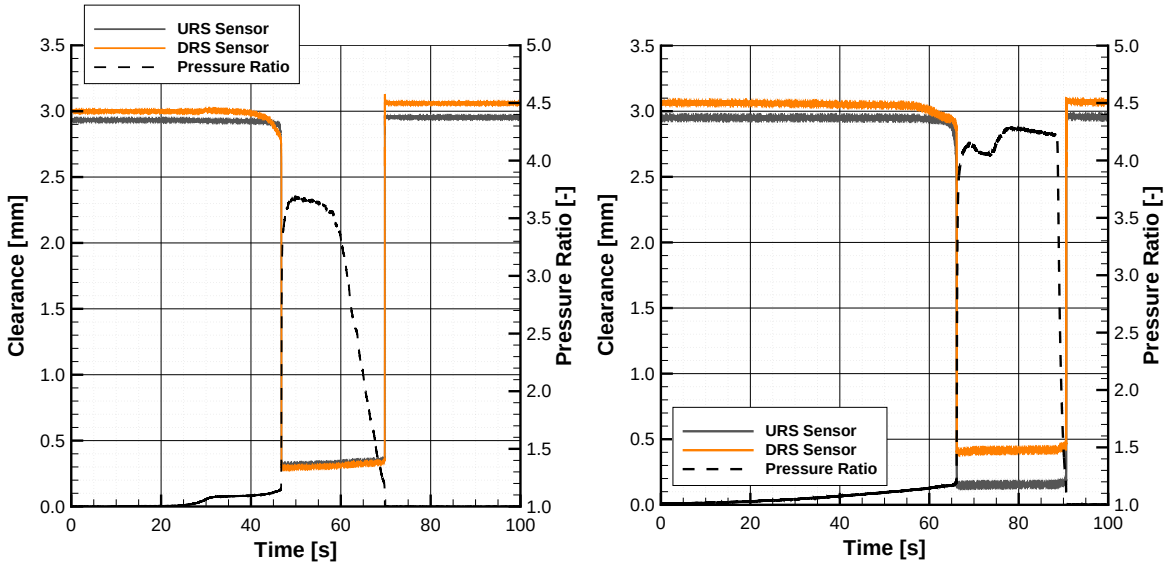

(a) Test 1 (b) Test 2

Figure 5.4: MacDonald 1 seal design: Close in and retraction

operating clearance was accompanied by a large pressure ratio (P_{in}/P_{out}) increase due to the sudden change in the seal leakage area. When the seal segment was at the operating clearance, the clearance was set by the balance of radial pressure force, friction and spring forces. This is in contrast to the retractable seal which relies on the operating clearance being set by the T slot. Once the seal segment was at the operating clearance changes in pressure ratio had minimal effect on the seal segment clearance. In test 2, shown in Fig. 5.4b, there was a difference between the clearance measured by the URS and DRS sensors, indicating that the clearance at each circumferential position in the rotor surface was not constant. This was termed **non-uniform operating clearance.**

After the seal segment had transitioned to the operating clearance, the inlet pressure was reduced and once the pressure had reduced sufficiently the seal segment transitioned back to the retracted position. This occurred at approximately 70 s in Fig. 5.4a and 90 s in Fig. 5.4b.

The two tests presented here in Fig. 5.4 show the 'MacDonald 1' Aerostatic Seal design operating experimentally, and demonstrating the Aerostatic Seal behaviour expected during start up and shut down of the turbine.

'MESS01' seal design

Similar tests as performed on the 'MacDonald 1' seal segment were also performed on the 'MESS01' seal segment design, and the results are shown in Fig. 5.5. A number of different back pressures were tested, and all the tests described were conducted without disassembling the test rig.

The testing was conducted with retracted mean clearance of $3.0\,\mathrm{mm}$ and with circumferential springs of nominal $17.6\,\mathrm{N\,mm^{-1}}$ stiffness. The spring pre load was $81\,\mathrm{N}$, and the spring ends were fixed into position with the spring holder inserts, as described in Section 3.5. The rotor central position was $15.13\,\mathrm{mm}$ from the seal holder (dimension b), and the segment $2.57\,\mathrm{mm}$ from the seal holder (dimension a), see Fig. 5.3. The test duration was $50\,\mathrm{s}$ and the pressure and voltages logged at $600\,\mathrm{Hz}$ and $1000\,\mathrm{Hz}$ respectively.

When testing with atmospheric back pressure, the bypass valve was 2 turns from shut. The inlet pressure was automatically controlled, the valve opened at $4\,\%\,\mathrm{s^{-1}}$ opening rate, held for $26\,\mathrm{s}$, and then closed at the same rate. The outlet flange was not attached to test rig.

Two tests were conducted with increased levels of back pressure. In each of these tests the inlet pressure was kept constant at $3.0\,\mathrm{bar(a)}$ and $6.0\,\mathrm{bar(a)}$, and the outlet pressure decreased to increase the pressure difference across the seal. The bypass valve was 1.5 turns from shut with $3.0\,\mathrm{bar(a)}$ inlet pressure and 0.75 turns from shut with $6.0\,\mathrm{bar(a)}$ inlet pressure. The inlet pressure was automatically controlled with a PD controller to hold inlet pressure at the desired value when testing with high back pressure. The back pressure valve was manually operated and started fully closed.

The testing of 'MESS01' with atmospheric back pressure, shown in Fig. 5.5a, was similar to the performance found with 'MacDonald 1'. The segment starts in the retracted position, and as the pressure difference across the seal segment was increased, the segment transitions to a low operating clearance. As the pressure was decreased the seal segment then transitioned back to retracted position.

Testing conducted with higher back pressure shown in Figs. 5.5b and 5.5c, and shows that same response found with atmospheric back pressure with both seal designs. Testing with increased back pressure did show that the operating clearance of the seal segment was reduced compared to the atmospheric back pressure tests. There was little effect on the mean clearance comparing the $3.0\,\mathrm{bar(a)}$ and $6.0\,\mathrm{bar(a)}$ inlet pressure tests.

It was also found that the pressure difference across the seal segment when the segment transitions down to the lower operating clearance was approximately the same, at 0.1 bar, with and without back pressure.

Another key observation in the seal performance was the non-uniform clearance around the circumference of the seal segment, shown by the difference between the URS and DRS sensors. This was also found in the 'MacDonald 1' tests - see Fig. 5.4, but was more extreme in the tests presented in Fig. 5.5.

5.2.2 Movement away from the rotor

One of the key differences between the Aerostatic Seal and the retractable seal is the ability for the seal to move away from the rotor; the retractable seal will move towards the rotor during start up and once it is at the operating clearance it will not move away until the turbine is taken off load.

To test the ability of the Aerostatic Seal to move away from the rotor, the seal was assembled in the non-rotating test rig without springs. Initially the seal segment rests on the rotor before pressure was applied; when pressure ratio increased the movement of the segment was tracked. The test rig was operated with no back pressure.

Figure 5.6a shows the results from such a test, which shows the seal moving to a higher clearance when the pressure ratio was increased. The clearance measured by the URS and DRS capacitance sensors and seal pressure difference is shown in Fig. 5.6a, with the clearance increasing at around 45 s. Further increase in inlet pressure causes the URS side of the segment to continue to increase clearance.

The mean seal segment clearance is plotted against pressure difference, shown in Fig. 5.6b, and shows that the seal segment initially 'lifts off' from the rotor surface around 0.25 bar. With a further increase in pressure difference the seal segment moved further away from the rotor, occurring at 1.0 bar. This increase in operating clearance is due to the URS side of the segment moving, the DRS side of the segment remains in roughly the same position as shown in Fig. 5.6a. As the seal was operated without circumferential springs, then the operating clearance non-uniformity must be due to circumferential pressure non-uniformity or friction non-uniformity. As a sanity check on the results, deflection of the rotor or the sensors positioned above the seal segment would result in the segment appearing to move downwards, away from the sensors. Therefore rig

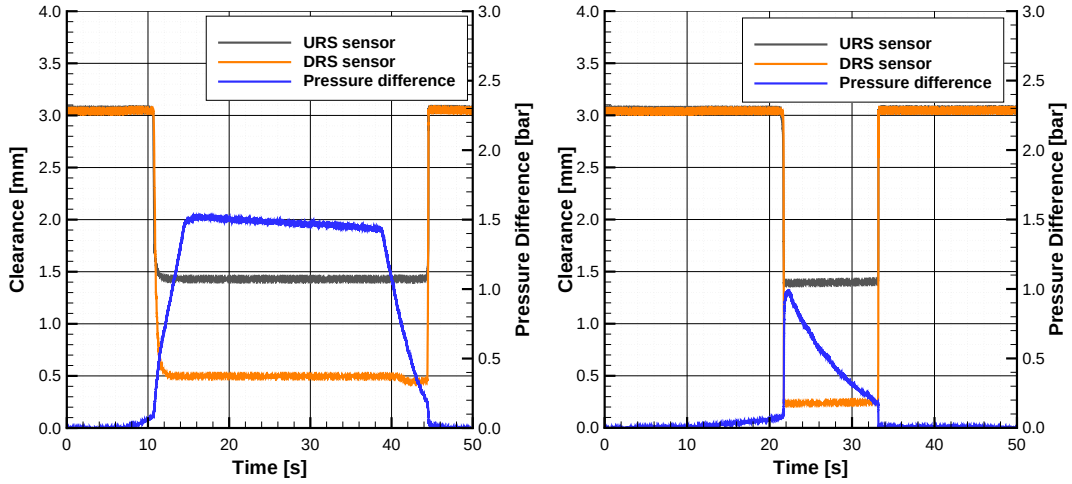

(a) Atmospheric back pressure

(b) 3.0 bar (a) inlet pressure

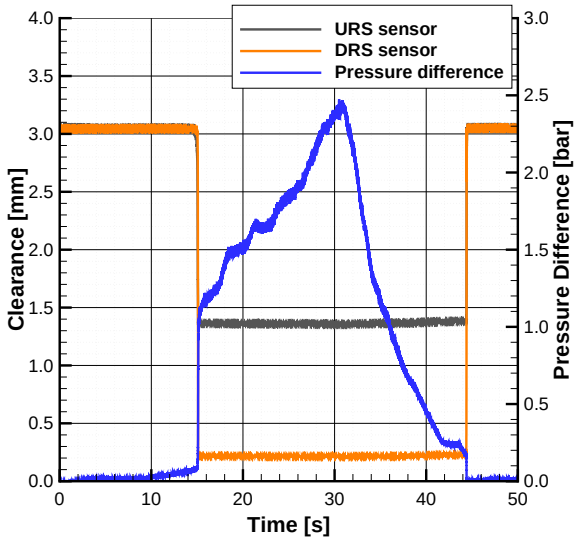

(c) 6.0 bar (a) inlet pressure

Figure 5.5: Seal response to changing inlet pressure - with and without back pressure

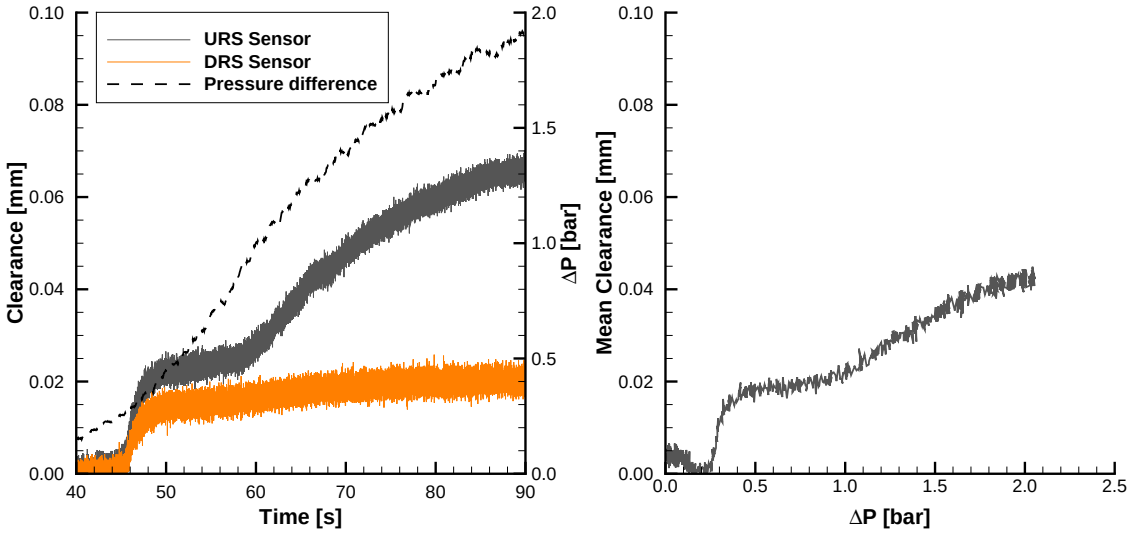

(a) Clearance vs time.

(b) Mean clearance vs with pressure difference.

Figure 5.6: Seal segment response without springs

deformations cannot be the cause of the measured segment movement as the seal segment has moved towards the sensors.

5.2.3 Discussion and Conclusion

The results presented here were enough to proceed with building and commissioning the 'Durham Rotating Seals Rig'. The Aerostatic Seal demonstrated the ability to move towards the rotor from an initially retracted position. Also, and more importantly, the Aerostatic Seal demonstrated the ability to move away from the rotor without any circumferential springs, and so the pressure forces were great enough to lift the segment away from the rotor, overcoming static friction and the weight of the seal segment. This conclusively demonstrates that the Aerostatic Seal functions differently from the retractable seal. Two seal designs have been tested, although no circumferential spring testing was only carried out for the 'MESS01' seal design, both seal designs were shown to move towards the rotor.

Operating with increased back pressure showed similar results compared to the atmospheric back pressure testing, although the mean operating clearance was slightly reduced. Critically it was demonstrated (in Fig. 5.5) that the pressure difference at which

the segment would transition to the operating clearance was roughly the same between the high and low back pressure tests, and which showed that the position of the seal segment was driven by the pressure difference.

A difference was observed between the clearance measured by the URS and DRS sensors, indicating that the clearance around the circumference of the seal segment was not uniform. This was noticed in both sets of seal designs tested and also with and without springs. The whole of Chapter 8 has been devoted to understanding the causes of non-uniform operating clearance.

5.3 Seal segment tangential rotation

One key degree of freedom so far not discussed is seal segment rotation about the tangential axis, referred to as 'seal segment tangential rotation', ϕ. See Fig. 5.2 for a reminder of the segment degrees of freedom.

Two seal tangential rotation tests were conducted on the 'MacDonald 1' Aerostatic Seal design. Measurements were not possible with the 'MESS01' seal design as the seal segment was shorter, and so the downstream capacitance sensor measurements were not reliable. The test set up was identical to the tests conducted with the 'MacDonald 1' seal design reported in Section 5.2.

Figure 5.7 shows the upstream and downstream capacitance sensor planes used for detecting tangential rotation of the seal segment. Note that the sensors are at different circumferential positions (by 2.5°) and so the circumferential clearance calculation tool was used to convert the measurements to the same circumferential position, details given in Appendix F. The tool calculates the clearance at any circumferential location from the two experimental clearance measurements at two circumferential locations. The definition of seal tangential rotation, ϕ, is shown in Fig. 5.7, positive defined as the upstream clearance being tighter than the downstream clearance.

The seal tangential rotation angle was then calculated from the difference in clearance between the upstream capacitance sensor plane and the downstream sensor plane, given in Eq. (5.1), and where c_{down} is the clearance measured by the downstream capacitance sensors and c_{up} the clearance measured by the upstream capacitance sensors.

The maximum rotation that can occur before the top surface of the seal segment touches the front face of the holder is $\phi \pm 0.8^{\circ}$.

$$\phi = \arctan\left(\frac{c_{\text{down}} - c_{\text{up}}}{51.28}\right) \tag{5.1}$$

The clearance data from a typical test is shown in Fig. 5.8. Figure 5.8a shows the measured clearance for all capacitance sensors during the test. The inlet pressure was gradually increased until the seal segment moved to the operating clearance at approximately 47 s, and then decreased until the seal segment retracts, occurring at approximately 70 s. At 30 s there was a slight change in clearance measured by the downstream sensors whilst the upstream sensors remained constant.

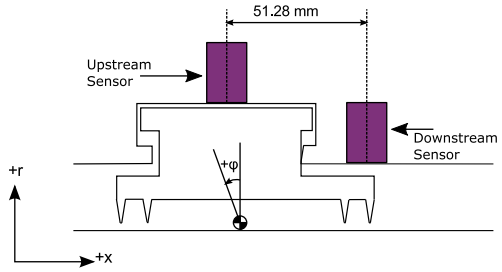

Figure 5.7: Cross section of seal segment showing upstream and downstream capacitance sensor planes

Initially the segment was tilted forwards in the seal holder, i.e. positive ϕ. Figure 5.8c shows the segment tangential rotation for the over the duration of the test. Once the segment had reached the operating position the measured angle was zero.

At 47 s the seal segment moves from the retracted position to the operating position. Looking at the tangential rotation angle ϕ in Fig. 5.8c, there was an initial large rotation of the seal segment, shown by the spike in the measured angle, before the segment then returns to a level of rotation close to the retracted position. The angle measured by both sets of sensors on the URS and DRS side of the segment show the same change in angle.

Figures 5.8b and 5.8d show all capacitance sensors and the segment tangential angle respectively, looking at the half second period of time when the seal segment was travelling from the retracted clearance to the operating clearance. The large change in the segment rotation angle occurs as the seal segment was moving, and so was not the cause of the seal segment motion.

The uncertainties of the measured clearance are given in Table 4.4, described in Section 4.3. Taking the difference between two clearances increases the uncertainty in the measurement: the uncertainty was 0.05° in the measured tangential rotation angle, which was similar to the level of measured rotation.

Overall the level of seal segment tangential rotation measured was small and the seal operated as expected with the low level of tangential rotation observed in the tests presented in this section. Similar levels of segment rotation were observed in the rotating test rig, see Section 6.3.3. Larger levels of tangential rotation occurred during the Gen Ⅱ testing in Chapter 7, and was shown to have a significant effect on the seal performance.

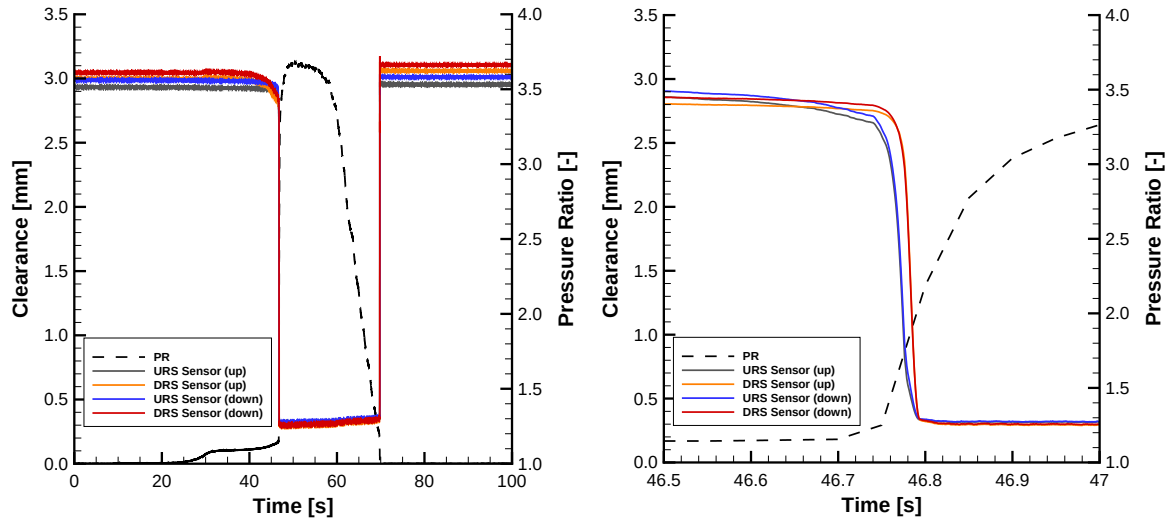

(a) Clearances

(b) Close in detail: clearances

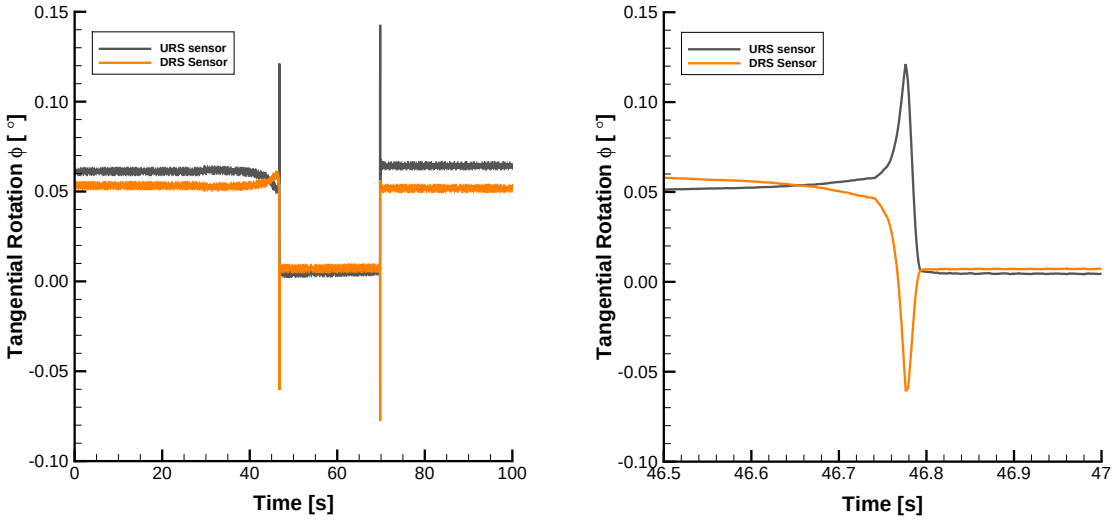

(c) Segment angle

(d) Close in detail: segment angle

Figure 5.8: Measured tangential rotation of 'MacDonald 1' seal design.

5.4 Frictional effects

The testing described in this section attempted to understand the effect friction had on the performance of the Aerostatic Seal. As demonstrated by the analytical model, the choice of friction coefficient used in the model had a large effect on the performance of the Aerostatic Seal.

To investigate this, a series of tests were carried out where the inlet pressure was increased and decreased a number of times, causing the seal segment to repeatedly move from the retracted position to the operating position within each test. Between each test the rig was disassembled and the contact face treated with grease to lower the coefficient of friction, or cleaned with isopropanol which was intended to increase the coefficient of friction. Also the circumferential springs were swapped between some of the tests to investigate the effect on the seal segment response, i.e. which side of the segment would be at the lowest clearance.

As the segment moves multiple times within each test configuration, the operating clearance could be measured multiple times to obtain an average value for each test configuration, and also to assess the variation within a test. The apparent coefficient of static friction was estimated from the measured pressure forces and spring forces acting on the seal segment just before the segment moves to quantify the effect of the different contact face surface treatment had on the level of friction.

5.4.1 Test procedure and Experimental Results

The testing described in this section was carried out with manual inlet pressure control and atmospheric back pressure. The pressure logging frequency was 20 Hz and the voltages (capacitance sensors, mass flow rate) was logged at 1000 Hz. The bypass valve was set to 2 turns from shut.

First, two 'non-greased' tests were carried out, non-greased A and non-greased B. Between these tests the rig was not reassembled, although the bypass valve was increased to 3 turns from shut in non-greased B. Opening the bypass reduces the rate of increase of inlet pressure to the seal due to more flow going through the bypass line. This had a minimal effect on the clearance of the seal, and is demonstrated later in this section.

Next two greased test were conducted, 'greased A' and 'greased B'. The greased case

was produced by applying a layer of grease (Shell Alvania grease RA) over the whole of the contact face of the seal segment, approximately 2 mm thick. Between test A and B, the circumferential springs were swapped between sides of the seal segment. This was to check if the circumferential springs would effect which side of the seal segment would go to the lowest clearance (i.e. the URS side of the segment or the DRS side of the segment). It was found to have no effect. The layer of grease was not reapplied before the 'Greased B' test.

After testing with grease applied on the contact face between the segment and the segment holder, the grease was cleaned off using industrial grade isopropanol. As the isopropanol would have cleaned off any contaminants present in the non-greased testing configuration, this was treated as a separate test to the 'non-greased' tests. (It was not normal procedure to clean the contact face between tests, and therefore small amounts grease on the seal segment and seal holder were present due to handing the parts during rig assembly.)

Finally the test rig was disassembled and reassembled with the circumferential springs swapped back. This was referred to as test 'non-greased C'. The seal segment initial position was the same as the 'greased' and 'cleaned' tests carried out previously.

Figure 5.9 shows a typical test in this manner and shows the seal segment moving from the retracted clearance to the operating clearance multiple times during a single test of 100 s duration. The particular test is non greased test B. The multiple increase and decrease of inlet pressure is evident in the pressure ratio, and each cycle is labelled on the figure. The operating clearance during cycle 1 is also marked on the figure, and is between the two dotted lines. It was observed that the DRS side of the segment always went to a significantly lower clearance than the URS side of the segment during the Non Greased A and B tests. This is the same effect found on earlier tests described in this chapter. It was also the DRS side of the segment that went to the lowest clearance in greased test A. After the rig was reassembled the side of the segment at the lowest clearance might change. It was only observed once when the low clearance side of the segment switched - this is described in Chapter 8.

To compare all of the Non Greased, Greased and Cleaned tests, the mean operating clearance for each cycle is shown in Fig. 5.10. The points indicate the segment operating clearance for each cycle, and the bars indicate the difference between the clearance

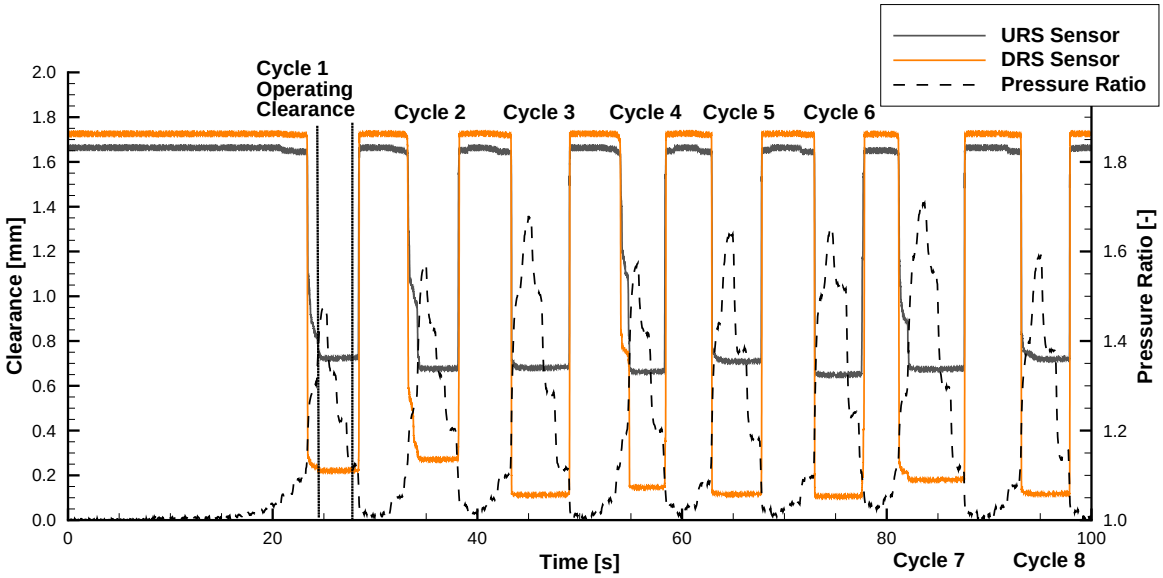

Figure 5.9: Seal segment response during non greased test B.

measured at the URS and DRS sensor positions for each cycle. The solid line indicates the mean of all the cycles. For clarity the configurations have been split up into greased, shown in Fig. 5.10a and greased and cleaned, shown in Fig. 5.10b.

The non-greased tests, shown in Fig. 5.10a, typically show the biggest variation in the operating clearance, and also have the greatest difference between URS and DRS sides of the segment. The operating clearances of the greased and cleaned test configurations, Fig. 5.10b, show less variation within each test. The level of circumferential clearance non-uniformity is much less for the greased and cleaned tests in general, although the greased tests show the occasional test where there was a particularly large difference between the URS and DRS side of the segment. Examples are cycles no. 3 and 7 for greased A configuration, and cycles no. 1,4 and 6 for the greased B configuration.

It is also apparent in Fig. 5.10 that there was significant variation between the mean clearance of the different contact face treatment (i.e. Non-Greased, Greased and Cleaned), and even between tests with nominally the same contact face treatment and set up. For example there is a difference of approximately $0.8\,\mathrm{mm}$ between the Greased A and B tests shown in Fig. 5.10b. The reasons for these differences are discussed in the rest of this section.

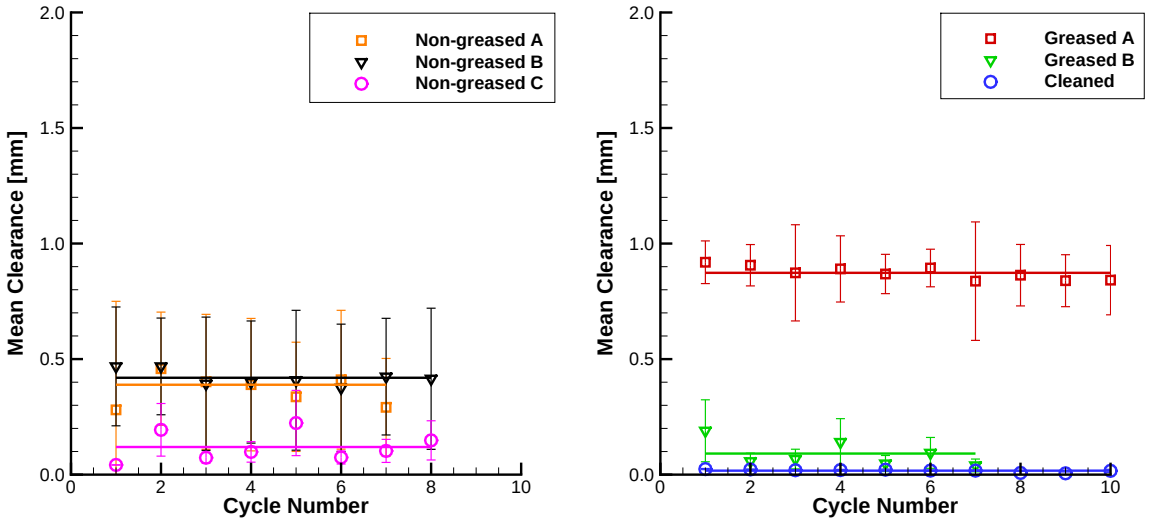

(a) Non greased repeated testing (b) Greased and cleaned repeated testing

Figure 5.10: Mean clearance for each individual test point

5.4.2 Effect of Friction on Seal Clearance

The first step to estimating the coefficient of friction acting between the seal segment and the seal holder was to determine the axial and radial forces. The axial and radial pressure forces were calculated by summing the static pressure measured on the surfaces of the seal segment. The pocket pressures were assumed to act over the same area assumed in the analytical model. It is shown with 3D CFD described in Section 5.5.5 that this assumption was valid. A correction was applied on the side pressure forces, which could not be measured as the side pressure taps were not installed when these tests were undertaken. The correction factor was determined experimentally, and which was based on side pressure measurements described in Section 5.5.4. The radial force applied on the segment due to the circumferential springs was added to the radial pressure force, and was calculated from the spring dimensions and the measured clearance of the seal segment. The weight of the seal segment was also accounted for. Immediately before the seal segment moves it was assumed that the radial and the frictional force was equal, and hence allowing calculation of the friction coefficient from the axial force. The coefficient of friction will include any effects due to mixed lubrication due to flow past the contact face, see Section 3.3.2. The point in time at which the seal segment

Config.	Retracted Clearance mm	Operating clearance mm	μ -
Non greased A	1.675	0.389	0.176
Non greased B	1.675	0.419	0.168
		Rig reassembled	
Greased A	1.274	0.873	0.148
		Rig reassembled	
Greased B	1.121	0.091	0.168
		Rig reassembled	
Cleaned	1.062	0.017	0.200
		Rig reassembled	
Non greased C	0.973	0.119	0.179

Table 5.1: Repeated test configurations and parameters.

was about to move was determined manually.

Table 5.1 summarises the mean segment retracted and operating clearance for all the greased, non-greased and cleaned tests and the calculated apparent coefficient of friction in the order the tests were conducted. The table indicates when the test rig was reassembled between tests. The values quoted are the arithmetic mean of the repeated 'close ins' and 'retractions' performed in each test. The coefficient of friction was calculated during 'close in'. The coefficient of friction could also be determined during retraction; however these values were much more variable and in some cases negative, and so were discarded. The pressure forces were higher during close in, and so the experimental uncertainty of the pressure force measurement was a lower percentage of the measured value.

The values of friction calculated showed greatest level of friction in the cleaned test and least in the greased tests. Critically there was no correlation in the calculated friction and the operating clearance of the seal segment, and there was also significant variation in the mean clearance at similar calculated coefficients of friction. Therefore another factor, other than friction, was responsible for significant variation in operating clearance.

5.4.3 Effect of Rig Setup on Seal Clearance

Comparing the mean operating clearance and apparent coefficient of friction between different 'non-greased' configurations in Table 5.1 shows a large variation in mean clearance (0.119 to 0.419 mm), but with only a small variation in coefficient of friction ($\mu = 0.168$

to $\mu = 0.179$). The same was also true for the Greased tests which varied from 0.091 to $0.873\,\text{mm}$ with only a variation in friction coefficient from $\mu = 0.168$ to $\mu = 0.148$. As the large variation in mean operating clearance occurred after the test rig was reassembled, then the variation was attributed to this rather than the small change in coefficient of friction. The factor causing the variation was found to be the relative angle of the rotor part of the test rig to the seal segment.

To demonstrate the effect of rotor angle on the performance of the seal, the clearance and pressure coefficient were plotted for a single 'close in', and are shown in Fig. 5.11 for Greased A and B tests. Figures 5.11a and 5.11b show the clearance for the Greased A and Greased B test respectively, and Figs. 5.11c and 5.11d the pressure coefficient for the Greased A and Greased B test respectively. The pressure coefficient has been used to non-dimensionalise the pressure in each of the seal pockets and on the top surface of the segment, and is defined by Eq. (3.1). Cp_1, Cp_2 and Cp_3 refer to the pressure coefficient in the first, second and third seal pocket (see Fig. 3.8), and Cp_t to the pressure coefficient on the top surface of the seal segment.

In the retracted position there was a difference in the measured pressure coefficient, with the Cp_1, Cp_2 and Cp_3 coefficients higher in greased A than greased B when the segment was retracted. Note that at high clearances the pressure coefficient in the upstream axial pocket of the was lower than the central pocket: this is discussed in Section 5.5. The segment was in a higher retracted clearance in greased A, and so the pressure coefficients would be expected to be lower in this configuration. When the seal segment has transitioned to the operating clearance the pressure coefficients have all increased, as would be expected. However it is clear that Cp_2 remains higher in greased A configuration, even though the segment was at a much higher clearance. It was the lower pressure below the seal segment in Test B that was the cause of the smaller mean clearance - lower pressure below the segment means lower radial force away from the rotor. The pressure coefficient remains higher in Greased Test A as the axial clearance was larger upstream than downstream, and therefore greater pressure drop occurs at the downstream restrictions.

After these tests, the base of the non-rotating test rig was modified to the version described in Chapter 4. The previous version which was used in these tests and the tests described in Sections 5.2 and 5.3 used jacking bolts to set the position of the rotor,

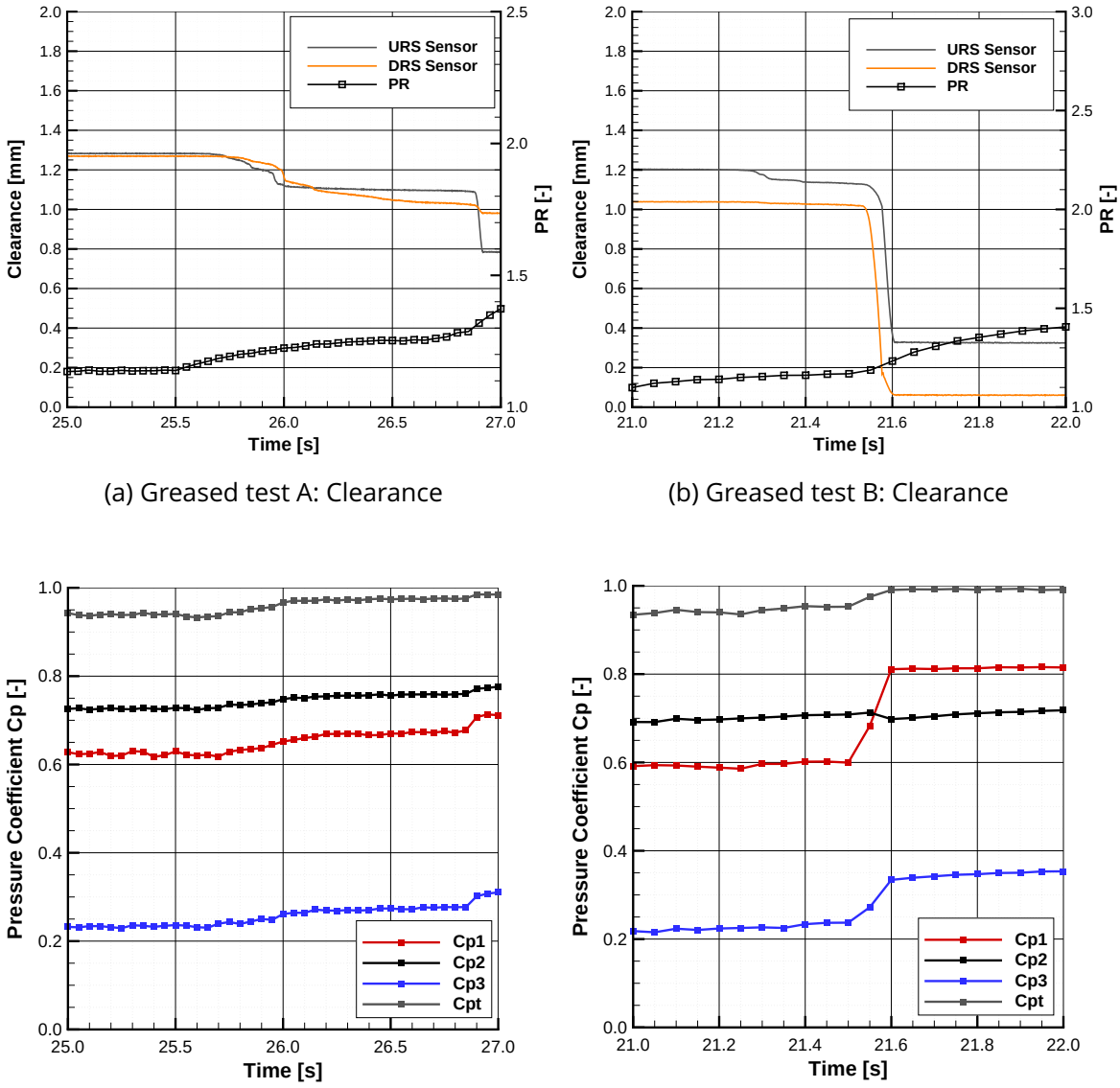

(a) Greased test A: Clearance

(b) Greased test B: Clearance

(c) Greased test A: Pressure coefficient

(d) Greased test B: Pressure coefficient

Figure 5.11: Comparing the greased test response

and repeatable positioning of the rotor between tests was difficult to achieve.

5.4.4 Conclusion of Frictional Measurements

The experimental campaign described in this section has found three key results:

1. There was some variation between the different contact face treatments, i.e. greased, non-greased and cleaned, and this was apparent in the calculated coefficient of friction. The variation was lower than expected, and may be due to the difficulty to measure coefficient of friction, which was inferred from the calculated pressure forces, and also the effects due to mixed lubrication effects due to the secondary leakage path through the contact face.

2. It was found that the mean clearance of the segment within each test was reasonable repeatable, although the clearance measured on each side of the segment varied significantly within each test. This is important for the Aerostatic Seal as it is desirable that the leakage is consistent throughout the operation of the turbine, and does not vary significantly after the turbine has been shut down and restarted.

3. There was a significant variation of mean operating clearance between tests when the test rig was reassembled. This was due to the set-up of the rotor which was difficult to assemble with the same tangential angle. Whilst this was unintended, it does show that the initial angle of the seal segment and rotor was extremely important for successful operation of the seal, and to prevent the seal operating at an excessively high clearance, increasing leakage, or at an excessively low clearance, introducing rubs between the seal and the rotor.

5.5 Fixed clearance testing

The pressure distribution underneath the Aerostatic Seal segment is vital to its function. Therefore a number of tests were carried out to measure the pressure distribution at fixed clearances. The seal segment was fixed in place by the use of shims and the pressure distribution and leakage mass flow rate measured.

The aim of these tests was first of all to demonstrate an increase of pressure below the seal segment and to provide pressure and mass flow rate data to validate the analytical prediction. 3D Reynolds Averaged Navier-Stokes (RANS) calculations were also conducted to provide further comparison and insight into the flow through the Aerostatic Seal.

5.5.1 Experimental Method

The seal position was fixed by placing two shims underneath the segment at each of the extreme URS and DRS sides of the segment and taped into position. Figure 5.12 shows the arrangement for fixing the seal segment. As the pressure was increased at inlet to the seal, the seal segment moved to a lower operating position, the clearance set by the shims. As the rig was operated without back pressure, it was possible to visually check that the seal segment was resting on the shims, as well as with the capacitance sensors. A range of shims were used, from no shims for a zero clearance test to $1.0\,\mathrm{mm}$ shims for a high clearance test. At shim sizes below $0.20\,\mathrm{mm}$, the seal segment was manually forced onto the shims as the positive radial force would move the seal segment away from the rotor. (This was further demonstration of the ability of the Aerostatic Seal to move away from the rotor.) The area of the shims was accounted for when calculating the mean clearance.

This method was chosen as the best method for fixing the seal segment (without re-machining a whole new fixed clearance seal test rig) as it ensured that the seal segment position was fixed during a test, and any segment movement was noticed during the test. As the segment was free to move down initially, then it also ensured that the segment is fully pushed against the contact face of the seal segment holder preventing large secondary leakage flows.

The seal was subjected to a continuous ramp in pressure, with pressure, clearance,

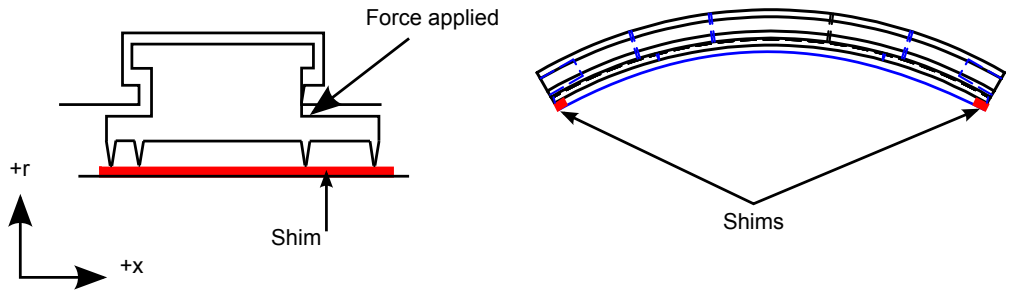

Figure 5.12: Seal segment fixing method

and mass flow rate measurements taken constantly. The mean of the pressure, clearance and mass flow rate was calculated over a small period of time (typically 0.2 s, although depending on the rate of increase in pressure) at pressure ratios of 1.2, 1.4, 1.5, and 1.6. The pressures were logged at 200 Hz, giving 40 samples for each measurement. There was no low frequency variation on the pressure signal observed. It was not possible to perform these tests at a pressure ratio lower than 1.2 as the seal segment would be retracted.

Pressure in each of the three seal cavities was non-dimensionalised using a pressure coefficient, Cp, defined by Eq. (3.1), and described in Chapter 3.

Most results have been taken at atmospheric back pressure, although some have been taken with higher back pressures. This was limited to higher clearances as there was no method of pushing the seal segment onto the shims to obtain low clearances.

5.5.2 Computational modelling

3D Reynolds Averaged Navier-Stokes (RANS) calculations have been carried out at three clearances. The purpose of these calculations was to visualise the key 3D flow features inside the non-rotating test rig and to evaluate the modelling assumptions in the analytical design tool.

A hybrid mesh was constructed using Pointwise V17.1R4, a commercially available meshing program. Figure 5.13 shows a cross section of the computational domain. Un-

Mean clearance / mm	No. of cells $\times 10^6$
0.550	5.53
0.230	7.59
0.058	7.92

Table 5.2: 3D RANS CFD test cases

structured cells were positioned around the feed holes, above the seal segment and where the feed holes connected to the leakage path under the seal segment, also shown in Fig. 5.13. The mesh included the side leakage gap between the seal segment and the side of the test rig walls. Three meshes were generated, each with a different clearance. The three CFD cases are listed in Table 5.2.

Mesh errors were checked when loading the mesh into FLUENT. High aspect ratio cells were inevitable on the surface of the rotor due to the low cell height underneath the fin tips. However as the high aspect ratio cells were aligned with the flow direction, the effect on the results was deemed minimal. The mesh quality was more important around the seal fin tips. Areas where the velocity of the fluid was low were less important such as the flow path up to the top surface of the seal segment. Computational resource limited the maximum number of cells to approximately 8×10^6, and so cells in the circumferential direction were sacrificed in favour of cells in the axial direction. Rotor rotation and swirl were not modelled as they were not present in the non-rotating rig. Ultimately the objective of the CFD was to examine bulk flow features and provide a comparison to the analytical and experimental results, and therefore time was not spent on further refinement of the CFD study.

The inlet and outlet of the seal was modelled with a total pressure inlet and pressure outlet boundary conditions, with the flow angle normal to the boundary. Inlet pressure was $1.4\,\text{bar(a)}$ and outlet pressure $1.0\,\text{bar(a)}$, giving a pressure ratio of $PR = 1.4$. Inlet temperature was $300\,\text{K}$. All walls were modelled as smooth and adiabatic with no slip. The turbulence parameters at inlet were set with turbulent intensity (Λ) equal to 0.054% and a turbulent length scale of $2.25\,\text{mm}$. The turbulent intensity was calculated by Eq. (5.2) using the Reynolds number based on the inlet velocity and hydraulic diameter [93]. The turbulent length scale was calculated as per Eq. (5.3) using the hydraulic diameter of the inlet [93].

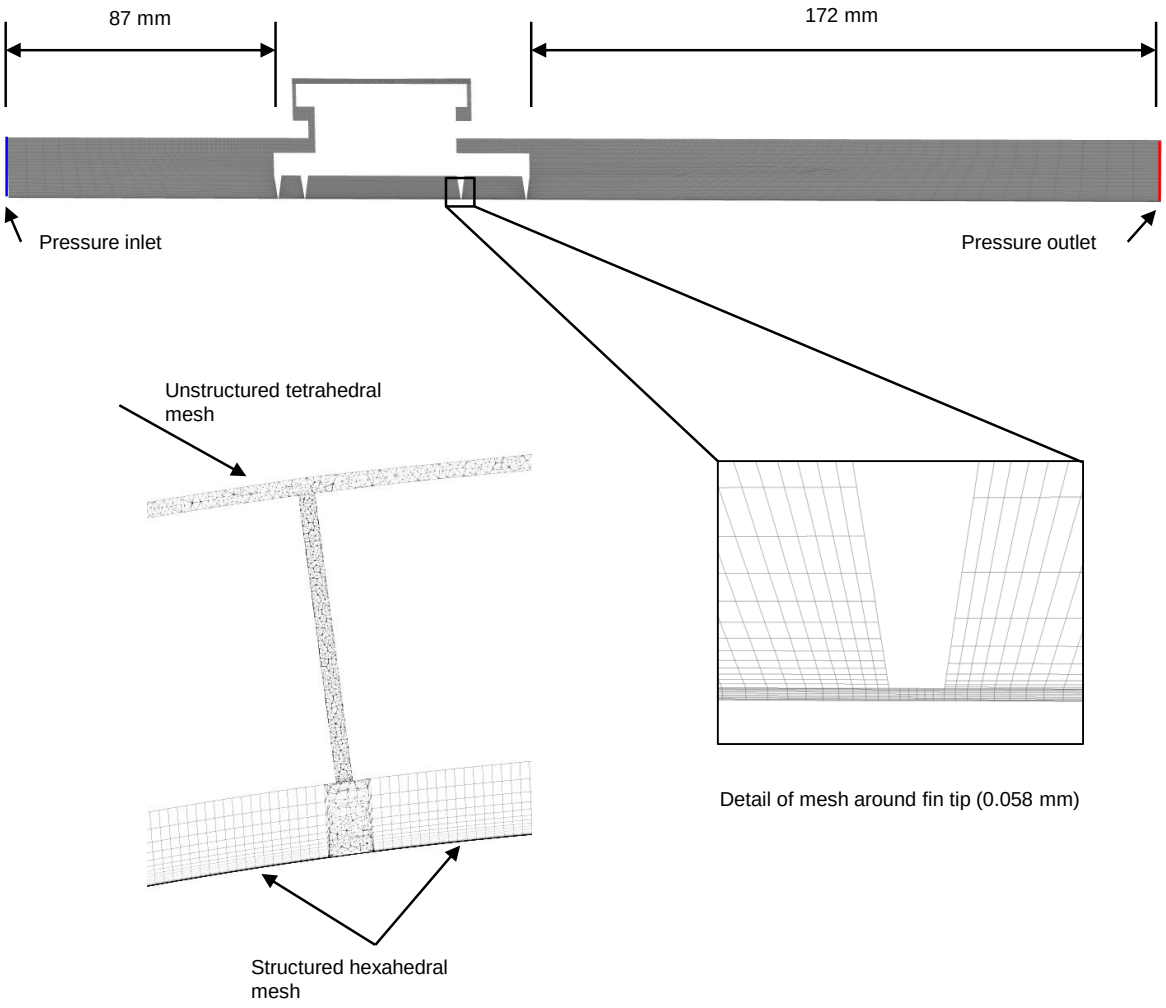

Figure 5.13: Cross section of computational domain.

Property	Value	Unit
Specific isobaric heat capacity	1006.43	$\mathrm{J\,kg^{-1}\,K^{-1}}$
Thermal conductivity	0.0242	$\mathrm{W\,m^{-1}\,K^{-1}}$
Dynamic viscosity	1.7894×10^{-5}	$\mathrm{kg\,m^{-1}\,s^{-1}}$
Molecular weight	28.966	$\mathrm{kg\,kmol^{-1}}$

Table 5.3: Fluid properties used in the CFD calculations.

$$\Lambda = 0.16(Re_{D_H})^{-\frac{1}{8}} \tag{5.2}$$

$$l = 0.07D_H \tag{5.3}$$

The calculation has been performed using the steady pressure based solver in FLUENT 15.0. The working fluid was air, modelled as an ideal gas, and with default FLUENT properties for air, given in Table 5.3. The SIMPLE scheme was used for pressure-velocity coupling. The gradient was calculated with the least squares cell based method. The turbulence model was the realisable $k-\epsilon$ model with enhanced wall treatment. A second order upwind discretisation has been used for the pressure, momentum, density and energy and first order upwind for turbulence terms. The calculation was run for a minimum of 9000 iterations, by which time the mass flow rate had stabilised and the scaled residuals had fallen below 1×10^{-4}.

The results in this section are described in three parts: 1) the seal axial pressure distribution in the pockets of the seal segment, 2) the seal pressure distribution between seal segments, and 3) the calculated radial force on the seal segment.

5.5.3 Pressure Distribution

The Aerostatic Seal axial pressure distribution and its variation with seal clearance is critical to obtain a successful seal design. The analytical, CFD and experimental pressures in each axial pocket in the seal is compared in Fig. 5.14. The pocket pressures have been normalised by the pressure difference across the seal segment, as per Eq. (3.1). Cp_1, Cp_2 and Cp_3 refer to the pressure coefficient in the 1st, 2nd and 3rd seal axial pocket respectively. Refer back to Fig. 3.8 for the cavity nomenclature. Cp_t refers to the pressure coefficient on the top surface of the segment. The results presented in Fig. 5.14

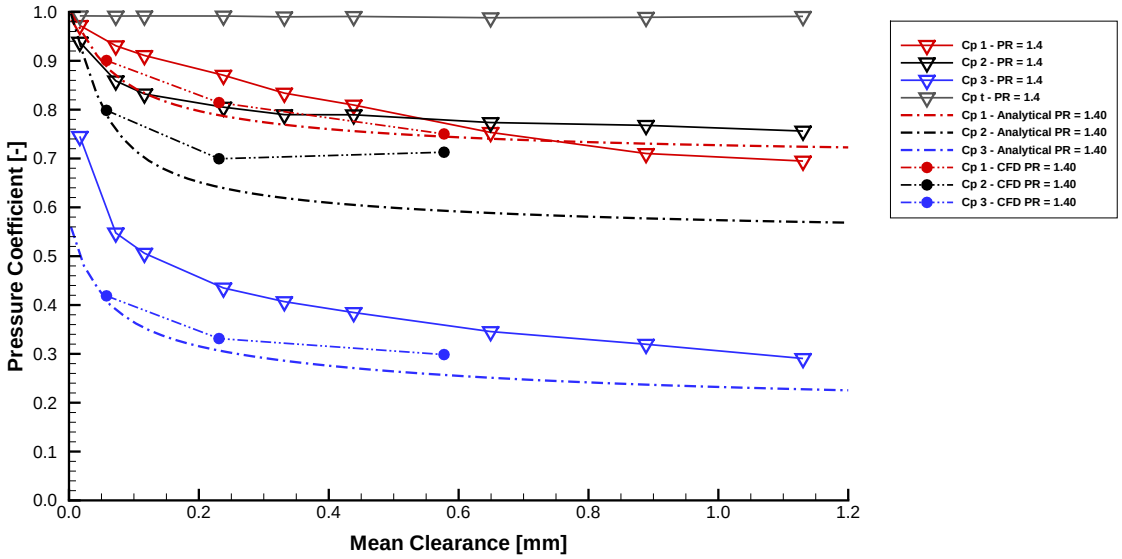

Figure 5.14: Variation in pressure coefficient with seal clearance

were with atmospheric back pressure and at a pressure ratio of $PR = 1.4$. As the seal segment and the rotor have the same diameter, when the segment was operating at a clearance, the clearance in the centre of the seal segment was larger than at the sides of the segment. Therefore the method described in Appendix F has been used to calculate the mean clearance.

The results shown in Fig. 5.14 show the key operating principles of the Aerostatic Seal. As the clearance of the seal segment was reduced the pressure in the seal cavities increases, and it is this increase in pressure which generates a positive radial force to prevent the seal segment from contacting the rotor surface. However there are two key differences between the experimental, CFD and analytical pressure distributions.

1. Over the full range of tested clearances the experimental pressure distribution was higher in all axial pockets.

2. At clearances greater than 0.55 mm the experimental pressure coefficient in the first pocket was lower than the second pocket, which was not captured in the analytical model. This was termed the 'pressure recovery effect'.

Pressure recovery occurs because the pitch between the first two labyrinth restrictions was small, and so at high clearances the vortex that forms in the cavity prevents diffusion and the associated mixing losses occurring. Therefore the jet that forms under

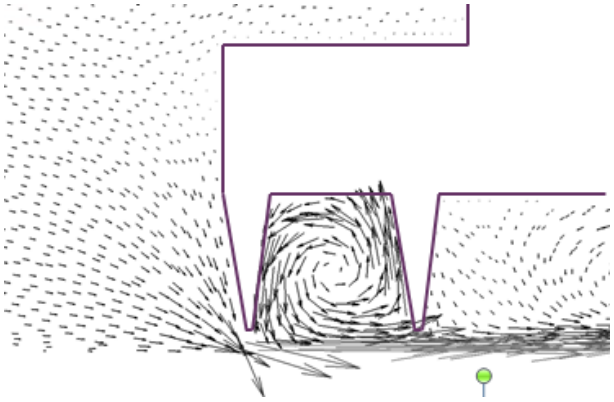

Figure 5.15: Large vortex in the first seal cavity

the first fin blows straight through into the second cavity, leading to pressure recovery. This effect was captured in the 3D CFD and is shown in Fig. 5.15. It is the same effect also reported by other researchers for a straight through labyrinth seal at high clearances [92], [94]. At low clearances the effect was not observed as the ratio of clearance to fin pitch was much lower, and at these low clearances, e.g. $0.05\,\text{mm}$, the analytical and CFD pressure distributions agree closely.

The reason that the experimentally measured pressure distribution was higher in all axial pockets was due to the seal segment lifting off the rotor surface at the upstream edge of the segment, thereby increasing the clearance at the upstream restrictions. This was observed in the clearance measured by the capacitance sensors. This tilting of the segment would decrease the pressure drop in the front restrictions as the leakage area was increased, and so a greater pressure drop would occur at the last restriction. In the CFD and analytical model the clearance at each restriction was the same. This was most significant at the lower clearances where the positive radial force was the greatest. The level of rotation measured was small, the largest angle being $\phi = 0.018°$. Therefore small angles have a large effect on the seal segment pressure distribution.

Reynolds Number Effects

Fixed clearance tests were carried out with elevated back pressure, which increased the pressure difference across the seal and the Reynolds Number for the same pressure ratio. In these tests the pressure ratio was $PR = 1.2$. The inlet pressure was held constant by the control valve, and the pressure ratio increased by lowering the back pres-

sure by steadily opening the back pressure valve. The lowest fixed mean clearance that could be obtained with back pressure was $0.56\,\text{mm}$. At lower clearances the seal segment would operate at a clearance higher than the clearance set by the shims due to the increased radial pressure force. Two sets of back pressure tests were conducted: a test with $5.60 \pm 0.22\,\text{bar(a)}$ inlet pressure and a test with $3.25 \pm 0.60\,\text{bar(a)}$ inlet pressure.

The experimental pressure distribution at higher back pressure is shown in Fig. 5.16. Atmospheric back pressure results are also included for comparison. Comparing the pressure coefficient measured, it is clear that the increased pressure difference across the seal has little effect on the pressure coefficient distribution, except on the pressure measured in the first cavity, Cp_1 which was lower at the increased Reynolds number tests. Therefore the pressure recovery effect was affected by axial Reynolds number. Other researchers [33] reported kinetic energy carry over was most influenced by axial Reynolds number, and the pressure recovery effect is an extreme example of kinetic energy carry over. The axial Reynolds number for the case with $5.60\,\text{bar(a)}$ inlet pressure was $Re_x = 10\,000$ at the highest clearance. When the inlet pressure was $3.25\,\text{bar(a)}$ $Re_x = 6700$, while for the test with atmospheric back pressure it was $Re_x = 2400$. The axial Reynolds number for transition from laminar to turbulent flow is around $Re_x = 6000$ [91] for flow through labyrinth seals.

5.5.4 Side Pressure Distribution

The flow around the side surfaces of the Aerostatic Seal is 3D, with flow from the top surface of the seal segment as well as flow travelling axially through the gap between the segments. The side pressure force is a significant contributor to the overall radial force acting on the segment, and so it is important that it is correctly modelled at the design phase of the Aerostatic Seal. Hence the side pressure distribution has been investigated experimentally and with CFD calculations.

Figure 5.17 shows the typical experimental side pressure distribution result for the URS and DRS side of the segment. The pressure has been non-dimensionalised as pressure coefficient using the same method as before, given by Eq. (3.1). Eight pressure taps distributed on each side of the test rig, and the position of the taps are given in Table 4.2 in Chapter 4. A 2D mesh was constructed on the side of the segment and then used to integrate the pressure acting over the surface to calculate the force acting on the side

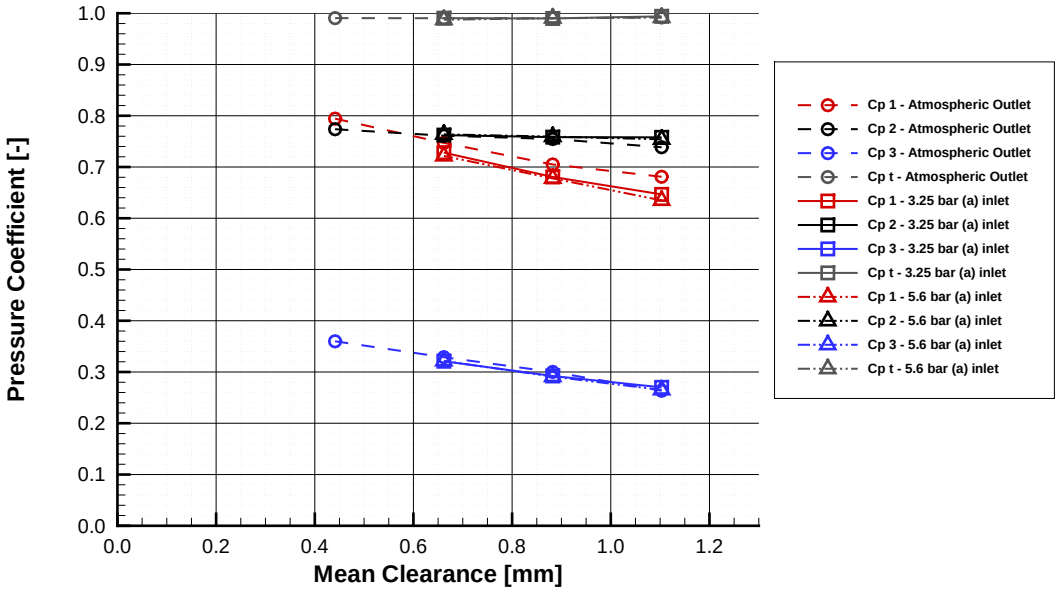

Figure 5.16: Variation in pressure coefficient at high back pressure, pressure ratio $PR = 1.20$.

of the segment. Inlet pressure was assumed to be acting at the black nodes, measured mean top pressure at the grey nodes, and outlet pressure at the red nodes, shown in Fig. 5.17.

By looking at the pressure distribution over the side surface of the segment, it can be seen that there is high pressure acting over a large part of the top part of the segment due to high pressure being present above the segment, and this driving flow from the top surface into the segment down into the sides of the segment. Also of note is that there is no obvious disruption of flow in the centre of the segment where the circumferential spring holes are situated. It could be expected that the spring would cause some blockage to the flow, however no effects were observed in these tests.

For comparison, Fig. 5.18 shows the side pressure distribution obtained in the 3D CFD. The side pressure gap is similar to the side gap experimentally. The experimental and numerical side pressure distributions show a similar pressure profile on the side surface of the seal segment. The CFD does not model the circumferential springs which were present in the experimental tests.

The side pressure force was normalised by the average of the inlet and outlet pressure acting over the side area of the seal segment to produce side force coefficient,

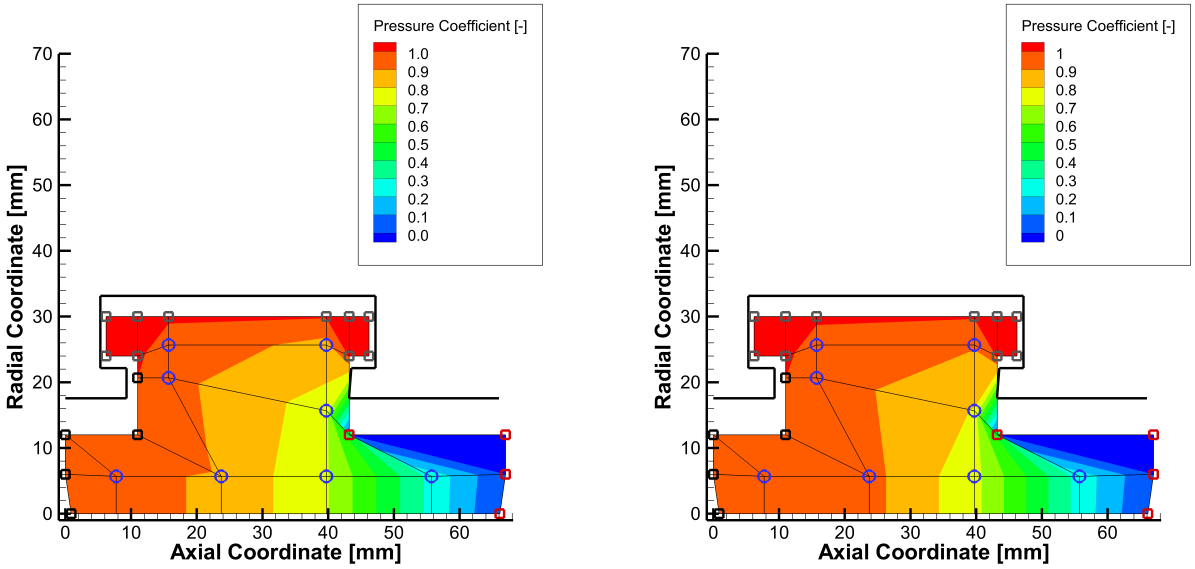

(a) URS side

(b) DRS side

Figure 5.17: Experimental pressure coefficient on side faces of seal segment and 2D mesh used for integration. 0.44 mm mean clearance.

defined as per Eq. (5.4). The side leakage area, the axial area of the clearance between the seal segments, varied at different seal segment clearances. Figure 5.19 plots the side pressure coefficient over the range of side leakage area tested, and at different pressure ratios. Over the range of areas tested, the side leakage area does not affect the measured side pressure coefficient, the force coefficient is approximately constant at $Cf_s = 1.4$. Each of the different pressure ratios were taken in the same test, which explains why the points all follow the same distribution. A single test was conducted with a lower segment position to achieve a lower side leakage area, which is the single point at a side area of 23 mm^2.

Critically, the side pressure on each side of the seal segment was the same, the maximum difference measured between each side of the segment was $2.1\,\%$.

$$Cf_s = \frac{F_s}{\frac{1}{2}\Delta P A_s} \tag{5.4}$$

The side pressure coefficient can be used in the analytical model - see equation Eq. (3.14).

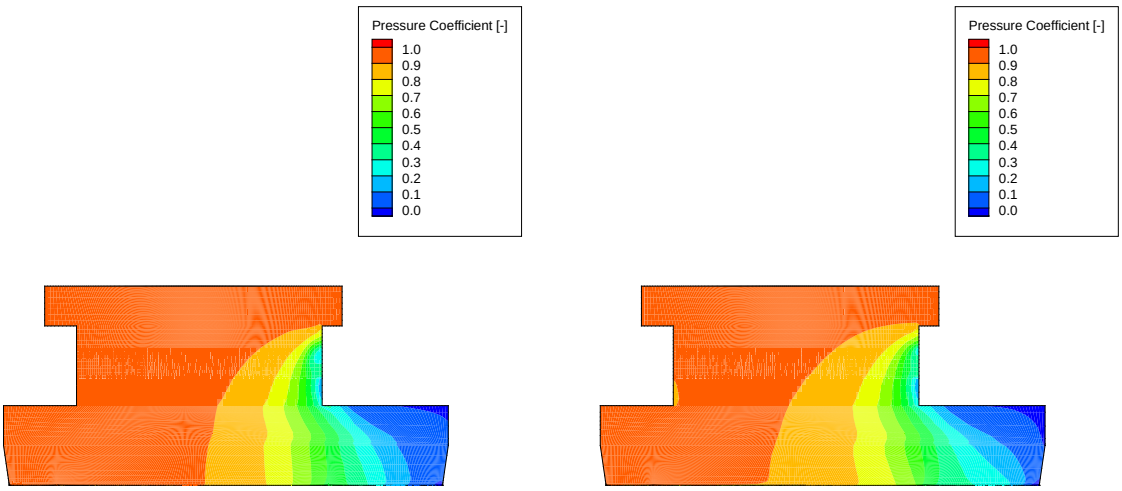

(a) 0.058 mm mean clearance

(b) 0.23 mm mean clearance

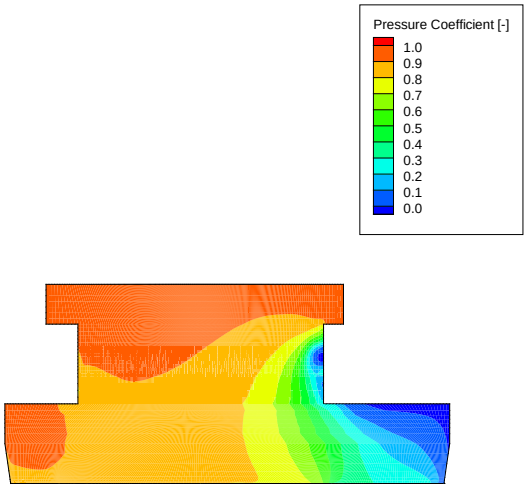

(c) 0.55 mm mean clearance

Figure 5.18: CFD side pressure coefficient distribution.

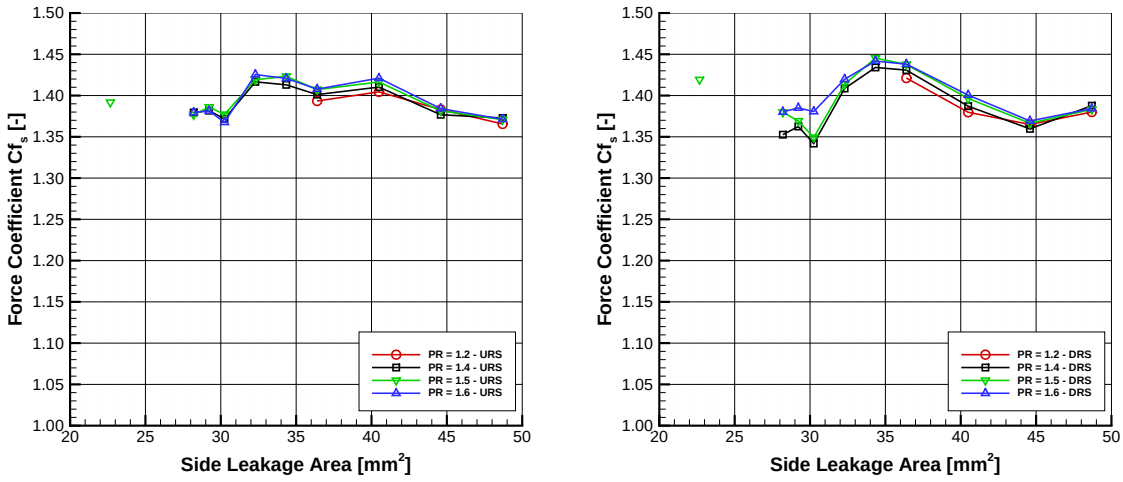

(a) URS side (b) DRS side

Figure 5.19: Side force coefficient.

Mean clearance / mm	Side Pressure Coefficient / 1
0.058	1.602
0.230	1.573
0.550	1.514

Table 5.4: CFD side pressure force coefficient.

Comparison to CFD

The CFD calculations were also used to calculate the side pressure force at each of the three seal clearances modelled. The side pressure coefficient was calculated and is given in Table 5.4. The CFD showed higher levels of side pressure force than measured experimentally. The side pressure was also affected by changes in seal segment clearance. The experimental position was set by the shims at the side of the seal segment, and which will have affected the flow of air from the top surface of the segment into the side leakage channel. The side leakage channel in the CFD case did not include the circumferential springs, which were present in the experimental case, and which would affect the flow. Also the experimental grid only consisted of 8 points which might not have captured all the pressure variations captured in the CFD.

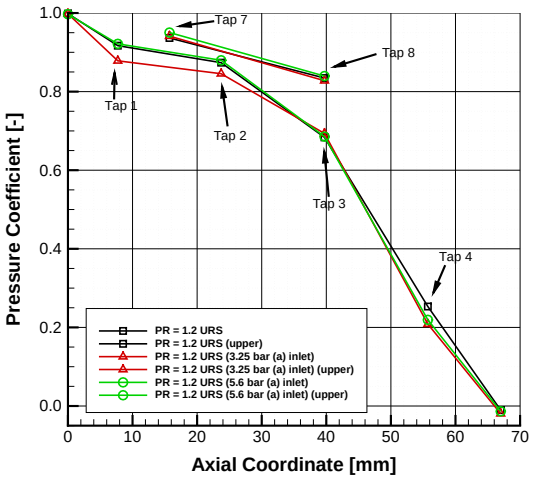

Figure 5.20: Axial side pressure coefficient distribution.

Side force at increased back pressure

The side pressure distribution was also investigated with increased back pressure. It was found that the pressure coefficient distribution was similar to the atmospheric back pressure results. The pressure coefficient has been plotted with axial distance along the side of the segment and shown in Fig. 5.20. Taps 1 to 4 are the lowest radial position, and taps 7 and 8 are the upper radial position on the side face of the segment. Tap 5 and 6 have been omitted for clarity, and only the URS side of the segment is shown, although the DRS side of the segment was similar. The pressure coefficient has been plotted for atmospheric back pressure, $3.25\,\mathrm{bar(a)}$ inlet pressure and $5.60\,\mathrm{bar(a)}$ inlet pressure. There was little variation in the side pressure coefficient between atmospheric and non-atmospheric back pressure tests.

In summary these results show that the side pressure force measured experimentally was found to be invariant with side leakage area, pressure ratio, and at high back pressure. As the side gap between the segment and the walls of the test rig were larger than would be implemented in steam turbine application, then the pressure distribution might be effected at very small side leakage areas. Also the rotating rig segment used keys between the segments, which would have an effect on the side pressure distribution.

5.5.5 Pressure force measurements

Pressures on the surface of the segment can be used to calculate the pressure forces acting on the segment. The pressure force can be combined with the segment weight and the circumferential spring force to calculate the total radial pressure force. The pressure was assumed to act over the same area as used in the analytical method, given in Fig. 3.9.

One of the first tasks was to analyse the error due to the discrete sampling of the pressure distribution in the non-rotating rig rotor surface. The CFD results were employed to do this. This was also important to understand for the analytical design methodology.

Table 5.5 lists all the forces calculated by CFD for each of the three clearances modelled. The force nomenclature and location on the seal segment was the same as in the analytical model, shown in Fig. 3.9.

The pressure forces have been calculated by two methods: the area integration method integrates the pressure field calculated in the CFD model over the surface of the seal segment. The mean pressure method calculates the mean pressure by sampling the pressure at the same location as the rotor pressure taps installed in the non-rotating test facility. Integrating the pressure over the seal segment area was expected to be the most accurate method as any localised pressure variations are measured. Table 5.5 lists the difference in the radial force on each surface of the seal segment for the two different calculation methods. The difference is also expressed as a percentage of the net radial pressure force F_{pr}. The largest difference in the force is F_{12}, the force from the central pressurised pocket, which is 4.24% at a clearance of $0.55\,\text{mm}$. Whilst this is a relatively large error as a percentage of the net radial pressure force, it amounts only to $-4.552\,\text{N}$. The net radial pressure force calculated by each method, also shown in Table 5.5, shows a small difference between the two methods, the largest difference was $1.2\,\text{N}$ at $0.55\,\text{mm}$. Therefore the experimental pressures measured on the rotor surface provide a good measurement of the pressure force on the whole seal segment, although error in radial pressure force on individual faces of the seal segment may be subject greater error.

Force	Pressure	Area mm^2	Clearance 0.058 mm		0.23 mm		0.55 mm	
			ΔF / N	$\frac{\Delta F}{F_{pr}}$ / %	ΔF / N	$\frac{\Delta F}{F_{pr}}$ / %	ΔF / N	$\frac{\Delta F}{F_{pr}}$ / %
F_1	P_{top}	1170	-0.061	0.45	-0.076	-0.08	-0.094	0.09
F_3	P_{top}	17741	1.138	-8.49	1.332	1.33	1.638	-1.52
F_5	P_{top}	1872	0.217	-1.62	0.314	0.31	0.329	-0.31
F_7	P_{in}	4158	0.065	-0.48	0.075	0.08	0.0655	-0.06
F_9	P_{in}	323	-0.004	0.03	-0.029	-0.03	-0.086	0.08
F_{10}	P_1	2562	0.004	-0.03	0.403	0.40	1.415	-1.32
F_{11}	P_2	15006	-0.485	3.62	-2.137	-2.14	-4.552	4.24
F_{12}	P_3	6222	0.001	-0.01	1.176	1.18	2.940	-2.74
F_{13}	P_{out}	414	0.012	-0.09	-0.292	-0.29	-0.232	0.22
F_{15}	P_{out}	7182	0.088	-0.66	-0.059	-0.06	-0.144	0.13
F_{pr} - Area integration / N			-13.4		-101.0		-107.5	
F_{pr} - Mean pressure / N			-14.4		-101.7		-108.7	

Table 5.5: CFD Radial Force comparison

Radial force comparison

The experimental, CFD and analytical radial force coefficients are shown in Fig. 5.21 at different mean clearances, and different pressure ratios. As the segment mean clearance was reduced, the radial force increases, which is key for the seal segment to move away from the rotor surface. To account for the effect of the different pressure differences across the seal at difference pressure ratios, the radial force coefficient, C_f, is based on the radially projected area of the segment and the pressure difference, given in Eq. (5.5). Pressure ratios of $PR = 1.4$ to $PR = 1.6$ show very similar force coefficients. The lowest pressure ratio tests, $PR = 1.2$, show a greater radial force coefficient and this was because the radial spring force which is the same at different pressure differences, dominates the radial force. At the higher pressure ratios, the pressure force was a greater contributor to total radial force produced.

$$Cf_r = \frac{F_r}{\Delta P A_r} \tag{5.5}$$

Figure 5.21 also shows the force coefficient at PR = 1.4 calculated by the analytical design tool and CFD simulation. As the experimental pressures in the seal pockets were measured to be higher than the analytical prediction, as shown in Fig. 5.14, the experimentally calculated pressure force was greater than the CFD and analytical model. The

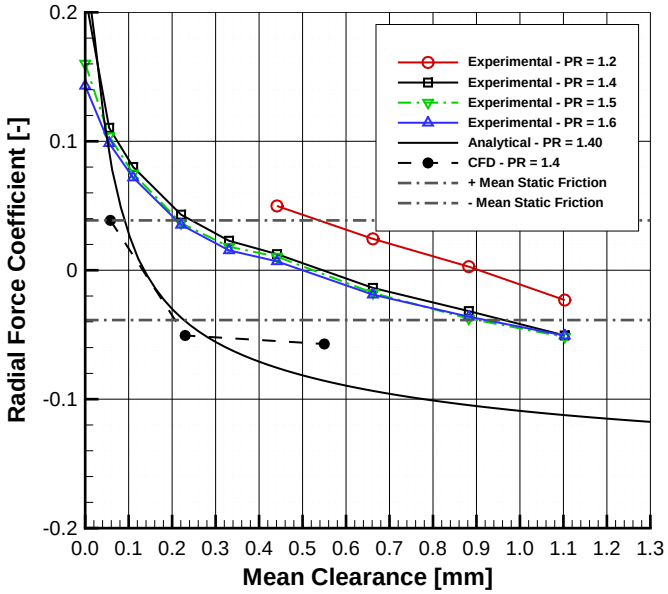

Figure 5.21: Radial force coefficient.

CFD and analytical model produce similar force coefficients at low clearance, but the analytical force was lower than that calculated by the CFD at higher clearances - i.e. over $0.25\,\text{mm}$. The reason for the disagreement is due to two things: 1) the pressure recovery effect after the P1 seal pocket, and 2) the tangential angle ϕ of the seal segment relative to the rotor. The CFD did not model the tangential angle between the rotor and the seal, and so the difference between the experimental results and the CFD modelling was largely due to this effect. The CFD did capture the pressure recovery effect, hence the disagreement between CFD and the analytical model at high clearance. As the difference between the radial force at high and low clearance was reduced due to the pressure recovery effect, then the responsiveness of the seal was also reduced.

During the fixed clearance tests, it was possible to observe the pressure ratio when the seal segment would retract. This allowed the minimum static clearance (see Section 3.2) to be calculated experimentally. Calculating the radial force and axial forces when the seal segment retracted allowed the apparent coefficient of friction to be determined experimentally. This gave a mean apparent static coefficient of friction was calculated as $\mu_{stat} = 0.14$. The radial force coefficient at which the seal segment moves away from the rotor was then plotted on Fig. 5.21, and by negating the force coefficient

(i.e. turning the negative force coefficient positive) the maximum friction line can also be plotted on Fig. 5.21.

5.5.6 Leakage Mass Flow Rate

Figure 5.22a shows the measured leakage at a pressure ratio of $PR = 1.4$ compared to the analytical model and CFD. Secondary leakage around the end of the segment and through the seal segment contact face has been excluded as the experimental set up and the CFD had different side leakage areas. Good agreement is shown between the analytical model, CFD and experimental data. There was slightly increased flow at higher clearances measured experimentally compared to the analytical model.

The secondary leakage is the flow through the seal at zero clearance. The flow rate at zero clearance was determined by fitting a linear least squares regression line through the experimental data and using this regression line to determine the flow at zero mean clearance. Secondary leakage has also been accounted for in the CFD results by measuring just the flow leaving the seal segment at the last labyrinth fin.

The experimental data has been used to calculate a secondary leakage discharge coefficient for use in the standard design and analysis methodology (as per Section 3.3.1). The mass flow rate at zero clearance was found at a number of pressure ratios, and used to calculate a discharge coefficient based on the area between the seal segment and the side of the non-rotating rig. The variation in discharge coefficient is shown in Fig. 5.22b. The discharge coefficient is greater than 1 as the area through the contact face has not been accounted for. Figure 5.22b shows increased discharge coefficient with increase pressure ratio. The mean discharge coefficient of $C_D = 1.8$ has been adopted in the analytical design methodology to account for secondary leakage.

5.5.7 Discussion

This section has observed some key operational characteristics of the Aerostatic Seal, both experimentally and numerically.

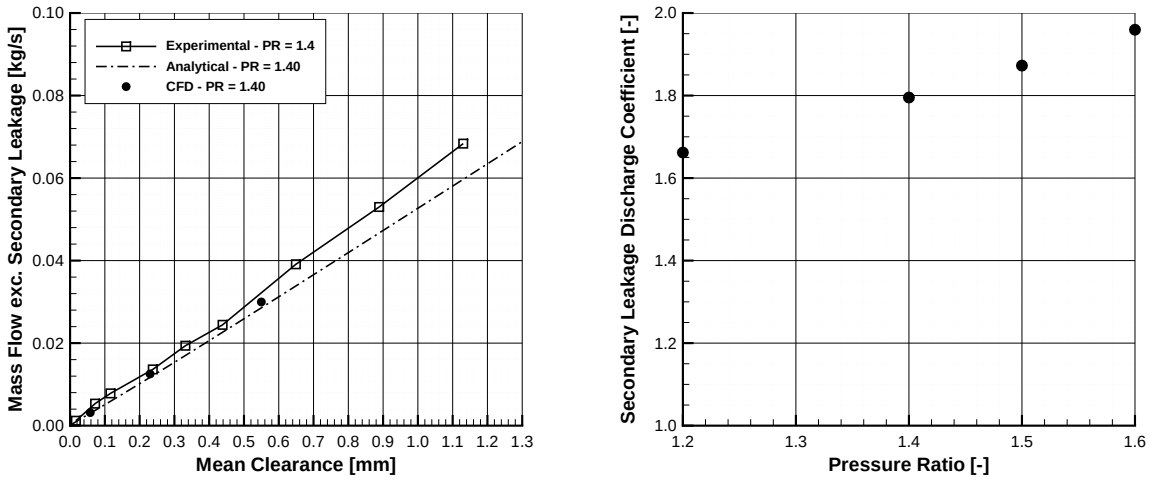

(a) Comparison of experimental, CFD and analytical model mass flow rate at $PR = 1.4$.

(b) Secondary leakage discharge coefficient variation with pressure ratio.

Figure 5.22: Seal mass flow rate and secondary leakage discharge coefficient.

Pressure Distribution

The pressure distribution measured highlighted some key effects. First was the pressure recovery effect in the P1 pocket observed at high clearances. This was captured in the numerical model, although not at all in the analytical model. This had the effect of increasing the pressures in the downstream pockets at higher clearances, and so decreasing the change in pressure force with clearance. This pressure force change needs to be maximised to achieve a more responsive Aerostatic Seal design. Adding extra fins and kinetic energy blockers would improve the situation.

Secondly there was the effect of seal segment tilt at low clearances, due to the high positive radial force. Even though the determined tilt angle was small at $\phi = 0.018°$, the effect on the pressure distribution was significant.

Testing at higher back pressure showed that the effect of axial Reynolds number on the pressure distribution was minimal, and therefore the results here are applicable to the higher Reynolds numbers at realistic steam turbine conditions.

The side pressure distributions were investigated, and it was found experimentally that the side pressure force coefficient could be modelled by a constant value of $Cf_s = 1.4$ for the range of different segment clearances and side leakage channel areas tested. The CFD showed a higher side pressure coefficient and more variation with clearance.

Pressure Force

Calculating the pressure forces analytically was found to over predict the change in force expected over the range of seal segment clearance, compared to both the numerical CFD simulations and the experimentally observed radial force. The coefficient of friction determined experimentally was quite low compared to the value assumed in the design tool. Preventing pressure recovery in the second pocket will increase the seal performance, and also make the analytical tool prediction better. This has been implemented in the proposed Gen Ⅲ design in Section 9.3.

One important finding from the CFD calculations was that the pressure measured in the experimental location on the rotor surface was within 5% of the mean pressure acting on the surface of the segment. The difference between the net radial pressure forces were much closer, the largest difference was 1.2 N.

Leakage mass flow rate

There was good agreement with the leakage predicted analytically and numerically to the leakage measured experimentally. It was found that leakage due to the flow at the sides of the segment was significant, and should be minimised as much as possible in a steam turbine application.

5.6 Conclusion

The experimental testing of the Aerostatic Seal in the non-rotating rig was described in this chapter, and has successfully demonstrated key behaviour required for a successful Aerostatic Seal design. Two seal designs were tested: 'MacDonald 1' and 'MESS01'.

In the course of the test campaigns, the following key behaviour was demonstrated:

1. Bidirectional movement of the seal segment, and the ability of the seal segment to move to an operating clearance where the segment was balanced by pressure, spring and frictional radial forces. Unexpectedly the seal segment showed non-uniform clearance behaviour, that is, one side of the seal segment operating at a lower clearance than the other (refer back to Fig. 5.2).

2. Testing was carried out to measure the tangential rotation of the seal segment. It was concluded that there was minimal segment rotation in the seal holder, the measured angles were within the measurement uncertainty. Further investigation was carried out in the rotating rig, presented in Chapter 6.

3. Repeated testing was carried out to investigate the effect of friction on the seal performance and to investigate other sources of variability. Friction was shown to have an effect on the performance of the seal, although mixed lubrication effects appear to have reduced the effect of friction. Tilt introduced due to the set-up of the rotor was another factor that would influence the operating clearance of the seal.

4. Fixed clearance testing demonstrated that the pressure below the seal segment increased with decreased clearance. Pressure recovery from the first to the second pockets was found, and which had a significant effect on the pressure distribution. Segment tilt at low clearances also effected the pressure distribution and explained some of the differences between the experimental and CFD and analytical pressure distribution. Side pressure distribution was measured experimentally and a constant side force coefficient was found. The experimental, CFD and analytical mass flow rate predictions showed good agreement. The performance of the seal segment could be increased if kinetic energy blockers were introduced in the first pocket.

As non-uniform clearance has been observed in all the tests described in this chapter, and also in the following two chapters, further analysis and test results are presented within Chapter 8. The next chapter tests the Aerostatic Seal in a rotating test facility.

Chapter 6

Experimental Results: Rotating Rig

6.1 Introduction

The demonstration of the Aerostatic Seal concept within the 'Durham Rotating Seals Rig' is presented in this chapter. A new seal was designed specifically for the test rig, 'ROT02', described in Chapter 3. Details on the construction of the test rig and the instrumentation is given in Section 4.4.

The key feature of the 'Durham Rotating Seals Rig' was an adjustable eccentric rotor, which enables the Aerostatic Seal to be tested with rotor radial excursions. Changing the rotor speed and rotor eccentricity allowed different rotor radial excursion rates[1] to be tested.

The test campaign was divided into three parts:

- Testing with the rotor in the low eccentricity position. This was to test the response of the seal during normal operation of the steam turbine, where there would be a small rotor run out.
- Testing with the rotor in the high eccentricity position. This was to test the seal response to large radial rotor excursions typically found during start up or fast changes in turbine load. Low rotor speeds were used to simulate slow rotor radial thermal expansion or contraction. High rotor speeds, up to 1500 rpm, were used to simulate high speed radial excursions due to rotordynamic effects during turbine start up.

[1] The speed at which the rotor surface would be moving towards or away from the seal segment.

Rotor speed rpm	Eccentricity 0.09 mm	0.55 mm
0	X	
26	X	
110		X
300		X
600	X	X
900	X	X
1200		X
1500	X	X

Table 6.1: Test matrix: High and low rotor eccentricity

- Assessment of leakage performance. The seal segments were fixed and the feed holes blocked to simulate a labyrinth seal. This was to enable a comparison of leakage through an Aerostatic Seal and a labyrinth seal.

A test matrix is shown in Table 6.1 for the high and low rotor eccentricity tests conducted. A number of different rotor speeds were tested in each rotor position. Within each test point a full sweep of inlet pressure was tested, up to a maximum pressure of $1.6\,\mathrm{bar(a)}$. The outlet pressure remained constant. The 26 rpm test was the slowest possible rotor speed, other than with the rotor stationary.

6.2 Low Eccentricity Tests

Initial testing was conducted with $0.09\,\mathrm{mm}$ rotor eccentricity and at rotor speeds of 0, 26, 600, 900 and 1500 rpm. Eccentricity is defined as the radial distance from the centre of rotor rotation to the centre of the rotor. Therefore the peak to peak variation in the position of the rotor surface is double the radial eccentricity quoted. The aim of the low eccentricity testing was to demonstrate Aerostatic Seal performance at similar levels of eccentricity found in a turbine under normal operating conditions.

Figure 6.1a shows the seal segment position from a typical low eccentricity rotor test at a rotor speed of $1500\,\mathrm{rpm}$. The position is relative to the mean rotor surface, so zero position is the rotor surface if it was positioned without eccentricity. With eccentricity the position of the rotor surface varies sinusoidally with time. Results are presented for all three instrumented seal segments (10, 12 and 2 O'clock) and for both up rotation (URS)

and down rotation (DRS) sides of the segment. See Fig. 4.9 for nomenclature. From 0 to 5 seconds the seal segments were in the retracted position as there was only a small pressure difference across the seal. There was some variation in retracted seal segment clearance between seal segments and also between the URS and DRS of the 10 O'clock seal segment. This was due to the carrier ring which houses the seal segment being slightly off centre from the rotor and manufacturing variations between the keys which set the initial clearance.

The inlet pressure was increased, and once sufficient pressure difference across the seal was achieved, at around 6 seconds, the seal segments moved towards the rotor surface. This happened quickly as once the seal segments started moving the friction force was reduced from static friction to dynamic friction. The seal segments then came to rest at the operating clearance where the mean clearance is not influenced by further increases in pressure ratio. At the operating clearance the difference in clearance between different sides of the seal segment was only around $0.05\,\mathrm{mm}$.

As a consequence of the rotor eccentricity, the 12 O'clock seal segment was excited by the rotor, shown in Fig. 6.1a, and enlarged in Fig. 6.1b. The seal clearance is the difference between the segment position and the rotor position. After 11 seconds this excitation is damped out by the frictional force. Also of note is the difference in responsiveness of the URS and DRS sides of the seal segment. A similar effect was observed in the non-rotating test facility Chapter 5, and so is not due to the addition of shaft rotation. There appears to be a slight vibration on the other seal segments in Fig. 6.1b; this was traced to a small oscillation of the output voltage from the amplifier circuitry of the inductive sensors, at approximately $800\,\mathrm{Hz}$, and not to movement of the seal segments.

The circumferential position of the seal segments was shown to have an effect on the response. The 12 O'clock segment was the first seal segment to move to the operating clearance. This was expected since the gravitational force vector is entirely in the radial direction. The 10 and 2 O'clock segments moved later and at a higher pressure ratio, and maintained a slightly higher clearance than the 12 O'clock segment, due to the reduced radial component of gravitational force.

A series of six repeated tests were conducted to asses the variability in operating clearance. The seal segments were not reassembled between tests. The mean clearance of each segment was calculated as per Appendix F. The mean clearance was con-

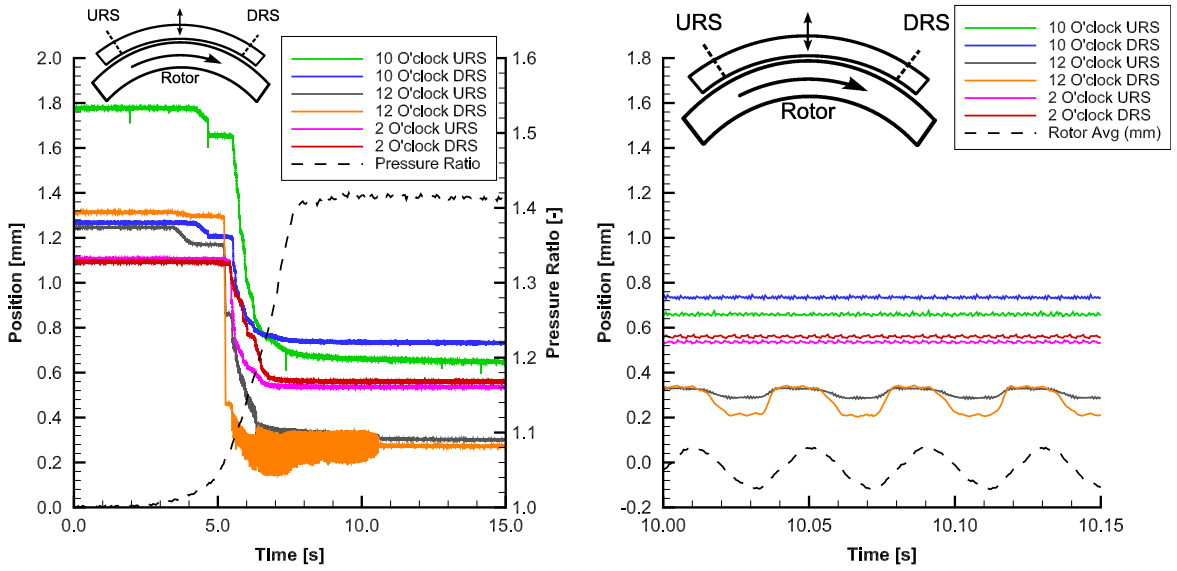

(a) Whole test

(b) Vibratory response

Figure 6.1: Seal segment response at low rotor eccentricity and 1500 rpm

Seal Segment	10 O'clock	12 O'clock	2 O'clock
Mean Clearance / mm	0.698	0.277	0.548
Range / mm	0.020	0.015	0.015

Table 6.2: Mean seal segment clearances, rotor speed 1500 rpm, low rotor eccentricity.

sistently greater for the 10 and 2 O'clock seal segment positions compared to the 12 O'clock position. Table 6.2 gives the mean and range of the six individual tests.

6.2.1 Effect of Rotor Speed

A number of tests were conducted at different rotor speeds from 0 to 1500 rpm and Fig. 6.2 plots the mean clearance of each segment with rotor speed. Over the range of speeds tested, there was no noticeable effect of rotor speed on the mean operational clearance measured. The only exception was 0 rpm where the operating clearance was significantly greater. The largest increase was the 12 O'clock segment which was about 0.11 mm higher than all the tests conducted with rotor rotation. The reason why is demonstrated in Figs. 6.3a and 6.3b which shows the 12 O'clock seal segment response at 0 rpm and 26 rpm respectively. In Fig. 6.3a the 12 O'clock seal segment moves fast during initial close in, and the clearance reduces as the pressure ratio increased. In

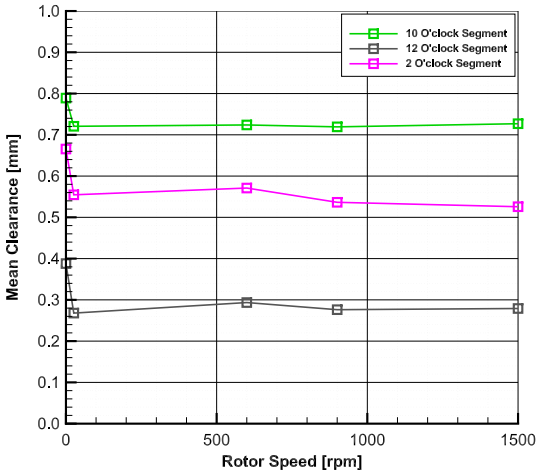

Figure 6.2: Effect of rotor speed on mean seal segment clearance.

Fig. 6.3b, the 12 O'clock seal segment operating at 26 rpm, the 12 O'clock seal segment initially moves to a similar clearances as with no rotation in Fig. 6.3a. However as the rotor position was changing due to the eccentricity of the rotor and increase of pressure, there are a number of secondary movements of the seal segments which further reduce the seal segment operating clearance.

Overall this result indicates that if the Aerostatic Seal was operating in a turbine with a well balanced rotor with no run out, then the operating clearance of the seal would be higher than if there was some rotor radial transient. However it is unlikely that there would be zero rotor radial transients at all, and so the operating clearance of the seal will be lowered.

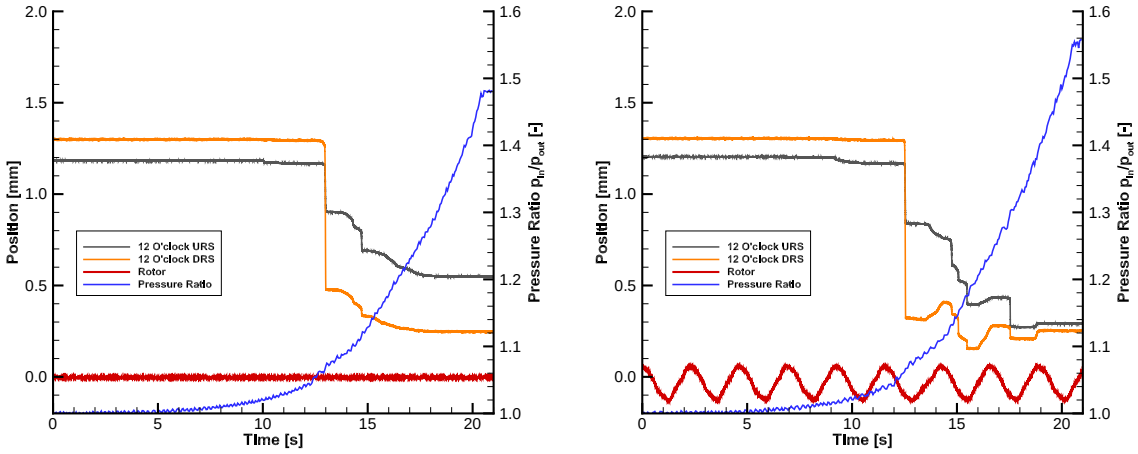

(a) Stationary rotor

(b) 26 rpm

Figure 6.3: Seal segment response with low eccentricity

6.3 High Eccentricity Tests

High eccentricity testing was conducted to assess how responsive the Aerostatic Seal was to more extreme rotor radial transients, and to demonstrate the ability of the seal to respond to the rotor. Testing was conducted at a range of inlet pressures and rotor speeds, as shown in the test matrix discussed earlier (Table 6.1).

Rather than show the seal segment position with time for all rotor speeds and at all pressures, it is more informative to focus on a small number of key results. Therefore the highest rotor speed has been chosen as it was most demanding for the seal to respond to, and the seal was able to respond to the rotor remarkably well. A pressure ratio of $PR = 1.5$ has been chosen as it was the design operating pressure ratio. Together the high rotor speed and high pressure represent the case where the turbine rotor goes through a transient event while under load. This is shown in Fig. 6.4.

Two further cases are shown: when the rotor was at high speed and the pressure low, shown in Fig. 6.5, and when the rotor speed was low and the pressure high, shown in Fig. 6.6. High speed and low pressure was chosen to demonstrate that at low pressure rotor tracking was more difficult as the pressure forces are lower. Low rotor speed was to demonstrate the seal behaviour when responding to low speed rotor transients due to gradual thermal growth of the turbine rotor. Finally the mean clearance for all speeds and a selection of pressures are shown in Fig. 6.7.

Figure 6.4 plots the URS and DRS seal segment position at a rotor speed of 1500 rpm and pressure ratio of $PR = 1.5$ for the 10, 12 and 2 O'clock seal segments. The rotor position at both URS and DRS sensor locations has been plotted as the rotor radial position was different at each sensor location due to the circumferential distribution of the sensors. The clearance at each of the sensor locations is the difference between the segment position and rotor position. Due to the large radial rotor movement the seal segment has to move in order to prevent contact between the segment and the rotor. The seal segment was stationary for a period of time at the high and low positions, and therefore before the seal segment could move it had to overcome static friction rather than dynamic friction. Both sides of the seal segment move at the same time. Note that at the lowest position the seal segment was limited by the T slot.

The 12 O'clock seal segment, Fig. 6.4b, was able to track the rotor the closest. The 10 and 2 O'clock seal segment responses, Figs. 6.4a and 6.4c respectively, show that the URS side of the seal segment consistently operates at a higher clearance. The 10 O'clock seal segment shows a greater difference in position between the URS and DRS of the segment; this was due to the uneven initial clearance, as found in Fig. 6.1a. This has lead to small rubs as the rotor moves towards the seal segment at $20.09\,\mathrm{s}$ and $20.13\,\mathrm{s}$. Whilst only the top three seal segments were instrumented, a camera positioned at the outlet of the rig provided confirmation that all seal segments responded to the rotor.

At low pressure ratios, just after the seal segment had 'closed in', the seal segment response was not fast enough to track the rotor position to the extent shown in Fig. 6.4. An example is given in Fig. 6.5, which shows the 12 O'clock seal segment response at 1500 rpm and at a pressure ratio of PR = 1.1. Note how the time taken to move towards the rotor is greater than the higher pressure ratio data shown in Fig. 6.4b. As a consequence the seal segment reached the lowest operating position as the rotor was moving to a greater radial position, which would lead to a greater chance of rotor contact. As the rotor goes through the 1^{st} critical speed, the pressure drop across each turbine stage will be low, and the rotor larger than during normal operation. Therefore the key point for the designer of the Aerostatic Seal is to ensure the seal segment remains retracted until the rotor is up to speed, and has gone through the rotor critical speed.

Also of interest is the segment response at low speeds. Figure 6.6 shows such a test at a rotor speed of 110 rpm and a pressure ratio of PR = 1.5. In this operating

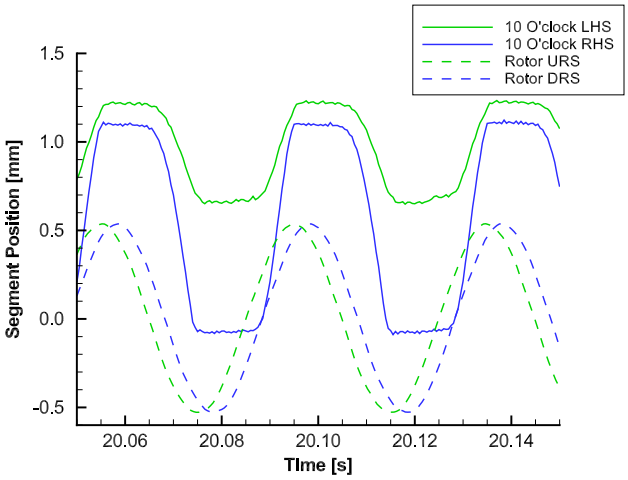

(a) 10 O'clock Segment

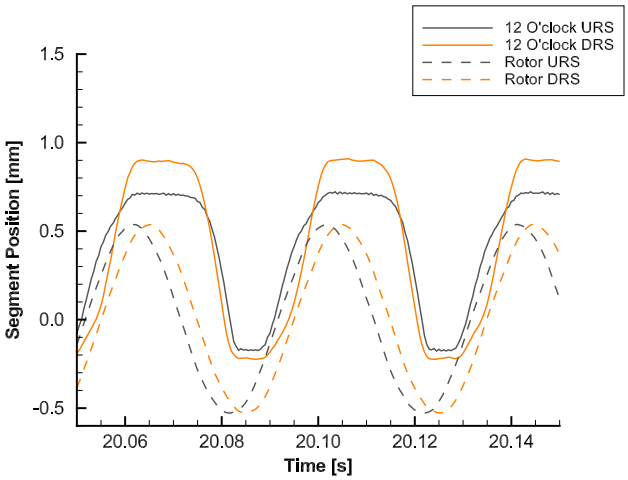

(b) 12 O'clock Segment

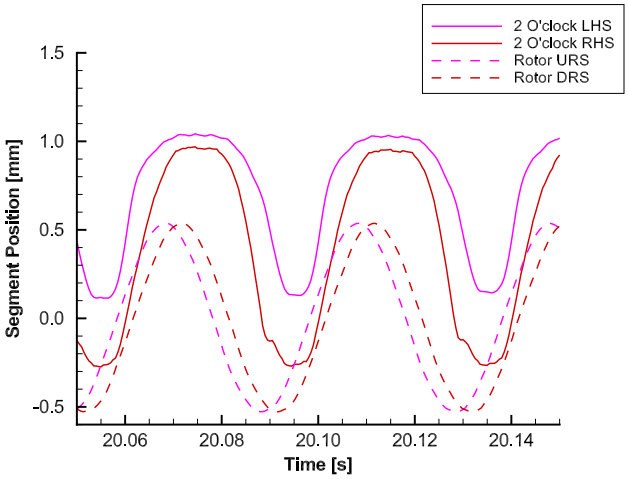

(c) 2 O'clock Segment

Figure 6.4: High eccentricity, high speed seal response: 1500 rpm, PR = 1.5

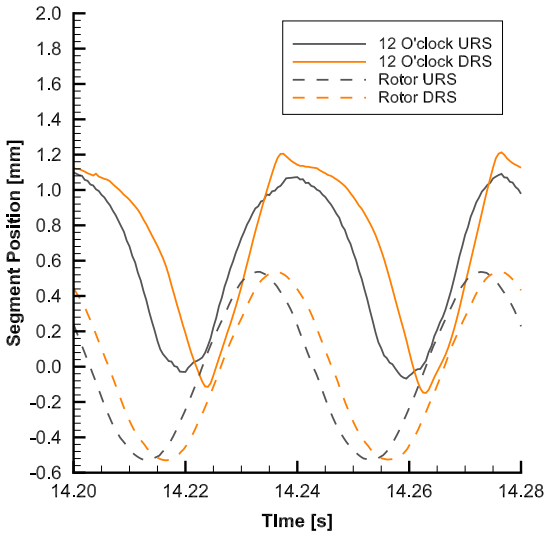

Figure 6.5: Seal response at high speed (1500 rpm) and low pressure ratio ($PR = 1.1$).

regime the seal segment response towards the rotor shows a number of discontinuities where the velocity of the seal segment changed. Note that at low rotor speeds the motor inverter driving the rotor created a significant level of electrical noise which is the evident on the signals shown in Fig. 6.6. Therefore in slow rotor movements such as thermal transients, it is much more likely that the seal segments will respond in a number of discrete movements.

Figure 6.7 shows the mean clearance for each measured seal segment over the full range of rotor speeds and pressure ratios tested. The mean segment clearance has been obtained by numerically integrating the seal position with respect to time over an integer number of rotor periods. Due to 0.55 mm eccentricity of the rotor, the minimum seal position that a fixed labyrinth seal could operate is 0.55 mm, which would lead to a mean clearance of 0.55 mm over a rotor period. This is also plotted in Fig. 6.7. As the mean clearance of the Aerostatic Seal is lower than the minimum mean clearance of a fixed seal, the potential benefit of a dynamic seal is demonstrated.

At a low pressure ratio of $PR = 1.1$ the influence of rotor speed was significant, particularly so for the 10 O'clock segment, and the seal was operating at a higher mean clearance. At a pressure ratio of $PR = 1.10$ the seal segments had only just moved from the retracted position, and the 10 O'clock segment was the last to move. However once

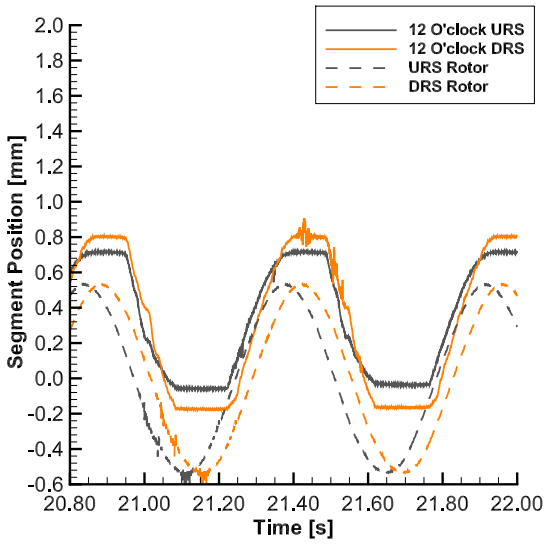

Figure 6.6: Seal response at low speed (111 rpm) and high pressure ratio ($PR = 1.5$).

the pressure ratio has increased to $PR = 1.15$ the effect of speed was reduced, and between pressure ratios of $1.3 < PR < 1.5$ the response almost independent of rotor speed.

The key observation is that the seal segments were able to maintain a mean clearance that was lower than the level of rotor eccentricity once sufficient pressure ratio had been obtained. This is true over the full range of rotor speeds for the 12 and 2 O'clock seal segments. The 10 O'clock segment response was not as good, and indicates that initial position of the seal segment influences performance.

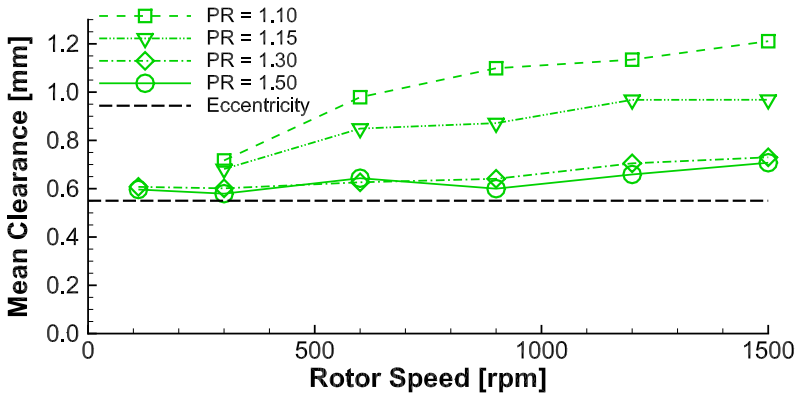

(a) 10 O'clock Segment

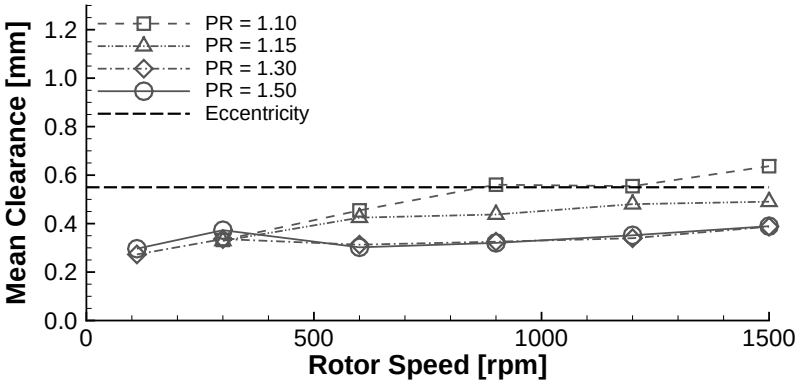

(b) 12 O'clock Segment

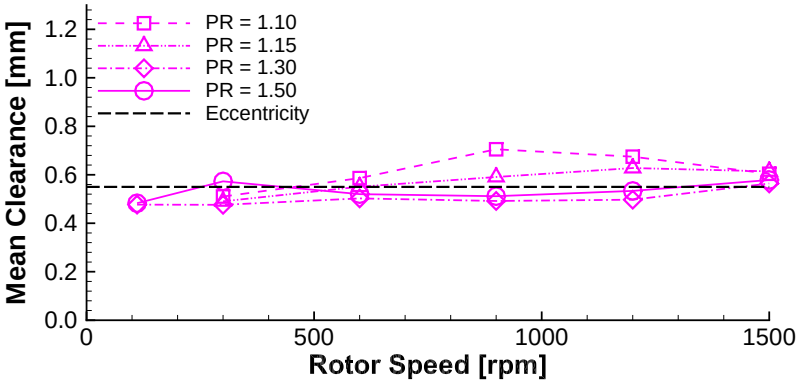

(c) 2 O'clock Segment

Figure 6.7: Mean seal segment clearance with high rotor eccentricity.

6.3.1 Circumferential Clearance Distribution

The position of each seal segment was measured at two circumferential locations, which allows the position of the seal segment at all circumferential angles to be calculated. Previously in this chapter seal segment position has been presented only at the sensor locations. This section presents one result where the variation in the position circumferentially has been calculated, and which shows some of the intricacies not obvious in the previous sections.

Figure 6.8 shows the 12 O'clock seal segment and rotor circumferential position over a single rotation with rotor speed 1500 rpm, and pressure ratio $PR = 1.5$. The positions have been plotted at eight key moments in time. The black line is the circumferential position of the rotor surface, and the orange line is the circumferential position of the seal segment. Arrows show the movement of the seal segment and rotor in each figure. The clearance is the vertical distance between the segment and the rotor lines in the plot, and has been indicated in Fig. 6.8a. In each of the plots, the rotor is travelling from the URS to DRS side of the seal segment, which is from -30° to 30°. 0° was the top dead centre (TDC) of the rotor. The URS and DRS sensor locations are given in each of the plots.

Note that the curvature of the rotor and segment changes in Figure 6.8 as the radial position of the segment and the rotor has been 'unwrapped' onto straight axes of the plot, and is not the seal segment and rotor deforming. The methodology for calculating the seal segment position at all circumferential locations is detailed in Appendix F.

Figure 6.8a shows the seal segment and rotor position at 20.0700 s, where the segment was stationary and the rotor moving to a lower position. At 20.0750 s (Fig. 6.8b) the seal segment starts to move towards the rotor, and by 20.0800 s (Fig. 6.8c) the DRS side of the segment has reached the lowest extent, followed by the URS side of the segment at 20.0820 s (Fig. 6.8d). It was the DRS side of the seal segment that was the first to move even though there was actually larger clearance at the URS side of the segment in Fig. 6.8b.

At 20.0850 s, shown in Fig. 6.8e, the rotor was at the lowest radial position, and the seal segment is stationary, resting in the T slot. The segment remained stationary until there was a momentary rotor-segment contact at 20.0885 s (Fig. 6.8f) as the rotor is moving to a larger radial position, at which point in the time the segment starts to move away from

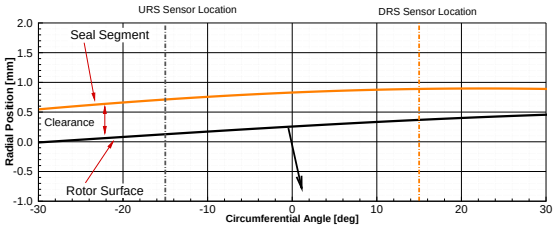

(a) t = 20.0700 s, 0% of time period, 0.55 mm mean clearance.

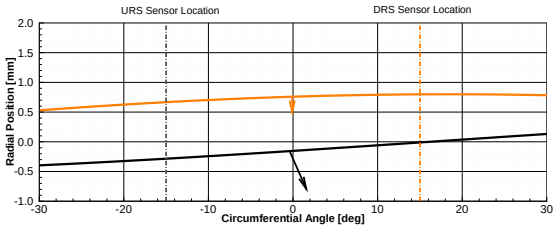

(b) t = 20.0750 s, 12.5% of time period, 0.87 mm mean clearance.

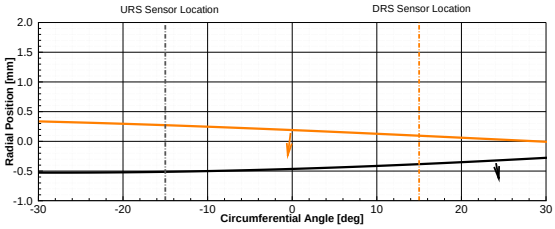

(c) t = 20.0800 s, 25% of time period, 0.62 mm mean clearance.

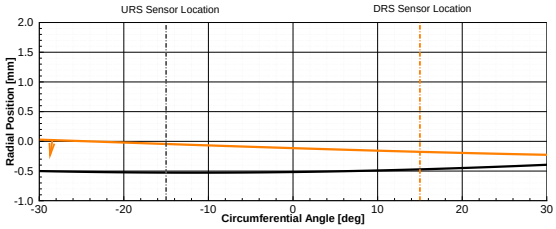

(d) t = 20.0820 s, 30% of time period 0.38 mm mean clearance.

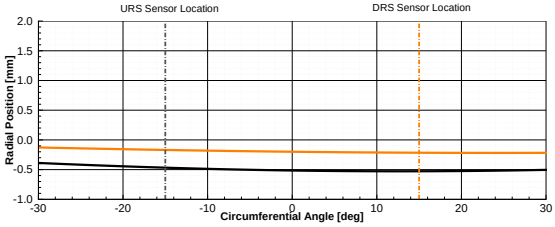

(e) t = 20.0850 s, 37.5% of time period, 0.30 mm mean clearance.

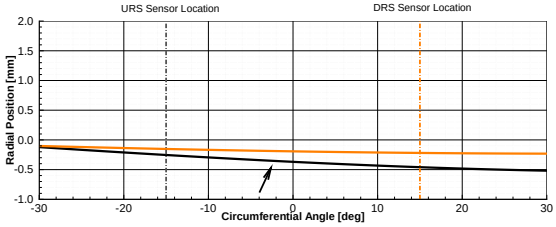

(f) t = 20.0885 s, 46.35% of time period, 0.17 mm mean clearance.

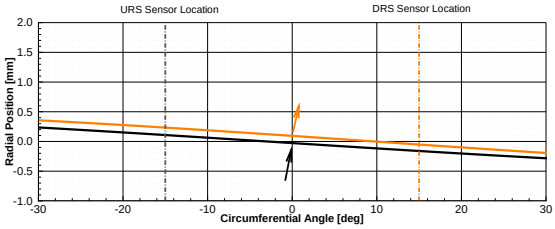

(g) t = 20.0930 s, 57.5% of time period, 0.12 mm mean clearance.

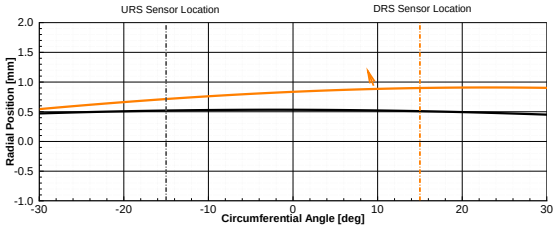

(h) t = 20.1020 s, 75.5% of time period, 0.30 mm mean clearance.

Figure 6.8: 12 O'clock seal segment circumferential clearance distribution at PR = 1.5 and rotor speed 1500 rpm.

the rotor. At 20.0930 s (Fig. 6.8g) the rotor and seal segment were travelling to a higher radial position. At 20.1020 s (Fig. 6.8h) the DRS side of the segment continued to move to a larger clearance while the URS side of the segment was stationary. The segment then remained stationary and the cycle begins again.

One of the main observations was that different sides of the seal segment move at different times, and the segment would pivot around the extreme URS side of the segment (i.e. at a circumferential angle of -30°). For example, when the segment is moving towards the rotor, in Figs. 6.8b and 6.8c, it was the DRS side of the segment which moves first, and which created an uneven clearance in Fig. 6.8c until the segment reached the lowest position allowable in the T slot.

Later on in the cycle, when the segment was moving away from the rotor, shown in Figs. 6.8f to 6.8h, there was a delay before the seal segment moved away from the rotor, which lead to a brief rotor contact, before the segment begun to move away from the rotor in Fig. 6.8g. The clearance was uniform as the segment moved away, and so while the URS pocket was at a very low clearance in Fig. 6.8f, the non-uniformity in the clearance means that the mean segment clearance was still large enough that the radial force generated was insufficient to move the segment away from the rotor without contact. Once the clearance had become uniform, the segment was able to move away from the rotor and actually accelerate away from it. In Fig. 6.8h the DRS side of the segment overshot due to the momentum of the seal segment, and so a non-uniform clearance was produced. A similar response was found when operating at lower rotor speeds down to 110 rpm. The other seal segments showed similar behaviour, i.e. brief moments of rotor contact on one side of the seal segment when the mean seal segment clearance was too large to generate sufficient force away from the rotor.

The key outcome from this section is that it is mean clearance (or seal area) that is the key parameter effecting the seal segment response. It was observed that when the seal area was large due to seal segment non-uniform clearance - i.e. one side of the segment at a low clearance than the other, that rotor contact would occur due to insufficient positive radial force to move the segment away from the rotor. The clearance of the circumferentially spaced pockets was not observed to be able to maintain a uniform clearance. Therefore further seal design optimisation is needed to correct the non-uniformity in the segment clearance, such as changing the size of the circumferen-

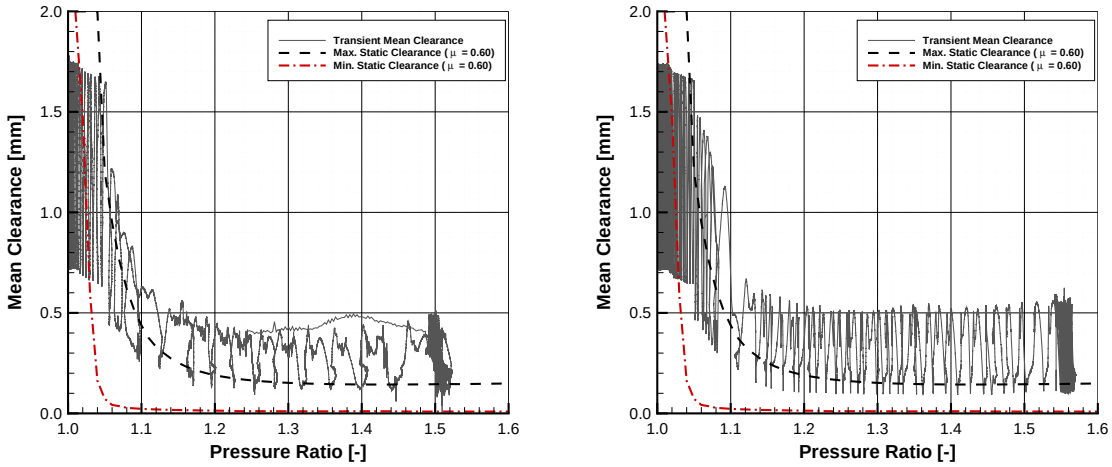

(a) 110 rpm

(b) 300 rpm

(c) 900 rpm

(d) 1500 rpm

Figure 6.9: Pressure ratio - clearance plots for the 12 O'clock seal segment.

tial pockets. Seal segment clearance non-uniformity is discussed in detail in Chapter 8.

6.3.2 Effect of Pressure Ratio

The effect of pressure ratio and rotor speed is shown in Fig. 6.9 where the mean clearance of the 12 O'clock seal segment has been plotted with pressure ratio and different rotor speeds. Figures 6.9a to 6.9d show the response at 110, 300, 900, and 1500 rpm respectively.

At a pressure ratio of $PR = 1.0$ there was no pressure difference across the seal seg-

ment and so the circumferential springs ensured that the segment was pushed to the maximum radial position. The graphs still indicate a change in clearance and this was due to the eccentricity of the rotor, which would vary the clearance even through the seal segments are stationary relative to the diaphragm. As the pressure ratio increased the range and mean clearance occupied by the seal segment reduces, with the minimum seal clearance coming to approximately $0.05\,\mathrm{mm}$. As the pressure ratio continues to increase, the measured maximum segment clearance increases in the 110 rpm rotor speed test. At higher rotor speeds, this is not apparent. At 900 rpm and 1500 rpm rotor speeds and pressure ratio in the interval $1.1 < PR < 1.2$ the minimum clearance becomes very close to the rotor and could in fact have contacted the rotor surface. This is due to the larger inertia of the seal segment at higher rotational speeds and reduced radial force due to the low pressure ratio and hence lower pressure difference.

Figure 6.9 also plots the maximum and minimum static clearances calculated analytically using the design methodology described in Chapter 3. The maximum static clearance is the largest clearance at which the seal segment would be stationary, and if the seal segment was operating at a higher clearance, then there would be a net radial force towards the rotor. The minimum static clearance is the smallest clearance at which the seal segment would be stationary. If the clearance was below this clearance then a net force would be produced away from the rotor. The maximum and minimum static clearance is discussed in more detail in Chapter 3. Plotting maximum and minimum static clearance with pressure is a useful tool in designing the Aerostatic Seal as it enables the calculation at which the seal segment will move from the retracted position to the operating position. The calculated values of the maximum and minimum static clearance are dependant on the coefficient of static friction.

The maximum and minimum static clearances have been plotted in Fig. 6.9, assuming a coefficient of static friction of $\mu_{stat} = 0.6$. Initially at low pressure ratios the seal segment is retracted, which is predicted by the analytical model. The actual retracted clearance is set up dependant and was limited by the keys between the seal segment in the experimental test. Once there was sufficient pressure difference across the seal, the clearance reduces. This was well predicted by the analytical model, as the clearance rapidly reduces when the seal segment clearance reaches the maximum static clearance line. This was the case in all of the different rotor speeds tested. The operating clear-

ance of the seal was not well predicted however, with the analytical model predicting that the operating clearance would be smaller than that measured experimentally. This is partially explained by considering that the lowest position of the seal segment was limited, and so the segment can not follow the rotor to its lowest eccentric position. I.e. the lowest position of the segment was approximately $-0.25\,\mathrm{mm}$ whereas the lowest radial position of the rotor was $-0.55\,\mathrm{mm}$. This would increase the clearance between the segment and rotor during the portion of the rotor cycle that it was at its lowest position. However the apparent minimum static clearance of the seal segment was greater than predicted. This indicates that there was more radial force away from the rotor that predicted by the analytical model.

The clearance of the 2 O'clock seal segment has also been plotted at different pressure ratios, shown in Fig. 6.10. The response is similar to the 12 O'clock seal segment, although the minimum and maximum clearances are greater due to the reduced radial gravitational force component. At low pressure ratio and high rotor speeds (1500 rpm and $1.1 < PR < 1.15$), the response of the segment is different with a significant reduction in maximum clearance, due to a fast seal velocity at high rotor speeds and a low radial force magnitude due to the low pressure ratio.

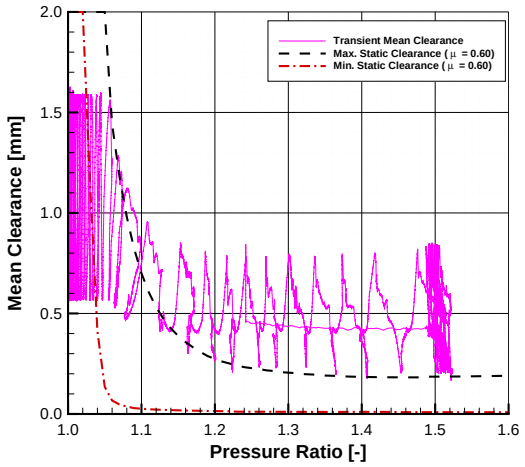

(a) 110 rpm rotor speed

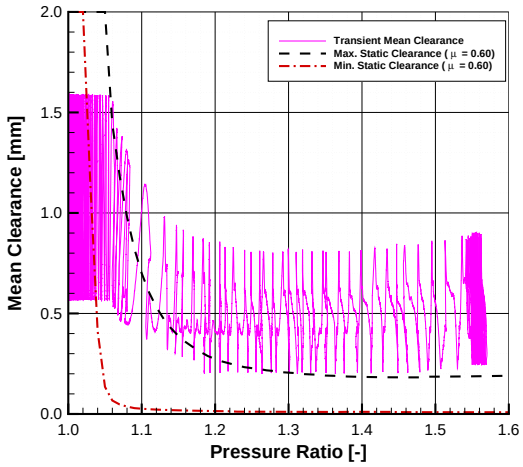

(b) 300 rpm rotor speed

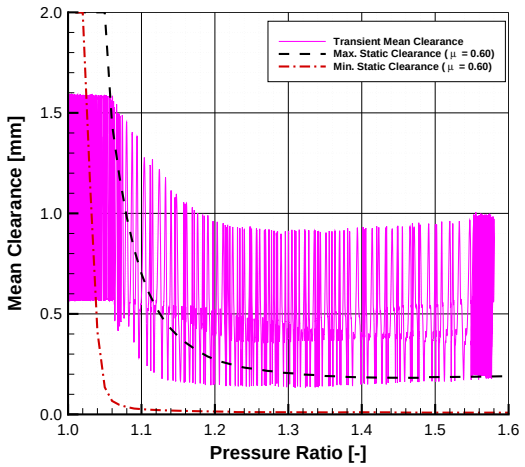

(c) 900 rpm rotor speed

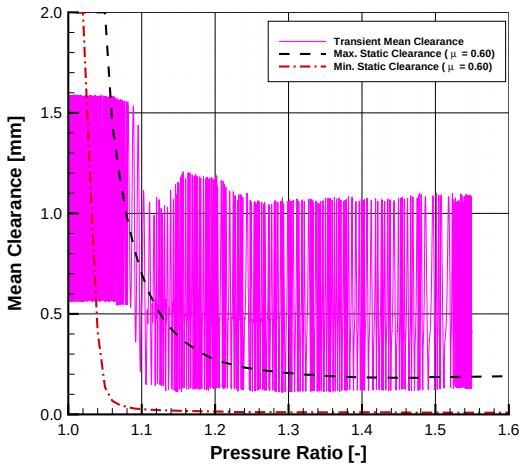

(d) 1500 rpm rotor speed

Figure 6.10: Pressure ratio - clearance plots for the 2 O'clock seal segment.

6.3.3 Seal Segment Tangential Rotation

Due to the pressure forces acting on the seal segment, there is a moment acting on the seal segment that tends to rotate the segment forward in the seal holder. See Chapter 3 for more details. The 'Durham Rotating Seal rig' was equipped with a pair of sensors that are able to detect seal segment rotation about the tangential axis of the seal segment, as described in Section 4.4. To prevent seal segment rotation, which could lead to the segment becoming jammed or a loss of positive radial pressure force, the analytical design tool checks that there is moment equilibrium over the range of seal segment clearances.

Figure 6.11 shows the typical tangential rotation of the 12 O'clock segment at 1500 rpm and with high rotor eccentricity. The response over the full test is shown in Fig. 6.11a, and the response shown over two rotor periods is shown in Fig. 6.11b. Recall that positive rotation angle ϕ is the segment tilting 'forward', shown in Fig. 6.12a, and negative tilting 'backwards', shown in Fig. 6.12b. From 5 s to about 8 s, the angle ϕ of the seal segment was 0°, shown in Fig. 6.11a, although the angle is relative to the diaphragm and so the segment is not necessarily parallel to the rotor surface. As the pressure was increased, from 7 s onwards, the seal segment tilts backwards, before stopping at an angle of $\phi = 0.2^\circ$. The seal segment than closes in around 14 s. Figure 6.11b shows greater detail during two rotations of the rotor. At the lowest *clearance* of the seal segment the tangential angle of the segment increases, indicating that the segment has tilted forward. Note that in Fig. 6.11b clearance is the difference between the segment position (solid lines) and the rotor (dashed lines).

In the set of tests reported here sensor measurements have shown that there was a small amount of segment rotation, with a maximum change in segment angle of approximately 0.16° between the retracted position and the minimum position. When retracted the seal segment is tilted such that the upstream was at a lower clearance, shown in Fig. 6.12a. At high clearance there is the greatest tendency for the seal segment to rotate forward due to the pressure moment acting on the segment. At the minimum segment position the segment is such that the upstream side is now at a slightly higher clearance, shown in Fig. 6.12b. As the angle of the seal segment is calculated from two measurements that are close together, then the uncertainty in the measurement (0.1°, see Section 4.4) is the same order as the measured angle.

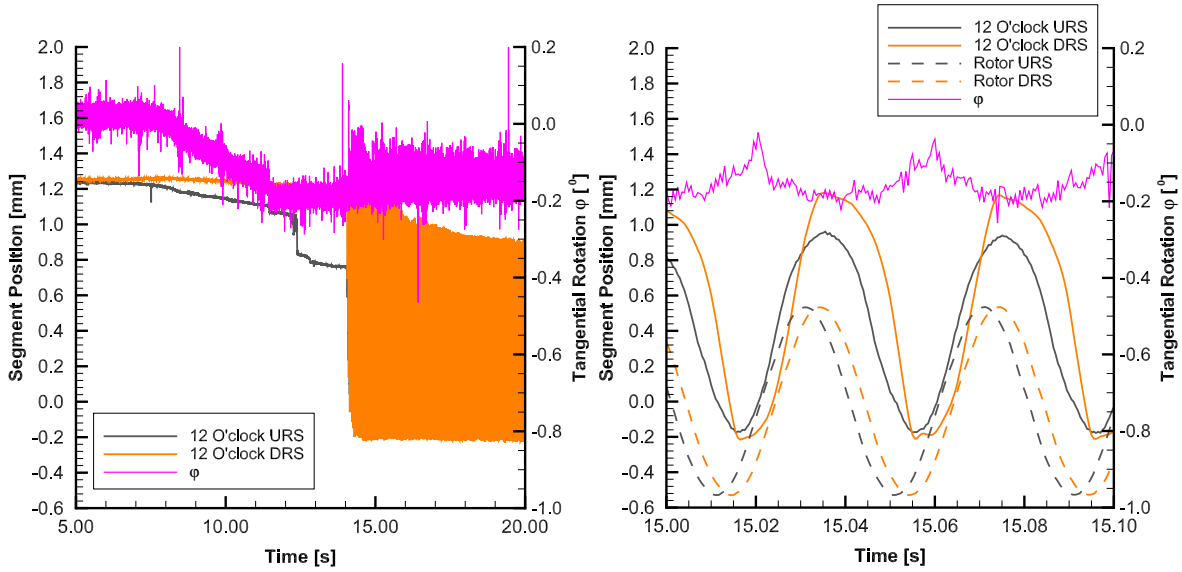

(a) Close in and operation (b) Detail

Figure 6.11: Seal segment tangential rotation during 1500 rpm and

In summary, measurements on the 12 O'clock seal segment indicate that the seal segments rotate about the tangential axis during operation. This was predicted by the analytical model as the 'ROT-02' seal design for the rotating rig was designed to maximise the seal responsiveness, and so at high clearance and high pressure moment stability would be lost, however the seal was expected to operate at low clearances in the stable operating region. The uncertainty in the the measurements was of the same order as the measured rotation, and so the exact level of segment rotation was difficult to quantify.

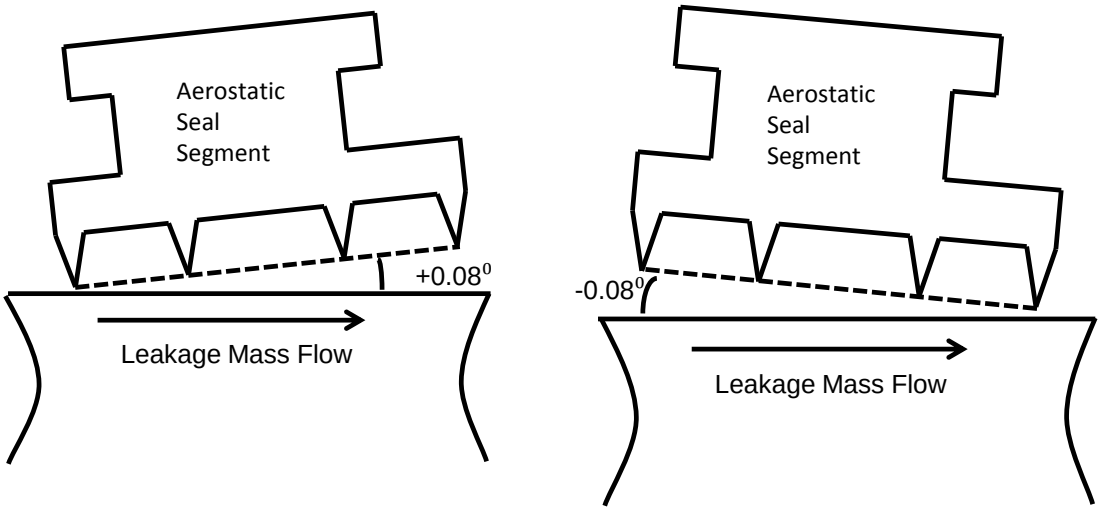

(a) Seal segment retracted (b) Seal segment lowest position

Figure 6.12: Seal segment tangential rotation, not to scale.

6.3.4 Contact Face Wear

After a number of tests in the rotating facility, wear was observed on the contact face of the seal segments. The majority of wear on the 12 O'clock segment was limited to the extremities of the contact face. Figure 6.13 shows the wear observed on the 12 O'clock seal segment and on the contact face of the seal holder. The cause of this pattern of wear is due to the distribution of contact face stress on the seal, which is due to the pressure moment acting on the seal segment. Areas of wear indicate areas of higher contact stress. This is discussed in detail in Chapter 8. Seal segments in the lower portion of the seal, such as the 6 O'clock segment shown in Fig. 6.14, show a more uniform distribution of wear. As gravity is acting in the opposite direction in the 6 O'clock seal segment, so the gravitational moment is also reversed, reducing the moment acting on the seal segment.

The level of wear shown in Figs. 6.13 and 6.14 are after approximately 1400 'cycles', with the segment moving towards and away from the rotor in one cycle. As a comparison, a steam turbine may be expected to operate up to 20 years and could go through a start up and shut down each day to meet peak electricity demand, then the number of cycles would be 7300. In reality the number of cycles would depend upon the operation

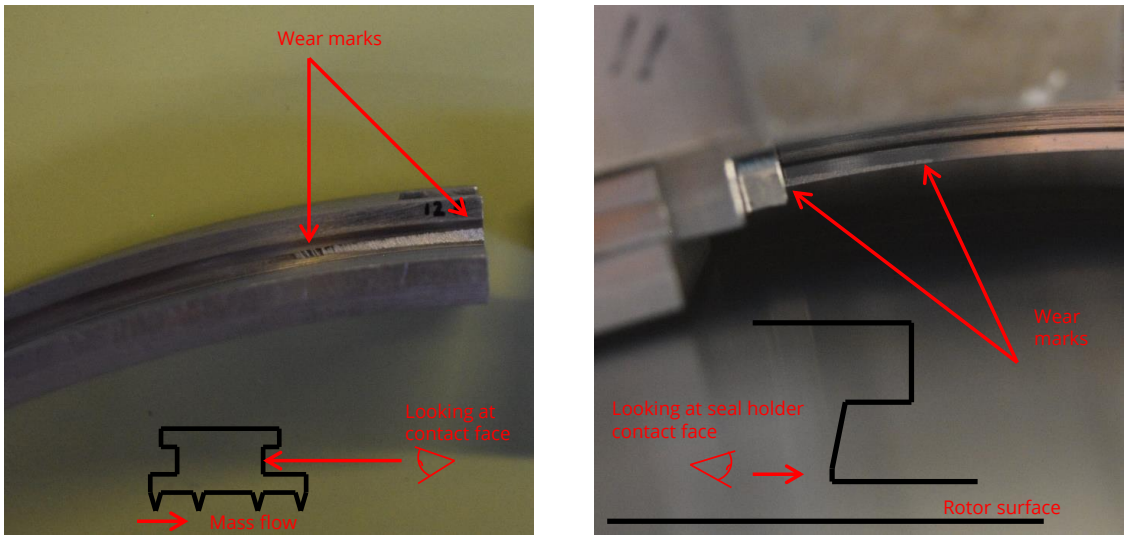

(a) Seal segment wear

(b) Seal holder wear

Figure 6.13: Wear on the 12 O'clock seal segment and seal holder contact faces.

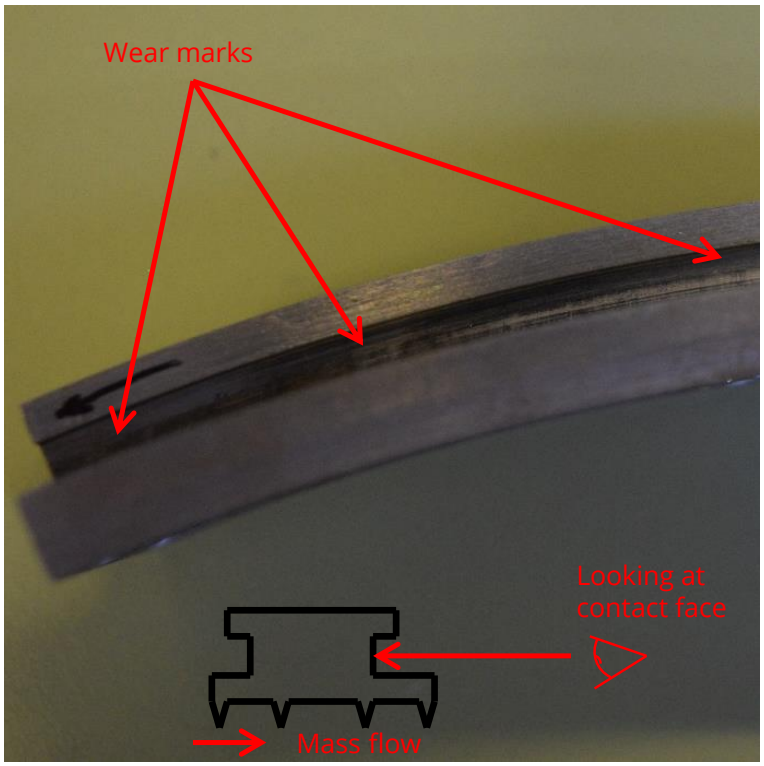

Figure 6.14: Wear on the 6 O'clock seal segment contact face.

of the turbine, maintenance intervals and other operational factors.

As the material of the Aerostatic Seal design tested is not representative of a steam turbine design, then the level of wear will not be realistic of turbine operation. Also surface treatments or coating could also be applied to reduce wear and also control friction.

6.4 Leakage Reduction

In order to assess the potential leakage reduction the Aerostatic Seal presents over a comparable labyrinth seal, the Aerostatic Seal segments were fixed in position with shims, shown in Fig. 6.15, and the feed holes covered with foil tape. The mean clearance of the whole seal, including the gaps between segments, was measured at $0.97\,\text{mm}$, and could tolerate $0.55\,\text{mm}$ eccentricity of the rotor without contact. The gap between the seal segments was 5% of the total leakage area.

Leakage mass flow rate was measured with a low rotor eccentricity at a fixed rotor speed over a range of pressure ratios and shows a substantial reduction in leakage flow compared to the fixed clearance case, shown in Fig. 6.16. Leakage mass flow measurements with fixed seal clearance was taken over a range of rotor speeds from 600 to 1500 rpm, and there was no discernible difference in leakage mass flow rate. This was confirmed by considering the ratio of Taylor number (Ta) to axial Reynolds number (Re_x). Waschka et al [91] found no effect of rotational speed on seal discharge coefficient for $Ta/Re_x < 0.2$. The maximum ratio of Ta/Re_x for the tests conducted with fixed segments was approximately $Ta/Re_x = 0.03$.

Leakage mass flow rate was measured with high rotor eccentricity at various rotor speeds from 300 to 1500 rpm. The eccentric rotor data shows that the leakage through the seal was not significantly increased due to large radial rotor excursions. At the ROT02 seal design pressure ratio of $PR = 1.5$, an approximate 35% reduction in leakage mass flow was measured.

Analytical predictions for the fixed labyrinth seal were used to add confidence to the measurements taken with the fixed seal segments, and included in Fig. 6.16. Hodkinson's model [31], which uses Martin's leakage equation [27], with a coefficient of discharge $C_d = 0.60$ gave a good match to the fixed seal leakage data. This analytical

Figure 6.15: Seal segments fixed into position with aluminium shims.

method was used to obtain a comparison of the leakage through the Aerostatic Seal to a non-segmented labyrinth seal, and has also been included in Fig. 6.16. The leakage through a labyrinth seal is proportional to the leakage area, and inversely proportional to the square root of the number of restrictions [31]. As the gaps between the segments are a single restriction, and the labyrinth seal has four restrictions, then the leakage per area through the gaps is twice that of the main seal. Therefore if the gap area is 5% of the total leakage area of the seal, then 10% of the leakage flow rate is through the gaps. Comparing the measured leakage of the Aerostatic Seal to the predicted leakage through a non-segmented seal, the leakage benefit is still approximately 30% at the design pressure ratio of $PR = 1.5$.

6.5 Discussion

The ideal operating characteristics of the Aerostatic Seal is to maintain a low clearance between the rotor and the seal. As there will inevitably be a small sub $0.1\,\mathrm{mm}$ run out

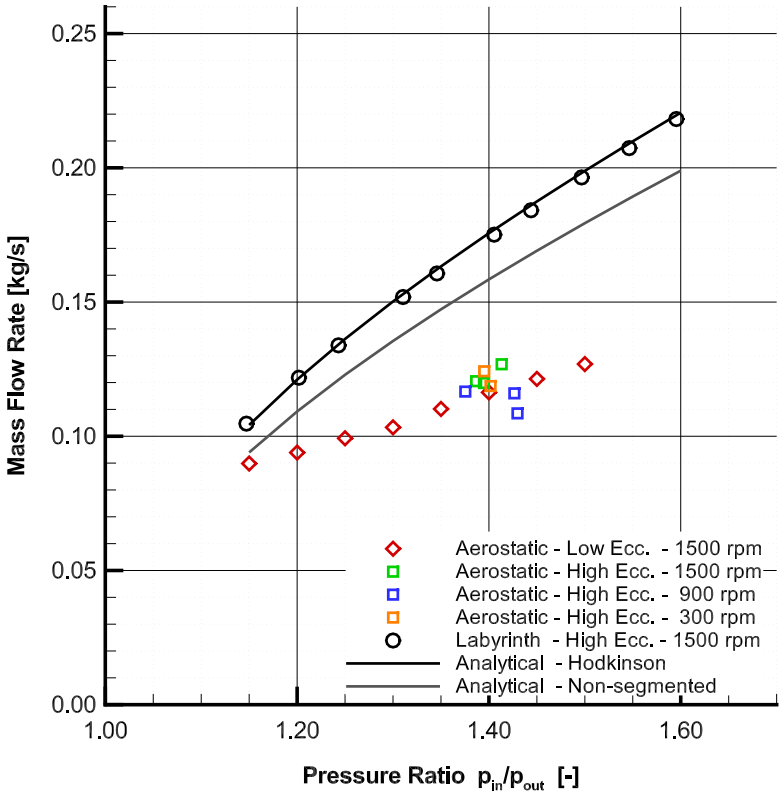

Figure 6.16: Leakage mass flow rate

on the rotor of a steam turbine, it is desirable that the seal segments do not respond to these small rotor movements to prevent excessive wear on the contact face. Only when there are large radial rotor excursions should the seal segments respond, or if thermal expansion reduced the seal clearance to an extent that there was a danger of the rotor contacting the seal.

Testing with the rotor in the low eccentricity position has demonstrated these desired operating characteristics of the Aerostatic Seal. The seal starts at a retracted position and moves to a low, static operating position. The behaviour was similar to the retractable seal (on which the Aerostatic Seal is based), although rather than setting the operating clearance with the T slot as in the retractable seal, in the Aerostatic Seal the clearance is set by the radial pressure and spring forces. The low level of eccentricity was able to excite the 12 O'clock seal segment, which operated at the lowest clearance, although this damped out after a few seconds. Seal segment circumferential location was shown to affect seal performance due to differing levels of gravitational force acting on the segment as it was found that the 10 and 2 O'clock segments operated at a higher clearance.

A series of repeated tests were conducted with the rotor in the low eccentricity position. These showed that the operating clearance was consistent over the tests for each seal segment, the range between tests less than the measurement uncertainty. It is important that the operating clearance is constant as different clearances will change the leakage through the seal, which would affect the turbine performance. The tests were conducted without re-assembling the test rig which would be expected to produce a greater change to the operating clearance by introducing or removing contaminants to the contact face, therefore changing the frictional behaviour.

Testing conducted with high rotor eccentricity has demonstrated the high speed response of the Aerostatic Seal to significant radial transients. The response of the seal to high levels of rotor eccentricity not only protects the seal segment labyrinth fins from damage, but it is also able to maintain a mean seal segment clearance that is lower than the rotor eccentricity. At low pressure ratios, the ability of the seal segments to respond to high speed rotor movements was reduced, and the mean clearance that the seal maintains increases.

The testing of the seal was conducted at a range of rotor speeds up to 1500 rpm

in the low and high rotor eccentricity position. These test indicated that the effect of rotor speed on the mean clearance of the seal segments was minimal, once the seal was operating at pressure ratios above approximately PR = 1.2. The greatest effect due to speed was between non-rotating and rotating tests, where the non rotating tests showed a larger mean clearance.

The 'Durham Rotating Seals Rig' was not designed to match steam turbine rotor surface velocity as it was half rotor diameter and half rotor speed. Therefore effects of the rotor velocity and entrained swirling flow due to the rotor are not included in the tests, however such effects are secondary to the rotor radial velocity due to rotor eccentricity. Equation (6.1) expresses the rotor radial displacement (v_r) as a function of rotor angular velocity (ω), rotor eccentricity (e) and time (t). Differentiating to get rotor radial velocity (Eq. (6.2)) and taking the maximum gives Eq. (6.3) which is only a function of rotor eccentricity and rotor angular speed. Therefore to match the peak rotor radial velocity, it is not necessary to match rotor speed and eccentricity, and so the testing described in this chapter is representative. The high rotor eccentricity setting tested here was beyond what would be expected during normal operation of the steam turbine when operating at 3000 (or 3600) rpm. Furthermore the turbine will go through the critical frequency as it is accelerating up to operating speed, and so will not be operating at 3000 rpm during the largest radial rotor excursions.

$$v_r = e\sin(\omega t) \tag{6.1}$$

$$\dot{v}_r = e\omega\cos(\omega t) \tag{6.2}$$

$$\dot{v}_{rmax} = e\omega \tag{6.3}$$

By analysing the clearance over the whole circumferential extent of the seal segments, it was found that the most important factor affecting the response of the segment was the mean segment clearance. Due to non-uniformities in the segment clearance, i.e. one side of the segment at a higher clearance than the other, and the inability of the circumferentially spaced pockets to correct this non-uniform clearance, there were short periods of time where the segment would contact the rotor because the

mean segment clearance was too high to generate sufficient radial force away from the rotor, despite one side of the segment being at a low clearance. Therefore it is required to further optimise the seal design to combat non-uniform segment clearance. Non-uniform clearance is further investigated in Chapter 8.

Upon disassembly of the seal segment after high rotor eccentricity testing, all seal segments showed wear on the contact face. As the seal will be expected to operate without maintenance for many years, this is undesirable. Hard facing materials are a possible solution to prevent wear on the contact face. It should also be borne in mind that during most of the operating life of the seal it will be stationary; the seal should only need to move during start up and shut down, or if there was some other event causing a large radial rotor excursion. As the material used to manufacture the seal segments used in these tests is not representative of steam turbine grade material, further investigation is left for testing in a steam environment.

The leakage mass flow rate assessment has shown that the Aerostatic Seal was able to reduce leakage over a similar labyrinth seal. Further improvements to the leakage performance of the Aerostatic Seal are possible by optimising the design of the seal segments for different circumferential positions (e.g. 10 O'clock, 2 O'clock segments etc.), and by reducing the mean operating clearance of the seal. These changes can be implemented by modifying the seal segment geometry, or employing different springs to alter the radial pre load on the seal segments. Further leakage reductions are possible by using steps or castellations on the rotor surface, preventing kinetic energy carry over from one cavity to the next.

6.6 Conclusion

The dynamic capabilities of the Aerostatic Seal have been conclusively demonstrated in this chapter. A campaign of testing has been conducted in the 'Durham Rotating Seals Rig' at two different rotor eccentricities to model radial rotor excursions and successful operation of the Aerostatic Seal was achieved.

The Aerostatic Seal could maintain a constant operating clearance with low levels of rotor eccentricity i.e. during normal steam turbine operation, and the measured operating clearance was found to be repeatable between different individual tests.

Tests conducted at high levels of rotor eccentricity showed that the seal was able to maintain a mean clearance lower than the level of rotor eccentricity, which is not possible with conventional non contacting seals such as labyrinth and retractable seals. There were occasional moments of rotor contact in the high rotor eccentricity testing, and this was because of one side of the segment being at a lower clearance than the other, and the pressure moment generated to correct this 'non-uniform' segment clearance was insufficient to prevent the lowest side from contacting the rotor. This was only for short periods of time during operation. The cause of this 'non-uniform' clearance is the subject of Chapter 8.

The leakage performance was measured and compared to a comparable segmented labyrinth seal by fixing the seal segments in place. This showed a potential leakage reduction of 35% at the design pressure ratio of $PR = 1.5$.

The following chapter investigates an Aerostatic Seal design variant that uses 'axial thrust compensation springs' to reduce the frictional force on the seal segment.

Due to the success of the experimental demonstration of the Aerostatic Seal, testing in steam was conducted. This is reported in Section 9.2.

Chapter 7

Axial Thrust Compensation

7.1 Introduction

It was shown analytically in Section 3.2.4 that the operating clearance of the Aerostatic Seal is sensitive to variations in friction coefficient. Many factors affect the level of friction, and in steam turbine operation may be due to wear over time, build-up of scale, and variabilities in steam quality. Also there will be a different coefficient of friction from application in the room temperature rig operating in air to high temperature rigs using realistic materials. Therefore it is desirable to be able to develop the Aerostatic Seal concept to be insensitive to variations in friction coefficient, or at least designed to operate within known limits.

One method to reduce the impact of friction on the Aerostatic Seal seal design is to reduce the reaction force. As the frictional force is proportional to reaction force, then the frictional force is reduced. At lower levels of frictional force the operating clearance is less sensitive to changes in friction.

The GenⅡ Aerostatic Seal design included 'axial thrust compensation' springs to reduce the reaction force from the contact face. The axial springs are positioned behind the seal segment and exert an axial force to counteract some of the axial pressure force and hence reducing the reaction force and thereby reducing the frictional force.

To test this concept the non-rotating rig was updated to include provision for axial thrust compensation springs, as described in Section 4.3.

The aim of the testing was to address the following questions:

1. Is the axial thrust compensation concept viable? Will the seal still work with the addition of axial thrust compensation springs?

2. Assuming that the concept is viable, what is the level of performance gain? It was expected that reducing the frictional forces acting on the seal segment will make it more responsive, and would translate into a reduction in the operating clearance of the seal.

3. What are the limits of operation? It is important to understand how much axial thrust can be applied before undesirable seal behaviour is observed.

7.2 Seal Design

The seal design, designated 'MESS04', was manufactured from the existing 'MESS01' design. The design included 4 lands for mounting axial thrust springs. It was possible to revert to seal design 'MESS01' by simply omitting the axial springs. Four axial thrust springs were installed, and were distributed about the centroid of the seal segment, as shown in Fig. 7.1. There were a limited number of axial spring locations possible due to the positioning of the rear capacitance sensors in the non-rotating rig. Therefore the axial thrust was adjusted to ensure no overall moment was applied to the seal segment when the axial springs were compressed. When the seal was retracted, and with a low pressure difference across the seal segment, the axial springs pushed the segment against the front face of the T slot, as shown in Fig. 7.2. Note that when the seal was pushed against the front face, the pressure on the outer surface of the segment becomes outlet pressure. This is important for the analysis of the results later on in this chapter.

As described in Chapter 3, the analytical tool was able to model seal designs with axial springs installed.

7.3 Experimental Procedure

The experimental procedure was similar to Gen I seal testing described in the Chapters 5 and 6. Testing was conducted over 50 s, starting with zero applied pressure, increasing

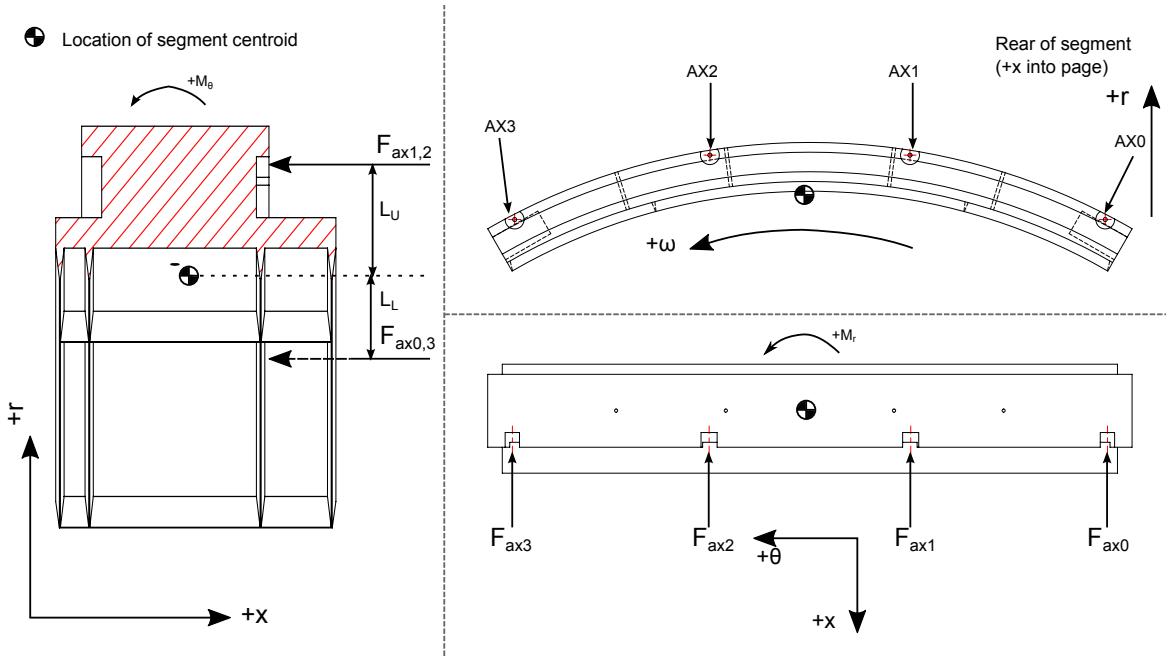

Figure 7.1: Axial spring location (denoted by AX0 - AX3), relative to seal segment centroid.

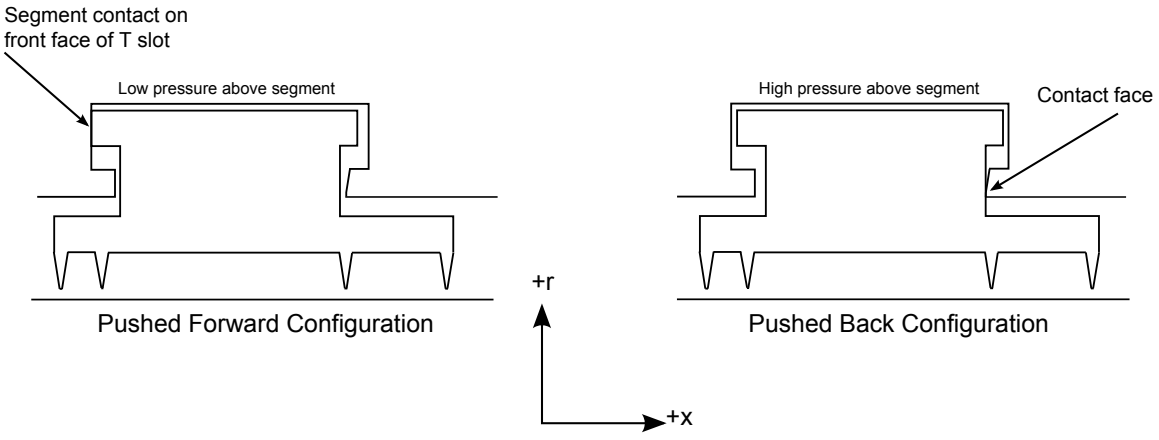

Figure 7.2: Seal segment axial position.

the pressure to a set point (dependant on the particular test undertaken), and then decreasing the pressure to zero. Typically the increase in pressure causes the seal segment to 'close' towards the rotor surface and operate at a set clearance (termed the 'operating clearance'), and decreasing the pressure beyond a certain value causes the seal segment to 'retract' or move back to the original clearance. Four load cells were mounted externally to the test rig and connected to the axial springs via the 'axial spring push rod' to measure the applied axial thrust from each of the axial springs, shown in Fig. 4.5. As the load cells were external, they could not be used when operating with back pressure as they would prevent the back pressure flange being attached to the rig. For full details regarding the non-rotating rig and the instrumentation set up, refer to Section 4.3. The rest of this section details the methodology unique to testing the axial thrust compensated seal design.

In order to ensure that the seal segment does not contact the side walls of the rig during operation, the side walls have been moved outwards by $0.5\,\mathrm{mm}$ using shims. As this opens up a small gap between side components and the seal holder, the air escaping the rig by not passing through the seal was increased. This leakage was quantified with the back pressure valve fully shut and the flow rate measured. This leakage was found to be significant at high pressure, and proportional to the pressure applied to the rig. A correction factor based on inlet and outlet pressure was used to account for the extra leakage.

The pressure readings taken during the following tests included the side pressure taps. As there were a limited number of pressure channels available on the pressure scanners, the central pockets taps were connected together, as shown in Fig. 7.3. Also note that the same nomenclature in Chapters 5 and 6 has been used to describe the seal, such as 'URS' and 'DRS'. See Fig. 5.2 for a full description.

As the 'axial spring push rod' (see Fig. 4.5) was acted on by the pressure on top of the seal segment, there will be a pressure force acting on the push rod in addition to the spring force. Therefore the measured force was corrected to just give the force applied by the axial springs.

All tests results reported here using the axial thrust compensated design have been conducted without reassembly of the rig between tests.

The test matrix is shown in Table 7.1. The symbol 'X' indicates a chosen test point. A

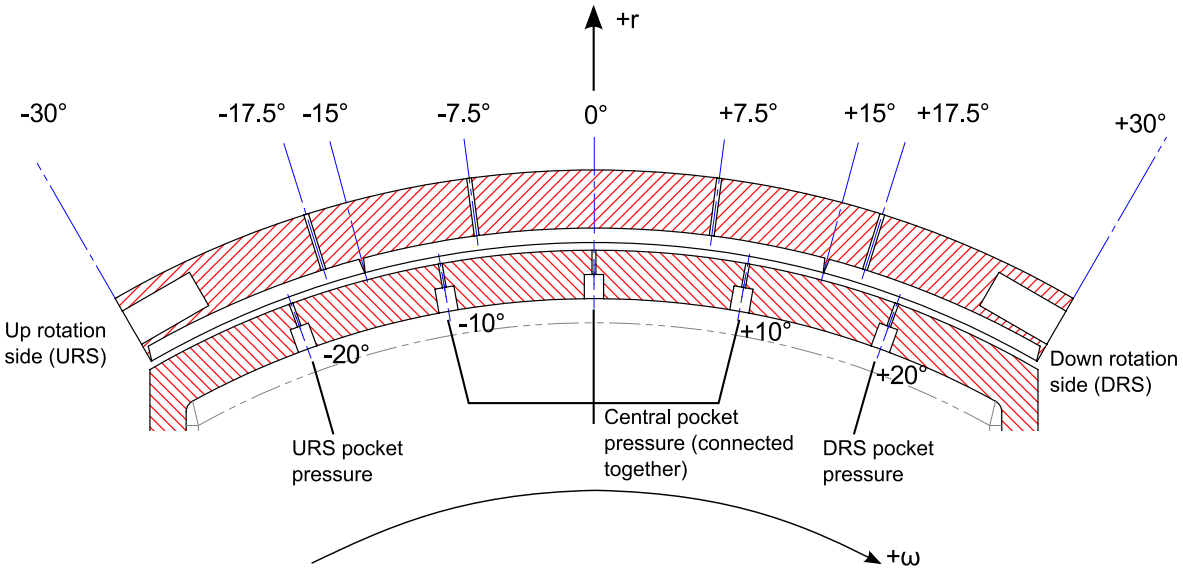

Figure 7.3: Circumferential pressure tap positions and connections.

Nominal F_{ax} N	k_{ax} N mm^{-1}	Atmospheric outlet pressure	3.0 bar(a) inlet pressure	6.0 bar(a) inlet pressure
0	N/A	X	X	X
40	2.03	X		
60	2.03	X		
60	5.28	X	X	X
70	5.28	X		
80	5.28	X		
100	5.28	X		
100	15.0	X	X	X
200	15.0	X		

Table 7.1: Test matrix: axial thrust compensated design

full sweep of axial thrust settings was performed with atmospheric back pressure, from no axial thrust up to 200 N. Three different axial thrust springs of different stiffness were used to be able to achieve the different axial thrusts. Two tests were performed with the same axial thrust setting but with different axial spring stiffness to assess the impact of axial spring stiffness. For full details of the axial springs used see Appendix D.

Tests were also carried out with increased levels of back pressure for 0 N, 60 N and 100 N axial thrust. In these tests the inlet pressure remained fixed at 3.0 bar(a) and 6.0 bar(a), and the outlet pressure was varied to achieve different pressures across the seal segment.

7.3.1 Atmospheric back pressure testing

The outlet 'flange' was removed completely if operating with load cells. When operating with normal axial spring holders (i.e. for back pressure testing) a test was conducted with the outlet flange in position but with the back pressure valve fully open. The aim of doing this was to check that the axial springs gave a similar performance to testing when the axial thrust was measured, and hence were applying a similar level of thrust.

The seal design 'MESS01' (on which the design 'MESS04' is based) was not designed for operating at atmospheric back pressure, and so the performance without back pressure was not as good as with back pressure. Furthermore the starting position of the seal segment was lowered to enable assembly with the axial springs, which increased the frictional force acting on the seal segment, degrading performance of the seal compared to the results reported in the previous chapter.

7.3.2 Back pressure testing

When operating with back pressure, the inlet pressure was nominally fixed by using the blow down rig pressure control valve (see Fig. 4.3), and $3.0\,\mathrm{bar(a)}$ and $6.0\,\mathrm{bar(a)}$ have been chosen as two operating points. The outlet pressure valve was initially almost closed, giving a small pressure drop across the seal. The back pressure valve was then manually opened to increase the pressure drop across the seal until the seal moved to the operating clearance and closed again until the seal segment retracted. The bypass helped to make the inlet pressure easier to control when the seal segment moved to the operating clearance.

7.4 Results

One of the key parameters of the Aerostatic Seal was the operating clearance, i.e. the clearance of the seal after it had closed in. The operating clearance has been used to characterise the Aerostatic Seal response to the different axial thrust levels tested. The operating clearance of each side of the seal segment is plotted in Fig. 7.4 for a range of axial thrusts. Figure 7.4a shows the operating clearance for tests conducted with atmospheric back pressure, and Fig. 7.4b the operating clearance with $6.0\,\mathrm{bar(a)}$ inlet

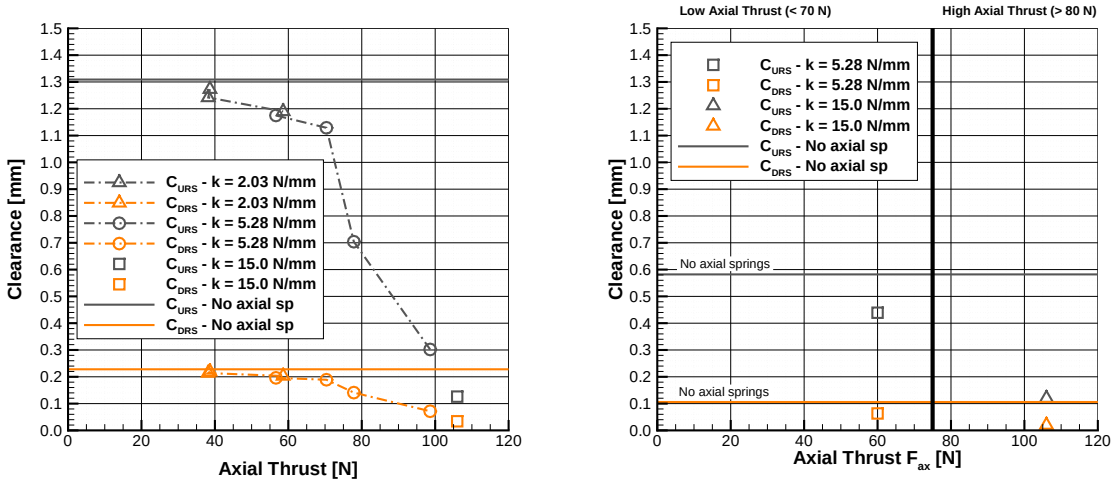

(a) Atmospheric outlet pressure

(b) 6.0 bar (a) inlet pressure

Figure 7.4: Seal operating clearance variation with axial thrust.

pressure. The test case when there were no axial springs is shown as a horizontal line for the clearance measured with the URS and DRS capacitance sensors. Different symbols are used to identify different axial string stiffness. It is clearly shown that increasing the axial thrust decreases the operating clearance of the seal segment. Up to and including 70 N of axial thrust the reduction in operating clearance was reasonably small, and at axial thrust greater than 70 N the reduction was much greater. This allows the response of the seal to be categorised into two operating regimes: 'low axial thrust', below 70 N, and 'high axial thrust', above 70 N.

Figures 7.4a and 7.4b clearly show that the seal segment still operates at an non-uniform clearance, as found in the previous chapters, i.e. the DRS side of the segment operates at a lower clearance than the URS side of the segment. Another important point is that there was virtually no difference between operating clearance for the same axial thrust and different axial spring stiffness.

This categorisation was also apparent observing the mass flow rate of air through the seal, which is shown in Fig. 7.5. The mass flow rate is presented with atmospheric outlet pressure and at a pressure ratio of $PR = 1.5$. This clearly shows the benefit of the axial thrust compensated design at reducing the mass flow rate through the seal.

There was also a difference in the seal response before reaching the operating clearance. This is not apparent in Figs. 7.4 and 7.5, but will be shown in detail in the following

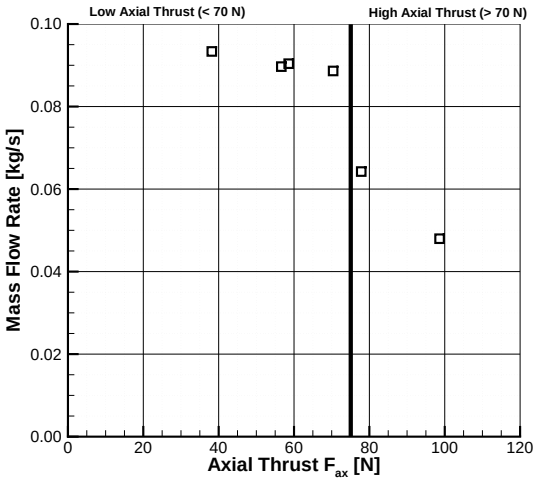

Figure 7.5: Mass flow rate variation with axial thrust, $PR = 1.5$, atmospheric back pressure.

sections. The response of the low operating regime was similar to the tests presented in Chapter 5 where the segment would transition from the retracted position to the operating clearance without contacting the rotor. In the high axial thrust regime the seal segment would contact the rotor when the pressure difference across the seal was low, before the segment would move away again and maintain a constant operating clearance. The exact pressure difference at which the segment would stop contacting the rotor and transition back to the operating clearance depended on the axial thrust applied.

Observing the dynamic performance of the seal as it transitioned from the retracted clearance to the operating clearance also allowed the identification of a further two axial thrust operating regimes. At axial thrust levels around 200 N there was the 'very high' axial thrust regime. Here there was an extended amount of time at which the seal segment would be in contact with the rotor. A final operating regime, termed 'pressure activated chatter', was discovered when the axial springs were not set up to balance the applied moment to the segment as intended. This resulted in a vibrational seal segment response as it transitioned from the retracted clearance to the operating clearance.

In summary, the use of axial springs reduced the operating clearance of the Aerostatic Seal. Further, it was found that there are four basic operating regimes:

- 'Low' levels of axial thrust, below approximately 70 N, where there is a small reduc-

tion on mean operating clearance.

- 'High' levels of axial thrust, greater than 70 N, giving a significant reduction in operating clearance. In the high level regime the seal segment will contact the rotor surface at low pressures. This is not evident in Fig. 7.4 or Fig. 7.5, but is evident in results presented in Section 7.4.2.

- 'Very high' levels of axial thrust, around 200 N, where there is a prolonged period of time where the seal segment is in contact with the rotor surface. This is an extension of the 'high' axial thrust regime.

- Vibratory response, termed 'pressure activated chatter' where the seal segment repeatedly contacts the rotor surface. This has typically been seen at axial thrust levels in the 'high' regime and when the applied moment due to the axial thrust was not correctly balanced about the segment centroid.

The rest of this section analyses each of these operating regimes in detail, and a final test which was conducted with the minimum clearance of the segment limited. The purpose of this final test was to investigate if dynamic movement of the seal could be achieved successfully with high levels of axial thrust and without rotor contact. For a table summarising the full set of results, see Appendix C.

7.4.1 'Low' axial thrust regime

As discussed previously, the 'Low' axial thrust response was characterised by a small decrease in the operating clearance of the seal segment, compared to the no axial spring case. As with the case with no axial springs present, the seal segment did not contact the rotor surface as in the 'high', 'very high' and 'vibrational' axial spring operating regimes.

To demonstrate the operational characteristics of the 'low' operating regime, Fig. 7.6 shows the 'close in' and 'retraction' behaviour of the seal segment of 60 N axial thrust, atmospheric back pressure, and with axial spring stiffness $k_{ax} = 5.28\,\mathrm{N\,mm^{-1}}$. During the test the pressure was slowly increased and decreased over 50 s, and the seal segment closed in on the rotor once sufficient pressure difference across the segment was present, and retracted once the pressure difference had sufficiently dropped. Figures 7.6a and 7.6b show the seal segment clearance during 'close in' and 'retraction'

respectively. The axial spring force measured by the load cells during close in and retraction is shown in Figs. 7.6c and 7.6d, and the pressure coefficient (defined as before, see Eq. (3.1)) during close in and retraction is shown in Figs. 7.6e and 7.6f. The close in and retraction behaviour will be discussed in turn.

Close in

Initially the seal segment was retracted and pushed against the front face of the T slot (as shown in Fig. 7.2). This can be observed in Fig. 7.6e as before 11.5 s the pressure on top of the seal segment was close to outlet pressure. Once the segment was pushed against the rear contact face the pressure on top of the segment was equal to inlet pressure. Note that the calculation of pressure coefficient had the effect of amplifying any noise on the pressure signal, especially when the pressure difference is small, such as when the segment was retracted.

As the pressure difference across the seal segment increased, the axial thrust measured by the load cells and the pressure coefficient on the upper surface of the segment also increased. This is shown in Figs. 7.6c and 7.6e respectively between 11.0 and 11.6 s, and is labelled with **'A'** on Fig. 7.6. The force measured by the load cells increased due to the seal segment being pushed backwards onto the contact face, as so the top surface of the segment was pressurised with fluid from the inlet to the seal, increasing the pressure in the top surface. As the top pressure coefficient has not increased to a value close to 1.0, and as the axial force has mostly increased in springs AX0 and AX3 which are below the seal segment centroid, then the seal segment was in a tilted forward configuration. This is further demonstrated by the seal pressure coefficients Cp_1, Cp_2 and Cp_3 which reduce between 11.0 and 11.6 s. The region labelled **'A'**, between 11.0 and 11.6 s, is termed 'pre close'. After the 'pre close', at 11.6 s, the seal segment moved down towards the rotor and was pushed back towards the contact face, indicated by the increase in AX1 and AX2 axial spring force and increase in pressure coefficient.

It was the behaviour of the seal segment during 'pre close' that is important for understanding if the segment operates in the 'low' or 'high' axial thrust operating regimes. Crucially, in the low operating regime, the seal segment has not tilted forward enough that the seal segment moves towards the rotor immediately, and that when the seal segment did move towards the rotor there was sufficient positive radial force to prevent

the segment contacting the rotor surface.

Retraction

The clearance, axial force and pressure coefficient of the seal during retraction are shown in Figs. 7.6b, 7.6d and 7.6f. The retraction sequence is similar to the 'close in' sequence, but in reverse. The seal segment begins to retract at 43.5 s and was accompanied by a reduction in pressure underneath the seal segment between 43.5 and 44.0 s. There was a slight reduction in the AX1 axial force, and a reduction in the top pressure coefficient Cp_t, which would indicate that the segment was tilting forward slightly. Between 43.5 and 44.0 s it was the C_{URS} side of the segment that retracts, and then at 44.0 s the segment retracts fully. At this point only the DRS side of the segment was pushed forwards by the axial springs. This was indicated by the AX2 and AX3 axial force reducing at 44.0 s and the AX0 and AX1 forces, which are on the URS side of the segment. The segment was fully pushed forward at 45.6 s.

Summary

This section has described a typical test in the 'low' axial thrust operating regime. The key finding was the existence of a new intermediate position of the seal segment between the segment being retracted and at the operating clearance. This new position has been termed *'pre close'*. Figure 7.7 shows the close in sequence. Initially the seal segment was retracted (Fig. 7.7a), before the 'pre close' phase (Fig. 7.7b). The segment then closes in (Fig. 7.7c) and then stops at the operating clearance (Fig. 7.7d). This sequence of events also applies in the other operating regimes. During the pre closed phase the seal segment was tilted forward, and which reduces the pressure below the seal segment, reducing the radial force. This reduced radial force was responsible for the reduction in operating clearance observed in the low axial thrust operating regime.

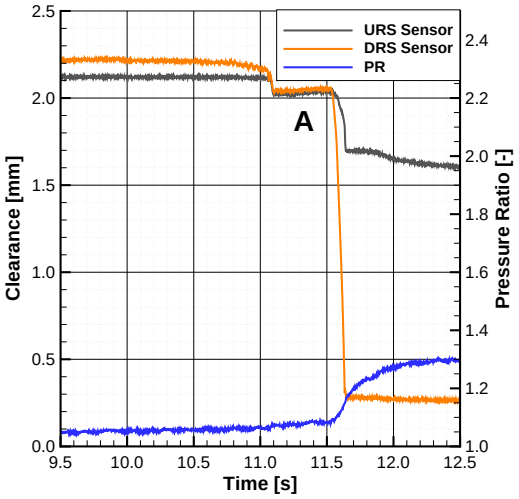

(a) Seal segment clearance: close in

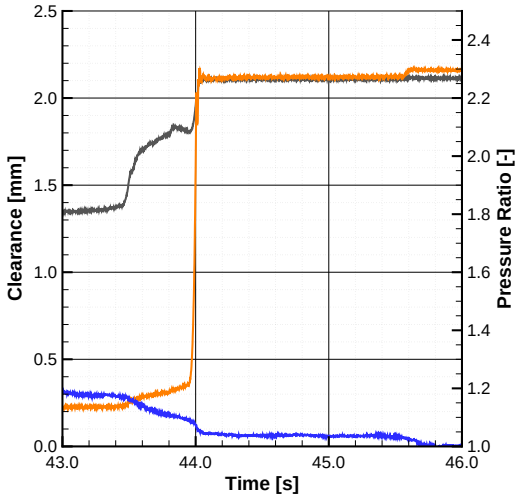

(b) Seal segment clearance: Retraction

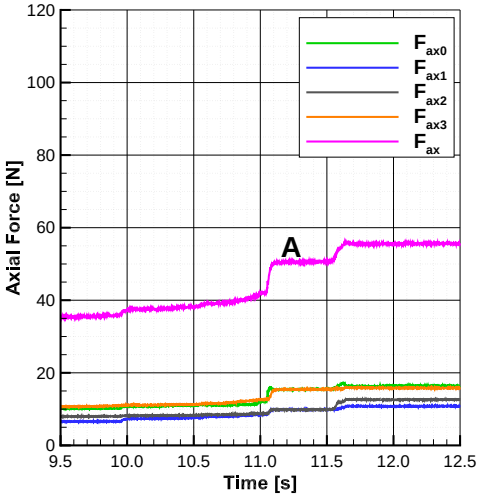

(c) Axial thrust: Close in

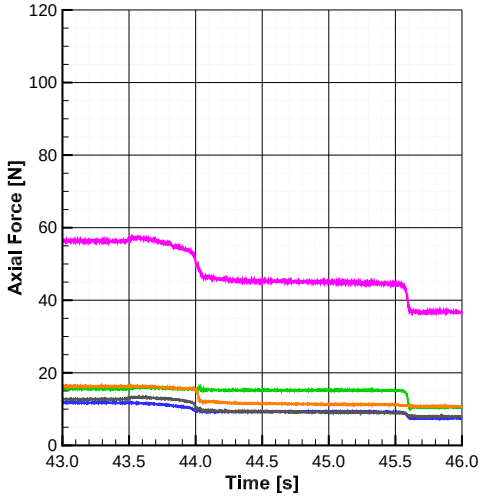

(d) Axial thrust: Retraction

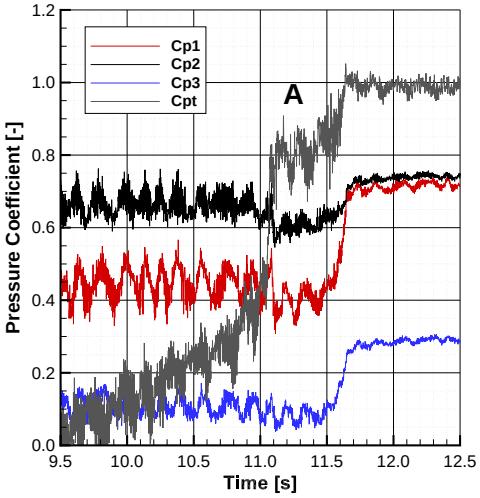

(e) Pressure coefficient: close in

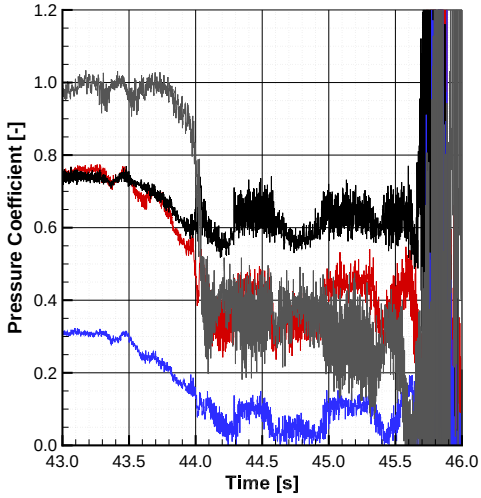

(f) Pressure coefficient: retraction

Figure 7.6: Typical low axial thrust response: nominal $F_{ax} = 60\,\text{N}$, $k_{ax} = 5.28\,\text{N}\,\text{mm}^{-1}$.

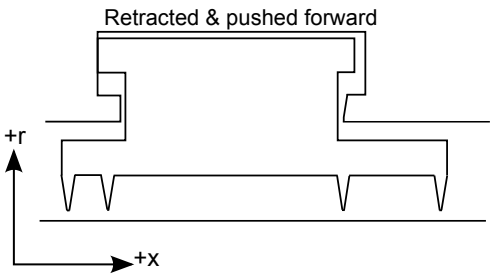

(a) Retracted and pushed forward.

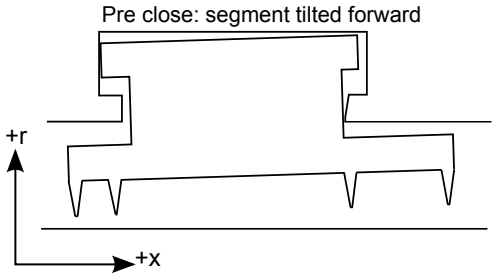

(b) Pre close: segment tilted forward.

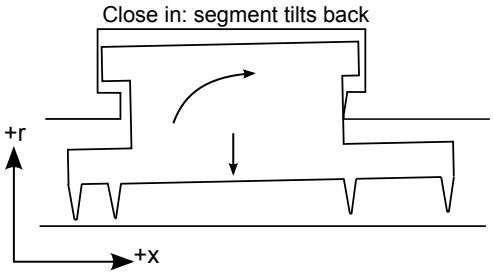

(c) Segment tilts back and closes in.

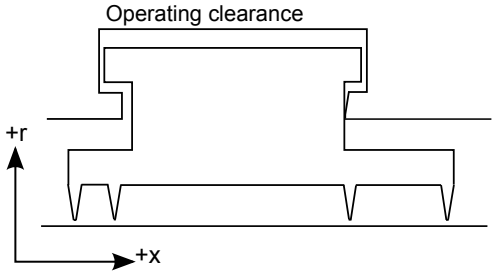

(d) Segment at operating clearance.

Figure 7.7: Generic close in sequence with axial thrust compensation

7.4.2 'High' axial thrust regime

Figures 7.8 and 7.9 show a typical result in the 'High' axial thrust operating regime, operating with total applied axial thrust of $98.6\,\mathrm{N}$ and axial spring stiffness of $5.28\,\mathrm{N\,mm^{-1}}$. Figures 7.8a, 7.8c and 7.8e show the seal segment clearance, axial spring thrust and pressure coefficient respectively, as the segment closes towards the rotor. Figures 7.8b, 7.8d and 7.8f shows the segment clearance, axial spring thrust and pressure coefficient in more detail. Figure 7.9 shows the seal segment retracting.

Immediately obvious from inspection of Fig. 7.8b is that the segment briefly touches the rotor surface on the DRS side of the segment before the clearance increases and an operating clearance is maintained. Operating clearance was much improved over the 'low' axial thrust operating regime.

As the pressure difference across the seal segment reduces towards the end of the test, seen in Fig. 7.9, the segment clearance reduced, and when the pressure difference was between $0.17\,\mathrm{bar}$ and $0.10\,\mathrm{bar}$ the seal segment lost lift and contacted the rotor surface all the way around the seal circumference. When the pressure difference was below $0.10\,\mathrm{bar}$, the segment retracted.

Close in

Initially the seal segment was retracted and pushed forward from the contact face by the axial springs. At 11.5 s the segment rotated forward about the tangential axis, indicated by the increase in F_{ax0} and F_{ax3} in Fig. 7.8c. Also the pressure coefficient above the seal segment Cp_t increased (Fig. 7.8e) indicating that less air was leaking through the contact face. This was the beginning of the 'pre close' phase.

At 12.5 s the DRS side of the seal segment started to move towards the rotor while the segment was rotated forward, seen in Fig. 7.8a. The URS side of the seal segment started to move down as AX1 and AX2 were compressed, indicating that the URS side of the segment closed in as it was pushed onto the contact face. In Fig. 7.8f there was a pronounced spike in the pressure above the seal segment (peak at 12.79 s), followed by a spike and then dip in the pocket pressure (P_2) around 12.80 s, caused by the decrease in contact face leakage as the segment was pushed back against the contact face. The spike in pressure on top of the segment increased the force towards the rotor surface leading to the segment touching the rotor on the DRS side of the segment, before the pressure underneath the seal segment increased sufficiently to move the seal segment away from the rotor again.

Retraction

Figure 7.9 shows the behaviour of the seal segment before and during retraction. Before the seal segment retracted, F_{ax1} and F_{ax2}, seen in Fig. 7.9b, have reduced compared to the initial axial thrust after 'close' (Fig. 7.8d), dropping from about 22.5 N to 20 N. This indicates that the seal segment is tilting forwards. The pressure coefficient above the segment (seen in Fig. 7.9c) also reduces slightly, again indicating that the segment is tilting forward and entering a 'pre retraction' phase. There was no reduction in the F_{ax1} and F_{ax2} thrust measurements, but as the segment was operating very close to the rotor surface any change in angle will have a more significant effect on the pressure distribution than at a higher clearance.

At 40.4 s the segment lost further radial force (see Figs. 7.9a and 7.9c) and fully contacted the rotor. Until 42.2 s the pressure difference across the seal segment was enough to keep the axial springs mostly compressed (there is an approximate 4 N drop in total).

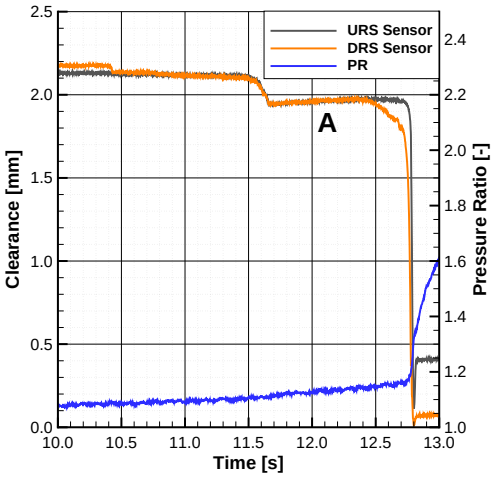

(a) Seal segment clearance: close in

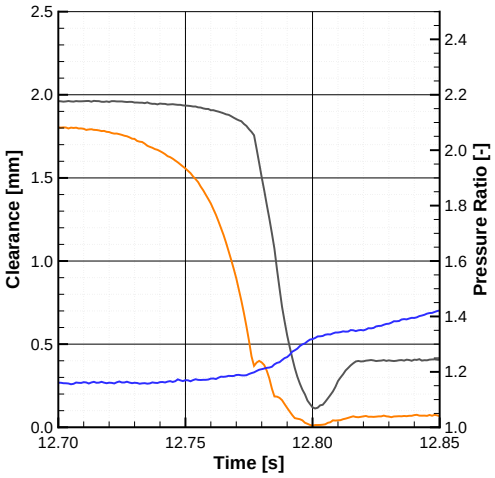

(b) Seal segment clearance: Detail

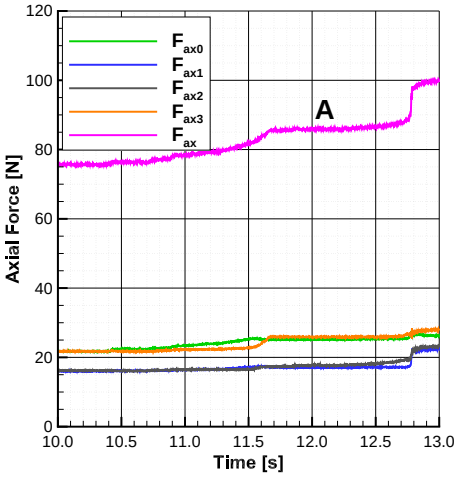

(c) Axial thrust: Close in

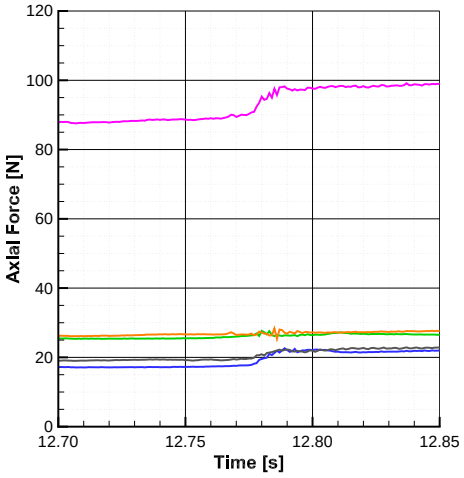

(d) Axial thrust: Detail

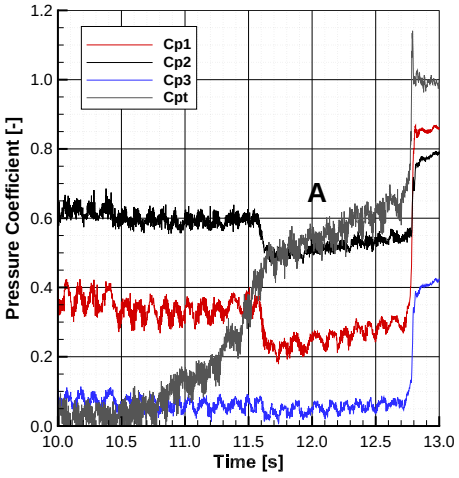

(e) Pressure coefficient: close in

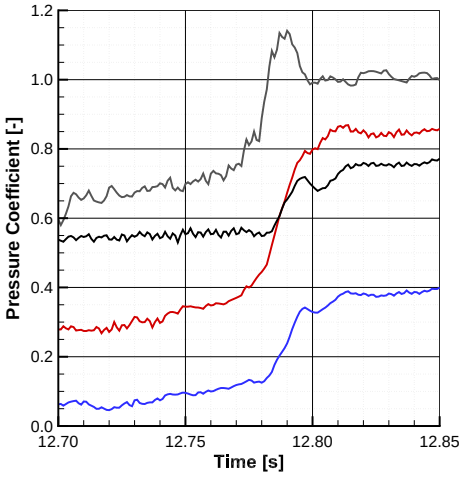

(f) Pressure coefficient: Detail

Figure 7.8: Typical 'high' axial thrust response during close in: nominal $F_{ax} = 100$ N, $k_{ax} = 5.28$ N mm^{-1}.

	Cp_1	Cp_2	Cp_3	Cp_t
'Low regime	0.35	0.58	0.05	0.80
'High regime'	0.24	0.50	0.05	0.49

Table 7.2: Comparison of pressure coefficient at beginning of pre-close phase: 'low' and 'high' operating regime

The seal segment retracted at 42.2 s and the axial springs decompressed, pushing the segment towards the front face of the T slot.

Summary

The 'pre close' and 'pre retraction' phases are important to understand why the behaviour of the seal segment has changed between the 'low' and 'high' axial thrust operating regimes. Table 7.2 shows the pressure coefficients at the beginning of the 'pre close' phase for the presented 'low' and 'high' operating regimes, and indicates that the seal segment was tilted forward more when in the high operating regime. The evidence is the lower pressure coefficients of the 'high' regime in Table 7.2. It is therefore concluded that it is tilting forward which causes the reduced clearance with increasing axial thrust, and led to rotor contact in the 'high' operating regime.

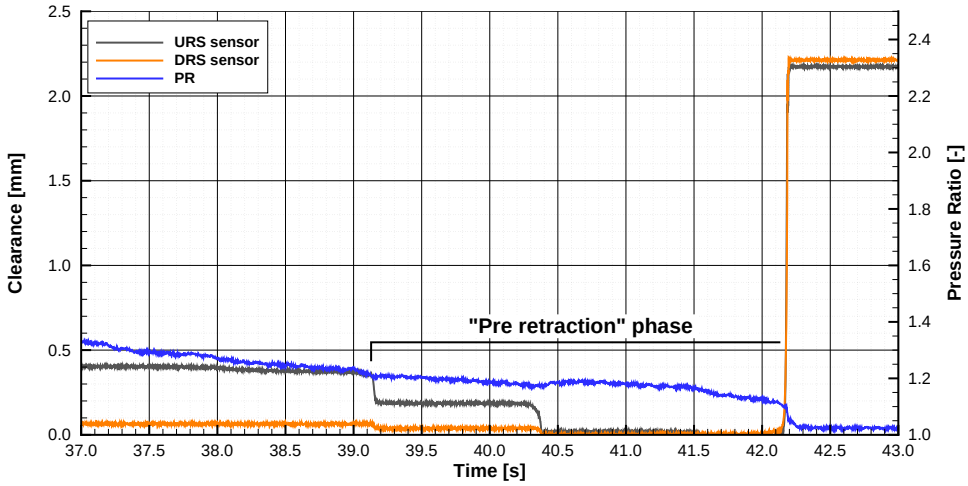

(a) Seal segment clearance

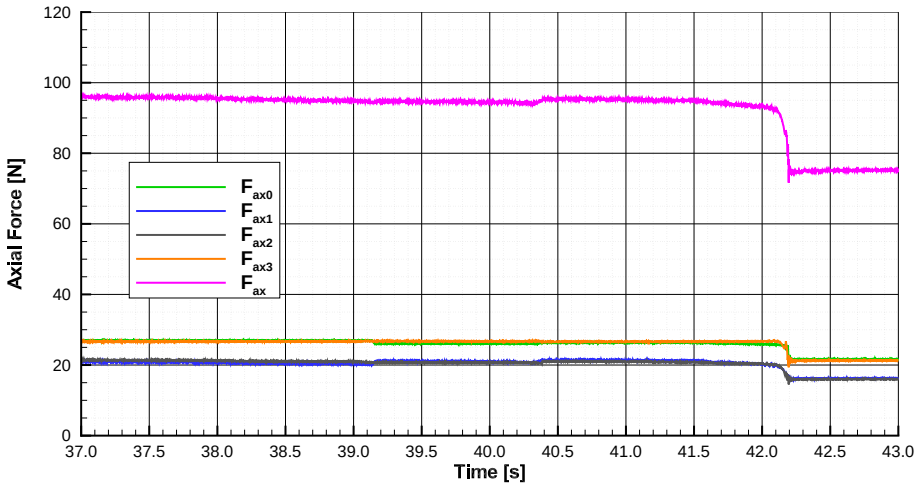

(b) Axial Thrust

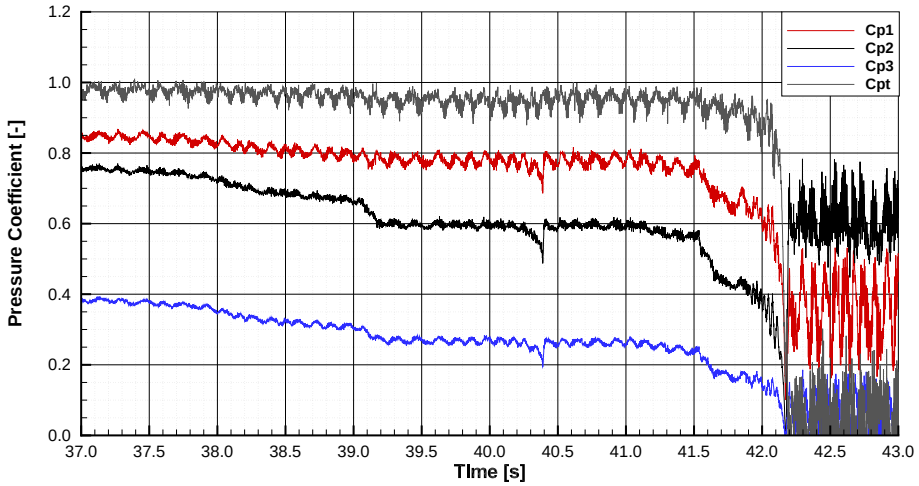

(c) Pressure coefficient

Figure 7.9: Typical 'high' axial thrust response during retraction: Nominal $F_{ax} = 100\,\mathrm{N}$, $k_{ax} = 5.28\,\mathrm{N\,mm^{-1}}$.

7.4.3 'Very high' axial thrust regime

The close in response of the seal segment to 'very high' levels of axial thrust is shown in Fig. 7.10. The axial thrust was increased to $F_{ax} = 204$ N. Figures 7.10a, 7.10c and 7.10e show the clearance, measured axial thrust and pressure coefficient respectively as the seal segment closes onto the rotor. Segment retraction is not shown but was similar to the 'high' axial thrust operating regime. Figures 7.10b, 7.10d and 7.10f show greater detail as the segment first closes. As shown in Fig. 7.10a, there was a significant period of time at which the seal segment was in contact with the rotor surface. As the pressure difference across the seal increases the clearance gradually increases until the operating clearance was achieved at approximately 34.8 s. 'Close in' occurred at a much increased pressure difference (0.244 bar compared to 0.152 bar at 98.6 N axial force), due to the higher axial thrust to overcome.

The behaviour of the seal segment before it closed was similar to operating in the 'high' axial thrust regime, with a 'pre close' phase at which the seal segment was tilted forward, indicated by the label **'A'** on Figs. 7.10b, 7.10d and 7.10f. A vibratory segment response was observed between 29.9 s and 30.0 s, immediately after close in.

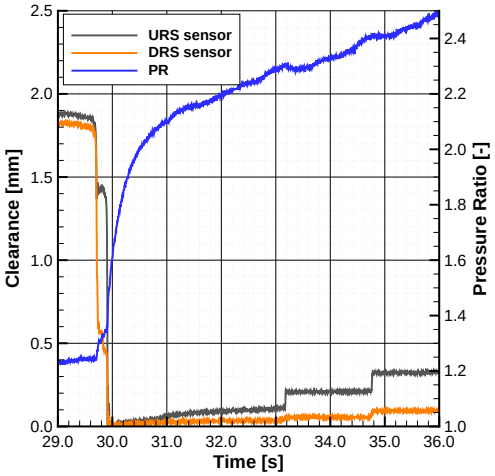

(a) Seal segment clearance: close in

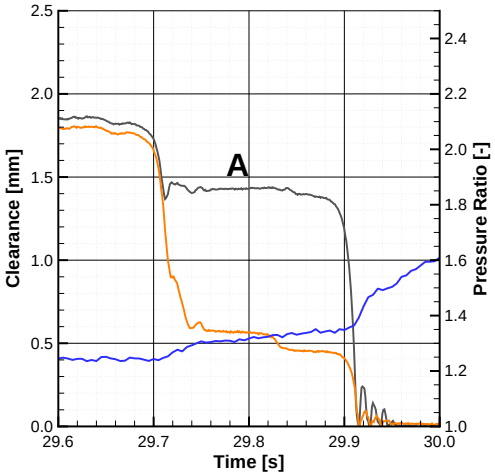

(b) Seal segment clearance: Detail

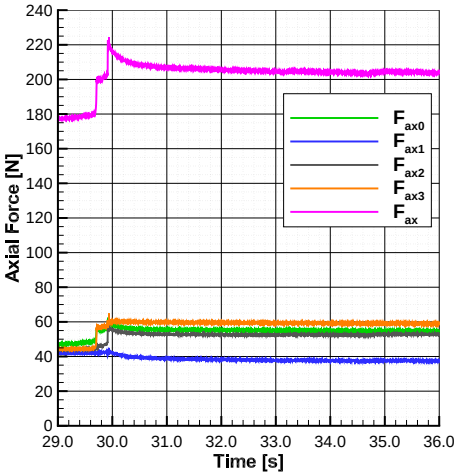

(c) Axial thrust: Close in

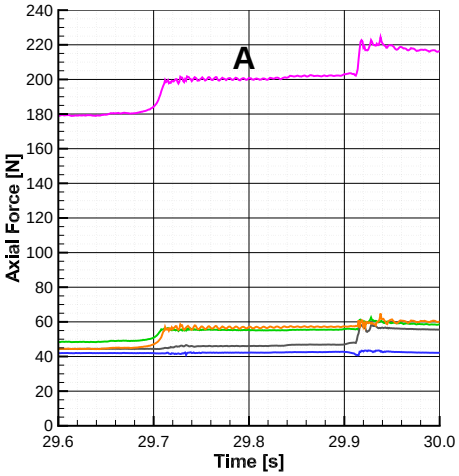

(d) Axial thrust: Detail

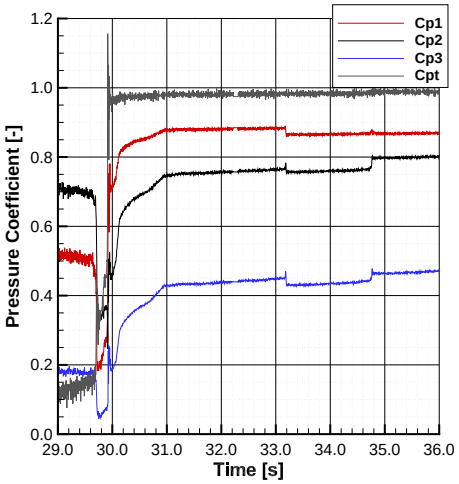

(e) Pressure coefficient: close in

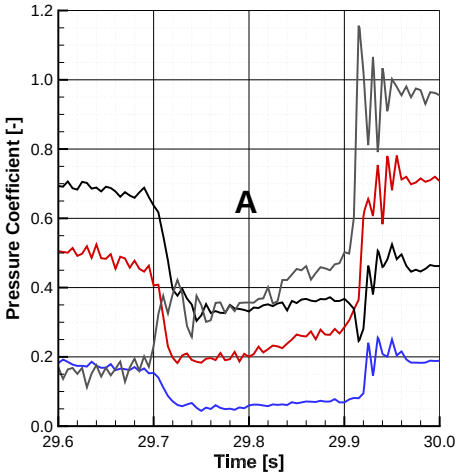

(f) Pressure coefficient: Detail

Figure 7.10: Typical 'very high' axial thrust response during close in: nominal $F_{ax} = 220\,\text{N}$, $k_{ax} = 15.0\,\text{N mm}^{-1}$.

7.4.4 Vibratory response

If the axial spring force applied about the centroid of the seal segment generates a significant net moment, then there will be a vibratory response, termed 'pressure activated chatter'. This was observed to occur over a range of total axial force, not just in the 'very high' operating regime where a slight vibratory response was also observed.

The clearance response of such a test is shown in Fig. 7.11, and in which the total axial force was 75 N and the axial spring stiffness 15.0 N mm^{-1}. Such a response in steam turbine operation would be damaging to the seal due to multiple rotor contacts. Once the pressure ratio increased to a high enough level, the seal segment operated at a constant operating clearance. Note that the pressure scanner logging frequency was 200 Hz in the test shown in Fig. 7.11, rather than the 600 Hz in the results presented previously. Also the initial starting clearance was lower in this test.

Table 7.3 summarises the axial forces applied to the seal segment when the segment is pushed onto the contact face, and the net applied moment applied about the tangential axis. Clearly there was greater moment applied by the axial springs trying to rotate the seal segment forwards.

As in the 'high' axial thrust regime, AX0 and AX3 are the first axial springs to be compressed (at 15.92 s in Fig. 7.11c), and indicate that the seal segment rotated forward, and that a 'pre close' phase of operation had developed.

At 15.97 s the seal segment started to move towards the rotor, with the central axial springs AX1 and AX2 being compressed afterwards at 15.99 s. As the segment was tilted forward when it closes in, it contacts the rotor and begins to vibrate, contacting the rotor surface as it does. When the segment contacted the rotor surface there was a build-up of the pressure below the segment, which started to move the segment away from the rotor and tilts backwards. However as the segment moved away it also tilted forwards again, indicated by the drop in F_{ax1} and F_{ax2}, and which produced a drop in

	Axial thrust / N					Applied Moment / N m
	F_{ax}	F_{ax0}	F_{ax1}	F_{ax2}	F_{ax3}	M_θ
'High thrust response'	98.6	25.5	22.3	23.4	27.5	0.074
'Vibratory response'	75.3	17.1	21.0	18.5	18.6	0.241

Table 7.3: Applied axial thrust and moment.

pressure both above and below the segment. The drop in segment pressure allowed the segment to drop back down onto the rotor surface and the process to begin again.

Once sufficient pressure had built up, the segment was able to operate at a constant operating clearance, as shown in Figs. 7.11b, 7.11d and 7.11f. As the seal segment was nearing the end of the vibrational phase, the frequency and amplitude of the vibrations was lower. Also the seal segment vibrates without touching the rotor surface.

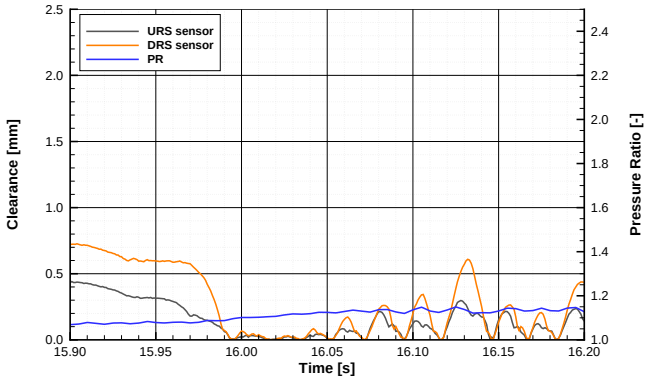

(a) Seal segment clearance during close in and vibratory phase

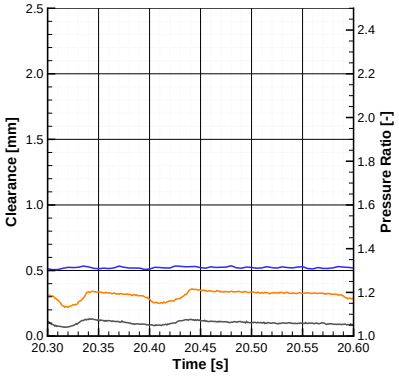

(b) Seal segment clearance at end of vibratory phase

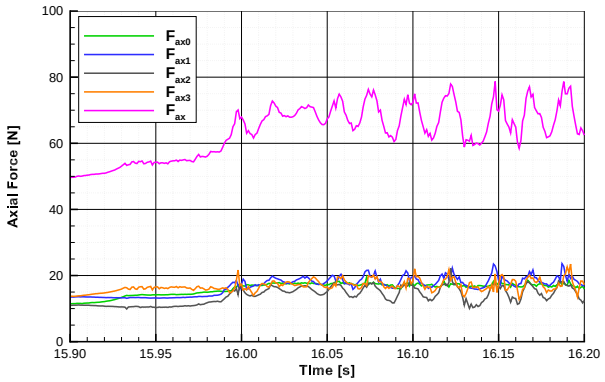

(c) Seal segment axial thrust during close in and vibratory phase

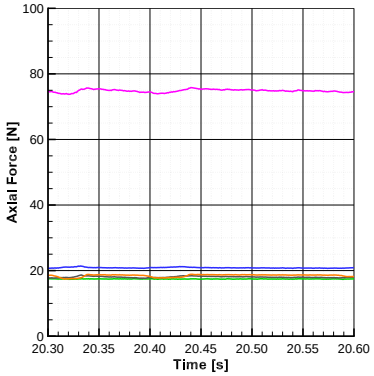

(d) Seal segment axial thrust at end of vibratory phase

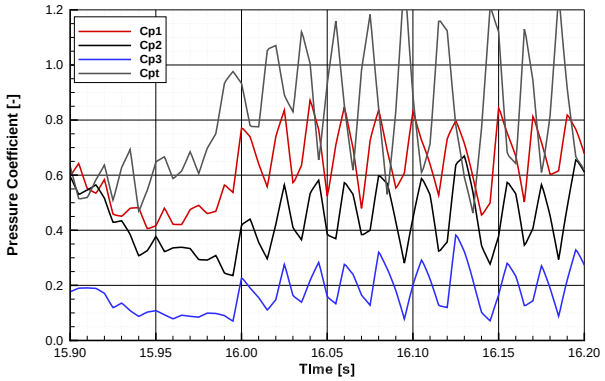

(e) Seal segment pressure coefficient during close in and vibratory phase

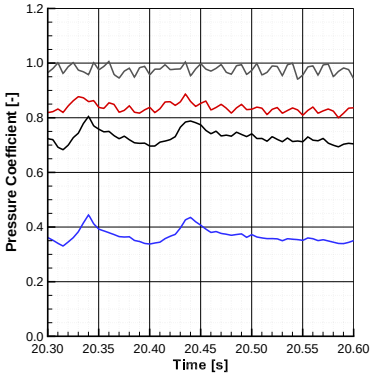

(f) Seal segment pressure coefficient at end of vibratory phase

Figure 7.11: Vibratory seal segment response

7.4.5 Limited clearance testing

A test was conducted with shims used to limit the minimum clearance of the seal segment. The purpose of such a test was to see if operating clearance reductions as great as the 'high' operating regime could be obtained without rotor contact.

Such a test is shown in Fig. 7.12. Shims were taped onto the rotor surface to limit the clearance of the seal segment to $0.1\,\text{mm}$. The total axial force applied was $F_{ax} = 106\,\text{N}$, $k_{ax} = 15.0\,\text{N mm}^{-1}$. The test was conducted at atmospheric back pressure, but without axial load cells installed. Figures 7.12a and 7.12c show the 'close in' clearance and pressure coefficient respectively, and Figs. 7.12b and 7.12d the retraction clearance and pressure coefficient respectively.

As the clearance was limited to $0.1\,\text{mm}$, rotor contact was prevented as the segment closed in. From about $7.5\,\text{s}$ to $7.7\,\text{s}$ the segment operated at $0.1\,\text{mm}$. Then, once the the pressure difference across the seal segment increased enough, $\Delta P = 0.66\,\text{bar}$ in this case, the seal segment moved away from the rotor surface. As the rig inlet pressure was reduced, shown in Fig. 7.12b, the seal segment lost lift, as in the 'high' and 'very high' operating regime, and came to rest on the $0.1\,\text{mm}$ shims before retracting.

Table 7.4 compares the operating clearance between a limited and unlimited test with the same total axial spring force. The axial spring settings were identical as both cases were run without adjusting the axial spring force. The case with the limited clearance operated at a higher mean clearance than the unlimited test. The pressure difference where the segment lost lift was similar, and was a result of the axial spring force rather than the different operating clearance. Table 7.4 also includes the operating clearance at the highest axial thrust in the 'low' regime and a case without axial springs. Whilst the operating clearance was increased over the unlimited case, the limited clearance case operates at a much lower clearance than either the $70\,\text{N}$ axial thrust case or the zero axial thrust case. It is also worth pointing out that the level of non-uniformity in the seal segment clearance was improved in the limited case compared to the unlimited case with and without axial springs.

	Axial thrust / N	Operating clearance / mm			ΔP loss of lift
	F_{ax}	c_{URS}	c_{DRS}	c_m	bar
'Clearance unlimited'	106	0.244	0.033	0.143	0.249
'Clearance Limited'	106	0.371	0.199	0.294	0.229
Best 'low' regime	70.4	1.129	0.189	0.680	N/A
Zero axial thrust	0	1.309	0.228	0.793	N/A

Table 7.4: Limited and non limited clearance tests at atmospheric outlet pressure.

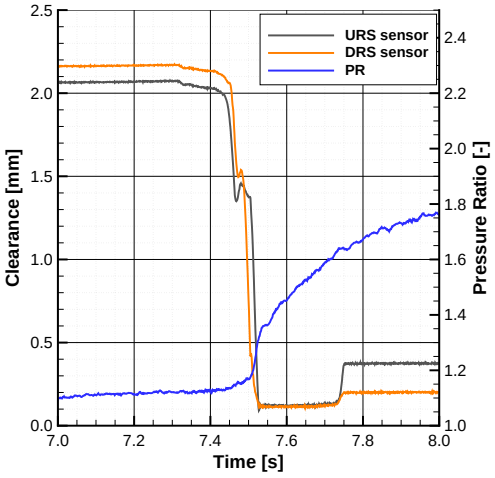

(a) Segment clearance: Close in

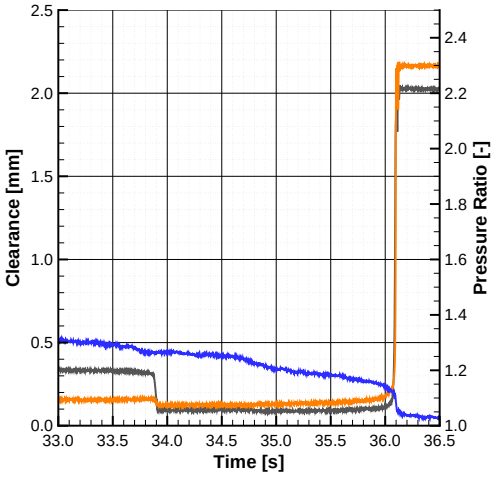

(b) Segment clearance: Retraction

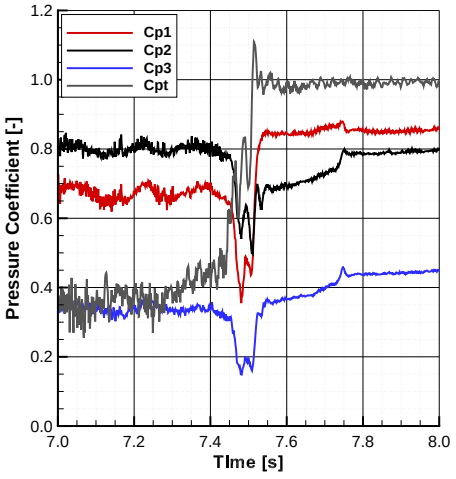

(c) Pressure coefficient: close in

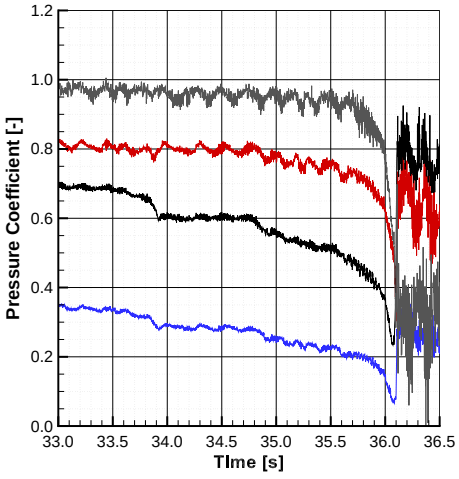

(d) Pressure coefficient: Retraction

Figure 7.12: High axial thrust regime with set minimum clearance: $F_{ax} = 106\,\text{N}$, $k_{ax} = 15.0\,\text{N}\,\text{mm}^{-1}$.

Summary

The purpose of this test was to demonstrate that the clearance of the Aerostatic Seal could be minimised by the use of axial thrust compensation springs in the 'high' operating regime setting by limiting the clearance of the segment in some way to prevent rotor contact. Compared to the 'high' operating regime, the operating clearance was slightly higher when the segment position was limited, although it was significantly lower than the 'low' axial thrust operating regime. This result is important for the Gen III design that is described in Chapter 9.

7.5 Discussion

The key to understanding why the seal behaves in the three operating regimes is moment stability. Increasing the axial thrust reduces the portion of the pressure difference that is balanced by the reaction force. Importantly the reaction force is distributed on the contact face, and does not need be evenly distributed. In fact the ability for the reaction force to act at a point on the contact face to balance the net pressure moment is crucial for the seal segment to maintain moment equilibrium, and not tilt forward. If the reaction force is reduced, then the range of pressure moments tolerated is reduced, decreasing the moment stability margin.

Moment stability

The moment stability contour is shown in Fig. 7.13 for seal design 'MESS04' operating with zero axial thrust, and at the same initial position as in the experimental results discussed above. Over the full range of operating clearances and pressure difference the moment criterion, ξ, remains within the stable region, i.e. between 0 and 1 (see Section 3.3.2).

Figure 7.14 shows the moment stability contour with axial thrust applied, Fig. 7.14a showing 40 N applied axial thrust and Fig. 7.14b 100 N applied thrust, as produced by the standard analytical model. Red and blue on the graphs are operating conditions where moment stability is not met, and with axial springs stable operating conditions are much reduced. The area with stable operation is reduced further with increased axial thrust.

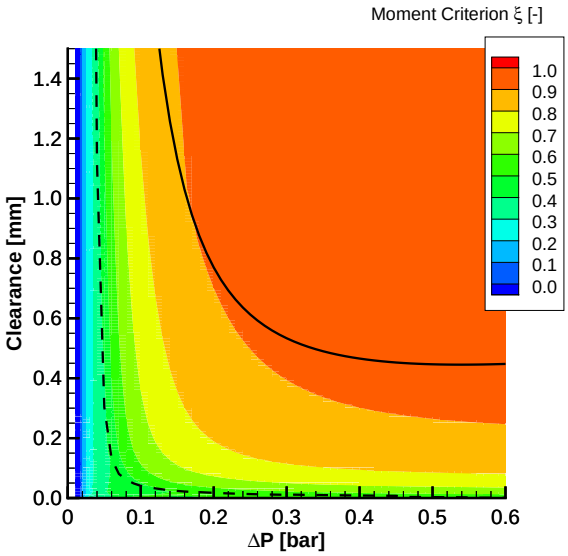

Figure 7.13: Moment contour with no axial thrust.

The transition from blue to red in both figures is when the pressure difference is able to overcome the axial spring thrust and push the seal segment against the rear contact face.

In the 'low' axial thrust operating regime the loss of moment stability was not as extreme as in the 'high' operating regime. This was confirmed by investigation of the seal axial pocket pressure distribution in Table 7.2, which showed less tilting forward in the low operating regime. In the 'high' operating regime moment stability was not regained until significant pressure difference had built up across the seal segment. This was observed in the analytical model as a greater pressure difference is required for the segment to get out of the unstable region back into the stable region.

To generalise the transition between the 'low' and 'high' operating regimes, axial pressure forces are considered. The transition point was observed to be when the axial spring force was approximately 80% of the axial pressure force at which the seal segment would close in when there were no axial thrust springs. As the seal segment is tilted forward in the 'pre close' phase, then the actual pressure forces acting on the seal segment are unknown as there is significant leakage through the contact face. The top pressure taps are able to measure the pressure on the top surface of the segment, and which might enable a better axial force to be calculated with further analysis, and allow the 'low' and 'high' axial thrust regimes to be generalised to other seal designs.

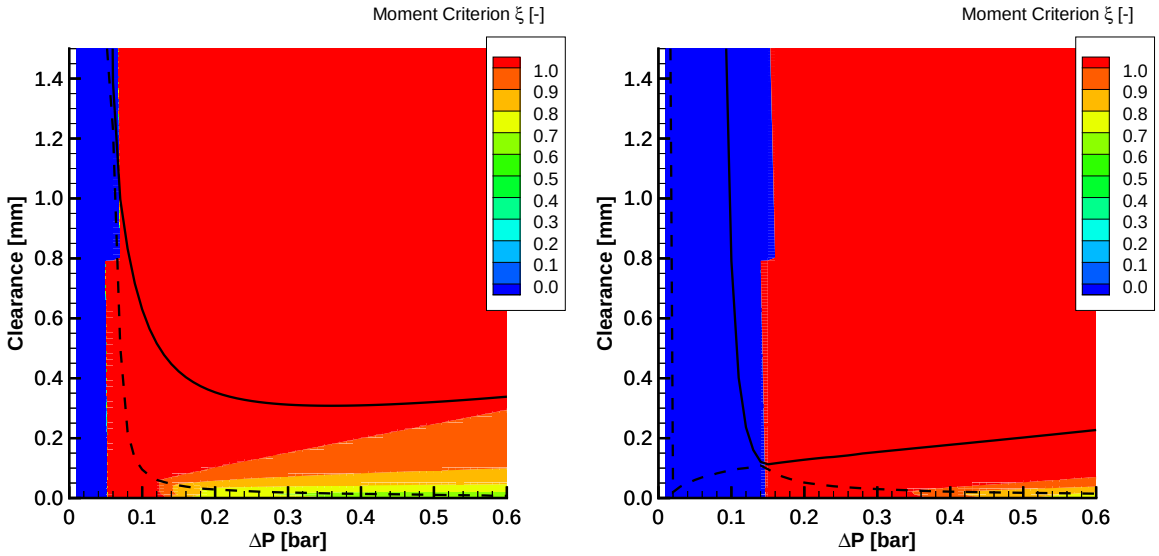

(a) 40 N Axial thrust

(b) 106 N Axial thrust

Figure 7.14: Analytical moment contour.

7.6 Conclusion

This chapter has described experimental testing conducted on an Aerostatic Seal with axial thrust compensation springs, in the non-rotating rig. A large number of tests were conducted with different levels of axial thrust. At the beginning of this chapter, three research questions were presented which have now been answered:

Is the axial thrust compensated design viable?

The axial thrust compensation has been confirmed to work experimentally. Applying axial force to the seal segment decreased the operating clearance of the seal.

What is the level of performance gain?

The level of performance gain was categorised into four operating regimes:

- 'Low' levels of axial thrust, below approximately 75 N. There was a small improvement in operating clearance, and consequently a leakage reduction of approximately 10 % was observed.
- 'High' levels of axial thrust, greater than 75 N. A significant reduction in operating

clearance was observed, although rotor contact was observed just after the seal closed, and also before the segment retracts.

- 'Very high' levels of axial thrust, around 200 N; an extension of the 'high' axial thrust regime. There was a prolonged period of time where the seal segment was in contact with the rotor surface.

- Vibratory response, termed 'pressure activated chatter' where the seal segment repeatedly contacted the rotor surface. This was due to unbalanced applied moment about the segment centroid due to axial spring force.

The only regime where there is no rotor contact is the 'low' axial thrust regime, although the level of operating clearance reduction was limited compared to the much greater reductions observed in the 'high' axial thrust regime. As significant rotor contact between the seal and the rotor would be damaging in steam turbine operation, then the 'low' operating regime is the safest. Moment stability is the governing factor dictating the performance of the Aerostatic Seal when operating with axial springs.

What are the limits of operation?

During the operation of the seal in a steam turbine it would be undesirable for the seal to come into contact with the rotor, as this would damage the seal, and in extreme cases may cause damage to the rotor due to frictional heat generation. Therefore the limit of operation is the 'low' axial thrust regime where the seal segment does not touch the rotor surface during operation. However the 'low' axial thrust regime had a relatively small improvement in operating clearance compared to the 'high' axial thrust operating regime.

A set of tests was conducted with using shims placed on the rotor surface to simulate restricting the segment minimum clearance in the T slot. This showed that high levels of axial thrust could be applied for the seal to operate at a low clearance, and the segment would move away from the rotor once the pressure had increased enough. This would prevent rotor contact and maximise the performance gain by using axial thrust compensation. This is a suggested design feature of the Gen Ⅲ Aerostatic Seal design discussed in Section 9.3.

One other disadvantage of the axial thrust compensated design is that by reducing the axial force on the seal segment, the moment stability margin is reduced. As stated in Section 3.4, the most responsive seal is obtained by maximising the axial length of the seal segment until the segment no longer has moment stability. Therefore adding axial springs may make a responsive seal design loose moment stability before much reduction in operating clearance was possible. Another way to reduce the frictional force would be to reduce the coefficient of friction by introducing a low friction coating. Whether one could be successfully operated inside a steam turbine will require more research into the suitability of different coatings. The HALO seal uses a nickel-boron coating to reduce friction which would be a starting point for further investigation.

It was found during all the axial thrust operating regimes that the seal segment still operated with significant differences in operating clearance at each end of the seal segment. This has been termed non-uniform operating clearance. As this is undesirable (see Section 6.3.1 for example), further analysis and experimental tests have been carried out, which is the subject of the next chapter.

Chapter 8

Non-Uniform Segment Clearance

8.1 Introduction

A non-uniform circumferential clearance has been observed in the operating clearance of the Aerostatic Seal. This was where one side of the seal segment would operate at a lower clearance that the other, and was also observed when the segment was transitioning from a retracted position to the operating position.

Non-uniform clearance is undesirable as the extreme sides of the seal segment may contact the rotor. As it is the mean segment clearance that controls radial force, then with non-uniform clearance one side of the segment may touch the rotor without positive radial force to move the segment away. This was demonstrated in the rotating rig and caused some minor rubs during the high rotor eccentricity testing - see Section 6.3.1.

The use of axial thrust compensation springs has not made the operating clearance more uniform, as discussed in Chapter 7.

Possible causes of uneven clearance that were considered:

- Different circumferential spring forces on each side
- Different coefficient of friction on each side.
- Different pressure distribution on each side of the segment.
- Varying reaction force around the circumference of the contact face.

The effect due to springs was eliminated as non-uniform clearance was observed when no circumferential springs were present, as demonstrated in Section 5.2. The spring stiffness was found to be similar between sides - see Appendix D.

This chapter investigates the causes and effect of non-uniform seal segment clearance, and aims to answer the following three questions:

1. Why does the seal segment move to a non-uniform clearance when transitioning from retracted to operating clearance?
2. Why does the segment not restore to a uniform clearance?
3. What are the consequences and effect on the overall Aerostatic Seal performance?

This chapter is split up into three main sections:

Experimental Observations

An experimental case is presented in Section 8.2 which demonstrates the seal segment operating at a different non-uniform clearance in the same set up. These tests were performed on the non-rotating rig, with side pressure taps and fully fixed springs. This was to investigate the causes of non-uniform clearance.

Analytical modelling and considerations

In Section 8.3 a 2D leakage model is described which was used to analyse the pressure moment acting about the axial direction at a range of different seal segment non-uniform clearances.

The frictional moment, opposing the pressure moment trying to self-right the seal segment was considered analytically. This was to investigate why the seal segment would not restore to a uniform clearance.

Non-uniform fixed clearance tests

Finally in Section 8.4 assessment of the pressure moment to restore non-uniform clearance was made experimentally. This was achieved by fixing the clearance of the seal segment into a non-uniform position in a manner similar to the method described in

Section 5.5. The circumferential pressure distribution on the rotor and on the sides of the seal segment was used to calculate the pressure moment acting on the segment to restore it to a uniform clearance. Comparison was also made to the analytical predictions made previously.

8.2 Experimental Non-Uniform Clearance

The purpose of the experimental tests described in this section was to investigate what factors were causing one side of the seal segment to operate at a lower clearance than the other. Two tests, test A and test B, are described which both had the same set up but in each test it was a different side of the segment that operated at the lowest clearance. The test rig was not reassembled between tests. Note that it was not intentional that the lowest side of the seal segment should switch sides between tests, but was observed when carrying out a series of tests under the same conditions. Typically the lowest side of the segment was consistent when conducting repeated tests, and would only change after the test rig was reassembled.

8.2.1 Experimental Method

The control valve was automatically controlled to achieve a steady opening rate of $8\,\%\,\mathrm{s}^{-1}$ and with atmospheric back pressure. The spring rate of the URS and DRS circumferential springs was $17.71\,\mathrm{N\,mm}^{-1}$ and $17.62\,\mathrm{N\,mm}^{-1}$ respectively and with the ends of the springs held in position inside the spring holes - see Section 3.5. The rotor central position was $15.13\,\mathrm{mm}$ from the seal holder (dimension b), and the segment $2.57\,\mathrm{mm}$ from the seal holder (dimension a), as shown in Fig. 5.3. The bypass valve was two turns from shut.

The axial pressure force acting on the segment was increased if a greater portion of the segment was inside the inner diameter of the contact face, due to an increased area of the segment surface with outlet pressure rather than inlet pressure acting on it. Therefore when setting up the test rig, care was taken to ensure that the seal segment was concentric to the holder. This was to prevent greater axial force on one side of the segment if that side of the rotor was at a smaller radial position than the other side.

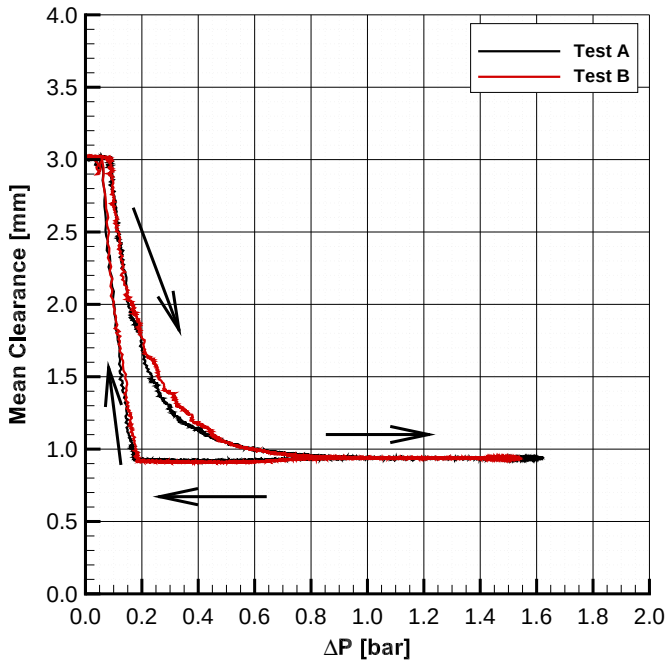

Figure 8.1: Mean clearance variation with pressure difference

8.2.2 Results

Figure 8.1 plots the mean clearance of the two tests with pressure difference. The mean operating clearance that was achieved was similar, and was 0.93 mm in test A and 0.95 mm in test B. The transition from the retracted to operating position is also similar, the only difference is between 0.2 bar and 0.4 bar pressure difference where there is a small difference in the trajectory of the segment. This shows that the mean operating clearance, which is important for the leakage characteristic of the seal, was very similar, although the response of the different sides of the segment is very different between two tests conducted one after the other.

To understand the reasons why the seal segment clearance would be non-uniform, the pressure moment acting about the axial direction of the segment, M_{px}, was calculated. This was achieved by multiplying the pressure force by the tangential distance from the centroid of the segment, as demonstrated in Fig. 8.2. Where there was only one side pressure tap in the pocket, then that pressure was assumed to act over the entire area of that pocket, and the force to act at the centre of pressure. Where there

were multiple pressure taps in the pockets, as in the central circumferential pocket and on top of the segment, then a linear distribution of pressure was assumed between each pressure tap, and the pressure force per unit segment width integrated to calculate the moment contribution. The moment due to each circumferential position of the seal segment pocket, $\mathrm{d}M_{px}$ is given in Eq. (8.1). The moment arm L and pressure P is a function of circumferential position θ. The total moment is then given by the sum of all these contributions for all circumferential positions and pockets. This is given by Eq. (8.2) where w is the axial length of the seal segment pocket and D is the diameter of seal segment. Eight pressure taps were available on each of the side surfaces of the segment. The same procedure was used as described in Section 5.5 to calculate the side pressure force, the force then multiplied by the tangential distance from the centroid.

$$\mathrm{d}M_{px}(\theta) = L(\theta)P(\theta)\,\mathrm{d}A \tag{8.1}$$

$$M_{px} = \frac{wD}{2}\int L(\theta)P(\theta)\,\mathrm{d}\theta \tag{8.2}$$

The transition from retracted to operating clearance is compared in Fig. 8.3. The clearance and pressure moment is plotted in Figs. 8.3a and 8.3c respectively for test A and in Figs. 8.3b and 8.3d for test B. Comparing the clearance response between the two tests shows that in test A it was the URS side of the segment operating at the lowest clearance, and in test B it was the DRS side of the segment operating at the lowest clearance. The lowest side of the segment operates at a similar clearance in each test, about $0.5\,\mathrm{mm}$ at the measurement position. Similarly the high clearance sensor measures similar clearance at the high clearance side. Together this means that the angle of the segment was in fact similar, only the other way around.

The pressure moments calculated experimentally, shown in Figs. 8.3c and 8.3d for test A and test B respectively, initially show the same slightly negative pressure moment. Critically this pressure moment was greater than the frictional moment calculated based on the axial pressure force. The frictional moment is a function of axial force, coefficient of friction and seal geometry. A coefficient of friction of $\mu = 0.2$ was chosen as this was slightly higher than the coefficient of friction found experimentally in Chapter 5. The calculation method is described in the next section. For test A the pressure moment

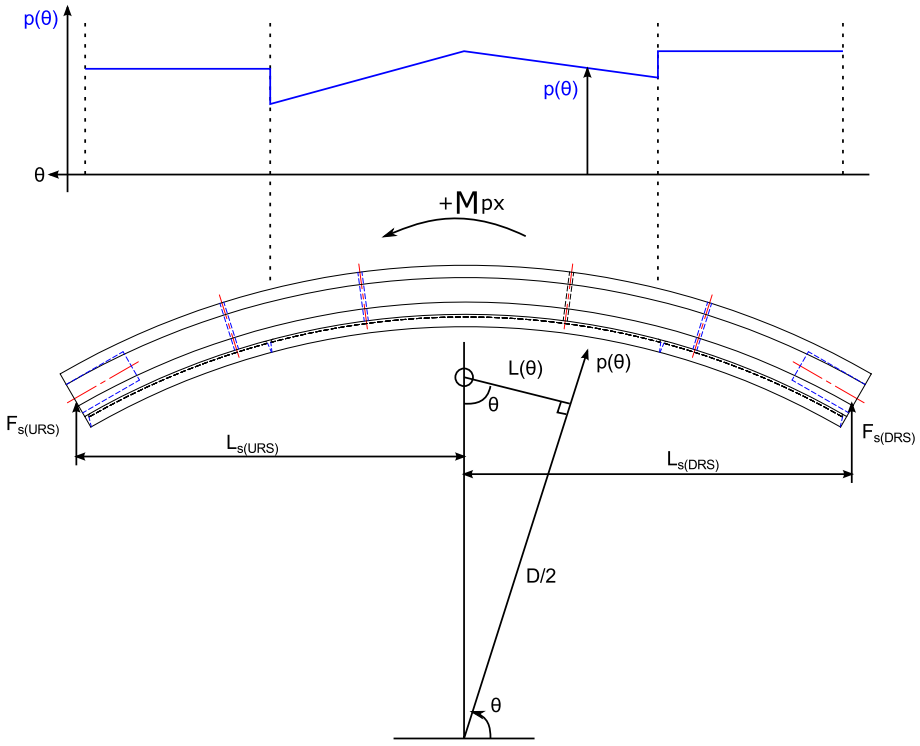

Figure 8.2: Pressure moment calculation method. (Viewed from upstream of the seal segment.)

stays negative and it was only after the seal segment reaches the operating clearance that the pressure moment was less than the frictional moment. Initially the response was the same for test B where the pressure moment was negative and greater than the frictional moment. Then at approximately 10.75 s the pressure moment increases and becomes positive. At the same time the URS side of the segment has become stationary and it is the DRS side of the segment that continues to decrease in clearance.

In conclusion two key observations were made in this section. Firstly there was a measured pressure moment which was larger than the calculated frictional moment when the seal was retracted. This pressure moment was responsible for the initial uneven operating clearance as the seal segment closes. Once the seal segment was at the operating clearance the pressure moment was not large enough to overcome the frictional moment, leading to the seal segment remaining in the non-uniform operating clearance.

Secondly the pressure moment acting on the seal segment was reversed when a different side of the segment that was at the lowest operating clearance. However as the pressure moment changes after the other side of the segment has begun moving,

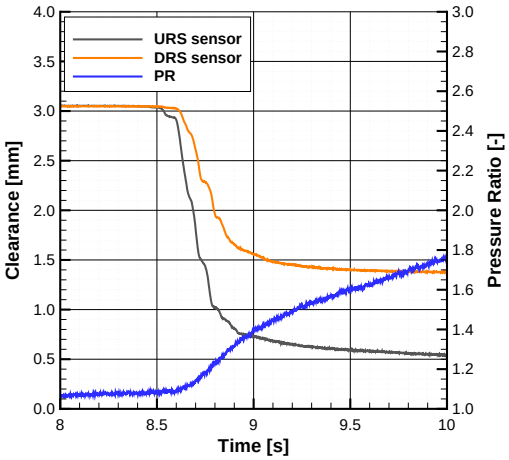

(a) Seal segment clearance: Test A

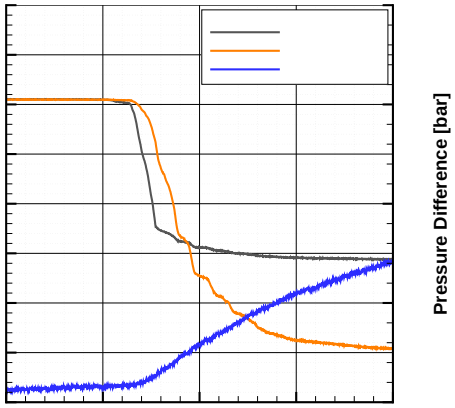

(b) Seal segment clearance: Test B

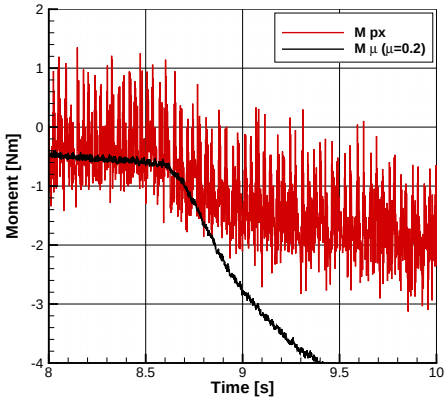

(c) Moment M_x: Test A

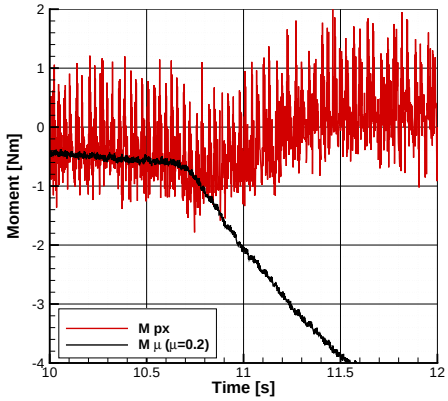

(d) Moment M_x: Test B

Figure 8.3: Comparison between tests: close in behaviour.

then it was evident that there must be an uneven frictional moment which contributes to non-uniform clearance.

8.3 Analytical modelling and considerations

There are two forces acting about the seal segment x axis, namely the pressure moment and the frictional moment. For the seal segment to be able to restore itself to a uniform operating clearance the pressure moment must overcome the frictional moment opposing motion.

An analytical 2D steady flow model has been developed to investigate the effect of uneven clearance on the segment pressure distribution. A range of seal segment clearances and angles was investigated.

The frictional moment acting about the seal segment centroid was calculated, which was not necessarily a straight forward calculation. This was because the frictional moment depends on the moment arm about the centroid of the segment, which varies with circumferential position on the contact face, and also the frictional force, which also varies on the contact face. The frictional force distribution was found by considering the force and moment equilibrium of the seal segment and Finite Element Analysis (FEA) calculation of the contact force.

8.3.1 2D seal leakage model

The standard analysis methodology, described in Section 3.3, models the flow through the seal segment operating at a mean clearance. This takes no account of seal segment clearance non-uniformity.

To model different clearances about the circumference of the seal segment, the segment was divided up into the circumferential pockets, and the flow through each of these modelled with a mean clearance. Now if one side of the seal segment is operating at a lower clearance then the mean clearance at that circumferential pocket is reduced accordingly. Circumferential flow will also exist between the circumferential pockets, and was also modelled.

Figure 8.4 shows a schematic plan view of an Aerostatic Seal segment, and the pocket pressures and leakage flow rates between each pocket. The direction of the leakage

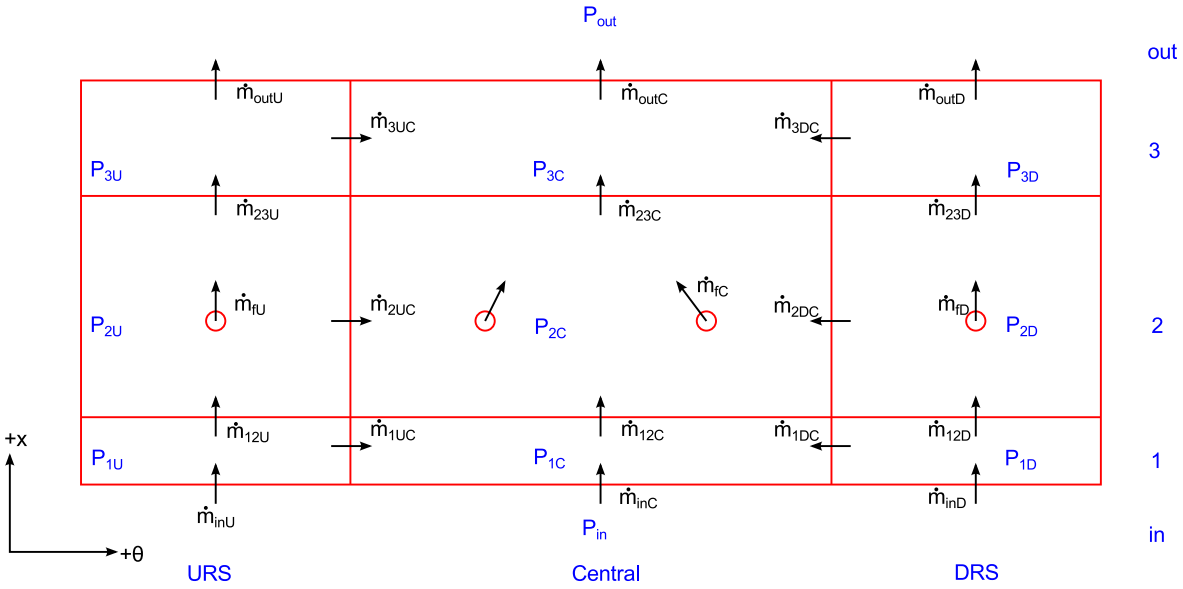

Figure 8.4: Plan view of seal segment showing 2D mass flow and pressure.

mass flow rate arrows indicates the direction taken as positive mass flow rate.

To begin with the clearance at the extreme URS and DRS side of the seal segment was specified and the area of the axial leakage path was calculated for each set of circumferential pockets using the tool described in Appendix F. A_U, A_C and A_D are the axial leakage path areas for the URS, central and DRS circumferential pockets respectively. The circumferential leakage area was also calculated between the central circumferential pocket and the URS and DRS pockets.

A modified version of the standard analysis methodology follows. For each circumferential pocket (URS , Central and DRS) the axial leakage and pocket pressures are calculated iteratively starting from an initial mass flow rate guess. The Eser and Kazakia leakage model was used, the same as in the standard analysis methodology, and is shown in Eq. (8.3) to Eq. (8.9) for the URS set of circumferential pockets. The only difference from the standard analysis method was that circumferential flow, $\dot{m}_{1UC}$, $\dot{m}_{2UC}$ and $\dot{m}_{3UC}$, was included in Eqs. (8.4), (8.6) and (8.9).

Leakage was not modelled between the between the URS and DRS circumferential pockets and the side leakage channel.

The model is assuming steady flow, as in the standard analysis methodology.

$$P_{1U} = \sqrt{P_{in}^2 - \left(\frac{\dot{m}_{in}}{C_D C_{ke} A_U}\right)^2 RT} \tag{8.3}$$

$$\dot{m}_{12U} = \dot{m}_{inU} - \dot{m}_{1UC} \tag{8.4}$$

$$P_{2U} = \sqrt{P_{1U}^2 - \left(\frac{\dot{m}_{12U}}{C_D C_{ke} A_U}\right)^2 RT} \tag{8.5}$$

$$\dot{m}_{23U} = \dot{m}_{12U} + \dot{m}_{fU} - \dot{m}_{2UC} \tag{8.6}$$

$$P_{3U} = \sqrt{P_{2U}^2 - \left(\frac{\dot{m}_{23U}}{C_D C_{ke} A_U}\right)^2 RT} \tag{8.7}$$

$$\dot{m}_{outU(n+1)} = \frac{C_d C_{ke} A_U}{\sqrt{RT}} \sqrt{P_{3U}^2 - P_{out}^2} \tag{8.8}$$

$$\dot{m}_{inU(n+1)} = \dot{m}_{out} + \dot{m}_{3UC} + \dot{m}_{2UC} + \dot{m}_{1UC} - \dot{m}_{fU} \tag{8.9}$$

Once the axial mass flow rates have converged, then the circumferential mass flow rates are calculated using the leakage equation of Eser and Kazakia. For example the circumferential flow rate from the first URS pocket to the first central pocket, $\dot{m}_{1UC}$, is calculated using Eq. (8.10). A_{1U} is the circumferential leakage area on the URS side of the seal segment and at the first axial pocket. As the circumferential pockets are much longer circumferentially than axially, the kinetic energy carry over was assumed to be zero. Note that the equation was split into a positive and negative version to reverse the flow should the outlet pressure be greater than the inlet pressure. Once the circumferential flow rate was calculated, the calculation procedure moves onto the next iteration, including the newly calculated circumferential flow rates.

$$\dot{m}_{1UC(n+1)} = \begin{cases} \frac{C_d A_{1U}}{\sqrt{RT}} \sqrt{P_{1U}^2 - P_{1C}^2} & \text{if } P_{1C} < P_{1U} \\ -\frac{C_d A_{1U}}{\sqrt{RT}} \sqrt{P_{1C}^2 - P_{1U}^2} & \text{if } P_{1U} < P_{1C} \end{cases} \tag{8.10}$$

Once the process has converged, then the pressure forces in each cavity are used to calculate the moment about the axial direction. The pressure is assumed to be uniform in each of the circumferential pockets, and so there is only a moment contribution from

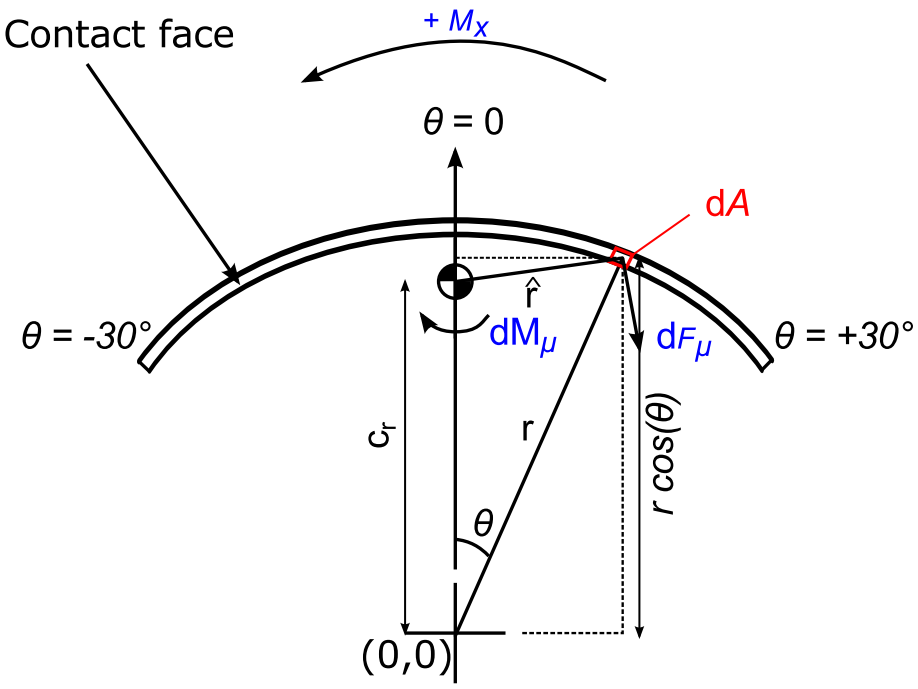

Figure 8.5: Contact face frictional moment about the centroid. (Looking onto the contact face from upstream.)

the URS and DRS circumferential pockets (P1, P2 and P3 for both). Analytically the side pressure, top pressure and central circumferential pockets do not contribute a moment. The moment was calculated about the centroid of the seal segment.

8.3.2 Frictional torque

For the seal segment to move back to a uniform operating clearance, the applied moment (i.e. pressure moment and moment due to the circumferential springs) must be greater than the frictional moment, i.e. $M_x > M_\mu$.

To calculate the frictional moment, first consider the area of the seal segment under contact, as shown in Fig. 8.5. For a small element of the contact area, of area $\mathrm{d}A$ and with contact stress σ, there is a frictional force acting given by Eq. (8.11). The origin for a polar coordinate system is at the centre of the seal segment, and c_r is the radial distance from the centre of the segment to the centroid of the segment. The frictional force is acting perpendicular to a line, labelled $\hat{r}$, from the centroid of the segment to the elemental area $\mathrm{d}A$, and generating a moment opposing the applied moment M_x in Fig. 8.5.

$$\mathrm{d}F_\mu = \mu\sigma\,\mathrm{d}A \tag{8.11}$$

The frictional torque due to each element of the contact face, $\mathrm{d}M_\mu$, is the the frictional force multiplied by the moment arm around the centroid of the segment, and is therefore:

$$\mathrm{d}M_\mu = \hat{r}\,\mathrm{d}F_\mu = \hat{r}\mu\sigma\,\mathrm{d}A \tag{8.12}$$

At each of the different circumferential positions, the frictional moment arm $\hat{r}$ changes. The total frictional torque preventing the seal segment moving back to an even clearance is found by integrating the frictional torque over the whole area of the contact face. This is similar to calculating the friction of a clutch [95].

$$M_\mu = \iint_A \mathrm{d}M_\mu \tag{8.13}$$

$$= \iint \mu\hat{r}^2\sigma\,\mathrm{d}r\,\mathrm{d}\theta \tag{8.14}$$

Therefore to calculate the frictional moment, one has to first determine the contact stress distribution, and integrate it and the moment arm over the contact face surface.

Contact face stress distribution

The contact face stress is not constant, but a function of the tangential and radial position. Consider the seal segment as a free body in equilibrium, shown in Fig. 8.6. Force equilibrium has to be satisfied in the axial direction and the moment equilibrium about the tangential and radial axes.

To achieve force equilibrium in the axial direction, the contact face reaction force must equal the axial pressure force. The reaction force can be found by integrating the contact stress over the contact face area. This yields Eq. (8.15) where $\sigma(r,\theta)$ is axial contact stress as a function of r and θ.

$$F_x = \iint_A \sigma(r,\theta)\,\mathrm{d}A \tag{8.15}$$

Taking moments about the tangential direction, centred on the centre of the seal

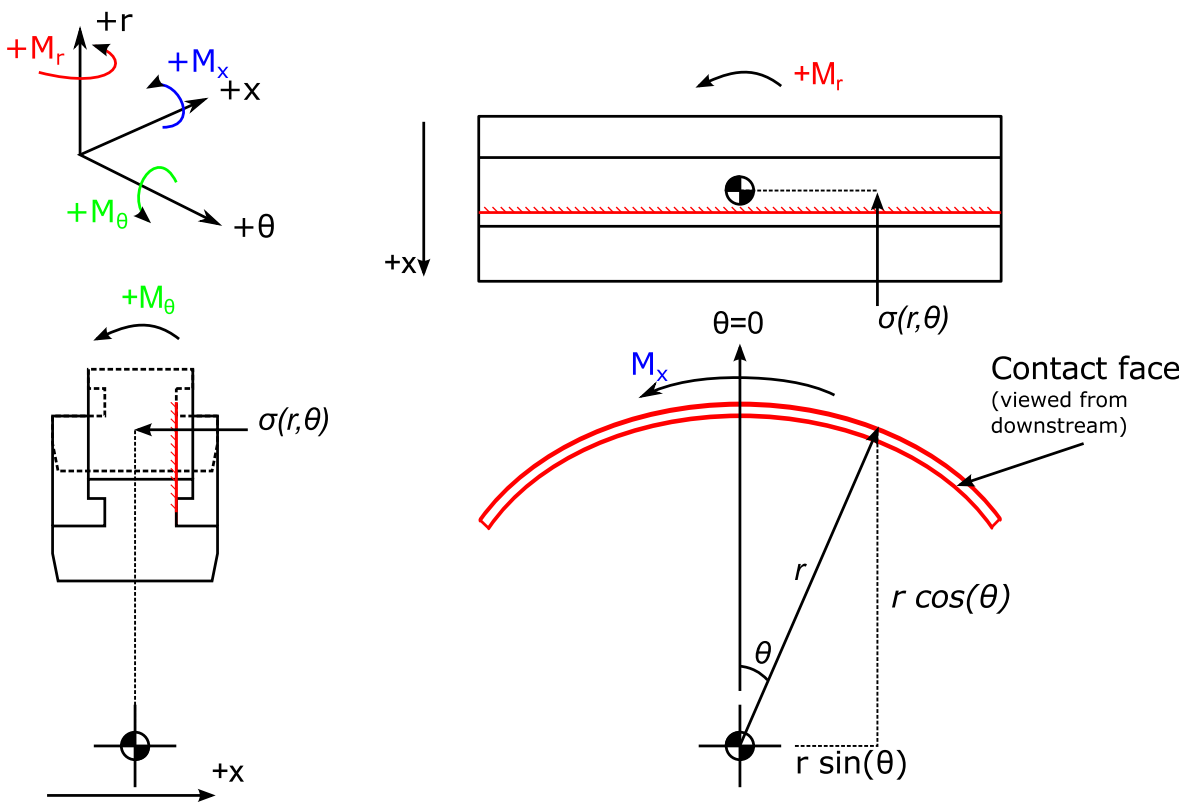

Figure 8.6: Contact face stress distribution about the centre of the segment.

segment (see Fig. 8.6), then the moment generated by the contact stress acting at each location on the contact face must balance the moment generated by the pressure acting on the seal segment surfaces. This requirement leads to Eq. (8.16), where there is now a $r\cos(\theta)$ term introduced.

$$M_\theta = \iint_A r\cos(\theta)\sigma(r,\theta)\,\mathrm{d}A \tag{8.16}$$

Similarly taking moments about the radial axis yields Eq. (8.17). Normally there is no net pressure moment acting about the radial direction, and so $M_r = 0$, however this might not be the case when operating with axial thrust compensation springs.

$$M_r = \iint_A r\sin(\theta)\sigma(r,\theta)\,\mathrm{d}A \tag{8.17}$$

To find the contact stress function $\sigma(r,\theta)$, Eqs. (8.15) to (8.17) have to be solved simultaneously. Unfortunately with only the three equilibrium equations there is an infinite number of possible solutions. Therefore to find a suitable contact face stress distribu-

tion function two things were carried out. Firstly an even polynomial function of contact stress was assumed and the equations solved analytically. Secondly finite element stress analysis (FEA) was carried out in SolidWorks. This simulation included modelling the elastic properties of the contact face which introduces an extra set of equilibrium equations. Ultimately the analytical method was unnecessary for calculating the frictional moment about the segment centroid, as the best agreement to the FEA stress analysis was a uniform contact stress distribution, but it is a fast method for calculating the maximum contact stress and so has some use for the designer of an Aerostatic Seal.

Analytical solutions

An analytical distribution of contact stress was assumed in the form of an even order polynomial, given in Eq. (8.18), where $n = 2, 4, 6$ etc. To meet the requirements of moment equilibrium about the radial direction when there is a net moment present, the equation has been split into two parts either side of the seal segment. This means the function is discontinuous, but will not introduce a discontinuity to stress as the stress is fixed at zero at $\theta = 0$. Constants k_1 and k_2 are given in Eqs. (8.19) and (8.20) respectively assuming the seal segment is of 60° (i.e. 6 per ring). The peak stress at each end of the seal segment, where $\theta = \pm\frac{\pi}{6}$, are given by σ_1 and σ_2 respectively. The angular location on the contact face, θ is measured in radians. It was assumed that there was no radial contact stress variation for simplicity and as the contact face in small. (In the 'MESS01' Aerostatic Seal design the contact face is $0.5\,\text{mm}$ in the radial direction.)

$$\sigma(\theta) = \begin{cases} k_1\sigma_1\theta^n & -\frac{\pi}{6} \leq \theta \leq 0 \\ k_2\sigma_2\theta^n & 0 < \theta \leq \frac{\pi}{6} \end{cases} \tag{8.18}$$

$$k_1 = \left(-\frac{6}{\pi}\right)^n \tag{8.19}$$

$$k_2 = \left(\frac{6}{\pi}\right)^n \tag{8.20}$$

Substituting Eq. (8.18) into Eqs. (8.15) to (8.17) and denoting the integrals as I yields Eqs. (8.21) to (8.23). The radial height of the contact face is t, and assumes that the

thickness is small compared to the circumferential length of the contact face.

$$
\begin{aligned}
F_N &= rt \int_{-\frac{\pi}{6}}^{\frac{\pi}{6}} \sigma(\theta)\,\mathrm{d}\theta \\
&= rt \left[k_1\sigma_1 \int_{-\frac{\pi}{6}}^{0} \theta^n\,\mathrm{d}\theta + k_2\sigma_2 \int_{0}^{\frac{\pi}{6}} \theta^n\,\mathrm{d}\theta \right] \\
&= rt \left[k_1\sigma_1 I_{F_N 1} + k_2\sigma_2 I_{F_N 2} \right] \qquad (8.21) \\
M_\theta &= rt \int_{-\frac{\pi}{6}}^{\frac{\pi}{6}} \sigma(\theta)\cos(\theta)\,\mathrm{d}\theta \\
&= rt \left[k_1\sigma_1 \int_{-\frac{\pi}{6}}^{0} \theta^n\cos(\theta)\,\mathrm{d}\theta + k_2\sigma_2 \int_{0}^{\frac{\pi}{6}} \theta^n\cos(\theta)\,\mathrm{d}\theta \right] \\
&= rt \left[k_1\sigma_1 I_{M_\theta 1} + k_2\sigma_2 I_{M_\theta 2} \right] \qquad (8.22) \\
M_r &= rt \int_{-\frac{\pi}{6}}^{\frac{\pi}{6}} \sigma(\theta)\sin(\theta)\,\mathrm{d}\theta \\
&= rt \left[k_1\sigma_1 \int_{-\frac{\pi}{6}}^{0} \theta^n\sin(\theta)\,\mathrm{d}\theta + k_2\sigma_2 \int_{0}^{\frac{\pi}{6}} \theta^n\sin(\theta)\,\mathrm{d}\theta \right] \\
&= rt \left[k_1\sigma_1 I_{M_r 1} + k_2\sigma_2 I_{M_r 2} \right] \qquad (8.23)
\end{aligned}
$$

The integration was performed for polynomials up to the eighth order, and was checked with Wolfram Alpha. The axial force and the moments about the radial and tangential axis can be found from the pressure distribution on the seal segment. Therefore the only unknowns remaining are the two peak stresses σ_1 and σ_2, and the system of equations can be solved.

Table 8.1 summarises the integrals and gives the peak stresses for seal design 'MESS01' operating at $1.25\,\mathrm{bar(a)}$ at inlet and $1.00\,\mathrm{bar(a)}$ at outlet. Two different clearances were tested: a high clearance case where the seal mean clearance was $1.5\,\mathrm{mm}$ and a low clearance case where the seal was operating at $0.003\,\mathrm{mm}$ clearance. The system of equations

n		I_1	I_2	k_1	k_2	High Clearance σ_1	High Clearance σ_2	High Clearance R_{σ_1}	High Clearance R_{σ_2}	Low Clearance σ_1	Low Clearance σ_2	Low Clearance R_{σ_1}	Low Clearance R_{σ_2}
		1	1	1	1	N mm^{-1}		1	1	N mm^{-1}		1	1
2	F_x	0.0478	0.0478	3.648	3.648	2.29	2.29	2.92	2.92	2.58	2.58	3.00	3.00
	M_θ	0.0440	0.0440										
	M_r	−0.0182	0.0182										
4	F_x	0.007 87	0.007 87	13.305	13.305	3.85	3.85	4.90	4.90	4.33	4.33	5.03	5.03
	M_θ	0.007 11	0.007 11										
	M_r	−0.003 32	0.003 32										
6	F_x	0.001 54	0.001 54	48.530	48.530	5.41	5.41	6.89	6.89	6.08	6.08	7.07	7.07
	M_θ	0.001 38	0.001 38										
	M_r	−0.000 681	0.000 681										
8	F_x	0.000 329	0.000 329	177.015	177.015	6.97	6.97	8.88	8.88	7.84	7.84	9.12	9.12
	M_θ	0.000 293	0.000 293										
	M_r	−0.000 149	0.000 149										

Table 8.1: Analytical contract stress distributions

was solved using Matlab.

The 'contact stress ratio', R_σ, was introduced which was defined as the local stress at a particular position divided by the uniform stress required to counteract the axial force, shown in Eq. (8.24). It is useful to compare the results to different pressure differences, although the value is linked to the seal geometry and clearance.

$$\sigma(r,\theta) = R_\sigma(r,\theta)\frac{F_x}{A_{cont}} \tag{8.24}$$

Increasing the polynomial order n increases the maximum stress required to achieve equilibrium. The peak stress ratio can be approximated as $n+1$, although this approximation is not as good at higher orders of polynomial.

Comparing the peak stress ratio between the high clearance and low clearance it was found that the stress was slightly higher when in the low clearance position. This was due to the greater axial force acting on the seal segment due to the segment being at a lower radial position. (This increases the area of the segment with pressure difference acting on it.)

Finite Element Analysis

A finite element stress analysis (FEA) was performed using the linear stress analysis solver in the SolidWorks CAD package, and which could analyse the contact face stress.

The contact was modelled with the no penetration constraint at the boundary. Only

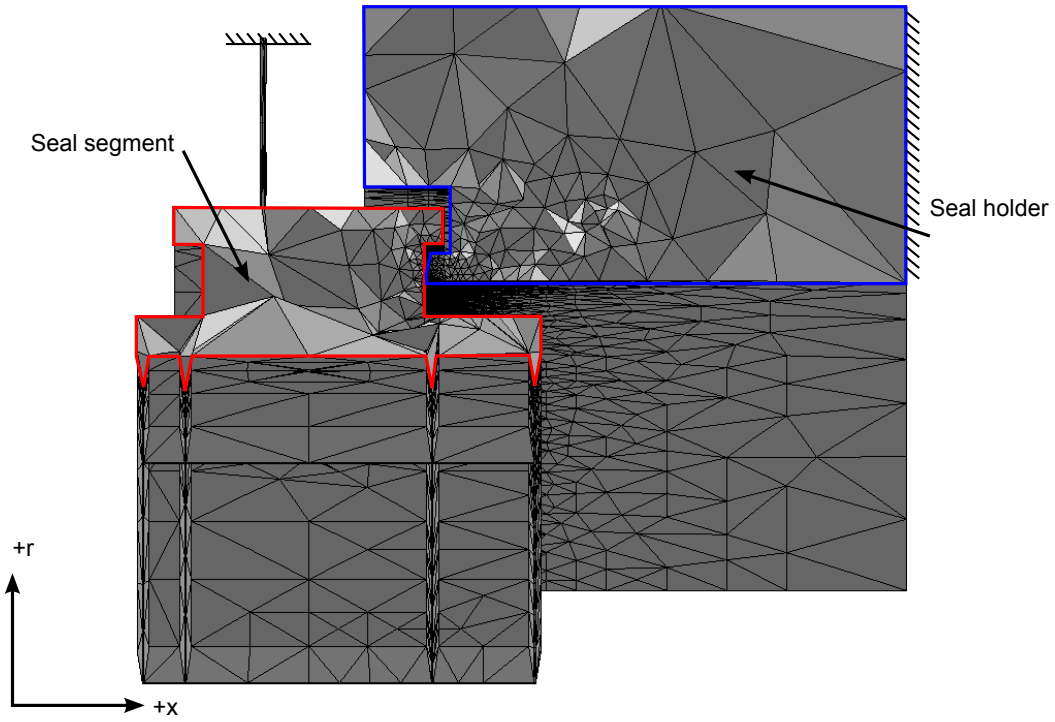

Figure 8.7: Mesh cross section for contact stress analysis.

the seal segment and seal holder were modelled. Different pressures were applied to each face to set up pressure moment and axial pressure force. A slender beam was introduced to prevent the seal segment moving radially, but without the beam taking a significant bending load due to the applied pressure moment. The pressures were chosen to give the same axial force and tangential moment as calculated in the analytical case.

Figure 8.7 shows the mesh used in the FEA model and the slender beam introduced into the model. The cell size on the contact face was set to $0.1\,\text{mm}$ and the cells were larger further away from the contact face where the stress distribution was not required with accuracy. Ideally a smaller mesh size would have been used on the contact face, but $0.1\,\text{mm}$ gave the largest number of elements that could be solved with the computing resource available.

The circumferential distribution of the contact face stress has been plotted for the minimum, maximum, mid radii of the contact face and mean stress average over the radial position, shown in Fig. 8.8. The stress ratio R_σ has been used to normalise the mean contact stress so a direct comparison can be made to analytically calculated stress

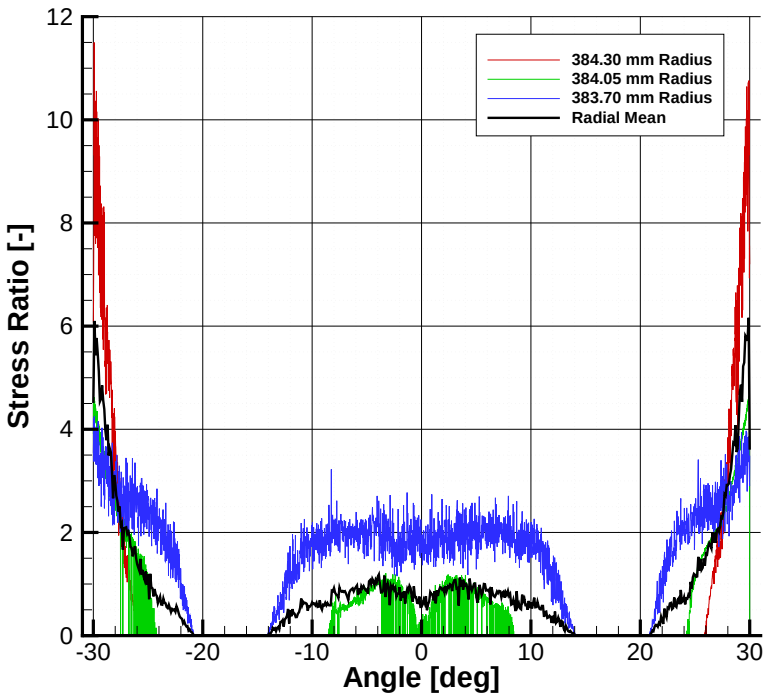

Figure 8.8: Circumferential distribution of contact stress

given in Table 8.1.

Figure 8.9 plots the circumferential distribution of contact stress calculated analytically and compares to the numerically calculated radial mean stress. Comparing the analytically assumed contact face stress distribution and the numerically calculated distribution, the analytical distribution does not capture the increase in stress at the top dead centre ($\theta = 0°$) of the segment. The sixth order polynomial gives the best agreement with the peak radial mean stress predicted by the FEA model.

Frictional moment

Once the contact face stress distribution has been calculated, it is now possible to calculate the frictional moment using Eq. (8.13). As the integration is difficult to solve analytically, it has been solved numerically using a spreadsheet assuming a number of different coefficients of static friction. The numerical integration was checked by using the integration scheme to calculate the contact face area and comparing to the area calculated analytically. An angular step size of $0.1°$ was found to give sufficient accuracy.

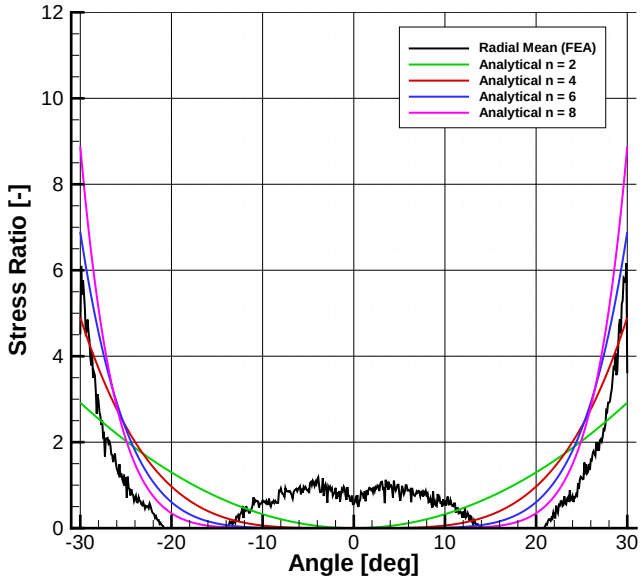

Figure 8.9: Circumferential distribution of contact stress: analytical and numerical.

The frictional moment factor, ζ, has been defined which relates the frictional moment to coefficient of friction and axial force for a given contact face geometry. The unit of frictional moment factor ζ is the *metre*. This is because it is a geometry factor describing the shape of the segment about the centroid of the segment and the non-dimensional stress distribution. It is defined in Eq. (8.25) and calculated by Eq. (8.26).

$$M_\mu = \mu \zeta F_x \tag{8.25}$$

$$\zeta = \iint_A \frac{\hat{r} R_\sigma}{A_{cont}} \, \mathrm{d}A \tag{8.26}$$

Table 8.2 gives the analytical and numerically calculated frictional moment for the 'high clearance' and 'low clearance' pressure distributions. Comparing the frictional moment calculated by FEA and the analytical model, the analytical method over predicts the frictional moment, even though the order of the stress distribution can be chosen to match the peak stress acting on the contact face. The best match for the frictional moment was constant contact stress i.e. $R_\sigma = 1$ over the whole contact face.

Wear was observed at the extreme circumferential positions on the contact face of

		Low clearance $F_x = 157$ N $M_\theta = -52.5$ N m $M_r = 0$ N m		High clearance $F_x = 172$ N $M_\theta = -61.0$ N m $M_r = 0$ N m	
		ζ m	M_μ N m	ζ m	M_μ N m
FEA		0.111	1.745		
Const. Stress		0.101	1.579	0.101	1.579
Analytical	$n = 2$	0.143	2.251	0.148	2.548
	$n = 4$	0.160	2.513	0.165	2.843
	$n = 6$	0.169	2.646	0.174	2.990
	$n = 8$	0.174	2.726	0.179	3.082

Table 8.2: FEA and analytical frictional moment.

the rotating rig seal segment, shown in Figs. 6.13 and 6.14. The volume of wear is proportional to the normal force applied, and for adhesive wear this is governed by the *Holm-Archard Equation* [90]. The wear volume is inversely proportional to hardness of the material. This provides experimental evidence that the contact face stress is highest in the side area of the seal segments. In the rotating rig, the 6 O'clock seal segment exhibited a different wear pattern. This could be due to different tangential moment acting on the seal segment due to the gravity vector acting radially away from the rotor.

8.3.3 Comparison to generated pressure moment

The goal of this section was to investigate the response of the Aerostatic Seal segment to non-uniform clearance. If the seal segment is at a non-uniform clearance the segment needs to generate sufficient pressure moment to overcome the frictional moment preventing the seal segment from moving. An analytical tool has been developed to calculate the pressure moment and a methodology to calculate the frictional moment. Now it is possible to combine these methodologies to understand the conditions at which the seal segment is able to restore a uniform clearance.

The 2D analytical method was used to calculate the pressure moment generated with the 'MESS01' seal segment design in a number of different non-uniform positions. The inlet and outlet pressure was $1.5\,\text{bar(a)}$ and $1.0\,\text{bar(a)}$ respectively and modelled assuming air at $20\,^\circ\text{C}$. The clearance of the URS side of the segment was fixed and the clearance at the DRS side of the segment varied from zero to the same clearance. This

was repeated for four fixed URS clearances: 0.1 mm, 0.2 mm, 0.4 mm and 0.8 mm. The generated pressure moment is shown in Fig. 8.10. For all the different fixed URS side clearances reducing the DRS side clearance, i.e. making the seal segment clearance more non-uniform, increased the pressure moment. If the URS side clearance was large, then the maximum pressure moment, which was when the seal segment is at zero clearance at the other side gives a more modest pressure moment compared to when the URS side clearance is small. Note that the analytical method would not converge at very low leakage areas, and this explains why the $C_{URS} = 0.1$ mm and $C_{URS} = 0.2$ mm were not tested all the way down to zero DRS clearance. Extrapolating the trend indicates that the seal would generate high pressure moment.

The reason why the high URS side clearance did not generate as much pressure moment is due to the greater clearance between the circumferential fin and the rotor, allowing flow to leak out from the DRS side pocket and reducing the pressure. Also the mean clearance of that pocket is greater due to the greater segment angle ψ which reduces the pressure in the pockets.

Together this means that at extreme segment non-uniformity the pressure moment is small, and so it is unlikely that the seal segment is able to restore uniform clearance. If the DRS side clearance was fixed and the URS side varied the results would be the same, only the pressure moment would be in the opposite direction.

Figure 8.10 also includes the frictional moment that the seal segment has to overcome, assuming the seal segment operating at the high clearance and based on the contact stress distribution calculated using SolidWorks and a coefficient of static frictions of $\mu_{stat} = 0.1$. (This is the horizontal dashed line.) Therefore the seal segment would start to restore itself to an even clearance only when the high clearance side of the seal segment is at a fairly low clearance of 0.2 mm and the low clearance side of the segment approaches zero. When the high clearance side of the segment is at higher clearances, such as 0.4 mm and 0.8 mm there is insufficient pressure moment to overcome the frictional moment. The coefficient of friction assumed was a little smaller than that calculated from the experiments conducted in Chapter 5 and so the frictional moment could be a little higher. Assuming a coefficient of friction of $\mu_{stat} = 0.6$, as in the design process would increase the frictional moment significantly, and as a consequence the segment will not restore to a uniform circumferential clearance.

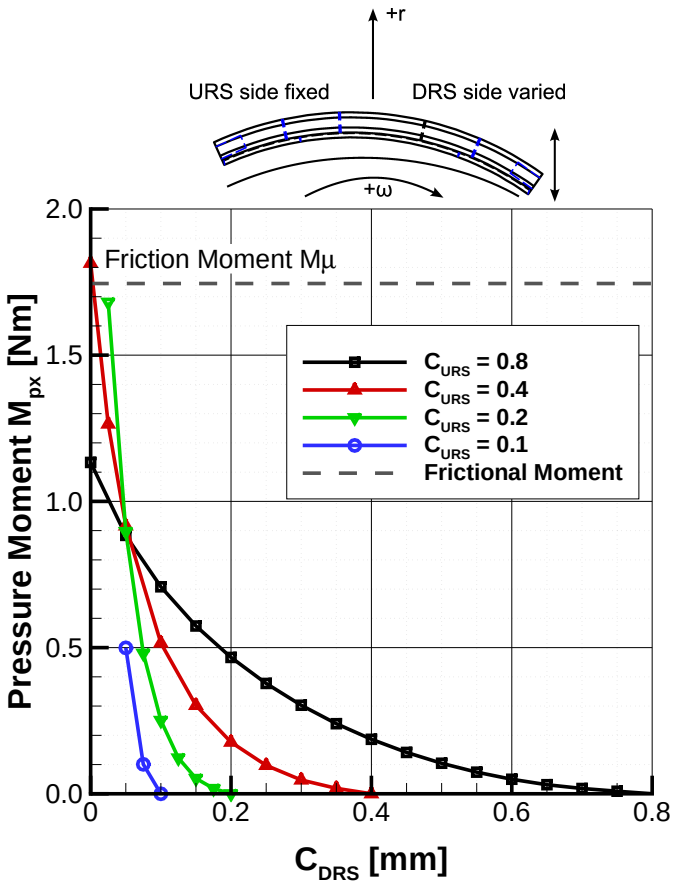

Figure 8.10: Pressure moment generated with segment non-uniform clearance.

As previously discussed in Section 5.5, the analytical model does not capture all of the observed behaviours of the Aerostatic Seal well, and so this analysis will also be effected by these limitations. However the model clearly demonstrates the difficulties for the seal segment to restore uniform clearance.

8.4 Fixed Non-uniform Clearance

This section investigates the effect of non-uniform clearance on the performance of the Aerostatic Seal, and tests the ability of the seal segment to restore uniform clearance experimentally. To achieve this a number of fixed clearance tests were carried in the same manner as previously discussed in Section 5.5.

The seal segment was fixed into a non-uniform clearance position by fixing different sized shims at each side of the segment. Three different positions were tested: $C_{URS} = 0.80\,\text{mm}$ and $C_{DRS} = 0.20\,\text{mm}$, $C_{URS} = 0.20\,\text{mm}$ and $C_{DRS} = 0.10\,\text{mm}$ and finally $C_{URS} = 0.20\,\text{mm}$ and $C_{DRS} = 0.00\,\text{mm}$. A further three tests were carried out at the same clearances but where the DRS side of was at the largest clearance rather than the URS side of the segment. The tests were conducted with atmospheric back pressure, and the results are reported at a pressure ratio of $PR = 1.5$. The seal segment was manually held onto the rotor surface and the inlet pressure varied, as described in Section 5.5. The mean of the pressures was taken over a small range of time, typically $0.2\,\text{s}$ giving a sample size of 120. What should be expected is that the side of the segment at the lowest clearance would have a higher pressure in the circumferential pockets to help restore the segment to a uniform clearance.

Fig. 8.11 shows the mean pressure coefficient when the seal segment was positioned at a non-uniform clearance. Figure 8.11a is where the URS side of the segment was at the highest clearance, and Fig. 8.11b when the DRS side of the segment was at the highest clearance. The high clearance was $0.80\,\text{mm}$ and the low clearance $0.20\,\text{mm}$. The pressure ratio was $PR = 1.5$. $Cp1$, $Cp2$, $Cp3$ is the pressure coefficient in the P1, P2, and P3 axial pockets.

First consider when the URS side of the segment was at the highest clearance, shown in Fig. 8.11a. The P1 pocket shows a significant difference between the two sides. At the high clearance side of the segment the pressure was below that of the downstream P2

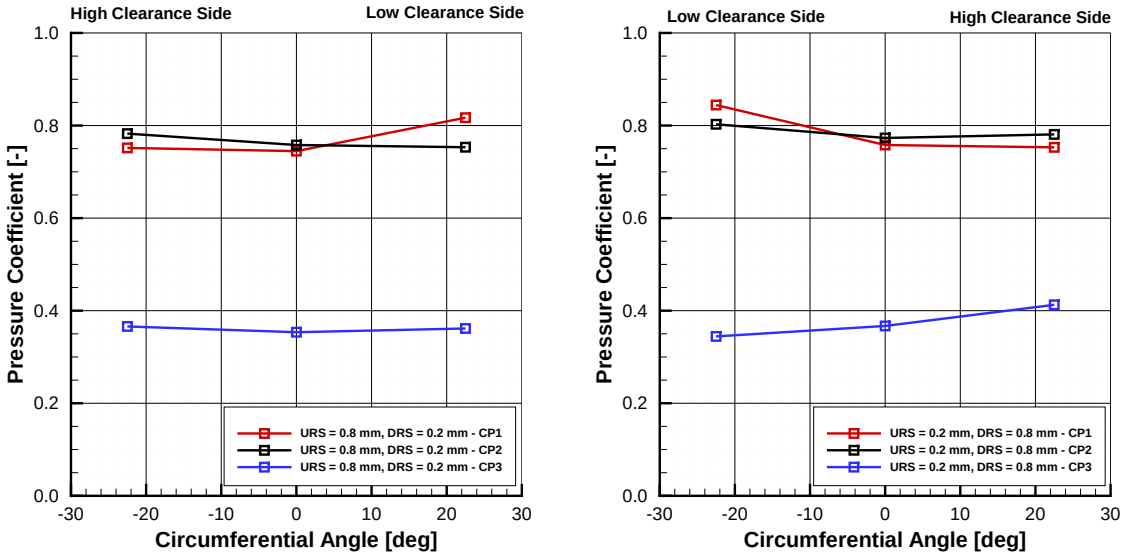

(a) $C_{URS} > C_{DRS}$ (b) $C_{URS} < C_{DRS}$

Figure 8.11: Circumferential pressure distribution with non-uniform segment clearance.

pocket. This was due to the pressure recovery effect in the first pocket at high clearance already observed in Section 5.5. The P2 pocket pressure was lower at the low clearance side where a high pressure is needed to restore the segment to a uniform clearance. The P3 pocket pressures are fairly even.

A similar result was found when the DRS side of the segment was at the highest clearance, shown in Fig. 8.11b. The P1 pressure was highest on the low clearance side. The P2 pressure slightly higher on the low clearance side and the P3 pocket pressure significantly higher on the high clearance side. This has a negative impact on the pressure moment and in fact there was a pressure moment acting to increase the clearance at the high clearance side of the segment.

The circumferential pressure distributions measured experimentally were used to calculate the pressure moment acting about the seal segment centroid. The results are shown in Table 8.3 and also include the analytically expected pressure moment. The analytical pressure moment could not be calculated when the clearance on one side of the segment was zero as the analytical method would not converge. The experimental pressure moment generated when the DRS side of the segment was at the highest clearance shows a pressure moment in the opposite direction to the analytically expected pressure moment.

C_{URS} mm	C_{DRS} mm	Exp. M_x N m	Analytical M_x N m	C_{URS} mm	C_{DRS} mm	Exp. M_x N m	Analytical M_x N m
0.80	0.20	-0.086	-0.47	0.20	0.80	0.31	0.47
0.20	0.10	-0.21	-0.25	0.10	0.20	-0.13	0.25
0.20	0.00	-0.34	-	0.00	0.20	0.40	-

Table 8.3: Experimental and analytical moment due to non uniform clearance.

The experimentally calculated moment was acting to make the circumferential clearance more uniform, except when $C_{URS} = 0.10$ and $C_{DRS} = 0.20$. There were differences between the same non-uniform clearance but different sides of the segment at the lowest clearance. The experimentally calculated moment was more variable. Variation between sides was most likely due to variations in the axial clearance due to manufacturing variations.

Overall the pressure moment generated by the seal segment was sensitive to small variations in the circumferential and axial clearance. The pressure moment was also influenced by the pressure recovery effect in the first pocket at high clearance.

8.4.1 Comparison to even clearance

For each of the non-uniform fixed clearances, the mean circumferential pressure coefficient and mean clearance were calculated. The pressure response was then compared in Fig. 8.12 to the response when the seal segment clearance was uniform in the tests described in Section 5.5. All tests were at a pressure ratio of $PR = 1.5$, and both sets of non-uniform tests are shown. The plot shows that there was little difference in the mean pressure coefficients calculated, and so the mean clearance is still the governing factor producing the radial pressure force. The only exception was at 0.1 mm where the $C_{URS} > C_{DRS}$ case pressure coefficient was slightly below the other non-uniform case and even case, indicated with the arrow in Fig. 8.12.

The effect of non-uniform clearance on the response of the seal segment was also observed in the testing conducted in the rotating rig - see Section 6.3.1. Here it was observed that the seal segment would not move away from the rotor when operating with non-uniform clearance until the mean clearance of the segment was low enough, even if the clearance in the side circumferential pocket was low. Therefore if the seal segment was to operate with a highly non-uniform clearance there is potential for the

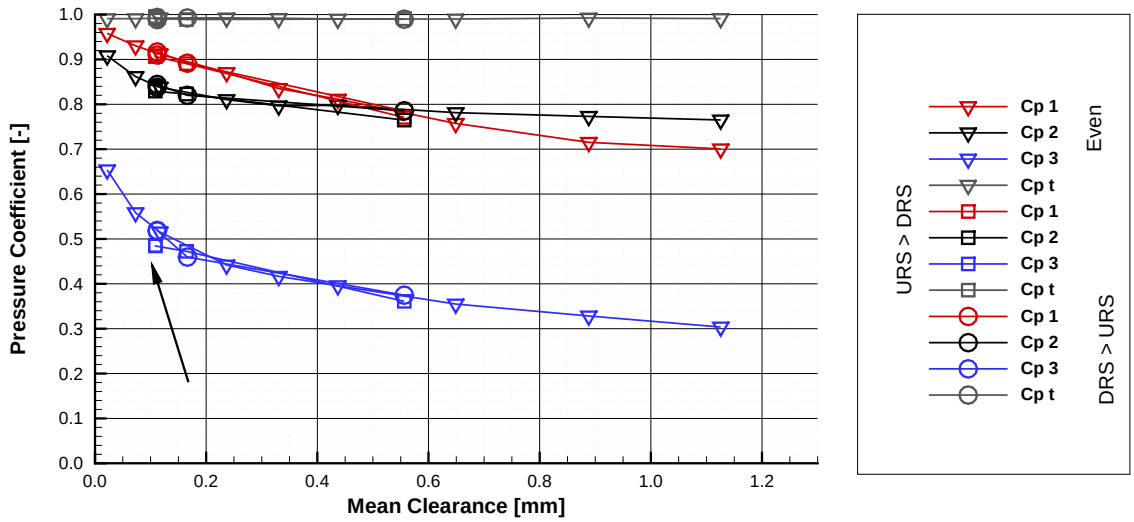

Figure 8.12: Pressure coefficient variation: even and uneven seal segment

rotor to rub on the lowest side of the segment before the segment will move away.

8.5 Conclusion

The subject of this chapter was understanding the aspects of non-uniform seal segment operation. The key question to answer was: why the seal segment initially goes to a non-uniform clearance, and why the segment does not restore itself to a uniform circumferential clearance.

- Small variations in the coefficient of friction around the circumference of the seal segment will lead to an uneven friction torque, and are responsible for the uneven clearance when the seal segment has closed.
- The circumferential pockets implemented in the seal design MESS01 do not generate sufficient self-righting moment to correct the uneven clearance, particularly if the clearance at one side was large. The contact face stress distribution is not evenly distributed circumferentially or radially, and has been investigated analytically and numerically. Experimentally observed pressure distributions confirm that little circumferential pressure moment is generated. The pressure distribution is not symmetric which could be due to variations in the clearance of the restrictions.

The frictional moment due to the contact face stress is large, and made larger by high stress areas furthest away from the centroid.

- It was found that the mean pressure coefficient when the seal segment was at a non-uniform clearance was similar to the uniform clearance tests performed previously.

The cause and effects of non-uniform operating clearance have been investigated in this chapter. The next chapter will now link all the experimental findings together in a recommended design for the Aerostatic Seal, and includes test results conducted in a steam environment.

Chapter 9

Steam Turbine Implementation

9.1 Introduction

The work described in previous chapters has experimentally tested a number of different Aerostatic Seal designs in rotating and non-rotating experimental facilities, all of which operated in air. The tests in air proved that the Aerostatic Seal was able to respond to high speed rotor radial transients. The next step was to test the seal in an environment closer to steam turbine operation.

The first section of this chapter summarises the experimental testing of the Aerostatic Seal in a high temperature steam test facility at TU Brauschweig in Germany. The rig was designed for testing seals in a steam environment. The rotor was able to be translated relative to the casing of the rig to simulate low speed transients. A new Aerostatic Seal design was manufactured, 'STR-IP6-07A1', described in Section 3.5, as well as the necessary seal carrier rings to interface with the facility. The design and manufacture of the Aerostatic Seal, and processing and interpreting the results was conducted as part of this thesis; the physical testing was undertaken by TU Braunschweig. The seal was manufactured from X22CrMoV12-1[1], a martensitic stainless steel that is representative of steam turbine materials. The results of the test campaign showed that the Aerostatic Seal was able to close in and retract, and also respond to the translation of the rotor.

The second section of this chapter describes a proposed generic Aerostatic Seal seal design for application into a steam turbine. The proposed design is based on experi-

[1] St12T is the GE/Alstom designation for X22CrMoV12-1

mental and analytical results gathered throughout the thesis.

9.2 The Aerostatic Seal in a steam environment

The results reported in Chapters 5 to 8 clearly demonstrate the dynamic capabilities of the Aerostatic Seal. The next step was to test the capability of the Aerostatic Seal to operate in a high temperature steam environment, using realistic steam turbine materials and with realistic rotor surface speeds.

The operation of the Aerostatic Seal depends on the level of friction between the seal segments and the seal holder. A literature survey was conducted into the effect of high temperatures on the coefficient of friction which revealed that generally friction coefficient increased with temperature. A table of coefficients of friction found by various researchers is given in Appendix G. Therefore the key for the experimental campaign was to show that the seal segments would still 'close in' towards the rotor surface as the pressure difference across the seal was increased, and the seal segments were able to track the rotor position during a rotor translation, showing that the expected increase in friction due to high temperature was not prohibitive to dynamic operation of the Aerostatic Seal.

Also of importance was the effect of prolonged operation of the seal. In previous testing at Durham University the tests were of short duration due to the nature of the test facility (maximum test duration was $100\,\mathrm{s}$). The testing in steam was conducted in a five day long test to see if any degradation in performance was found during the course of the test.

9.2.1 Rig and Seal Design

The Aerostatic Seal was tested in the rotating seal test facility at TU Braunschweig. High pressure and temperature steam is supplied to the facility from a power station boiler.

The test facility is constructed in a double flow arrangement with the high pressure steam entering the high pressure chamber in the centre, and flowing outwards through two seals under test. Each side was referred to as the 'motor side' and the 'displacement side'. The rotor diameter is $299.8\,\mathrm{mm}$, and so is roughly half that of a typical power generation steam turbine. A cross section of the facility is shown in Fig. 9.1.

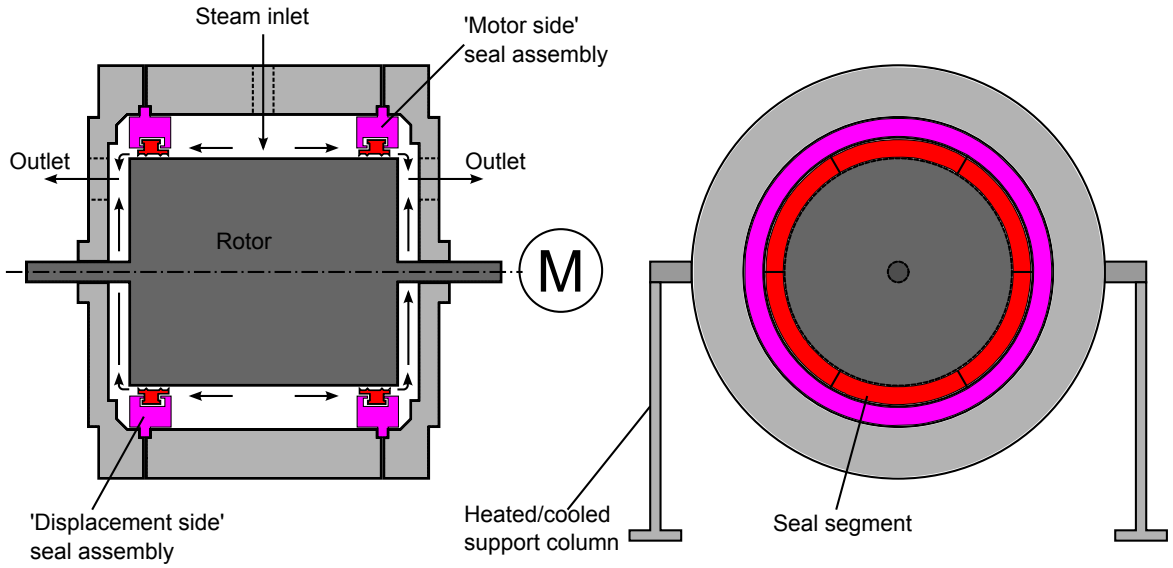

Figure 9.1: Cross section of rotating steam facility at TU Braunschweig.

The maximum possible inlet pressure to test facility was 50 bar, and typically 400 to 500 °C temperature depending on the operation of the power plant. The steam exiting each side of the test facility was directed back to the boiler, and the pressure at the outlet of the seal depending on the boiler pressure and the pressure losses in the pipework leading back to the boiler. The rotor is driven by a 80 kW motor capable of 10 000 rpm to match rotor surface velocity.

The facility also has the ability to translate the high pressure casing relative to the rotor to simulate low speed rotor excursions. Relative movement of the rotor and casing is achieved by heating or cooling the high pressure chamber support legs, thereby altering the thermal expansion of the legs and moving the casing. The relative position between the rotor and casing was measured during operation and a PID control loop used to accurately control the level of eccentricity. Full details on the facility and its capability can be found in previously published works [50], [54], [96].

The facility was equipped with instrumentation to measure the mass flow rate through the seal at each side, the rotor speed, torque and eccentricity, and inlet and outlet pressures and temperatures. The mass flow rate through the seal was measured on the outlet of the test facility for the motor side and displacement side seals using an orifice plate. The pressure was measured on the cover plate immediately behind each seal, and the temperature by a probe directly behind the seal enveloped in the steam flow.

Upstream pressure was measured in the central high pressure chamber, and upstream temperature measured by a thermocouple located in the steam flow in the high pressure chamber. Rotor speed and torque were measured by the motor controller.

The design for use in the steam tests was conducted using the standard analytical design methodology. The details of the design are available in Section 3.5 in Chapter 3.

The TU Braunschweig steam test facility was limited to $0.5\,\mathrm{kg\,s^{-1}}$ total mass flow rate. Therefore the design inlet pressure was at the low end of the facility capability to ensure that the mass flow through the seals would not go beyond $0.5\,\mathrm{kg\,s^{-1}}$when retracted. The rotor speed was chosen to produce a surface velocity of $137\,\mathrm{m\,s^{-1}}$ which was representative of a typical steam turbine rotor surface velocity.

Previous testing of the Aerostatic Seal used seal segments manufactured from structural mild steel as this was readily available and with good machining characteristics. The seal segments and seal carrier ring designed for testing in steam was manufactured from X22CrMoV12-1, which is a 12% chromium martensitic stainless commonly used for steam turbine components. As with other segmented steam turbine gland seals, the seal segments and seal carrier ring were machined from forged rings.

Testing in the Durham Rotating Seals test facility (see Chapter 6) found that there was wear on the contact face of the seal segments due to movement of the segments. Therefore it was decided to introduce a chromium carbide coating on the seal segment contact face to prevent excessive wear for a steam turbine application.

The literature survey carried out to investigate the effect of temperature on the coefficient of friction included frictional coefficient data of chromium carbide at elevated temperature, as seen in Appendix G. Although no published data was found for chrome carbide on X22CrMoV12-1, in a high temperature steam environment, and with similar normal force, it was found that generally the high temperature and high surface roughness would increase the coefficient of friction. Therefore the chrome carbide coating on the contact face was ground to achieve a smooth and even surface finish, as recommended by DellaCorte and Sliney [97].

The circumferential springs used in the seal design were custom designed to meet the geometric and spring force requirements of the Aerostatic Seal design. The springs were manufactured from Inconel 718, and the spring rate was $10.2\,\mathrm{N\,mm^{-1}}$ at $500\,^{\circ}\mathrm{C}$.

9.2.2 Results and Discussion

The testing was conducted in two parts. First there was a five day long test with the seal segment free to move radially in the seal holder. Second there was a test with the seal segments fixed at a known clearance to aid calculation of the seal clearance in the first test.

Figure 9.2 gives the inlet pressure and temperature, outlet pressure, rotor eccentricity and speed, and mass flow rate for the whole five day test. Figure 9.2a is for the 'displacement side' seal, and Fig. 9.2b the 'motor side' seal. Initially the test facility was heated by letting a small quantity of steam through the inlet valve and the rotor speed increased to 8760 rpm, which gave a typical rotor surface speed of a 3600 rpm steam turbine. The inlet valve was then opened gradually to increase the pressure difference across the seal, until the seal segments 'close in' towards the rotor. Once close in had occurred the inlet pressure was held constant. The rotor was then gradually displaced four times over approximately 30 to 60 minutes to observe the capability of the seal to track the position of the rotor. Between the rotor translations the inlet pressure was maintained to keep the seal at the operating clearance for 23 hours to observe if there was any change in seal response to the rotor translation after the seal had operated at high temperature and pressure for a long duration. Throughout the test the logging frequency was $0.5\,\mathrm{Hz}$.

The test began around midday on day 1, at which point the test rig temperature and inlet pressure was increased. The temperature of the inlet steam was typically around $420\,^{\circ}\mathrm{C}$ during the test, and set by the operation of the power plant boiler. Initially the inlet pressure was increased quite rapidly and which led to rotor contact and the rotor stopping, which was rotating at 500 rpm. On the second attempt the rotor speed was increased to 8760 rpm, the inlet pressure increased more slowly and the seal segments closed in successfully. Seal segment close in was accompanied by an increase in the inlet pressure. The mass flow rate through the seal stayed fairly constant due to the increased inlet pressure, despite the seal moving to a lower operating clearance. The inlet pressure was reduced to $7.5\,\mathrm{bar(g)}$. The outlet pressure stayed constant for both seals at approximately $3.1\,\mathrm{bar(g)}$. The outlet pressure was expected to be $6.0\,\mathrm{bar(a)}$ at outlet, but as there was no independent control over the outlet pressure this could not be changed. As shown in the previous testing in air, increased pressure across the seal

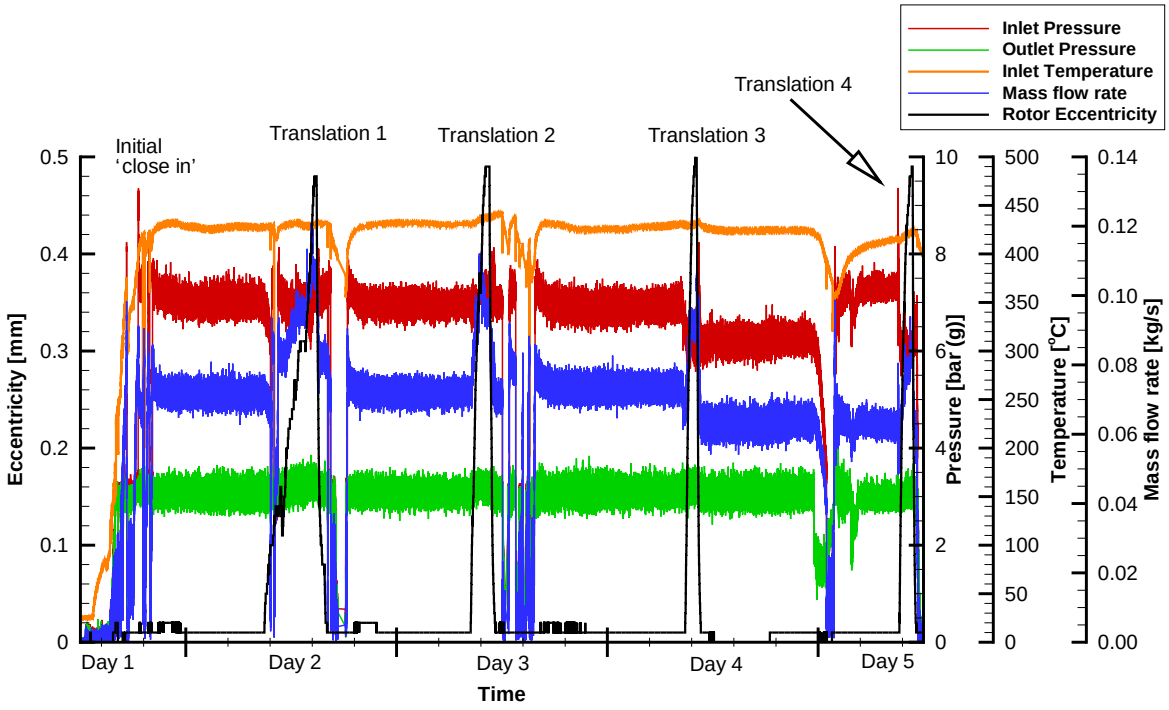

(a) Displacement side seal

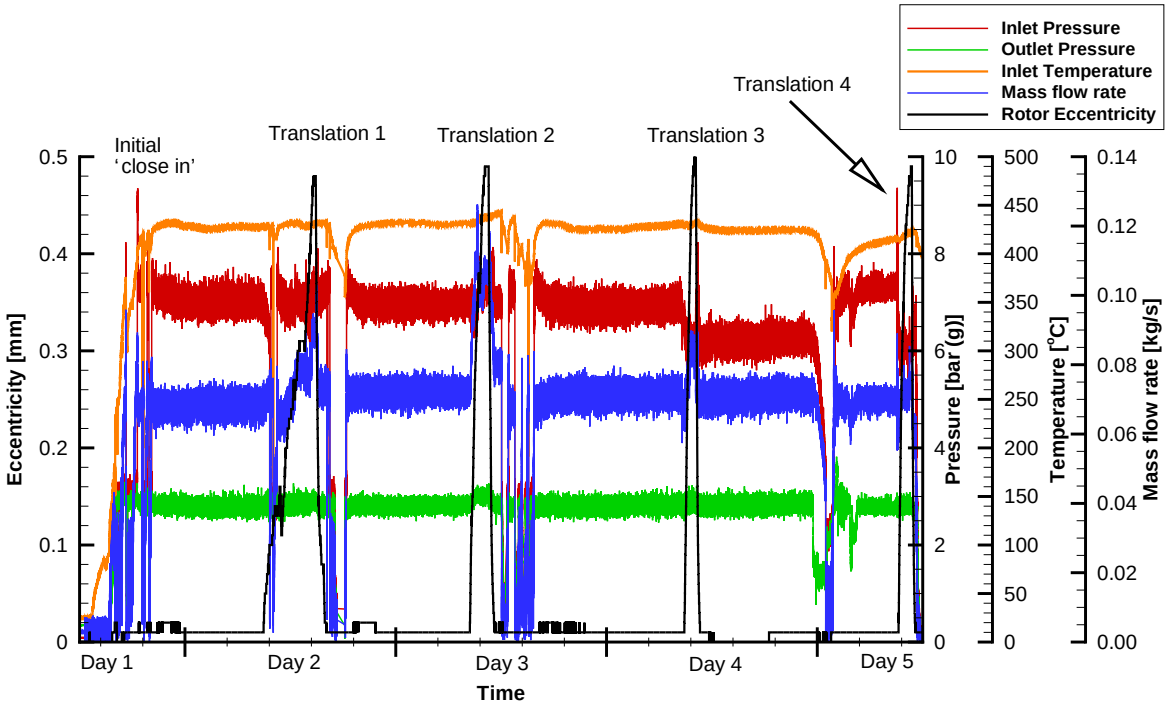

(b) Motor side seal

Figure 9.2: Overview of steam test results

does not affect the operation of the seal after it has closed in.

Steady operation was maintained over the night and the first translation of the rotor took place around midday of day 2. During the translation the rig was tripped a number of times which would cause the rotor speed to reduce to 500 rpm and the inlet valve to shut, causing the seal to retract. The causes were not to do with the Aerostatic Seal, but the test facility operating parameters going beyond the limits due to higher than normal power station ambient air temperature. The inlet pressure was increased again to achieve seal close in and the rotor translation continued to $0.5\,\text{mm}$ eccentricity and back again.

The translations of the rotor were repeated a further three times (day 3, 4 and 5), and are labelled on Fig. 9.2. After the 2$^{\text{nd}}$ translation the rig again tripped out a number of times before steady operation was re-established. The pressure for the 3$^{\text{rd}}$ translation was reduced to $7.5\,\text{bar}(\text{a})$ rather than $7.5\,\text{bar}(\text{g})$. The pressure after the 3$^{\text{rd}}$ translation, between day 4 and 5 was reduced due to an issue with the boiler at the power plant. After the 4$^{\text{th}}$ translation test the rig was shut down and allowed to cool.

The following sections discuss the segment 'close in' and rotor translation in detail.

Seal 'close in' behaviour

The mass flow rate and pressure difference for a 30 minute time period is shown in Fig. 9.3. The displacement side seal is shown in Fig. 9.3a, and the motor side seal shown in Fig. 9.3b. Initially the mass flow rate and pressure drop across the seal was low and the seal segments were in the retracted position. The outlet pressure was constant throughout the test at 3.6 bar (a), and the inlet steam temperature approximately constant at $420\,^{\circ}\text{C}$. The rotor was held in the centric position throughout this part of the test.

From 18:05 the inlet steam valve was opened slowly which increases the mass flow rate through the seal. At 18:34 the seal segments close in, causing a large increase in the pressure difference across the seal, and a slight drop in the mass flow rate through the seal. The leakage through the seal depends on the leakage area of the seal, the pressure ratio across the seal, and the fluid density. (Pressure ratio (PR) has been defined at the absolute inlet pressure divided by the absolute outlet pressure.) Therefore despite the seal segment moving towards the rotor and reducing the leakage area of the seal, the mass flow remains virtually the same as the pressure ratio across the seal has increased.

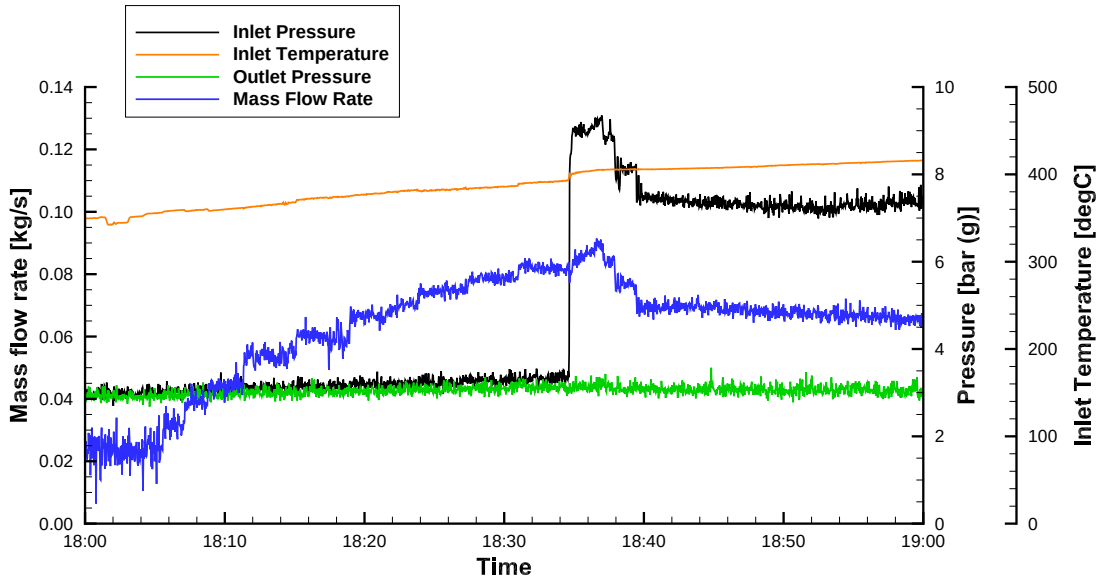

(a) Displacement side seal

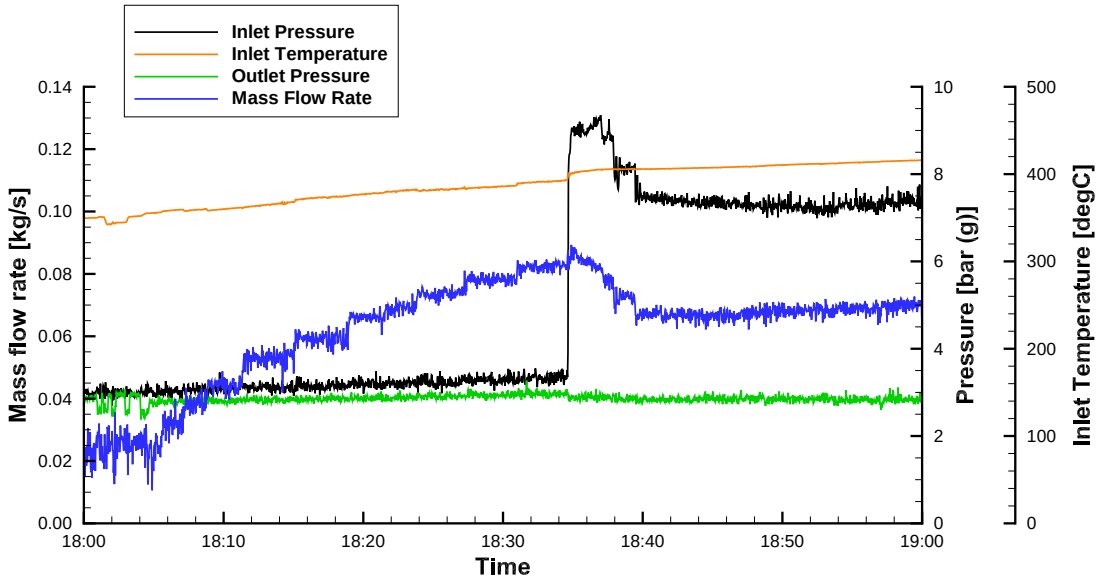

(b) Motor side seal

Figure 9.3: Close in behaviour of Aerostatic Seal

Rotor translation

Four rotor translations were carried out within the test, inter spaced with periods of running with the rotor in the centric position. As the rotor was moved the seal segments above the rotor need to move away from the rotor, and the segments below the rotor need to move towards the rotor to maintain the same operating clearance.

Figure 9.4 shows the seal rotor eccentricity, mass flow rate and inlet and outlet pressures seal during the 3rd rotor translation. The displacement side seal is shown in Fig. 9.4a and the motor side seal in Fig. 9.4b.

During the translation of the rotor from the centric to eccentric position the inlet pressure to the seals decreases and the mass flow rate through the seals increases indicating that the clearance of the seals was increasing, indicated by the arrows labelled as '**0**' in Fig. 9.4. The outlet pressure stayed constant throughout the rotor translation. The inlet pressure however also shows sudden increases in pressure indicating that the seal segments are decreasing the seal clearance, for example the region marked '**1**' in Fig. 9.4a, and the region marked '**2**' in Fig. 9.4b. The mass flow rate through the seal stays constant. When the motor side seal reduces clearance, the displacement side seal was subject to an increased pressure, and vice versa. This was because both seals were connected to the same inlet plenum chamber.

Maximum eccentricity of the rotor was achieved at approximately 10:05, and held for approximately 5 minutes. The motor side seal then moves to a lower clearance (labelled as **2**), identified by an increase in inlet pressure and a reduction in mass flow rate. The displacement side seal stays at the same clearance as the mass flow rate also increases. At 10:10 the rotor started to return to the non-eccentric position.

As the rotor was returned to the centric rotor position, the motor side seal clearance reduces, labelled as '**4**' and '**6**' in Fig. 9.4b. During the same time the displacement side seal shows no easily identifiable movements to reduce clearance, however at the region marked with an arrow labelled '**3**', the clearance reduces gradually. This will be discussed further in the following section.

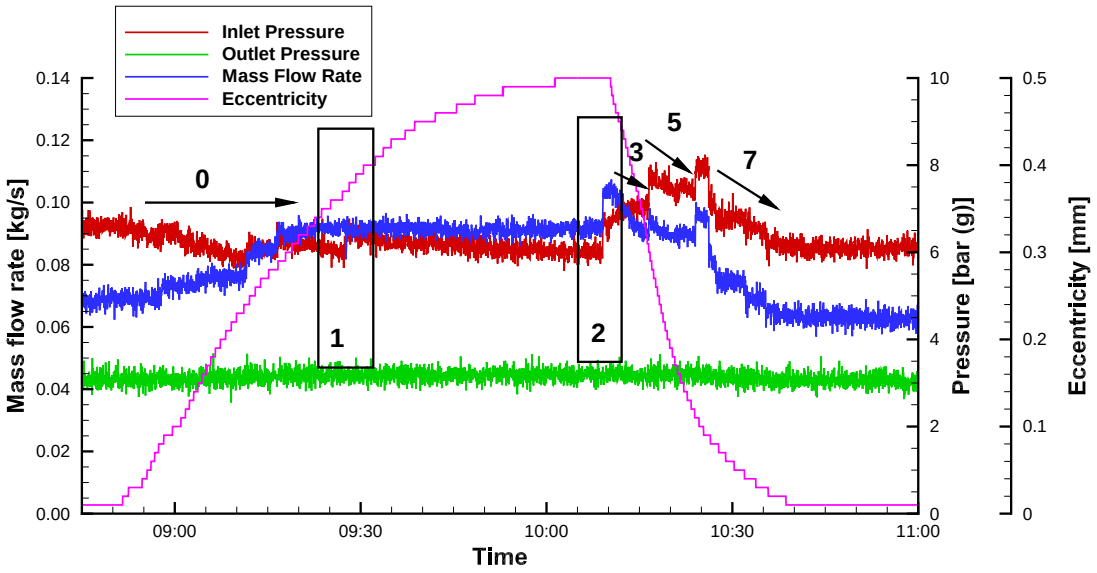

(a) Displacement side seal

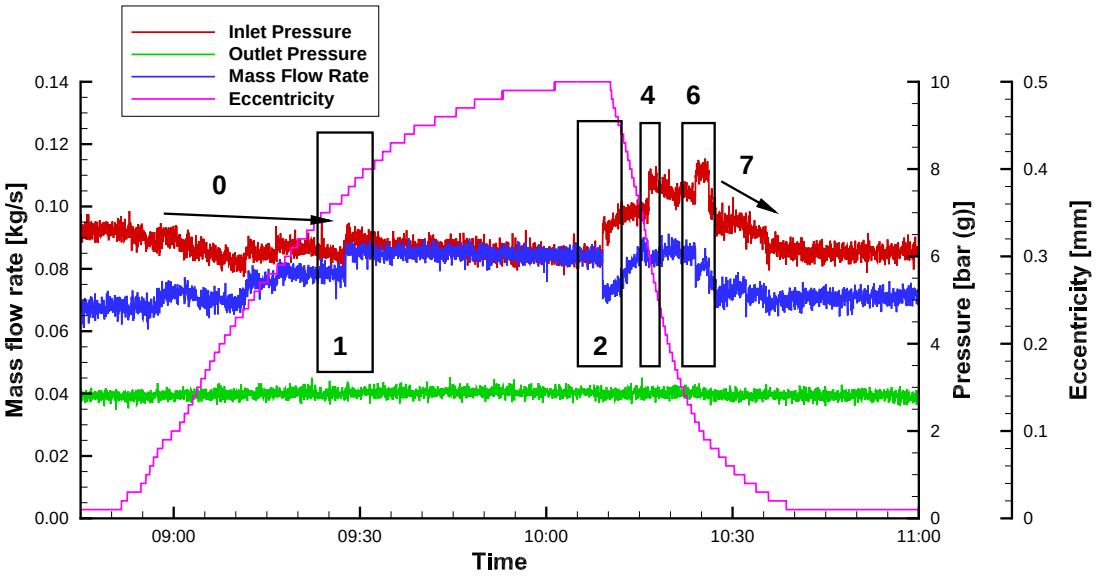

(b) Motor side seal

Figure 9.4: Displacement and motor side seal response during 3rd rotor translation.

9.2.3 Clearance and Friction Calculation

During the tests conducted with steam there was no method to directly measure the clearance of the individual seal segments. Therefore the seal mass flow rate and pressure ratio was used to estimate the mean clearance of the seal during operation by comparing the experimental results to the analytical model. Figure 9.5 shows experimental mass flow rate and pressure ratio during close in, and is the same data as plotted in Fig. 9.3. The black and red lines, with no points, refer to the displacement and motor side seals respectively. The experimental data has been smoothed to remove noise, and which was amplified by converting the inlet and outlet pressure into pressure ratio.

The experimental results have been plotted over a contour plot of clearance calculated using the analytical model described in Section 3.3. The outlet pressure was fixed at $4.1\,\mathrm{bar(a)}$, similar to the experimental tests. The mass flow rate at the maximum static clearance was calculated by the analytical tool for a range of static friction coefficients, and is shown as thick pink lines for the maximum static clearance. Side leakage through the seal was also calculated by the analytical model and is why the mass flow rate through the seal is not zero when at zero clearance.

Figure 9.5 allows the clearance of the seal during 'close in' to be estimated, indicating that the seals have transitioned from a retracted clearance of approximately $0.80\,\mathrm{mm}$ to an operating clearance of approximately $0.09\,\mathrm{mm}$. Arrows on the graph show the seal segment as it transitions from a retracted clearance to the lower operating clearance.

To validate the analytical model for calculation of the seal clearance, a test was conducted with the seal segment fixed at a known cold clearance. The results from such a test are also plotted on Fig. 9.5. The outlet pressure of the seals varied more in the fixed test than during the active seal test, due to the increased flow rate. Therefore the measured mass flow rate has been normalised by the inlet pressure, temperature and the specific heat capacity at constant pressure, as shown in Eq. (9.1). Standard temperature T_s was $673\,\mathrm{K}$, i.e. $400\,^{\circ}\mathrm{C}$. Standard inlet pressure P_{ins} was calculated from the pressure ratio and the desired outlet pressure of $4.1\,\mathrm{bar(a)}$, as shown in Eq. (9.2). The standardised specific heat capacity c_{p_s} was calculated from the standardised inlet pressure and temperature using the *XSteam* Matlab code freely available [87]. This method of standardising the flow is similar to that other authors have used to compare different seals [59], [77], but includes c_p to account for property changes due to the change of steam

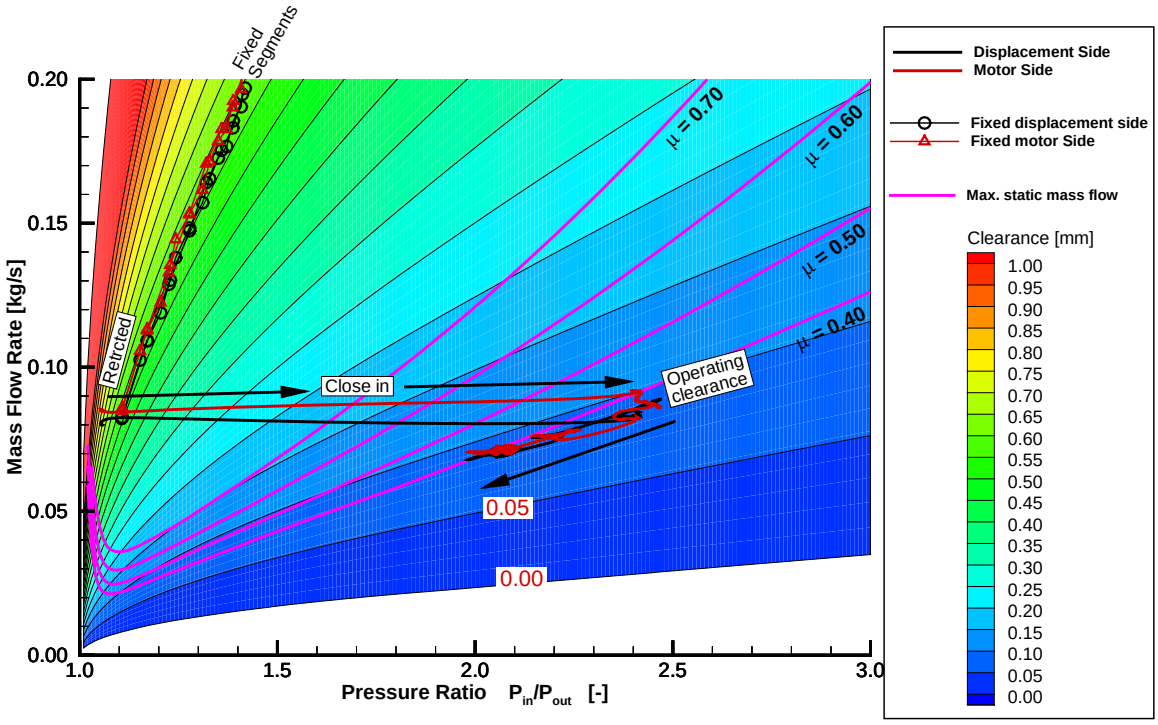

Figure 9.5: Mass flow rate and pressure ratio during 'close in'

pressure and temperature.

$$\hat{\dot{m}} = \dot{m}\sqrt{\frac{c_p}{c_{p_s}}}\sqrt{\frac{T}{T_s}}\frac{P_{ins}}{P_{in}} \tag{9.1}$$

$$P_{ins} = PR \times 4.1\,\text{bar(a)} \tag{9.2}$$

Table 9.1 shows the measured cold clearances after the active seal segment test, and before the fixed seal test. As both the rotor and the Aerostatic Seal carrier ring were made from martensitic stainless steel, it was assumed that the coefficient of linear expansion was the same for both materials, and hence there would be no effect on the clearance of the fixed seal segments. TU Braunschweig calculated that the rotor radius would increase by 0.08 mm due to the rotation of the rotor. Therefore the hot and rotating clearances were 0.08 mm smaller than the cold clearances. The cold clearance was measured with feeler gauges with resolution of 0.05 mm. The side leakage discharge coefficient (see Section 3.3) was modified from $C_D = 1.8$ to $C_D = 1.0$ to give agreement between the analytical model and the fixed seal segment tests. The side leakage dis-

	Clearance	Max. / mm	Min. / mm	Mean / mm
Retracted	Displacement Side	1.30	1.00	1.15
	Motor Side	1.20	1.00	1.15
Fixed	Displacement Side	0.70	0.55	0.65
	Motor Side	0.85	0.60	0.70

Table 9.1: Measured cold clearances.

charge coefficient is different from the value found from the non-rotating rig due to the addition of keys between the seal segments.

Overall this section has described the methodology for estimating the seal mean clearance, allowing the mean clearance to be estimated during 'close in'.

Rotor Translation

Figure 9.6 shows the mass flow rate and pressure ratio during the 3rd translation plotted on the same contours of clearances as in Fig. 9.5. The mass flow rate and pressure ratio was smoothed to remove signal noise. Labels on the figure indicate the same points labelled on Fig. 9.4. Initially the seal was occupying a location on the graph with a clearance of about $0.10\,\mathrm{mm}$. Translating the rotor causes the clearance to increase and the pressure ratio to drop due to the increased seal area, and so the seal operating point moves to the left on the graph (labelled as **'0'** in Fig. 9.6), indicating increased clearance. The displacement side seal, shown in Fig. 9.6a, reduces clearance when the seal clearance reaches $0.18\,\mathrm{mm}$ (labelled **'3'**). Similarly the motor side seal, shown in Fig. 9.6b, reduces the seal mean clearance when the clearance reaches around $0.16\,\mathrm{mm}$ (labelled **'2'**). Previously it was discussed that the displacement side seal segment gradually reduced clearance at point **'3'** in Fig. 9.4, but which was not easily identifiable. This gradual reduction in clearance is much easier to see in Fig. 9.6.

From the performance map of the translation, in Fig. 9.6, it was possible to determine the apparent coefficient of static friction by observing the point on the clearance contour when the segment transitions to a lower clearance. For the displacement side seal, shown in Fig. 9.6a, this was $\mu_{stat} = 0.70$, and for the motor side seal, shown in Fig. 9.6b, this was approximately $\mu_{stat} = 0.65$. Note that the coefficient of friction from the resting point of the segment during close in, shown in Fig. 9.5, was lower at $\mu_{dyn} = 0.40$. This

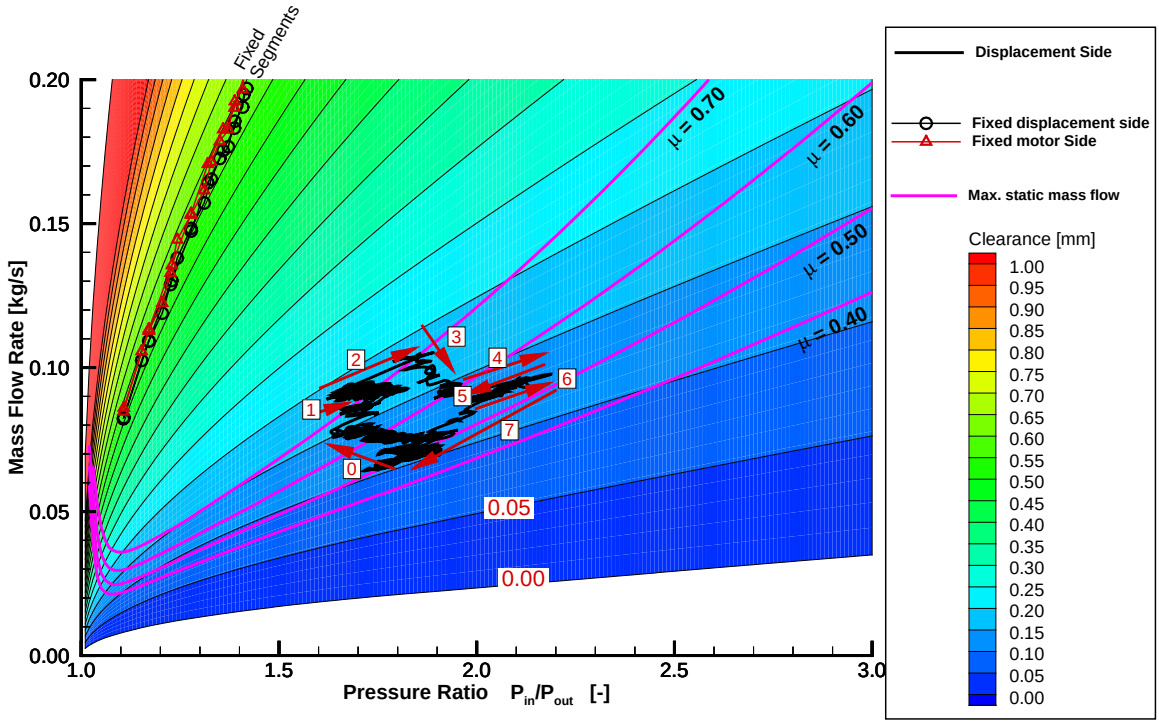

(a) 3rd Translation: displacement side seal

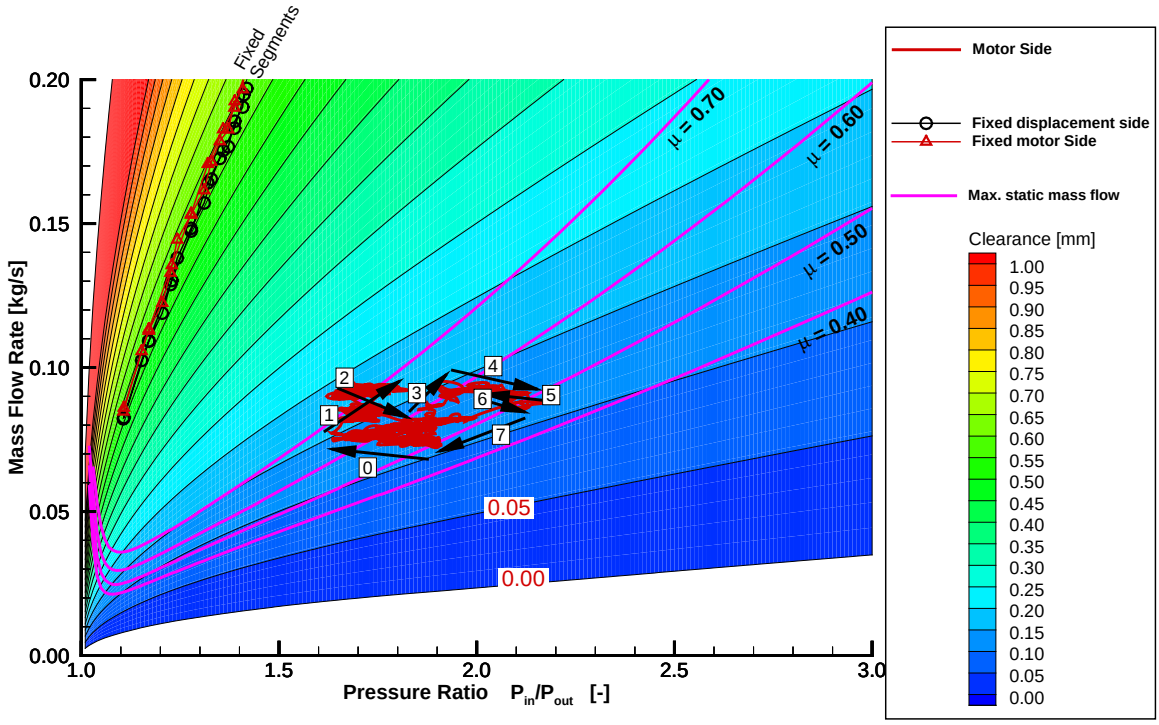

(b) 3rd Translation: motor side seal

Figure 9.6: Mass flow rate and pressure ratio during 3rd rotor translation.

would be consistent with dynamic friction.

9.2.4 Steam Testing: Conclusion

Successful steam testing represents a major milestone for the development of the Aerostatic Seal. The key finding was that the effects of high temperature steam and realistic steam turbine materials do not prevent the Aerostatic Seal from operating dynamically. The testing also matched typical steam turbine rotor surface velocity. As the test was conducted with the same rotor speed throughout, it was not possible to observe any effect on the leakage performance of the seal. However operating at typical steam turbine surface velocity was not a barrier to successful operation of the Aerostatic Seal.

A single five day long test was conducted. The first major finding was that the seal was still able to move from a retracted position to a low operating clearance to the rotor, despite the higher levels of friction due to higher temperature components and a chromium carbide contact face coating on the seal segments. Based on the measured mass flow rate and pressure ratio, the operating clearance of the displacement and motor side seal was $0.09\,\mathrm{mm}$.

The seal was subject to four low speed rotor displacements during the test. During these displacements the seal segments were able to respond to the rotor movements. The response was characterised by discrete seal segment movement due to pressure forces on the seal segments overcoming static friction. During the maximum translation of the rotor, the seal clearances were typically larger than the operating clearance, the displacement and motor side seal clearances being $0.11\,\mathrm{mm}$ and $0.10\,\mathrm{mm}$ respectively when the rotor was at the maximum translation in the case presented.

The apparent coefficient of static friction was found to be between $\mu_{stat} = 0.65$ and $\mu_{stat} = 0.70$ from the rotor translation test conducted. This was comparable to the value used in the design code for the seal. As the coefficient of static friction was not excessive, then it is expected that responsive seal designs are possible for application in a steam turbine, made from realistic materials and with a chrome carbide contact face coating on the seal segments.

9.3 Proposed steam turbine implementation

Based on the results obtained as part of this project, the base Aerostatic Seal design has been developed. This section presents a proposed Aerostatic Seal design for a low reaction steam turbine diaphragm. The proposed design is shown in Fig. 9.7. Key seal design features are shown in Fig. 9.7, and are described below.

A: New stepped restrictions

The most obvious development from the standard Gen Ⅰ and Ⅱ Aerostatic Seal designs are the inclusion of the stepped restrictions in the P1 and P3 pockets. The extra restrictions have two key functions: 1) reduce the leakage through the seal segment by increasing the number of restrictions, and 2) preventing the 'pressure recovery' effect observed when the seal segments are at a high clearance. The analytical design tool does not capture the pressure recovery effect, and eliminating this effect will increase the accuracy of the analytical tool.

To accommodate the steps in the rotor surface the P1 and P3 pockets can no longer be circumferentially divided. For developing the proposed design it is recommended to understand the effect on the radial force generation and the ability of the seal segment to operate at a uniform circumferential clearance. It is assumed that the P1 pocket will see an increase in pressure due to flow from the sides of the segment - see the side pressure distribution measured experimentally in Fig. 5.17, and the P3 pocket will see a reduction in pressure.

The steps on the rotor surface also reduce the axial pressure force acting on the seal segment. This is because some of the pressure drop is across the raised restrictions, and so axial force associated with that pressure drop is partially taken by the step on the rotor surface. The reduction of axial force will reduce the frictional force, but also reduce the tangential moment that can be accommodated by the axial reaction force. As the pressure moment acting on the segment is proportional to the square of the segment axial length, then the segment will have to be shorter axially - see Section 3.4.

It is expected that the stepped restrictions will help the moment to restore uniform segment clearance if one side of the segment was at a lower operating clearance. It was found in Chapter 8 that the pressure recovery effect would increase the pressure in

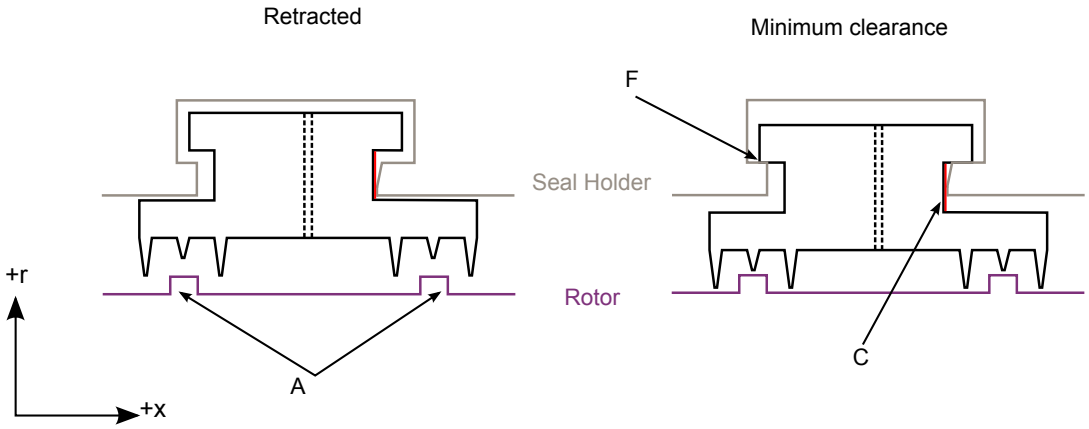

Figure 9.7: Proposed Aerostatic Seal design for application in a steam turbine.

the P2 pocket at the high clearance side of the segment, and so the generated pressure moment to restore uniform clearance was reduced.

B: Seal segment keys

As in the Aerostatic Seal design for the Durham Rotating Seals Rig, and the tests conducted in steam, the proposed Gen Ⅲ design also features 'keys' between all seal segments, as shown in Fig. 3.1. This is a departure from typical retractable seal designs which only have keys at the half joint of the diaphragm. The advantage of using keys between all segments is that there is no coupling of the radial and circumferential forces between segments through the circumferential springs. Also it is proposed to use the keys to set the retracted position of the segments to ensure that the retracted segment clearance is the same on each side of the segment.

C: Contact face treatment

A chromium carbide coating was applied to the contact face of the Aerostatic Seal segments in the tests in steam described above, on the advice of GE Rugby, and is shown in red on Fig. 9.7. The aim of the coating was to prevent wear on the contact face as was observed in the Durham Rotating Seals Rig. In the steam tests the coating was plasma sprayed and then ground smooth. One difficulty that was encountered during the manufacture of the seal for the steam tests was ensuring a smooth and even application on the contact face in the small area of the contact face. This may become easier with full

scale seal segments rather than the half scale segment used in the steam testing.

There may be other coatings that would provide wear resistance other than chrome carbide, and that offer advantages in application (chrome carbide is plasma sprayed and then ground smooth, increasing the number of manufacturing processes), or that also reduces friction such as nickel boron coating as applied to the HALO seal.

D: Diaphragm dishing compensation

One mechanical aspect of steam turbine construction is 'dishing' of the diaphragm due to the pressure differential across the stator [70]. Conical dishing of the diaphragm can be tolerated by the Aerostatic Seal due to the angled contact face design which prevents the sealing point on the contact face of the segment moving to a significantly larger radius and hence increasing the axial and frictional force. In the conically dished case the seal segments remain parallel to the rotor as the contact point is at the same axial location.

However as the diaphragm is constructed in two parts and bolted together, the diaphragm does not dish conically. There is greater axial deflection of the diaphragm at the half joint, which leads to the seal segments tilting forward as a results of the diaphragm deflection by as much as 0.2° [98]. As discussed earlier in Chapters 5 and 7, if the Aerostatic Seal segment tilts forward, then the radial force generated was reduced and the segment could contact the rotor surface. Therefore it is proposed to manufacture the Aerostatic Seal with labyrinth fins that are machined to different heights to correct the axial clearance variation due to the segment tilting forward due to diaphragm dishing. It would be desirable to over compensate the dishing compensation to allow a safety margin to prevent loss of radial force if the rotor dishing was greater than calculated in the turbine design phase, and to allow for creep of the diaphragm after long term operation of the turbine.

E: Axial thrust compensation springs

If the seal segment was manufactured such that the seal segment operated with an even axial clearance distribution when the diaphragm was dished, then when the load on the turbine was reduced and the diaphragm deflection lower, the Aerostatic Seal

segment would be in a 'tilted back' configuration. When the segment was tilted backwards, the radial force was increased, and resulted in the seal operating at a higher clearance. Furthermore, the seal segment will still be tilted backwards when at full load if the diaphragm dishing was over compensated. The Aerostatic Seal operating at a higher clearance increases the leakage through the seal and diminishes the potential efficiency improvement possible by using the Aerostatic Seal .

To reduce the operating clearance of the Aerostatic Seal, it is proposed to use axial thrust compensation springs. In Chapter 7, it was shown that in the 'high axial thrust' operating regime, there was a significant reduction in the operating clearance of the seal. This was because the axial thrust compensation springs would tilt the seal segment forward as the seal segment was transitioning to the operating clearance, reducing the radial force on the seal segment. In the 'high' axial thrust operating regime the seal segments contact the rotor when they are tilted forwards. It is proposed to limit the minimum clearance to prevent this.

F: Fixed minimum clearance

The Gen Ⅲ Aerostatic Seal design proposes to limit the minimum clearance of the seal to some small clearance - $0.10\,\mathrm{mm}$ is suggested. This performs two functions: prevent the seal segment contacting the rotor if the seal was in some way damaged, such as the feed holes became blocked. Also by limiting the minimum clearance, the best operating regime of axial thrust compensation springs can be used without the risk of seal segment damage at some pressure conditions. The function of the seal segment operating with limited clearance was investigated in Section 7.4.5.

9.4 Conclusion

The objective of this chapter was to further progress the development of the Aerostatic Seal by bringing the technology to a level ready for first test in a steam turbine.

Firstly testing was conducted in a steam test rig at TU Braunschweig which proved the Aerostatic Seal would operate in a high temperature steam environment.

Secondly the results from the steam testing and the testing conducted using air at Durham University was used to propose a generic Aerostatic Seal design. This design

embodies multiple features that are a direct result of the testing conducted in this thesis. The two most critical are the pressure recovery effect observed in the first pocket and axial variation of clearance. It was proposed to counter these effects by introducing stepped restrictions in the P1 and P3 pockets, and by over compensating for diaphragm deflection by reducing the height of the upstream fins.

Chapter 10

Conclusion

The Aerostatic Seal is a proposed dynamic seal concept, imagined for application in steam turbines, however also applicable to other turbines. The project described within this thesis has developed the Aerostatic Seal from concepts analytically investigated in a series of MEng final year projects [23]–[26] to technology demonstration inside a steam test rig. The development of the Aerostatic Seal has been through experimental testing in a series of test rigs. A non-rotating test rig operating in air modelled a single Aerostatic Seal segment allowing pressure measurements in the seal cavities. A rotating test rig operating in air modelled a whole seal and used an adjustable eccentric rotor to model rotor radial transients. Finally the steam test rig at TU Braunschweig was used to perform a test with high temperature steam, realistic rotor surface velocity and realistic seal and seal holder materials.

In the introduction to this thesis, four major research objectives were set out. First was development of an analytical design and analysis methodology for Aerostatic Seals, described in Chapter 3. The methodology uses the analytical model of Eser and Kazakia [86] to calculate the pressure and mass flow rate through the seal, and calculates the radial and axial force variation with seal segment clearance. The methodology performs a static analysis to find the clearances at which the seal segment will move away from the rotor, towards the rotor, or remain stationary to gauge the dynamic qualities of a particular design. To generate seal designs, a set number of design variables is looped through, and analysed at a high and low clearance. All feasible seal designs are then ranked and the top ten analysed and output to the designer. The response of a particular seal design was dependant on the value of the coefficient of friction. Three

designs were generated: ‘MESS01’ for the non-rotating rig, ‘ROT-02’ for the rotating rig, and ‘STR-IP6-07A1’ for steam testing at TU Braunschweig. A fourth design, ‘MacDonald1’ was generated by MacDonald [26] using a modified version of the design tool developed by Rafferty [24].

The second research objective was proof of concept (or otherwise) of the Aerostatic Seal. Demonstration of the dynamic capabilities of the Aerostatic Seal was initially obtained in the non-rotating rig by demonstrating that the Aerostatic Seal segment would move towards the rotor surface when at a high clearance, and away from the rotor surface when the segment was at a low clearance and without springs. The most dramatic demonstration of the Aerostatic Seal however was in the ‘Durham Rotating Seals Rig’. The rig used an adjustable eccentric rotor to model rotor radial transients. In the low rotor eccentricity position the seal segments would close in towards the rotor but operate at constant clearance (the 12 O’clock segment would sometimes be excited by the low levels of rotor eccentricity, although this would dampen out after approximately 5 s). In the high rotor eccentricity position the seal segments were able to respond to large rotor radial transients over the full range of rotor speeds tested, and critically the measured seal segment was able to maintain a mean clearance that was smaller than the level of rotor eccentricity. This would not be possible with a labyrinth seal and conclusively demonstrates the dynamic capabilities of the Aerostatic Seal.

Following the successful testing in the ‘Durham Rotating Seals Rig’, the Aerostatic Seal was then tested in steam. Similar operating characteristics were found, where the seal was able to move from a retracted clearance to a lower operating clearance. By testing in high temperature steam, with realistic rotor surface velocity, and with realistic steam turbine materials in the construction of the seal segments and seal carrier rings, it was demonstrated that the Aerostatic Seal would have a good chance of functioning as intended in a steam turbine. The seal was also subjected to a low speed rotor translation and showed that the seal could respond to the rotor movement.

In the course of demonstrating the potential of the Aerostatic Seal, the following behaviour of the seal was discovered, and is listed below:

- Pressure recovery effects occurred when the pitch to clearance ratio of the seal restrictions was small, i.e. the pitch was small and the clearance large. This was where a powerful vortex would form in the pocket leading to pressure recovery

in the subsequent pocket. Critically the effect on the Aerostatic Seal was that the first two restrictions would function as a single restriction, leading to increased pressure in the pockets, and increased radial pressure force. As a result the seal was not as responsive as predicted analytically, and the radial force was greater than expected. This was also confirmed with CFD.

- Non-uniform clearance. This was when one side of the seal segment would operate at a lower clearance than the other. This could lead to rubs between the seal segments and the rotor, as found in the rotating rig (see Section 6.3.1). The causes were investigated in Chapter 8, which concluded that the initial non uniformity was caused by circumferential variations in the contact face frictional force. Once the circumferential clearance of the seal segment was non-uniform, then the segment would not restore a uniform clearance as the pressure moment was too small to overcome the rotational friction on the contact face. Furthermore if one side of the seal segment was at a very large clearance, then this would reduce the correcting moment further.

  It was also found that the effect of pressure recovery had an adverse effect on the ability of the seal segment to correct circumferential clearance non-uniformity.

- Axial variation of clearance was observed to be a significant factor determining the operating clearance of the seal segment. This could be due to the seal segment tilting forward or backwards, as observed in the axial thrust compensated design. Tilting forward reduces the pressure in the seal axial pockets, reducing the radial force away from the rotor, and can therefore cause the seal segment to come into contact with the rotor.

  Axial variation in clearance can also be due to the positioning of the rotor. It was found in Section 5.4 that variation in the rotor position had a significant effect on the operating clearance of the seal segment, greater than the effect due to greasing the contact face. In the fixed seal segment test conducted in Section 5.5, it was found that a reduction in clearance of the downstream restriction would increase the radial force acting on the segment, causing the operating clearance of the seal segment to be increased.

  Due to diaphragm deflection in steam turbine operation, this sensitivity to axial

clearance variation is significant, although it has been addressed in the proposed Gen Ⅲ Aerostatic Seal design.

- Testing in the 'Durham Rotating Seals Rig', showed that at low levels of rotor eccentricity the seal segments operated at a constant position. This is desirable as it prevents wear on the contact face from the segment responding to small rotor movements. In this case the seal segment operating clearance was greater than the low rotor eccentricity setting.

- It was found in the rotating rig that the key driver for radial force generation was the mean segment clearance. Variations due to the non-uniformity of the seal segment were not observed. This was also confirmed in the non-rotating rig when operating with fixed non-uniform seal segment positions as the pressure distribution was the same as the uniform seal circumferential pressure distribution.

- The Aerostatic Seal demonstrated a 35% leakage reduction over a fixed seal in the rotating rig. By further optimisation of the design, as in the seal design for the steam tests conducted, the leakage reduction could be improved by reducing the operating clearance of the seal.

- Tangential rotation was measured during normal operation of the 'MacDonald1' seal segment in the non-rotating rig, and the 'ROT-02' seal design in the rotating rig. In both cases the level of forward tangential rotation was of the same order as the measurement uncertainty, and therefore it was concluded that the measured differences were likely to be due to measurement error. In the tests with axial springs, which allowed the measurement of seal segment tangential rotation using the axial spring load cells, the effect of the segment tilting forward was noticeable by the loss of pressure below the segment and on the top surface of the segment, which was not observed in the non-rotating rig during normal operation without axial springs.

- Mean seal operating clearance was unaffected by rotor rotational speed, at both high and low eccentricity. The only exception was at zero rotor speed. The leakage was also unaffected at the rotor speed and clearance tested which was confirmed by considering the ratio of Taylor number to axial Reynolds number Ta/Re_x.

A diversion was made to investigate the Gen II Aerostatic Seal design with used axial thrust compensation springs, and which was the subject of Chapter 7. Different levels of axial thrust were tested, and it was found that there were four distinct operating regimes depending on the level of applied axial thrust:

- 'Low' levels of axial thrust. There was a small improvement in operating clearance, and consequent reduction in leakage mass flow rate was observed.
- 'High' levels of axial thrust. A significant reduction in operating clearance was observed, although rotor contact was observed just after the seal closed, and also before the segment retracts.
- 'Very high' levels of axial thrust; an extension of the 'high' axial thrust regime. There was a prolonged period of time where the seal segment was in contact with the rotor surface.
- Vibratory response, termed 'pressure activated chatter' where the seal segment repeatedly contacted the rotor surface. This was due to unbalanced applied moment about the segment centroid due to axial spring force.

The third key objective set out at the beginning was validation of the Aerostatic Seal design and analysis methodology. The analytical methodology was largely successful at predicting the performance of the Aerostatic Seal at low clearances and designed the manufactured Aerostatic Seal successfully. This was demonstrated by the good agreement at low clearance with the CFD tests conducted in Section 5.5. Experimental agreement was not as good due to compounding effects such as axial variation in clearance in the fixed seal segment tests. At high clearance the pressure recovery effect dominates the pressure distribution in the P2 and P3 seal segment axial pockets, which the analytical model did not capture. As the proposed Gen III seal design proposes to eliminate the pressure recovery effect with kinetic energy blockers on the rotor surface, then it is expected that the analytical methodology would be much more successful.

The following relate specifically to the analytical methodology:

- The side pressure forces were determined experimentally in the non-rotating rig. It was found that a constant side pressure coefficient $Cf_s = 1.4$ would relate the side

pressure force to the pressure difference successfully, and was found to be constant with clearance. This was contrary to the CFD results which found decreasing the seal segment clearance increased the side pressure coefficient. The latest seal segment designs use 'keys' between the seal segments which were not modelled in the non-rotating rig.

- A 2D analytical model was developed in Chapter 8, and included the frictional moment opposing the restoration of uniform circumferential clearance which was discussed extensively in the chapter. This could be extended into 3D by including the effect of axial variation in clearance. As the methodology did not include the pressure recovery effect as in the 1D model, then the model failed to fully capture all the effects of non-uniform circumferential clearance, although the model was still useful to understand some of the causes of the segment non-uniformity.

The fourth and final objective set out at the beginning of the project was identification of key design parameters and variables. These are embodied in the proposed Gen Ⅲ design described in Section 9.3. The following were the key features of the proposed seal design:

- Castellated rotor surface: prevents the pressure recovery effect increasing the responsiveness of the seal design, and also reduces the axial force on the segment.
- The seal design uses 'keys' between the segments, as in the rotating rig and the steam tests conducted at TU Braunschweig.
- Chromium carbide contact face treatment to prevent wear, or some other hard facing surface coating/treatment.
- Diaphragm dishing over compensation by increasing the clearance of the upstream seal restrictions.
- Axial thrust compensation springs: These are to ensure that the seal segment operates at a low clearance even if the seal has been over compensated for diaphragm dishing. The axial springs are intended to be in the 'high' axial thrust regime, and with the minimum seal segment position limited to prevent rotor contact.

Overall the significant contribution of this work was the development of an analytical design methodology for the Aerostatic Seal, experimental proof of concept in a non-rotating and rotating test facility, and a proposed concept design based on these results.

Bibliography

[1] A. Richardson, *The Evolution of the Parsons Steam Turbine*. Cambridge University Press, 1911, ISBN: 1108070086 (*p.* 1).

[2] R. A. Budenholzer and F. Landis. (Nov. 25, 2017). History of steam turbine technology, Encyclopaedia Britannica Online, [Online]. Available: https://www.britannica.com/technology/turbine/History-of-steam-turbine-technology (visited on 11/25/2017) (*p.* 1).

[3] A. Leyzerovich, *Large power steam turbines*. Pennwell Corp, 1997, volume 1, ISBN: 0-87814-717-9 (*p.* 1).

[4] "Electricity information: Overview 2017," International Energy Agency, Tech. Rep., 2017. [Online]. Available: https://www.iea.org/publications/freepublications/publication/ElectricityInformation2017Overview.pdf (visited on 11/25/2017) (*pp.* 1–2).

[5] G. Locatelli, C. Bingham, and M. Mancini, "Small modular reactors: A comprehensive overview of their economics and strategic aspects," *Progress in Nuclear Energy*, volume 73, number Supplement C, pages 75–85, 2014, ISSN: 0149-1970. DOI: 10.1016/j.pnucene.2014.01.010 (*p.* 2).

[6] Siemens, *Steam turbines for CSP plants*. [Online]. Available: https://www.energy.siemens.com/hq/pool/hq/power-generation/steam-turbines/downloads/steam-turbine-for-csp-plants-siemens.pdf (visited on 11/25/2017) (*p.* 2).

[7] *Achieving fusion power*. [Online]. Available: http://www.ccfe.ac.uk/Fusion_power.aspx (visited on 09/02/2017) (*p.* 2).

[8] D. J. C. MacKay, *Sustainable Energy - without the hot air*. UIT Cambridge, 2008, Available free online from http://www.withouthotair.com, ISBN: 978-0-9544529-3-3 (*p.* 2).

[9] I. MacLeay, K. Harris, and A. Annut, "Digest of united kingdom energy statistics 2011," Department of Energy and Climate Change, Tech. Rep., 2011 (*pp.* 2–3).

[10] ——, "Digest of united kingdom energy statistics 2011," Department of Energy and Climate Change, Tech. Rep., 2012 (*pp.* 2–3).

[11] A. Annut, C. Michaels, M. Williams, J. Forster, W. Spry, M. Earp, M. Kerai, J. Hemingway, and S. Khan, "Energy trends, December 2013," Department of Energy and Climate Change, Tech. Rep., 2013. [Online]. Available: https://www.gov.uk/government/statistics/energy-trends-december-2013 (visited on 11/20/2017) (*pp.* 2–3).

[12] A. Annut, C. Michaels, M. Williams, W. Spry, M. Earp, and M. Kerai, "Energy trends, December 2014," Department of Energy and Climate Change, Tech. Rep., 2014. [Online]. Available: https://www.gov.uk/government/statistics/energy-trends-december-2014 (visited on 11/20/2017) (*pp.* 2–3).

[13] K. Harris, "Energy trends december 2015," Department of Energy and Climate Change, Tech. Rep., 2015. [Online]. Available: https://www.gov.uk/government/statistics/energy-trends-december-2015 (visited on 11/20/2017) (*pp.* 2–3).

[14] ——, "Energy trends december 2016," Department for Business, Energy and Industrial Strategy (BEIS), Tech. Rep., 2016. [Online]. Available: https://www.gov.uk/government/statistics/energy-trends-december-2016 (visited on 11/20/2017) (*pp.* 2–3).

[15] M. Topel, Å. Nilsson, M. Jöcker, and B. Laumert, "Investigation into the thermal limitations of steam turbines during start–up operation," *Journal of Engineering for Gas Turbines and Power*, volume 140, number 1, page 012 603, 2018. DOI: 10.1115/1.4037664 (*p.* 3).

[16] W. Beer, L. Propp, and L. Voelker, "A simplified analytical approach for calculating the start-up time of industrial steam turbines for optimal and fast start-up procedures," in *ASME Turbo Expo 2015: Turbine Technical Conference and Exposition*,

Paper No. GT2015-43284, volume 8, 2015, pages 15–19, ISBN: 978-0-7918-5679-6. DOI: 10.1115/GT2015-43284 (*p.* 3).

[17] R. Chen, A. P. He, Y. L. Yang, X. Z. Ye, P. N. Jiang, and W. X. Hua, "Life assessment technology of steam turbine rotor," in *ASME Turbo Expo 2013: Turbine Technical Conference and Exposition*, Paper No. GT2013-95456, American Society of Mechanical Engineers, 2013, ISBN: 978-0-7918-5520-1. DOI: 10.1115/GT2013-95456 (*p.* 3).

[18] G. Marinescu, M. Sell, A. Ehrsam, and P. B. Brunner, "Experimental investigation into thermal behavior of steam turbine components: Part 3 - startup and the impact on LCF life," in *ASME Turbo Expo 2013: Turbine Technical Conference and Exposition*, Paper No. GT2013–94356, American Society of Mechanical Engineers, 2013, ISBN: 978-0-7918-5516-4. DOI: 10.1115/GT2013-94356 (*p.* 3).

[19] B. A. Couture, L. B. Keeling, and M. W. Kowalczyk, "Clearance and seals design for new heat™ steam turbine," in *ASME 2006 Power Conference*, American Society of Mechanical Engineers, 2006, pages 359–366. DOI: 10.1115/POWER2006-88201 (*p.* 3).

[20] A. S. Leyzerovich, *Steam turbines for modern fossil-fuel power plants*. The Fairmont Press, Inc., 2008, ISBN: 0-88173-548-5 (*p.* 3).

[21] J. J. Lee, S. Y. Kang, T. S. Kim, and S. S. Byun, "Thermo-economic analysis on the impact of improving inter-stage packing seals in a 500 MW class supercritical steam turbine power plant," *Applied Thermal Engineering*, volume 121, number Supplement C, pages 974–983, 2017, ISSN: 1359-4311. DOI: 10.1016/j.applthermaleng.2017.04.138 (*p.* 4).

[22] J. Seaton, *Sealing system*, European Patent No. EP3002487 A1, 2016 (*p.* 4).

[23] A. Auld, "Novel self-adjusting seal design for steam turbine applications," MEng Research Project, Durham University, 2011 (*pp.* 5, 24–25, 27–29, 34, 42, 228, 252).

[24] D. Rafferty, "Design of an novel self-adjusting seal design for steam turbine applications," MEng Research Project, Durham University, 2012 (*pp.* 5, 25–26, 28–29, 34, 42, 52, 228–229).

[25] A. Durnan, "Testing a new steam turbine sealing concept," MEng Research Project, Durham University, 2013 (*pp.* 5, 26, 28–29, 67, 228).

[26] M. MacDonald, "Investigating the dynamic performance of a self-adjusting seal for steam turbine applications," MEng Research Project, Durham University, 2014 (*pp.* 5, 26, 28–29, 59, 228–229).

[27] H. M. Martin, "Labyrinth packings," *Engineering*, volume 85, number 10, pages 35–36, Jan. 1908 (*pp.* 9, 40, 145, 248–249).

[28] H. Sneck, "Labyrinth seal literature survey," *Journal of Lubrication Technology*, volume 96, number 4, pages 579–581, 1974. DOI: 10.1115/1.3452498 (*p.* 9).

[29] R. E. Chupp, R. C. Hendricks, S. B. Lattime, and B. M. Steinetz, "Sealing in turbomachinery," *Journal of Propulsion and Power*, volume 22, number 2, pages 313–349, 2006, Also available as report NASA/TM–2006–214342 at https://ntrs.nasa.gov/archive/nasa/casi.ntrs.nasa.gov/20060051674.pdf. DOI: https://doi.org/10.2514/1.17778 (*pp.* 9, 16–17).

[30] A. Egli, "The leakage of steam through labyrinth seals," *Trans. Asme*, volume 57, number 3, pages 115–122, 1935 (*pp.* 10, 249, 251).

[31] B. Hodkinson, "Estimation of the leakage through a labyrinth gland," *Proceedings of the Institution of Mechanical Engineers*, volume 141, number 1, pages 283–288, 1939. DOI: 10.1243/PIME_PROC_1939_141_037_02 (*pp.* 10, 145–146, 249–251).

[32] S. Chaplygin, "Gas jets," 1944, NASA Technical Memorandum No. 1063. [Online]. Available: https://ntrs.nasa.gov/search.jsp?R=20030066368 (*pp.* 10, 51, 250).

[33] S. Suryanarayanan and G. L. Morrison, "Analysis of flow parameters influencing carry-over coefficient of labyrinth seals," in *ASME Turbo Expo 2009: Power for Land, Sea, and Air*, Paper No. GT2009-59245, 2009, ISBN: 978-0-7918-4884-5. DOI: 10.1115/GT2009-59245 (*pp.* 10, 110, 253).

[34] Y. Dogu, M. C. Sertçakan, K. Gezer, M. Kocagül, E. Arıcan, and M. S. Ozmusul, "Labyrinth seal leakage degradation due to various types of wear," *Journal of Engineering for Gas Turbines and Power*, volume 139, number 6, page 062 504, 2017. DOI: 10.1115/1.4035658 (*p.* 13).

[35] H. Zimmermann, A. Kammerer, and K. Wolff, "Performance of worn labyrinth seals," *ASME paper*, volume 94, 1994. DOI: 10.1115/94-GT-131 (*p.* 13).

[36] H. Chougule, A. Mirzamoghadam, and D. Ramerth, "CFD simulation of single step and double notched tooth for labyrinth seals," in *Proceedings of ASME Turbo Expo 2014: Turbine Technical Conference and Exposition*, Paper No. GT2014-26286, American Society of Mechanical Engineers, 2014, ISBN: 978-0-7918-4573-8. DOI: 10.1115/GT2014-26286 (*p.* 13).

[37] A. D. Vakili, A. J. Meganathan, S. Ayyalasomayajula, S. Hesler, and L. Shuster, "Advanced labyrinth seals for steam turbine generators," in *ASME Turbo Expo 2006: Power for Land, Sea and Air*, Paper No. GT2006-91263, American Society of Mechanical Engineers, 2006, ISBN: 0-7918-4238-X. DOI: 10.1115/GT2006-91263 (*p.* 13).

[38] N. Herrmann, K. Dullenkopf, and H.-J. Bauer, "Flexible seal strip design for advanced labyrinth seals in turbines," in *Proceedings of ASME Turbo Expo 2013: Turbine Technical Conference and Exposition*, ASME Paper No. GT2013-95424, American Society of Mechanical Engineers, 2013, ISBN: 978-0-7918-5520-1. DOI: 10.1115/GT2013-95424 (*p.* 14).

[39] Y. Kuwamura, K. Matsumoto, H. Uehara, H. Ooyama, Y. Tanaka, and S. Nishimoto, "Development of new high-performance labyrinth seal using aerodynamic approach," in *ASME Turbo Expo 2013: Turbine Technical Conference and Exposition*, Paper No.: GT2013-94106, American Society of Mechanical Engineers, 2013, ISBN: 978-0-7918-5520-1. DOI: 10.1115/GT2013-94106 (*p.* 14).

[40] R. E. Brandon, "Segmented labyrinth-type shaft sealing system for fluid turbines," US Patent US4436311A, 1984 (*p.* 14).

[41] N. Little, E. Sulda, and T. Terezakis, "Efficiency improvement on large mechanical drive steam turbines," in *Proceedings of the 30th Turbomachinery Symposium*, Available from https://oaktrust.library.tamu.edu/bitstream/handle/1969.1/163347/t30pg057.pdf?sequence=1&isAllowed=y, 2001, pages 57–64 (*pp.* 14, 16).

[42] E. M. Curtis, J. D. Denton, J. P. Longley, and B. Rosic, "Controlling tip leakage flow over a shrouded turbine rotor using an air-curtain," in *ASME Turbo Expo 2009: Power for Land, Sea, and Air*, Paper No. GT2009-59411, American Society of Me-

chanical Engineers, 2009, pages 885–894, ISBN: 978-0-7918-4888-3. DOI: 10.1115/GT2009-59411 (*p.* 14).

[43] S. I. Hogg and I. G. Ruiz, "Fluidic jet barriers for sealing applications," in *ASME 2011 Turbo Expo: Turbine Technical Conference and Exposition*, Paper No. GT2011-45353, American Society of Mechanical Engineers, pages 779–788, ISBN: 978-0-7918-5465-5. DOI: 10.1115/GT2011-45353 (*p.* 15).

[44] M. Hilfer, "Fluidic sealing fundamental physics and development for turbomachinery implementation," Available at Durham E-Theses Online: http://etheses.dur.ac.uk/11830/, PhD thesis, Durham University, 2016 (*p.* 15).

[45] S. Hogg and M. Hilfer, *A seal assembly*, US Patent App. 14/894,791, 2014 (*p.* 15).

[46] A. C. Rai, D. Prabhudharwadkar, S. Murthy, A. Giametta, and D. Johns, "Effect of air-curtains on labyrinth seal performance," in *ASME Turbo Expo 2016: Turbomachinery Technical Conference and Exposition*, Paper No. GT2016-57188, American Society of Mechanical Engineers, 2016, ISBN: 978-0-7918-4978-1. DOI: 10.1115/GT2016-57188 (*p.* 15).

[47] S. Dinc, M. Demiroglu, N. Turnquist, J. Mortzheim, G. Goetze, J. Maupin, J. Hopkins, C. Wolfe, and M. Florin, "Fundamental design issues of brush seals for industrial applications," *Journal of Turbomachinery*, volume 124, number 2, pages 293–300, 2002. DOI: 10.1115/2001-GT-0400 (*pp.* 16, 25–27).

[48] H. Schwarz, J. Friedrichs, and J. Flegler, "Axial inclination of the bristle pack, a new design parameter of brush seals for improved operational behavior in steam turbines," in *ASME Turbo Expo 2014: Turbine Technical Conference and Exposition*, American Society of Mechanical Engineers, 2014, ISBN: 978-0-7918-4558-5. DOI: 10.1115/GT2014-26330 (*p.* 16).

[49] M. Neef, E. Sulda, N. Sürken, and J. Walkenhorst, "Design features and performance details of brush seals for turbine applications," in *ASME Turbo Expo 2006: Power for Land, Sea, and Air*, Paper No. GT2006-90404, American Society of Mechanical Engineers, pages 1385–1392, ISBN: 0-7918-4238-X. DOI: 10.1115/GT2006-90404 (*p.* 16).

[50] M. Raben, J. Friedrichs, and J. Flegler, “Brush seal frictional heat generation - test rig design and validation under steam environment,” *Journal of Engineering for Gas Turbines and Power*, volume 139, number 3, page 032 502, 2017. DOI: 10.1115/1.4034500 (*pp.* 17, 210).

[51] A. K. Owen, T. V. Jones, S. Guo, and S. Hogg, “An experimental and theoretical study of brush seal and shaft thermal interaction,” in *ASME Turbo Expo 2003*, Paper No. GT2003-38276, American Society of Mechanical Engineers, 2003, ISBN: 0-7918-3688-6. DOI: 10.1115/GT2003-38276 (*p.* 17).

[52] Y. Dogu and M. F. Aksit, “Brush seal temperature distribution analysis,” *Journal of engineering for gas turbines and power*, volume 128, number 3, pages 599–609, 2006. DOI: 10.1115/1.2135817. [Online]. Available: http://www.ewp.rpi.edu/hartford/~ernesto/F2009/FWM/Papers/Papers4Projects/Dogu2006.pdf (*p.* 17).

[53] P. F. Crudgington and A. Bowsher, “Brush seal blow down,” *AIAA paper*, number 2003-4697, 2003. DOI: 10.2514/6.2003-4697 (*p.* 17).

[54] M. Raben, J. Friedrichs, T. Helmis, and J. Flegler, “Brush seals used in steam environments - chronological wear development and the impact of different seal designs,” *Journal of Engineering for Gas Turbines and Power*, volume 138, number 5, page 051 901, 2016. DOI: 10.1115/1.4031531 (*pp.* 17, 210).

[55] R. F. J. Flower, *Brush seal with asymmetrical elements*, US Patent 5,135,237, 1992 (*p.* 17).

[56] H. Nakane, A. Maekawa, E. Akita, K. Akagi, T. Nakano, S. Nishimoto, S. Hashimoto, T. Shinohara, and H. Uehara, “The development of high-performance leaf seals,” *J. Eng. Gas Turbines Power*, volume 126, pages 342–350, 2004. DOI: 10.1115/1.1615257 (*pp.* 17–18).

[57] I. H. Jahn, A. K. Owen, G. Franceschini, and D. R. Gillespie, “Experimental characterisation of the stiffness and leakage of a prototype leaf seal for turbine applications,” 2008, Paper No. GT2008-51206. DOI: 10.1115/GT2008-51206 (*p.* 17).

[58] I. H. Jahn, D. Gillespie, and P. Cooper, “Hydrodynamic air-riding in leaf seals,” 2013, Paper No. GT2013-95585. DOI: 10.1115/GT2013-95585 (*p.* 18).

[59] M. P. Proctor and I. R. Delgado, "Leakage and power loss test results for competing turbine engine seals," in *ASME Turbo Expo 2004: Power for Land, Sea, and Air*, Paper No. GT2004-53935, American Society of Mechanical Engineers, 2004, pages 441–451. DOI: 10.1115/GT2004-53935 (*pp.* 18, 218).

[60] M. C. Johnson and E. G. Medlin, *Laminated finger seal with logarithmic curvature*, US Patent 5,108,116, 1992 (*p.* 18).

[61] M. P. Proctor, A. Kumar, and I. R. Delgado, "High-speed, high-temperature finger seal test results," *Journal of propulsion and power*, volume 20, number 2, pages 312–318, 2004. DOI: 10.2514/1.9256 (*p.* 18).

[62] M. P. Proctor, "Non-contacting finger seals static performance test results at ambient and high temperatures," in *52nd AIAA/SAE/ASEE Joint Propulsion Conference, AIAA Propulsion and Energy Forum, (AIAA 2016-4921)*, American Institute of Aeronautics and Astronautics, 2016. DOI: 10.2514/6.2016-4921 (*p.* 19).

[63] H. Zhao, G. Chen, L. Wang, H. Su, and F. Lu, "Dynamic performance of a c/c composite finger seal in a tilting mode," *Chinese Journal of Aeronautics*, volume 30, number 4, pages 1603–1614, 2017, ISSN: 1000-9361. DOI: 10.1016/j.cja.2016.11.002 (*p.* 19).

[64] A. Thatte and X. Zheng, "Hydrodynamics and sonic flow transition in dry gas seals," in *ASME Turbo Expo 2014: Turbine Technical Conference and Exposition*, Paper No. GT2014-26706, American Society of Mechanical Engineers, 2014. DOI: 10.1115/GT2014-26706 (*pp.* 20, 24).

[65] Y. Le Moullec, "Conceptual study of a high efficiency coal-fired power plant with CO 2 capture using a supercritical CO 2 brayton cycle," *Energy*, volume 49, pages 32–46, 2013. DOI: 10.1016/j.energy.2012.10.022 (*p.* 20).

[66] R. A. Bidkar, E. Sevincer, J. Wang, A. M. Thatte, A. Mann, M. Peter, G. Musgrove, T. Allison, and J. Moore, "Low-leakage shaft-end seals for utility-scale supercritical CO2 turboexpanders," *Journal of Engineering for Gas Turbines and Power*, volume 139, number 2, page 022 503, 2017. DOI: 10.1115/1.4034258 (*pp.* 20–21, 28).

[67] R. Bidkar, G. Musgrove, M. Day, C. Kulhanek, T. Allison, A. Peter, D. Hofer, and J. Moore, "Conceptual designs of 50 MWe and 450 MWe supercritical CO2 turbomachinery trains for power generation from coal. part 1: Cycle and turbine," in *The 5th International Symposium-Supercritical CO2 Power Cycles, San Antonio TX*, 2016, pages 1–17 (*p.* 20).

[68] ——, "Conceptual designs of 50 MWe and 450 MWe supercritical CO2 turbomachinery trains for power generation from coal. part 2: Compressors," in *The 5th International Symposium-Supercritical CO2 Power Cycles, San Antonio TX*, 2016, pages 1–17 (*p.* 20).

[69] *Turbomachinery sealing solutions*. [Online]. Available: https://www.flowserve.com/sites/default/files/2016-07/FSD113eng_Turbomachinery_0.pdf (visited on 07/28/2017) (*pp.* 20–21).

[70] *Steam turbine diaphragm dishing repair*. [Online]. Available: https://www.gepower.com/content/dam/gepower-pgdp/global/en_US/documents/service/steam%20turbine%20service/steam-turbine-diaphragm-dishing-repair.pdf (visited on 11/17/2017) (*pp.* 21, 225).

[71] W. Shapiro and C. C. Lee, "Advanced helium purge seals for liquid oxygen (LOX) turbopumps," 1989, Available from https://ntrs.nasa.gov/search.jsp?R=19890011868 (*pp.* 21–22).

[72] M. Arghir and A. Mariot, "Theoretical analysis of the static characteristics of the carbon segmented seal," *Journal of Tribology*, volume 139, number 6, page 062 202, 2017, Paper No. TRIB-16-1340. DOI: 10.1115/1.4036272 (*pp.* 21, 24).

[73] *SXL axial and radial segmented shaft seals for hydro-turbines*. [Online]. Available: http://thordonbearings.com/system/documents/documents/21/original/SXL_Segmented_Shaft_Seal_Brochure.pdf?1278427675 (visited on 07/28/2017) (*p.* 21).

[74] *Rexnord segmented seals*. [Online]. Available: https://www.rexnord.com/ContentItems/TechLibrary/Documents/Aerospace/AR5-002_ProductSheet (visited on 07/28/2017) (*p.* 21).

[75] J. F. Justak, *Non-contacting seal for a gas turbine engine*, US Patent US 2008/0265513 A1, 2008 (*p.* 22).

[76] J. F. Justak and C. Doux, "Self-acting clearance control for turbine blade outer air seals," in *ASME Turbo Expo 2009: Power for Land, Sea, and Air*, Paper No. GT2009-59683, American Society of Mechanical Engineers, 2009, pages 1229–1237, ISBN: 978-0-7918-4884-5. DOI: 10.1115/GT2009-59683 (*p.* 22).

[77] L. San Andrés and A. Anderson, "An all-metal compliant seal versus a labyrinth seal: A comparison of gas leakage at high temperatures," *Journal of Engineering for Gas Turbines and Power*, volume 137, number 5, page 052 504, 2015. DOI: 10.1115/1.4028665 (*pp.* 22, 27, 218).

[78] J. Justak, "Hydrogen compressor seal case study," Proc. 42nd Turbomachinery Symposium, Texas A & M University, Houston, TX, 2013 (*p.* 22).

[79] D. T. Stiles, M. R. Sandberg, J. F. Justak, E. Wilcox, M. J. Kuzdzal, C. A. Rohrs, H. F. Miller, *et al.*, "Application of dynamic pressure-balanced seals in a multi-stage centrifugal compressor," in *Proceedings of the 45th Turbomachinery Symposium*, Available from https://oaktrust.library.tamu.edu/handle/1969.1/159791, Turbomachinery Laboratories, Texas A&M Engineering Experiment Station, 2016 (*pp.* 22–23).

[80] *Halo seals*. [Online]. Available: http://www.atgi.us/pdf/ATGI_Halo_Seal_Brochure.pdf (visited on 07/28/2017) (*p.* 22).

[81] M. Arghir, M.-H. Nguyen, D. Tonon, and J. Dehouve, "Analytic modeling of floating ring annular seals," *Journal of Engineering for Gas Turbines and Power*, volume 134, number 5, page 052 507, 2012. DOI: 10.1115/1.4004728 (*pp.* 23, 44).

[82] A. Mariot, M. Arghir, P. Hélies, and J. Dehouve, "Experimental analysis of floating ring annular seals and comparisons with theoretical predictions," *Journal of Engineering for Gas Turbines and Power*, volume 138, number 4, page 042 503, 2016. DOI: 10.1115/1.4031347 (*pp.* 23, 44).

[83] P. J. Blau, "The significance and use of the friction coefficient," *Tribology International*, volume 34, number 9, pages 585–591, 2001, ISSN: 0301-679X. DOI: 10.1016/S0301-679X(01)00050-0 (*p.* 35).

[84] S. Wittig, L. Dörr, and S. Kim, "Scaling effects on leakage losses in labyrinth seals," *Journal of Engineering for Power*, volume 105, page 305, 1983. DOI: 10.1115/1.3227416 (*p.* 37).

[85] D. W. Childs, *Turbomachinery rotordynamics: phenomena, modeling, and analysis*. John Wiley & Sons, 1993, ISBN: 0-471-53840-X (*pp.* 40, 248, 250, 252).

[86] D. Eser and J. Y. Kazakia, "Air flow in cavities of labyrinth seals," *International Journal of Engineering Science*, volume Vol. 33, number 15, pages 2309–2326, 1995. DOI: 10.1016/0020-7225(95)00072-6 (*pp.* 41, 51, 228, 250, 252).

[87] M. Holmgren, *X steam for matlab*, Code available from https://uk.mathworks.com/matlabcentral/fileexchange/9817-x-steam--thermodynamic-properties-of-water-and-steam, 2006 (*pp.* 42, 218).

[88] J. W. Powell, *Design of Aerostatic Bearings*. Machinery Publishing Co. Ltd., 1970, ISBN: 0-204-85333-5 (*pp.* 42, 254).

[89] J. Greenwood and J. Williamson, "Contact of nominally flat surfaces," in *Proceedings of the Royal Society of London A: Mathematical, Physical and Engineering Sciences*, The Royal Society, volume 295, 1966, pages 300–319. DOI: 10.1098/rspa.1966.0242 (*p.* 44).

[90] V. Popov, *Contact mechanics and friction: physical principles and applications*, 1st edition. Springer, 2010, ISBN: 978-3-642-42505-9 (*pp.* 44, 200).

[91] W. Waschka, S. Wittig, and S. Kim, "Influence of high rotational speeds on the heat transfer and discharge coefficients in labyrinth seals," *Journal of turbomachinery*, volume 114, number 2, pages 462–468, 1992. DOI: 10.1115/1.2929166 (*pp.* 50, 110, 145).

[92] H. Zimmermann and K. Wolff, "Comparison between empirical and numerical labyrinth flow configurations," in *ASME Gas Turbine Conference and Exhibition, Anaheim, CA*, Paper No. 87-GT-86, 1987. DOI: 10.1115/87-GT-86 (*pp.* 51, 109, 251).

[93] A. FLUENT, *Fluent user's guide*, version 15.0, ANSYS Inc. (*p.* 105).

[94] S. Wittig, U. Schelling, S. Kim, and K. Jacobsen, "Numerical predictions and measurements of discharge coefficients in labyrinth seals," in *ASME 1989 International Gas Turbine Conference and Exhibition*, Paper No. 87-GT-188, 1987. DOI: 10.1115/87-GT-188 (*p.* 109).

[95] J. E. Shigley, *Mechanical Engineering Design*, 3rd edition. McGraw-Hill, 1977, ISBN: 0-07-056881-2 (*p.* 192).

[96] M. Raben, H. Schwarz, and J. Friedrichs, "Operating performance and wear investigations of brush seals for steam turbine applications," in *ASME Turbo Expo 2013: Turbine Technical Conference and Exposition*, Paper No. GT2013-95442, American Society of Mechanical Engineers, 2013, ISBN: 978-0-7918-5514-0. DOI: 10.1115/GT2013-95442 (*p.* 210).

[97] C. DellaCorte and H. E. Sliney, "Composition optimization of self-lubricating chromium-carbide-based composite coatings for use to 760 C," *ASLE transactions*, volume 30, number 1, pages 77–83, 1987, Available from https://ntrs.nasa.gov/archive/nasa/casi.ntrs.nasa.gov/19860011097.pdf. DOI: 10.1080/05698198708981733 (*pp.* 211, 269).

[98] J. Seaton, *Proposed further work on the aerostatic gland*, personal communication, Jun. 2017 (*p.* 225).

[99] W. J. Kearton and T. H. Keh, "Leakage of air through labyrinth glands of staggered type," *Proceedings of the Institution of Mechanical Engineers*, volume 166, number 1, pages 180–195, 1952. DOI: 10.1243/PIME_PROC_1952_166_022_02 (*pp.* 248, 250, 253).

[100] J. Morrow, "On the theory of labyrinth packing," *Proc. University of Durham Phil. Soc.*, volume 3, 1910 (*p.* 248).

[101] H. L. Callendar, *Properties of Steam and Thermodynamic Theory of Turbines*. London: E. Arnold, 1920, pages 264–267 (*p.* 248).

[102] A. Stodola, *Steam and gas turbines*, 6th edition. McGraw-Hill, 1927, volume 1 (*p.* 248).

[103] J. K. Vennard, *Elementary fluid mechanics*, 4th edition. John Wiley & Sons, Inc., 1961 (*p.* 249).

[104] F. Dollin and W. Brown, "Flow of fluids through openings in series," *Engineer*, volume 164, number 4259, pages 223–224, 1937 (*p.* 249).

[105] J. K. Scharrer, "Theory versus experiment for the rotordynamic coefficients of labyrinth gas seals: Part I - a two control volume model," *ASME Journal of Vibration, Acoustics, Stress, and Reliability in Design*, volume 110, number 7, pages 270–280, 1988. DOI: 10.1115/1.3269513 (*p.* 250).

[106] M. I. Gurevich, *The theory of jets in an ideal fluid*. Academic Press, 1965 (*p.* 250).

[107] U. Yucel and J. Kazakia, "Analytical prediction techniques for axisymmetric flow in gas labyrinth seals," *Journal of engineering for gas turbines and power*, volume 123, number 1, pages 255–257, 2001. DOI: 10.1115/1.1340630 (*pp.* 250, 252).

[108] G. Vermes, "A fluid mechanics approach to the labyrinth seal leakage problem," *Journal of Engineering for power*, volume 83, pages 161–169, 1961. DOI: 10.1115/1.3673158 (*p.* 252).

[109] H. Zimmermann and K. Wolff, "Air system correlations, part 1: Labyrinth seals," in *ASME 1998 International Gas Turbine and Aeroengine Congress and Exhibition*, Paper No. 98-GT-206, 1998. DOI: 10.1115/98-GT-206 (*p.* 253).

[110] S. Sen, "Influence of chromium carbide coating on tribological performance of steel," *Materials & design*, volume 27, number 2, pages 85–91, 2006. DOI: 10.1016/j.matdes.2004.10.005 (*p.* 269).

[111] J. Lindgren and W. Johnson, "Friction and wear behavior of chromium carbide coatings," *Surface and Coatings Technology*, volume 32, number 1-4, pages 249–260, 1987. DOI: 10.1016/0257-8972(87)90111-3 (*p.* 269).

[112] B. Mann and B. Prakash, "High temperature friction and wear characteristics of various coating materials for steam valve spindle application," *Wear*, volume 240, number 1, pages 223–230, 2000. DOI: 10.1016/S0043-1648(00)00390-2 (*p.* 269).

[113] D. Cornelius and W. Roberts, "Friction and wear of metals in gases up to 600 C," *ASLE TRANSACTIONS*, volume 4, number 1, pages 20–32, 1961. DOI: 10.1080/05698196108972416 (*p.* 269).

[114] I. Inman and P. Datta, "Development of a simple 'temperature versus sliding speed' wear map for the sliding wear behaviour of dissimilar metallic interfaces ii," *Wear*, volume 265, number 11, pages 1592–1605, 2008. DOI: 10.1016/j.wear.2008.03.009 (*p.* 269).

Appendix A

Labyrinth Seal Leakage Models

The Aerostatic Seal is made up of a series of restrictions, similar to a labyrinth seal, coupled to a central feed hole. Therefore to be able to understand the flow through the Aerostatic Seal and to be able to calculate the pressure on the surface, which give rise to the force moving the seal segment away and towards the rotor, labyrinth seal leakage models are used.

Leakage Equations

There are three main basic equations which relate the leakage mass flow rate of fluid through a labyrinth seal to the inlet and outlet pressure: the St. Venant Wantzel equation, Martin's equation [27] and Neumann's equation [85], [99]. Many researchers have derived similar equations and methods, such as Morrow [100], Callendar [101] and Stodola [102]. However the three listed above are the most widely used.

These base equations are then combined with a discharge coefficient, C_D, which accounts for the vena contracta and pressure recovery in the cavity, and a kinetic energy carry over coefficient, C_{ke}, to account for the kinetic energy carried over into the next cavity.

St. Venant Wantzel Equation

The St. Venant Wantzel formula, Eq. (A.1), is derived from the Euler equations, assuming zero inlet velocity, a perfect gas, isentropic acceleration going into the restriction, and

that all the kinetic energy generated at the narrowest part of the restriction is destroyed [103]. The equation calculates the mass flow rate for a single restriction, and so for multiple restrictions an iterative method is required to find the mass flow rate through the whole labyrinth seal. P_i is the static pressure upstream of the restriction, and P_{i+1} is the static pressure downstream of the restriction

$$\dot{m} = \frac{A_c P_i}{\sqrt{RT_i}} \sqrt{\frac{2\gamma}{\gamma - 1} \left\{ \left(\frac{P_{i+1}}{P_i} \right)^{\frac{2}{\gamma}} - \left(\frac{P_{i+1}}{P_i} \right)^{\frac{\gamma+1}{\gamma}} \right\}} \tag{A.1}$$

The St. Venant Wantzel equation can be extended by not assuming zero inlet velocity [103], shown in Eq. (A.2), although in practise the extra accuracy gained in this part of the calculation is insignificant compared the other errors and assumptions. A_{up} is the area of of the channel upstream of the restriction.

$$\dot{m} = \frac{A_c P_i}{\sqrt{RT_i} \sqrt{1 - \left(\frac{P_{i+1}}{P_i} \right)^{\frac{2}{\gamma}} \left(\frac{A_c}{A_{up}} \right)^2}} \sqrt{\frac{2\gamma}{\gamma - 1} \left\{ \left(\frac{P_{i+1}}{P_i} \right)^{\frac{2}{\gamma}} - \left(\frac{P_2}{P_1} \right)^{\frac{\gamma+1}{\gamma}} \right\}} \tag{A.2}$$

Martin's Equation

Martin's equation [27], given in Eq. (A.3), derived in 1908, was the first equation specifically designed for use in labyrinth seals. The equation gives the flow rate through the whole seal in one step, rather than for each restriction. The equation was derived assuming isothermal flow, and that all the kinetic energy is destroyed in the cavities of the seal. Martin's equation was extended by Dollin and Brown [104] for any polytropic process.

$$\dot{m} = \frac{A_c P_{in}}{\sqrt{RT_{in}}} \sqrt{\frac{1 - \left(\frac{P_{out}}{P_{in}} \right)^2}{N - \ln \left(\frac{P_{out}}{P_{in}} \right)}} \tag{A.3}$$

Martin's equation has seen wide usage by other authors such as Egli [30] and Hodkinson [31].

Neumann's equation

Typically referred to as Neumann's equation in other literature [85], [86], [105] although the same equation was found earlier by Kearton and Keh [99]. The version derived by Kearton and Keh is given in Eq. (A.4). The equation assumes isothermal flow, all kinetic energy is destroyed in the seal cavities and zero velocity in the seal cavities.

$$\dot{m} = C_D \frac{A_c}{\sqrt{RT}} \sqrt{F(P_i^2 - P_{i+1}^2)} \tag{A.4}$$

F is a pressure ratio factor, defined in Eq. (A.5), where δP is the pressure drop across a fin.

$$F = 1 + \frac{\delta P}{P_i} + 0.5 \left(\frac{\delta P}{P_i}\right)^2 + 0.75 \left(\frac{\delta P}{P_i}\right)^3 + ... \tag{A.5}$$

If the pressure drop at each restriction is small, then F can be taken as 1.

As reported by Kearton and Keh [99], Eq. (A.4) will deviate from the St. Venant Wantzel formula, Eq. (A.1), by around 3.5% at $P_2/P_1 = 0.80$.

Discharge Coefficient

Authors often use constant coefficients of discharge with their formula for the leakage of steam through a labyrinth seal. For example Hodkinson [31] uses C_D = 0.5, Kearton and Keh [99] C_D = 0.672 for all restrictions except the final restriction where C_D = 0.74. Neumann uses Chaplygin's formula [32], [106] for the discharge coefficient through an orifice for compressible flow, given in Eqs. (A.6) and (A.7). Eser and Kazakia [86] and Yucel and Kazakia [107] revert back to a constant discharge coefficients of C_D = 0.716 and C_D = 0.611 respectively.

$$C_D = \frac{\pi}{\pi = 2 - 5S_i + 2S_i^2} \tag{A.6}$$

$$S_i = \left(\frac{P_i}{P_{i+1}}\right)^{1-\frac{1}{\gamma}} - 1 \tag{A.7}$$

Due to the different velocity profiles under each labyrinth restriction, the discharge coefficient should not be the same for each restriction. The profile of the first restric-

tion shows a larger vena contracta. Further through the seal, the vortex in each cavity reduces the downwards radial momentum of the fluid, reducing the vena contracta effect and producing a greater velocity near the restriction. Therefore the coefficient of discharge will be increasing for subsequent restrictions, as found by Zimmermann and Wolff [92].

Kinetic energy carry-over

The kinetic energy carry over was first treated in detail by Egli [30]. He defined a kinetic energy carry over coefficient C_{ke} by considering a seal with no kinetic energy carry over, and a seal with kinetic energy carry over but with more restrictions to give the same leakage performance. As the leakage is approximately proportional to the square root of the number of restrictions, then the kinetic energy carry over coefficient becomes the square root of the ratio of restrictions, as shown in Eq. (A.8). N_i is the number of restrictions in a seal with no kinetic energy carry-over, and N is the number restrictions in a seal with kinetic energy carry over.

$$C_{ke} = \sqrt{\frac{N}{N_i}} \tag{A.8}$$

Hodkinson

Hodkinson [31] extends the work of Egli [30] by linking the fraction of the kinetic energy carried over to the carry over coefficient. He defines Γ as the fraction of kinetic energy generated at a restriction that is not destroyed and carried into the next restriction. For a single restriction, Hodkinson [31] defines the relationship between this fraction Γ and the kinetic carry-over coefficient C_{ke} by Eq. (A.9). Likewise if the are multiple restrictions, Hodkinson derived Eq. (A.10) assuming density was approximately constant.

$$C_{ke} = \sqrt{\frac{1}{1-\Gamma}} \tag{A.9}$$

$$C_{ke} = \sqrt{\frac{1}{1-\frac{\Gamma(N-1)}{N}}} \tag{A.10}$$

Hodkinson then used his experimental leakage results to find a relationship between the ratio of kinetic energy carried into the next cavity, Γ, and the ratio of fin clearance and fin pitch c/s, assuming that the flow under the fin spreads out uniformly into the cavity, and neglecting the vena contracta. Equation (A.11) shows the relation found by Hodkinson, who also found the best fin to his data when $\tan\theta = 0.02$, or $\theta = 1.15°$.

$$\Gamma = \frac{c/s}{c/s + \tan\theta} \tag{A.11}$$

Vermes

Vermes [108] derived another equation to find Γ, this time based on seal clearance, fin pitch and the fin width, shown in Eq. (A.12). Boundary layer theory was used to arrive the formula. Equation (A.9) is used to then calculate the kinetic energy carry-over coefficient.

$$\Gamma = \frac{8.52}{\frac{s-\tau}{c} + 7.23} \tag{A.12}$$

Neumann

Neumann (via Childs [85]) presented another method of calculating Γ, shown in Eq. (A.13). This is combined with Eq. (A.10) to get the kinetic energy carry-over coefficient.

$$\Gamma = 1 - \frac{1}{\left(1 + 16.6\frac{c}{s}\right)^2} \tag{A.13}$$

Eser and Kazakia [86] used the same model as Neumann for calculating the kinetic energy carry over.

Yucel and Kazakia

Yucel and Kazakia [107] use Eq. (A.14) to find the kinetic energy carry-over coefficient directly, and for all fins except the first. This method was used in the analytical model of the Aerostatic Seal used by Auld [23].

$$C_{ke} = 1 + 0.0791(N - 1) \tag{A.14}$$

Zimmermann and Wolff

Zimmermann and Wolff [109] altered the correlation of Hodkinson, based on their unpublished results. Their altered equation is given by Eq. (A.15)

$$C_{ke} = \sqrt{\frac{1}{1 - \frac{\Gamma(N-1)}{N}}} \sqrt{\frac{N}{N-1}} \tag{A.15}$$

Suryanarayanan and Morrison

Suryanarayanan and Morrison [33] extend Hodkinson's kinetic energy carry over model through CFD analysis, measuring the divergence angle of the jet to work out the kinetic energy carry over coefficient. They found it was largely Re_x and c/s dependant, and independent of compressibility effects (i.e. pressure ratio). They present the following equation for kinetic energy carry over as a function of axial Reynolds number and c/s:

$$C_{ke} = \left(1 - 6.5\frac{c}{s}\right)\left(Re + \left(1 - 6.5\frac{c}{s}\right)^{\frac{-1}{2.454\frac{c}{s}}}\right)^{2.454\frac{c}{s}} \tag{A.16}$$

Conclusion

A large number of equations and correlations have presented. They are of relevance to the Aerostatic Seal as the pressure distribution is governed by the flow through the labyrinth restrictions as well as the feed hole in the centre of the seal segment.

Of the three leakage equations presented here, the most useful for analysis of the Aerostatic Seal is Neumann's equation, given in Eq. (A.4). Martin's equation (Eq. (A.3)) only relates the inlet and outlet pressures with the leakage flow rate, and so there the intermediate pressures are not calculated. The st. Venant Wantzel equation is generally considered to be more accurate [99], although it is much more difficult to use it to calculate pressure as required in the Aerostatic Seal design and analysis method (see Section 3.3).

Appendix B

Pipe Friction Model for Feed Holes

A pipe friction model was considered for the calculation of the flow through the feed hole. The St. Venant Wantzel formula is widely used in aerostatic bearing calculations [88]. As the length of the feed hole would vary in different Aerostatic Seal designs and could be much longer than assumed in aerostatic bearings, then a pipe friction model has the advantage that the length of the feed hole is involved in the calculation of the mass flow rate.

The pipe friction model is iterative and obtains a pressure balance between the inlet and outlet conditions using the Darcy pipe friction model. First an initial approximation is made for the inlet static pressure P_{in} and the inlet Mach number calculated assuming compressible isentropic flow using Eq. (B.1). The inlet static temperature T_{in}, density ρ_{in}, velocity v_{in} and hence mass flow rate $\dot{m}_{in}$ are calculated using Eqs. (B.2) to (B.5). From the density and velocity at inlet, the Reynolds number can be calculated (Eq. (B.6)) and used to estimate the friction factor using the Blasius smooth wall relationship (Eq. (B.7)). If the roughness of the feed hole was known then the Colebrook-White equation could be used instead. Finally the Darcy formula (Eq. (B.8)) is used to provide an updated value for the inlet static pressure based on the friction factor where K_{in} and K_{out} are loss coefficients for the inlet and outlet of the feed hole respectively, and L_c is the length of the feed hole. The inlet loss is taken as $K_{in} = 0.75$, based on CFD results. To ensure convergence an under relaxation factor is included on the new value of static pressure. Once the inlet static pressure has converged, the feed hole mass flow rate is given by Eq. (B.5).

$$M_{in(n)} = \sqrt{\frac{2}{\gamma - 1}\left[\left(\frac{P_{0in}}{P_{in(n)}}\right)^{\frac{\gamma-1}{\gamma}} - 1\right]} \tag{B.1}$$

$$T_{in(n)} = \frac{T_{0in}}{1 + \frac{1}{2}(\gamma - 1)M_{in}^2} \tag{B.2}$$

$$\rho_{in(n)} = \frac{P_{in(n)}}{RT_{in(n)}} \tag{B.3}$$

$$v_{in(n)} = M_{in(n)}\sqrt{\gamma R T_{in(n)}} \tag{B.4}$$

$$\dot{m}_{(n)} = \rho_{in(n)} A_f v_{in(n)} \tag{B.5}$$

$$Re_{(n)} = \frac{\rho_{in(n)} v_{in(n)} d}{\eta} \tag{B.6}$$

$$f_{(n)} = 0.079 Re_{(n)}^{-\frac{1}{4}} \tag{B.7}$$

$$P_{in(n+1)} = P_2 + \left(\frac{4L_c f}{d} + K_{in} + K_{out}\right)\frac{1}{2}\rho_{in(n)} v_{in(n)}^2 \tag{B.8}$$

The above analysis assumes that the inlet flow Reynolds number can be used to determine the friction factor for the whole feed hole, and that the feed hole is not choked. Furthermore the analysis assumes that the pressure drop through the feed hole can be approximated by incompressible Darcy friction factor.

The calculated flow through a typical Aerostatic Seal feed hole is shown in Fig. B.1. Over the range of subsonic pressure ratios, the pipe friction method and the St. Venant Wantzel equation (also referred to as the orifice method) are in close agreement. As there was no other data to give preference to one method or the other, the St. Venant Wantzel equation was used in the analytical methodology as it computationally quicker.

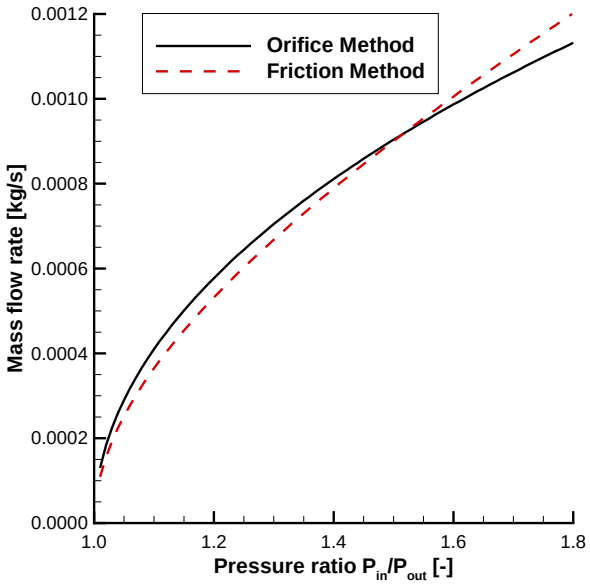

Figure B.1: Flow through feed holes: comparison of methods.

Appendix C

Additional results table: Axial Thrust Compensation

k /	Axial thrust / N					1.0 bar Outlet				3.0 bar Inlet				6.0 bar Inlet			
N mm^{-1}	F_{ax}	F_{ax0}	F_{ax1}	F_{ax2}	F_{ax3}	C_{URS}	C_{DRS}	ΔP / Pa		C_{URS}	C_{DRS}	ΔP / Pa		C_{URS}	C_{DRS}	ΔP / Pa	
								Close	Retract			Close	Retract			Close	Retract
N/A	0	N/A	N/A	N/A	N/A	1.371	0.228	14263	10503	0.948	0.171	14619	14864	0.582	0.106	18003	15702
2.03	38.2	10.6	8.6	8.0	10.9	1.24	0.20	10794	11950	N/A	N/A	N/A	N/A	N/A	N/A	N/A	N/A
2.03	58.6	6.0	13.0	13.2	16.3	1.190	0.203	12115	9649	N/A	N/A	N/A	N/A	N/A	N/A	N/A	N/A
5.28	56.6	15.8	11.3	13.7	15.8	1.175	0.196	9481	8899	N/A	N/A	N/A	N/A	N/A	N/A	N/A	N/A
5.28	60.0	16.7	13.3	13.3	16.7	0.840	0.136	9659	18259	0.503	0.086	10217	21525	0.439	0.063	8623	20208
5.28	70.4	19.5	15.5	15.9	19.5	1.129	0.189	8528	9299	N/A	N/A	N/A	N/A	N/A	N/A	N/A	N/A
5.28	77.8	20.5	17.5	18.6	21.4	0.704	0.141	11837	13262	N/A	N/A	N/A	N/A	N/A	N/A	N/A	N/A
5.28	98.6	25.5	22.3	23.4	27.5	0.302	0.072	15177	11049	N/A	N/A	N/A	N/A	N/A	N/A	N/A	N/A
15.00	106.0	35.0	18.0	18.0	35.0	0.126	0.034	14874	11898	0.110	0.033	15428	8985	0.120	0.020	16411	8057
15.00	204	56.7	37.7	52.9	59.0	0.323	0.094	24449	N/A	N/A	N/A	N/A	N/A	N/A	N/A	N/A	N/A

Table C.1: Key axial spring test results.

Appendix D

Springs

Measurement of spring stiffness

Measurements have been taken to calculate the spring stiffness of the circumferential and axial springs. All springs were supplied by 'Flexo Spring Ltd'. Springs were manufactured to British Standard BS 1726: Part 1 Grade 2. The material was BS5216, Grade ND3 spring steel.

Circumferential springs

The measured circumferential spring stiffness is given in Table D.1. Spring 'Sp1 14.42' was tested 6 times to evaluate the repeatability of the spring constants measured. All the other springs were tested once. The range for the six repeated tests was $0.11\,\mathrm{N\,mm^{-1}}$.

Some springs were measured with and without the 'base' to see the effect on the spring rate. The base was a small insert which would stop the end of the circumferential spring moving inside the spring hole, as shown in Fig. 3.17. Due to the interference fit between the spring and the base, then it may have introduced extra stiffness due to friction between the spring and the base. The difference due to the base was $0.13\,\mathrm{N\,mm^{-1}}$ which was approximately the same as the measured range of spring stiffness. Therefore it was concluded that the difference was negligible.

Axial springs

The measured axial spring stiffness is given in Table D.2.

Spring Name	Nominal rate N mm^{-1}	Measured Rate N mm^{-1}	Free length mm	Outer diameter mm	Wire diameter mm	Nominal Free Length mm	Solid length mm	No. coils	Material	Flexo Sp No.
URS 8.92	8.92	8.67	44.06	10.3	1.63	44.5	22.6	13.9	Spring steel	143414
DRS 8.92	8.92	8.69	44.14	10.3	1.63	44.5	22.6	13.9	Spring steel	143414
URS 17.59	17.59	17.71	38.09	10.2	1.83	38.1	23.3	12.8	Spring steel	143512
DRS 17.59	17.59	17.62	38.06	10.2	1.83	38.1	23.3	12.8	Spring steel	143512
Sp1 14.83	14.83	15.04	44.22	10.2	1.83	44.5	27.0	14.8	Spring steel	143514
Sp2 14.83	14.83	15.05	44.22	10.2	1.83	44.5	27.0	14.8	Spring steel	143514
Sp3 14.83	14.83	15.03	44.22	10.2	1.83	44.5	27.0	14.8	Spring steel	143514
Sp4 14.83	14.83	15.01	44.22	10.2	1.83	44.5	27.0	14.8	Spring steel	143514

Table D.1: Static rig circumferential springs.

Spring Name	Nominal rate	Measured Rate	Outer diameter	Wire diameter	Nominal Free Length	Solid length	No. coils	Material	Flexo Sp No.
	$N\,mm^{-1}$	$N\,mm^{-1}$	mm	mm	mm	mm	mm		
AX00a	2.03	1.91	8.1	0.91	27.5	10.2	11.2	Spring steel	B7-4240-2M
AX01a	2.03	1.89	8.1	0.91	27.5	10.2	11.2	Spring steel	B7-4240-2M
AX02a	2.03	1.93	8.1	0.91	27.5	10.2	11.2	Spring steel	B7-4240-2M
AX03a	2.03	1.90	8.1	0.91	27.5	10.2	11.2	Spring steel	B7-4240-2M
AX00b	5.28	5.12	8.8	1.22	27.5	14.0	11.5	Spring steel	B9-4247-2M
AX01b	5.28	5.10	8.8	1.22	27.5	14.0	11.5	Spring steel	B9-4247-2M
AX02b	5.28	5.06	8.8	1.22	27.5	14.0	11.5	Spring steel	B9-4247-2M
AX03b	5.28	5.09	8.8	1.22	27.5	14.0	11.5	Spring steel	B9-4247-2M
AX00c	15.0	15.7	9.6	1.63	27.5	18.0	11.1	Spring steel	C1-4254-2M
AX01c	15.0	16.5	9.6	1.63	27.5	18.0	11.1	Spring steel	C1-4254-2M
AX02c	15.0	16.1	9.6	1.63	27.5	18.0	11.1	Spring steel	C1-4254-2M
AX03c	15.0	16.3	9.6	1.63	27.5	18.0	11.1	Spring steel	C1-4254-2M

Table D.2: Static rig axial springs.

Appendix E

Orifice Plate Mass Flow Rate Calculation

Orifice plates have been used to measure the mass flow rate of air through the non-rotating rig and the 'Durham Rotating Seals Rig'.

The international standard BS EN ISO 5167-2 was used to design a set of orifice plates and orifice plate holders. A code was developed and incorporated into the Durham Software for Windtunnels suite of programs, based upon the equations detailed in BS EN ISO 5167-2.

The mass flow rate was determined by:

$$\dot{m} = \frac{C_D}{\sqrt{1-\beta^4}} \epsilon \frac{\pi}{4} d^2 \sqrt{2\rho_1 \Delta P} \tag{E.1}$$

$$\beta = \frac{d}{D} \tag{E.2}$$

The discharge coefficient C_D was calculated by the Reader-Harris/Gallagher equation given in Eq. (E.3) for an orifice plate with corner tappings and outer diameter less than $71.12\,\text{mm}$. ρ_1 is the density of the fluid at the upstream pressure tapping. D is the diameter outer diameter, and d is the orifice diameter.

$$C_D = 0.5961 + 0.0261\beta^2 - 0.216\beta^8 + 0.000521\left(\frac{10^6\beta}{Re_D}\right)^{0.7} + (0.08188 + 0.0063A)\beta^{3.5}\left(\frac{10^6}{Re_D}\right)^{0.3} + 0.011(0.75 - \beta)\left(2.8 - \frac{D}{25.4}\right) \quad \text{(E.3)}$$

The 'expansibility' factor ϵ is given by:

$$\epsilon = 1 - (0.351 + 0.256\beta^4 + 0.93\beta^8)\left[1 - \left(\frac{P_2}{P_1}\right)^{1/\gamma}\right] \quad \text{(E.4)}$$

P_1 and P_2 are the pressures at the upstream and downstream pressure taps respectively.

Orifice plate holders were designed for this project to accept a wide range of orifice plate designs with different orifice sizes, to optimise the measurement capability for differing flow rates. The designed orifice plate holders were designed to bolt between two 2 inch flanges, as shown in Fig. E.1. The holders feature corner tappings to measure the pressure differential, and the corner tappings were sized according to BS EN ISO 5167-2.

A Matlab code was developed to specify the desired orifice plate size and calculate the uncertainty in the mass flow measurement over the range of mass flow rates measured.

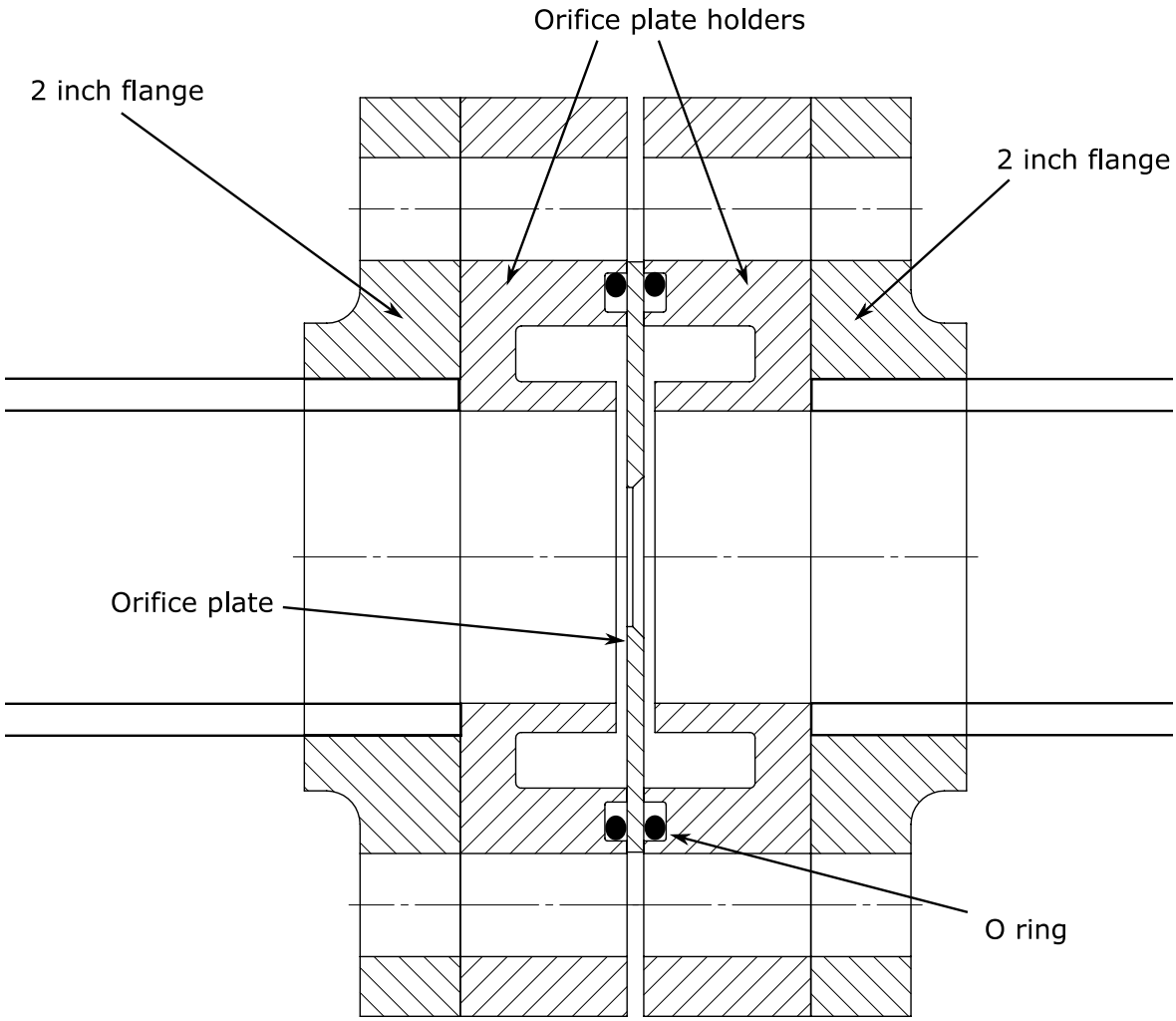

Figure E.1: Cross section of orifice plate and holder

Appendix F

Calculation of Seal Mean Clearance

The circumferential clearance calculation method is described in this appendix.

The calculation method calculates the clearance at all circumferential locations given the measured clearance between the rotor surface and seal segment teeth at two specified points. The clearance area and the segment angle about the axial plane (ψ) is also calculated.

θ_{URS} and θ_{DRS} are the circumferential locations of the displacement sensors (i.e. capacitive or inductive sensors. The rotor and seal segment are assumed to have the same radius which is a design choice in all but the 'MacDonald 1' seal design. Fig. F.1 shows the nomenclature for the calculation method.

A polar coordinate system is set up based at the centre of the rotor. The centre of the seal segment is (g_x, g_y), with polar coordinates (r_g, θ_g).

Step 1: Calculate the Cartesian coordinates of the measured seal segment positions (X_{URS}, Y_{URS}) and (X_{DRS}, Y_{DRS}).

$$(X_{URS}, Y_{URS}) = \left(\left[\frac{D}{2} + c_{URS} \right] \cos(\theta_{URS}), \left[\frac{D}{2} + c_{URS} \right] \sin(\theta_{URS}) \right) \tag{F.1}$$

$$(X_{DRS}, Y_{DRS}) = \left(\left[\frac{D}{2} + c_{DRS} \right] \cos(\theta_{DRS}), \left[\frac{D}{2} + c_{DRS} \right] \sin(\theta_{DRS}) \right) \tag{F.2}$$

Step 2: Find the location of the segment centre in Cartesian coordinates. From URS and DRS clearance measurements, c_{URS} and c_{DRS} respectively, the mean point between the sensor location, (b_x, b_y), can be found.

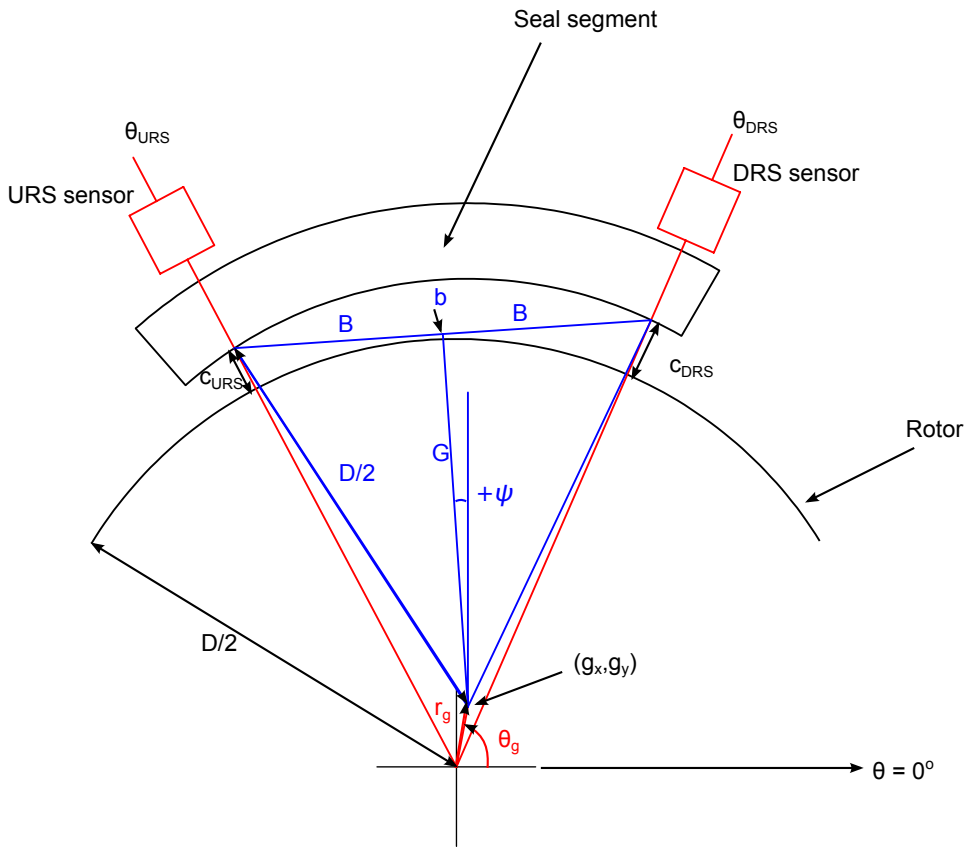

Figure F.1: Seal mean clearance calculation diagram

$$(b_x, b_y) = \left(\frac{X_{URS} + X_{DRS}}{2}, \frac{Y_{URS} + Y_{DRS}}{2} \right) \tag{F.3}$$

$$B = \sqrt{(b_y - Y_{URS})^2 + (b_x - X_{URS})^2} \tag{F.4}$$

$$G = \sqrt{\frac{D^2}{4} - B^2} \tag{F.5}$$

$$\psi = \arctan\left(\frac{Y_{DRS} - Y_{URS}}{X_{DRS} - X_{URS}} \right) \tag{F.6}$$

$$(g_x, g_y) = (b_x + G\sin(\psi), b_y - G\cos(\psi)) \tag{F.7}$$

In polar coordinates, the centre of the seal segment is

$$(r_g, \theta_g) = \left(\sqrt{g_x^2 + g_y^2}, \arctan\left(\frac{g_y}{g_x} \right) \right) \tag{F.8}$$

Once the seal segment centre has been found, then the equation in polar coordinates for the seal segment surface relative to the centre of the rotor is:

$$r(\theta) = r_g \cos(\theta - \theta_g) + \sqrt{\frac{D^2}{4} - rg^2 \sin^2(\theta - \theta_g)} \tag{F.9}$$

The seal segment leakage area is then calculated by numerically integrating between the seal segment and the rotor. The integration has been performed using a spreadsheet as well as a Matlab function to calculate the mean clearance of experimental results.

$$\mathrm{d}A = \frac{1}{2}(r_s^2 - r_r^2)\,\mathrm{d}\theta \tag{F.10}$$

Finally the mean clearance can be found from the seal leakage area.

$$c_m = -\frac{D}{2} + \frac{\sqrt{(\pi D)^2 + 24\pi A}}{2\pi} \tag{F.11}$$

$\mathrm{d}\theta$ was set to 0.1° to ensure accuracy. Accuracy was checked with the 3D CAD program SolidWorks which gave agreement within 0.02%

Appendix G

Friction at High Temperature

There is a reasonable amount of friction data available in tribology and wear literature, although there is wide variation in quoted values, mostly due to the wide range of factors influencing friction and subtle changes in the material and test set up. Table G.1 summarises a range of relevant data for the coefficient of friction, mostly at elevated temperature, for chrome carbide on metal. This data was used to inform the design of the 'STR-IP6-07A5' seal for testing in steam.

The range in dynamic friction coefficient is 0.35 – 0.72.

Source	Material 1	Material 2	Temperature °C	Load	Coefficient	Environment
DellaCorte & Sliney [97]	Chromium Carbide	Cobolt Alloy	25-760	4.9 N	0.50-0.60	He
Sen [110]	Chromium Carbide	Hardened AISI D2	19 ± 3	5 N	0.72	Air
Sen [110]	Chromium Carbide	CrC Coated AISI D2	19 ± 3	5 N	0.48	Air
Lindgren & Johnson [111]	Chromium Carbide (Cr3C2-NiCr on 800H base material)	Chromium Carbide (Cr3C2-NiCr on 800H base material)	400	0.69 MPa	0.35-0.70	He
Lindgren & Johnson [111]	Chromium Carbide (Cr3C2-NiCr on 800H base material)	Chromium Carbide (Cr3C2-NiCr on 800H base material)	400	6.9 MPa	0.55-0.70	
Mann & Prakash [112]	Chromium Carbide coated steel disks	Graphite filled Stellite weld deposited chrome-moly vanadium steel pins	550	100 N	0.42-0.47	Air 40% humidity
Cornelius & Roberts [113]	Tungsten-chromium tool steel SM 18	Nitrided steel LK 5	550		0.4	CO2 (Similar in Helium)
Inman & Datta [114]	Nimonic 80A	Stellite 6	630		0.38-0.55	Air

Table G.1: Published friction coefficients at elevated temperature, including chrome carbide

Appendix H

Aerostatic Seal Designs

The full dimensions of all the seal designs are reported here. Table H.1 lists all the dimensions. Figure H.1 shows the seal segment nomenclature.

Parameter	Unit	MacDonald 1	MESS01	ROT-02	STR-IP6-07A2
Fluid	-	Air	Air	Air	Steam
Diameter	mm	732	732	366	300
No. segments per ring	-	6	6	6	6
α	degree	60	60	60	59.7
β	degree	30	30	30	30
θ_{f1}	degree	7.5	7.5	7.5	7.5
θ_{f2}	degree	17.5	17.5	22.5	22.5
Seal Material	-	Aluminium	S355J2	S355J2	X22CrMoV12-1
Design P_{in}	bar(a)	6.0	6.0	1.5	7.5
Design P_{out}	bar(a)	5.16	5.16	1.0	6.0
Design T_{in}	°C	20	20	20	500
No. feed holes	-	4	4	4	4
d	mm	4.0	2.0	1.0	1.2
Segment width	mm	70.0	67.0	37.0	29.0
x_1	mm	5.0	5.0	4.0	9.0
x_2	mm	52.0	37.0	18.0	11.0
x_3	mm	5.0	15.0	10.0	4.0
τ_r	mm	2.0	2.0	1.0	1.0
τ_t	mm	0.5	0.25	0.5	0.25
L_1	mm	10.7	11.0	5.0	4.0
L_2	mm	37.0	37.0	20.0	18.0
L_3	mm	22.0	19.0	12.0	7.0
L_4	mm	4.8	4.8	1.5	2.0
L_5	mm	3.0	3.0	1.5	2.0
H_1	mm	6.0	6.0	3.0	2.5
H_2	mm	8.0	6.0	3.5	2.5
H_3	mm	10.0	6.0	3.0	5.0
H_4	mm	6.0	6.0	3.0	6.0
H_{3a}	mm	0.1	6.2	2.0	3.3
H_c	mm	4.6	0.5	0.5	0.5
H_{3b}	mm	5.3	5.3	1.0	1.2
H_{hold}	mm	4.6	4.6	2.0	3.3
c_n	mm	0.4	0	0	0
k_{sp}	N mm^{-1}	14.42	8.92	5.01	10.2
F_{spl}	N	122	73.6	9.0	10.2
x_{spx}	mm		27.4	15.0	9.0
x_{spr}	mm		16.0	8.51	8.0
x_{spd}	mm	32.0	32.0	19.0	19.0
d_{sp}	mm	16.0	16.0	7.0	7.0
h_{ax}	mm	-	27.0	-	27.0
θ_{ax1}	mm	-	35	-	54
θ_{ax2}	mm	-	25	-	20
Retracted clearance	mm	Set up dependant		1.5	1.2
Minimum clearance	mm	Set up dependant		-0.5	-0.5

Table H.1: Implemented seal designs: geometry and design parameters.

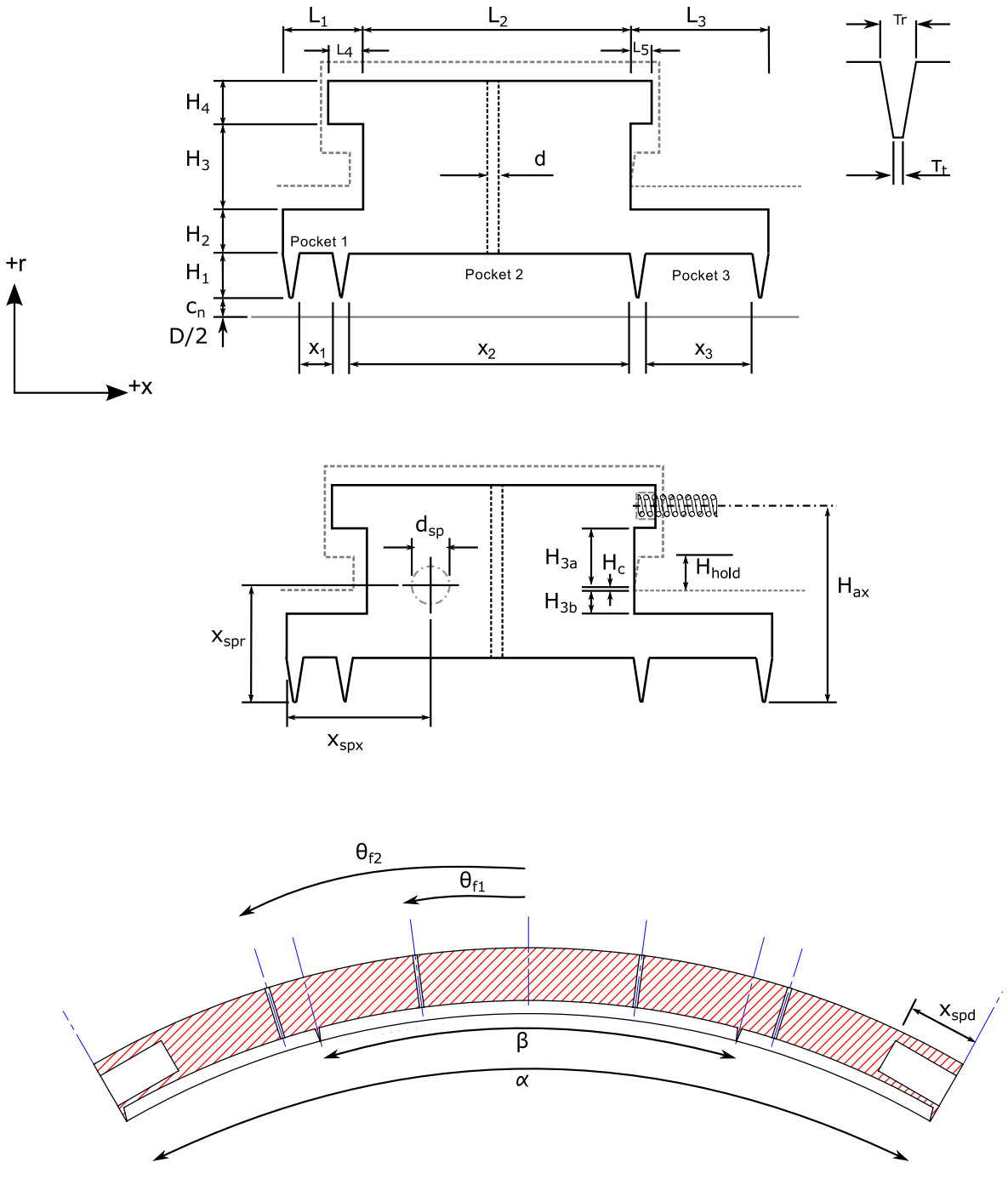

Figure H.1: Seal nomenclature